Trickle Flow Hydrodynamic Multiplicity

Trickle Flow Hydrodynamic Multiplicity

A thesis submitted to the Faculty of Engineering, the Built Environment and Information Technology of the University of Pretoria, Pretoria, South Africa, in partial fulfilment of the requirements for the degree of Philosophiae Doctor (Chemical Engineering)

Werner van der Merwe

27 November 2007

"Hydrodynamics has little significance for the engineer because of the great mathematical knowledge required for an understanding of it and the negligible possibility of applying its results."

Prandtl (1904)

ABSTRACT

Title: Trickle Flow Hydrodynamic Multiplicity

Name: Werner van der Merwe

Promoter: Prof. Willie Nicol

Department: Chemical Engineering

Degree: PhD (Chemical Engineering)

Trickle flow is encountered in a variety of process engineering applications where gas and liquid flow through a packed bed of stationary solid. Owing to the complexities of three interacting phases, a fundamentally exhaustive description of trickle flow hydrodynamics has not been achieved. A complicating factor in describing the hydrodynamics is the fact that the hydrodynamic state is dependent not only on the present operating conditions but also on their entire history, including fluid flow rate changes and pre-wetting procedures. This phenomenon is termed hydrodynamic multiplicity and is the subject of this work. Hydrodynamic multiplicity greatly complicates both the experimental investigation into the behaviour of a trickle flow column and the theoretical modelling of the observed behaviour.

Broadly speaking, this study addresses hydrodynamic multiplicity on three levels. First, a conceptual framework is proposed that can be used to study hydrodynamic multiplicity with limited resources. It is based on the absolute limiting values that the hydrodynamic parameters can adopt for a certain set of conditions, and encompasses both flow rate hysteresis loops and pre-wetting procedures. There are 5 such hydrodynamic modes. When the existing literature is critically evaluated in light of this framework, it is established that the reported experimental studies have not addressed all the issues. Previous modelling

attempts are also shown to be unable to qualitative explain all the existing data. Moreover, authors have suggested different (and often contradictory) physical mechanisms responsible for hydrodynamic multiplicity.

Secondly, an experimental investigation intended to supplement the existing literature and illustrate the utility of the proposed framework is launched. This includes bed-scale measurements of liquid holdup, pressure drop and gas-liquid mass transfer for a variety of conditions including different flow rates, pressures, particle shapes, particle porosity and surface tension. The second part of the experimental effort uses radiography and tomography in new ways to visualise the temporal and spatial characteristics of the different hydrodynamic modes. The tomographic investigation incorporates advanced image processing techniques in order to culminate in a pore-level evaluation of the hydrodynamic modes that reveals additional features of hydrodynamic multiplicity.

Thirdly, the experimental insights are condensed into a set of characteristic trends that highlight the features of hydrodynamic multiplicity. A pore-level capillary mechanism is then introduced to qualitatively explain the observed behaviour. The mechanism shows how the differences in advancing and receding contact angles and the characteristics of the packed structure (or pore geometries) are ultimately responsible for the observed hydrodynamic multiplicity behaviour.

Lastly, the effect of hydrodynamic multiplicity on trickle bed reactor performance is discussed. It is established experimentally that depending on the reaction conditions, different modes yield optimal performance. The idea of optimizing the performance by manipulating the hydrodynamic state is introduced.

In totality, this work advances the understanding of trickle flow hydrodynamics in general and hydrodynamic multiplicity in particular.

Keywords: hydrodynamics, trickle flow, multiphase, hysteresis, pre-wetting, tomography, radiography, image processing, packed bed, multiplicity.

ACKNOWLEDGMENTS

Many people have contributed to making this work possible. Thank you all.

My supervisor, Prof. Willie Nicol, for continued support and guidance, and most of all for supporting professional development opportunities.

Sasol Technology Research and Development for financial support, in particular the efforts of Arno de Klerk. The financial assistance of the National Research Foundation (NRF) towards this research is hereby acknowledged. Opinions expressed and conclusions arrived at, are those of the author and are not necessarily to be attributed to the NRF.

Prof. Muthanna Al-Dahhan and Prof. Mike Dudukovic at the Chemical Reaction Engineering Laboratory (CREL) at Washington University in St Louis, for hosting the high pressure and reaction work in sections 4.4 and 8.3. The assistance of all the other personnel at CREL is also appreciated.

Considerable assistance in generating some of the data came from fellow workers: Dylan Loudon and Ina van der Westhuisen for parts of Chapter 4, Zeljko Kuzeljevic for some of the high pressure data in section 4.3, Frikkie de Beer for technical assistance in the visulaization studies of Chapters 5 and 6, and Arjan van Houwelingen, who collobarated on, amongst other things, the industrial data in section 8.1. Many thanks to Carl Sandrock, Renier Schwarzer, Arjan van Houwelingen, Dylan Loudon and Wouter de Vos for many hours of stimulating discussion on both academic and extra-curricluar topics.

Finally, a debt of gratitude to Annel, who, more than anyone else, believed.

Werner van der Merwe, November 2007

TABLE OF CONTENTS

List of Tables

Number *Page*

List of Figures

Number *Page*

Nomenclature

Symbol	***Definition (units)***
A	Cross-sectional area (m^2)
A	Convolution target in Chapter 6
A	Ergun constant in Chapters 2 and 4
a	Hole area in Chapter 7 (m^2)
a1, a2, a3	Size of ***A***
$A_{\alpha S}$	Interfacial area between phase α and the solid (m^2)
B	Convolution kernel in Chapter 6
B	Second Ergun constant
b	Stoichiometric coefficient
b1, b2, b3	Size of ***B***
C	Concentration in Chapter 8 ($kmol/m^3$)
C	Constant in Chapter 7
C	Convolution of ***A*** with ***B***
c1, c2, c3	Size of ***C***
d	Capillary diameter in Chapter 7
D	Column diameter (cm)
D	Difference operator (convolution kernel)
D	Diffusivity in Chapter 8 (m^2/s)
d	Particle diameter (m)
D_{AX}	Axial dispersion coefficient (m^2/s)
D_h	Hydraulic diameter (m)
d_t	Hydraulic diameter of tube in Chapter 7 (m)
E	Attenuation coefficient (1/m)
E	Edge image
ex, ey, ez	Voxels coordinates
F	Filtered image

F	Force (N)
f	Wetting efficiency
f_s, f_v	Shear and velocity slip factors
F_α	F-function parameter
G	Gas superficial flux (kg/m^{2}s)
g	Gravity acceleration (m/s^2)
Ga	Galileo number
h	Height in Chapter 7 (m)
h	Hough-transform value in Chapter 6 (normalized)
H	Packed height (cm)
$\boldsymbol{I}$	Image
$k_{GL}a_{GL}$	Volumetric gas-liquid mass transfer coefficient (1/s)
$k_{LS}a_{LS}$	Volumetric liquid-solid mass transfer coefficient (1/s)
k_α, $k_{\alpha i}$	Relative permeabilities of phase α
l	Characteristic tube length (m)
L	Liquid superficial flux (kg/m^{2}s)
M	Maldistribtuion factor
m	Mass (kg)
$\boldsymbol{n}$	Normal vector
N	Number of observations (Chapter 2)
N	Number of particles in Chapter 6
P	Pressure in Chapter 4 (Pa)
P	Productivity in Chapter 8 (kmol/s)
Q	Volumetric flow rate (m^3/s)
r	Particle radius (m)
r_c	Radial distance from central axis (pixels or m)
Re	Reynolds number
$\boldsymbol{S}$	Solids image
$\boldsymbol{T}$	Ternary image

t	Threshold in Chapter 6
t	Time (s)
u	Direction normal to edge in Chapter 6
U	Interstitial (or characteristic) velocity (m/s)
u	Velocity (m/s or mm/s)
$\boldsymbol{u}$	Velocity vector (m/s)
$u_{L,pulse}$	Pulsing velocity (m/s)
v	Number of overlaps
V	Volume (m^3)
W_{Pd}	Mass palladium (kg)
X	Conversion
x	Generic hydrodynamic parameter in Chapter 2
x	Thickness in Chapter 5 (m)
z	Length (m)

Greek	***Definition (units)***
ΔH	Heat of reaction (kJ/kmol)
$\Delta P/\Delta z$	Pressure drop (kPa/m)
Δs	Image resolution (pixels or m)
Ω	Stresses
Ψ	Momentum vector
$\beta_{L/G}$	Liquid/Gas saturation
δ	Reduced liquid saturation in Chapter 2 and 4
ε	Porosity
ε_L	Liquid holdup
ϕ	Capillary correction factor for liquid in Chapter 7
γ	Gas- or liquid limitation factor in Chapter 8
λ, ψ	Parameters in Chapter 2

μ	Viscosity (Pa.s)
θ, ϕ	Spherical voxel coordinates in Chapter 6
θ, θ'	Contact angle and bottom contact angle in Chapter 6
ρ	Density (kg/m^3)
ρ_i	Intensity density (1/m^3)
σ	Surface tension (N/m)
σ_α	Tension vector (N/m)
ψ	Capillary correction factor for gas in Chapter 7

Subscripts

0, *o*	Reference
A	Gas phase reagent in Chapter 8
B	Liquid phase reagent in Chapter 8
crit, rec	Critical, receding (Chapter 7)
G, L, g, l	Gas, liquid
i, j, k, m, n, p	Indices in Chapter 6
p	Particle
res	Residual
sub	Substrate
T	Total
v	Volumetric
α	Indicates phase α
β, γ	Indicates liquid and gas phases in Chapter 2

Chapter 1. Introduction

Trickle flow is encountered in packed beds of stationary particles that are subjected to co-current gas and liquid flow at relatively low fluid superficial velocities. Typical applications where trickle flow may be encountered are trickle bed reactors, catalytic distillation columns, trickling filters and absorption columns.

The study of trickle flow hydrodynamics has been the subject of a multitude of research works over the last five decades. Sadly, a rigorous and fundamentally exhaustive mathematical description of trickle flow dynamics has not yet been achieved. Owing to the difficulties involved in modelling the complexities of three inter-acting phases, it seems that such a fundamental description is unlikely to be developed in the foreseeable future. However, as will be seen from the subsequent chapter, significant progress towards this goal has been made, especially with regards to obtaining phenomenological (semi-empirical) models that capture hydrodynamic trends with reasonable degrees of accuracy. Nevertheless, these models nearly always disagree quantitatively and the level of accuracy is often insufficient to inspire confidence in using their predictions for design purposes. It is for this reason that most authors recommend incorporating as much of the underlying physics as possible into any hydrodynamic investigation.

Hydrodynamics is quantified in terms of *hydrodynamic parameters* (like pressure drop and liquid holdup) that are related in some way to the gas-liquid-solid contacting effectiveness and the operational efficiency of the reactor or column. A phenomenon that greatly complicates the mathematical description of trickle flow hydrodynamics is the fact that these hydrodynamic parameters are path-variables (which are dependent on the history of operation) as opposed to state-variables (which depend only on the present operating conditions). This phenomenon manifests itself in the form of hysteresis loops or multiple hydrodynamic states – in this work these are collectively referred to as

hydrodynamic multiplicity. Although the existence of multiplicity was recognized as early as 1978 (Kan & Greenfield, 1978), it has generally not featured in hydrodynamic models. For example, in their respective comprehensive reviews, Gianetto & Specchia (1992), Larachi et al. (2000), Dudukovic et al. (2002) and Kundu et al. (2003) recommend numerous pressure drop and liquid holdup correlations – none of which incorporate the existence of hydrodynamic multiplicity.

This work addresses the issue of trickle flow hydrodynamic multiplicity. The main objective is to identify the fundamental mechanism behind the observed behaviour. The strategy that was followed to achieve this is outlined in Figure 1. The figure also provides a handy guide to the structure of this thesis as every major chapter directly addresses one or more of the blocks in this figure.

The first step is to critically evaluate previous work in this field. Since any of the hydrodynamic parameters can take on a continuum of values, it is necessary to establish a framework by which the phenomenon can be understood conceptually and studied experimentally. The proposed framework makes it possible to re-interpret the literature and thereby identify issues that need to be addresses experimentally. Experimental investigations therefore form the next major part of this work. This is done both at the bed-scale (macro) and the cluster-of-particles scale (meso). The re-interpretation of the literature and the experimental results makes it possible to compile a list of trends that are the characteristic manifestations of hydrodynamic multiplicity. These characteristic trends then lead to the identification of the controlling physical mechanism that is responsible for the existence of hydrodynamic multiplicity. The trends also set the benchmark by which multiplicity should be modelled.

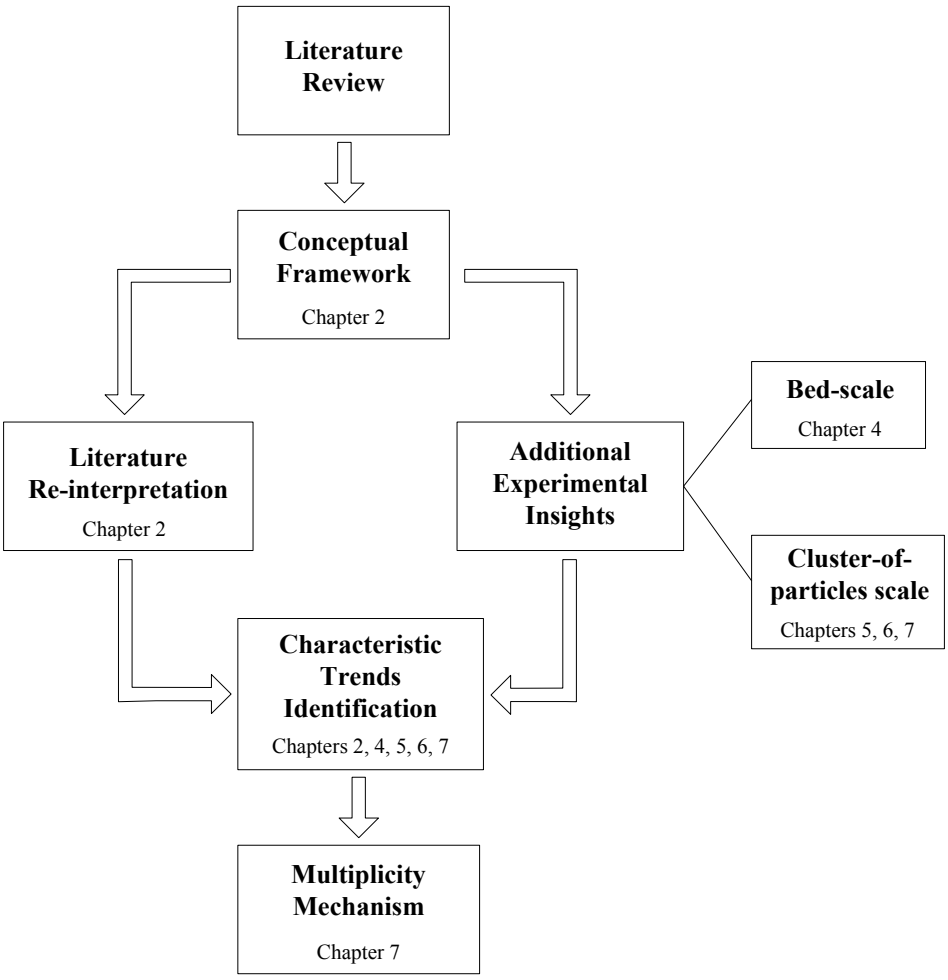

Figure 1. Schematic of the structure of this work.

To round off the work, a final chapter explores the implications of hydrodynamic multiplicity for the typical operation of a trickle bed reactor (both theoretically and experimentally). The novel idea of using hydrodynamic multiplicity to optimize the reactor performance based on the characteristics of the reaction system is introduced.

It is the purpose of this work to advance the fundamental understanding of trickle flow hydrodynamics in general and hydrodynamic multiplicity in particular.

Chapter 2. Literature

This chapter reviews the results of previous hydrodynamic multiplicity studies (Literature Review block in Figure 1). On the basis of the results of these studies a conceptual framework is introduced (Conceptual Framework block) and the literature is re-interpreted in terms thereof (Literature Re-interpretation block). The chapter concludes with listing those characteristic multiplicity trends that can be extracted from literature (part of the Characteristic Trends Identification block in Figure 1). Note that this follows the investigative strategy set out in Figure 1.

There is a large body of literature dedicated to trickle flow hydrodynamics in general and an in-depth review of each study would be superfluous. The reader is referred to several review articles (Satterfield, 1975, Gianetto et al., 1978, Al-Dahhan et al., 1997, Dudukovic et al., 2002, Sie & Krishna, 1998, Kundu et al., 2003). Instead, the scope of this chapter is limited to presenting only the information that is pertinent to the discussion of hydrodynamic multiplicity. In addition, relevant information from multiple sources are summarized into tables where possible. The first section of this chapter deals with definitions and hydrodynamic concepts in general. The second section reviews experimental investigations into hydrodynamic multiplicity and identifies issues that need further experimental clarification. The third section first summarizes the common approaches adopted to model general trickle flow hydrodynamics and then reviews the existing proposals to incorporate multiplicity into hydrodynamic models. This section also includes a critical evaluation of the potential of existing modelling approaches to be extended to include hydrodynamic multiplicity.

2.1 Trickle Flow Hydrodynamics in General

Trickle flow hydrodynamics are studied by measuring hydrodynamic parameters that are linked in some way to the performance of the trickle flow column. Definitions of the most commonly encountered hydrodynamic parameters are given in Table 1. Note that non-isothermal effects are not included in this work, except briefly in connection with the reaction case study reported in Chapter 8.

Table 1. Definitions of hydrodynamic parameters

Parameter	**Notation**	**Definition**
Liquid holdup (liquid saturation)	ε_L (β_L)	Volume of liquid in the bed as a fraction of the total bed volume (volume of liquid as a fraction of the void volume).
Pressure drop	$\left(\frac{\Delta P}{\Delta z}\right)$	Two-phase pressure drop per unit bed length.
Wetting efficiency	f	The fraction of the external solid surface area that is wetted by the liquid.
Gas-liquid mass transfer coefficient	$k_{GL}a_{GL}$	Volumetric gas-liquid mass transfer coefficient. Note that it includes the specific gas-liquid area, primarily because it is difficult to measure the area independently.
Liquid-solid mass transfer coefficient	$k_{LS}a_{LS}$	Volumetric liquid-solid mass transfer coefficient (including the liquid-solid mass transfer area).
Liquid phase axial dispersion	D_{AX}	A measure of the mixedness of the liquid phase obtained from residence time distribution analysis.
Liquid maldistribution factor	M	A measure of the cross-sectional distribution of the liquid in the bed. The exact definition depends on the application.

Table 2 is a summary of the methods by which these parameters are evaluated experimentally. It also includes order-of-magnitude estimates for each parameter as typically encountered in the trickle regime in trickle bed reactors. The different hydrodynamic parameters influence the column's performance as summarized qualitatively in Table 3 (more detail given in context in Chapter 8). The impact is

potentially large and provides a motivation for the study of hydrodynamics. The purpose of any trickle flow unit is to achieve optimal interaction between the gas, liquid and solid phases. For different applications the degrees of optimal interaction between the phases may be different. For example, in a gas-liquid packed absorption column, the key operational parameter is the volumetric gas-liquid mass transfer coefficient. A high degree of gas-liquid interaction is therefore desirable. On the other hand, in a liquid-limited trickle bed reactor, external and internal liquid phase reactant mass transfer rates will likely be more important.

Table 2. Experimental methods by which parameters are determined

Parameter	**Method(s) of determination**	**Approximate range**
Liquid holdup	Gravimetry (weighing) Mean residence time (tracer methods) Radiography Tomography	0.01 – 0.3
Pressure drop	Differential pressure transducer	0.1 – 20 kPa/m
Wetting efficiency	Residence time distribution analysis Colorimetry Physical methods (force balance)	0.2 – 1.0
Gas-liquid mass transfer coefficient	Physical desorption	10^{-2} – 10^{0} s^{-1}
Liquid solid mass transfer coefficient	Dissolution techniques Electro-chemical probe	10^{-2} – 10^{0} s^{-1}
Liquid phase axial dispersion	Residence time distribution analysis	10^{-4} – 10^{-2} m^2/s
Liquid maldistribution factor	Annular collector Radiography Tomography	Only relative values are meaningful

Composed from: Saez & Carbonell (1985), Al-Dahhan & Dudukovic (1995), Nemec et al. (2001), Al-Dahhan et al. (2000), Kundu et al. (2003), Marcandelli et al. (2000), Basavaraj et al. (2005), Colombo et al. (1976), Goto & Smith (1975), Piche et al. (2002), Satterfield (1975), Dudukovic et al. (2002), Sederman & Gladden (2001).

Table 3. Impact of hydrodynamics on reactor/column performance

Parameter	Impacts performance as follows:
Liquid holdup	Roughly indicative of the liquid-solid contacting efficiency. High holdup also indicates good radial spreading of liquid and large mass transfer areas. Possibly impacts the extent of homogeneous side reactions.
Pressure drop	Indicative of the overall operating cost (the gas recycle compression is often a main operating cost driver). Sometimes taken as indication of the degree of gas-liquid interaction.
Wetting efficiency	Proportional to the external liquid-solid mass transfer area. Also impacts the particle effectiveness. Different effects in gas- and liquid limited reactions.
Gas-liquid mass transfer coefficient	Potential rate limiting step in applications where gas-liquid mass transfer is critical (for example gas-limited reactions and absorption columns).
Liquid solid mass transfer coefficient	Potential rate limiting step for liquid-limited reactions.
Liquid phase axial dispersion	Significant deviation from plug-flow reduces performance. Also related to the wetting efficiency.
Liquid maldistribution factor	Potentially impacts bed utilization (i.e. some catalyst particles may be completely inactive or catalysing gas phase reactions).

Evaluated from: Satterfield (1975), Dudukovic (1977), Beaudry et al. (1987), Gianetto et al. (1978), Nijhuis et al. (2003), Rajashekharam et al. (1998), Wu et al. (1996), Kan & Greenfield (1978).

2.1.1 Flow Regimes

Co-current gas-liquid flow in packed beds adopts a variety of flow morphologies depending on the bed properties and the operating conditions (Gianetto & Specchia 1992). This has historically been illustrated in the form of a flow chart (Charpentier et al., 1969), as shown in Figure 2. Also shown in Figure 2 are schematic snap-shots of the morphologies in the different flow regimes. Hydrodynamic multiplicity occurs only in the trickle and transition regimes (red shaded area) and the focus will be exclusively on these. Figure 3 indicates the operating regions of 58 of the most recently published studies on trickle bed reactors. Although most of these were performed at laboratory or pilot scale, the trickle and transition regimes are clearly important. The pulsing flow regime has significantly higher pressure drops and volumetric gas-liquid and liquid-solid

mass transfer rates than the trickle regime. Reactors are often operated close to the trickle-to-pulse flow boundary because a good balance between high mass transfer rates (effectiveness) and pressure drop (operating efficiency) is achieved here (an example being oil hydroprocessing, Sie & Krishna, 1998).

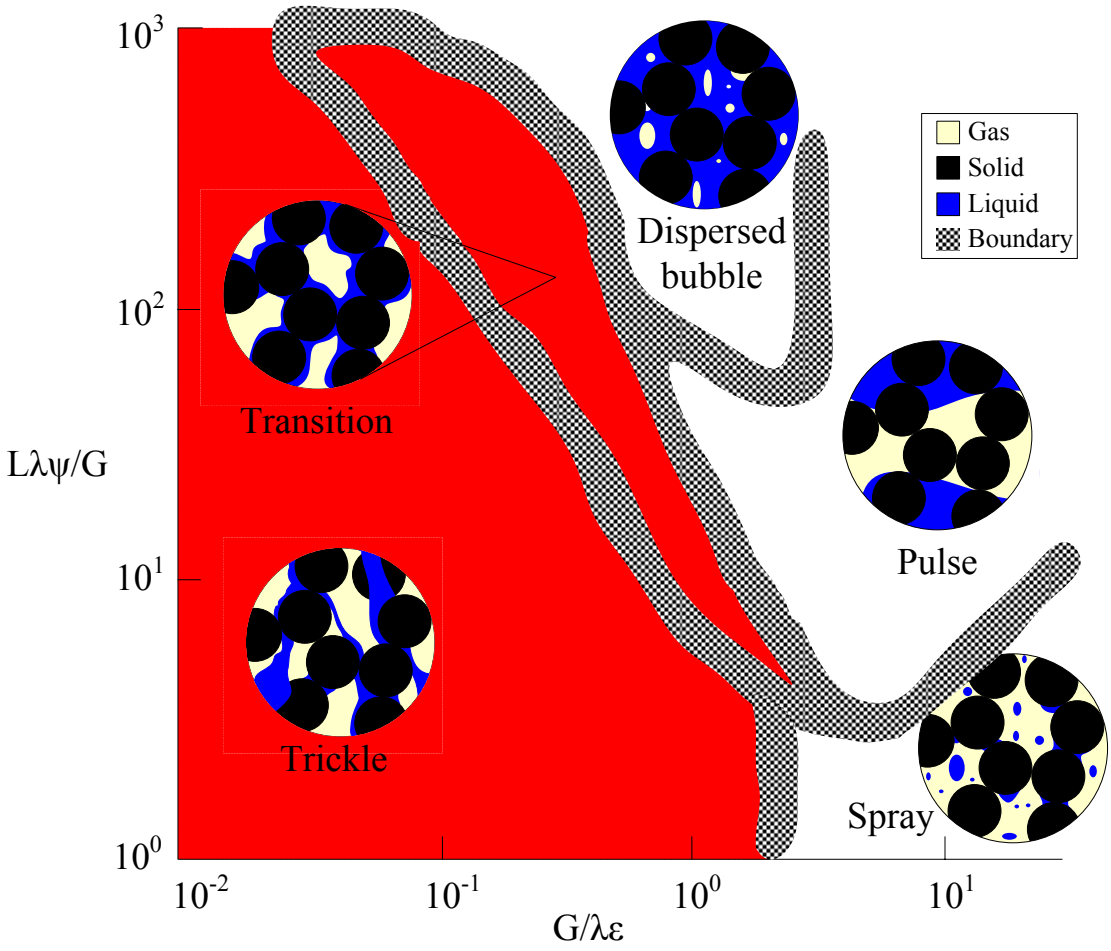

Figure 2. A flow regime map showing the different flow morphologies – the red shaded area shows the regimes where multiplicity exists (based on Charpentier & Favier, 1975, with adaptations from Gianetto et al., 1992, Satterfield, 1975, Sie & Krishna, 1998 and Larachi et al., 1999)

In the pulse, bubble and spray regimes, the flow pattern is transient, while Anadon et al. (2004) has shown that local high frequency instabilities exist in the transition regime. No systematic study of the stability of the flow pattern in the trickle flow regime has been reported, although Kan & Greenfield (1978) and Christensen et al. (1986) report that in

their studies the flow pattern remained stable for at least 24 hours and 2 hours respectively (see Chapter 5).

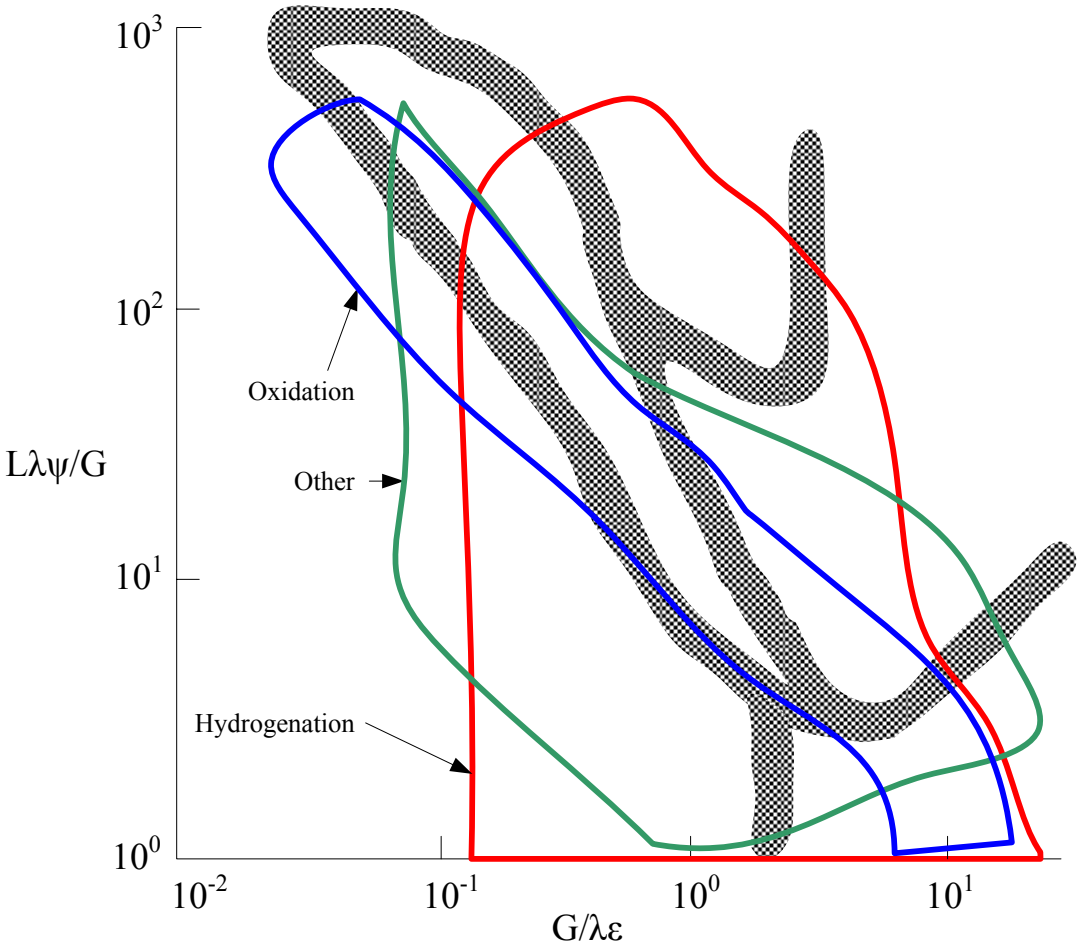

Figure 3. A flow regime map showing the operating velocity ranges of 58 recent trickle bed reactor studies

2.1.2 Hydrodynamic Trends (not associated with multiplicity)

An exhaustive database of experimental data on holdup and pressure drop is now available in literature. From these published results it is possible to qualitatively evaluate the effects of various system and operating conditions on these two hydrodynamic parameters. Table 4 is a form of an inter-connectedness diagram (after Kundu et al., 2003) showing how certain conditions affect the hydrodynamic parameters.

Table 4. Qualitative effect of bed and operating conditions on trickle flow hydrodynamics (based on experimental data)

Bed or Operating Condition	Holdup	Pressure drop	G-L mass transfer	L-S mass transfer	Wetting efficiency	Axial dispersion	Maldistribution factor
Porosity	↓	↓	↑	↑	↓	↑	↓
Particle size	↓	↓	↓	↓	↓	↑	↑
Liquid density	–	↑	↓	?	↓	–	–
Liquid viscosity	↑	↑	↑	?	↑	↓	?
Surface tension	–	↑	↓	?	↓	?	↓
Liquid superficial velocity	↑	↑	↑	↑	↑	↑	↓
Gas superficial velocity	↓	↑	↑	↑	↑	–	↓
Gas viscosity	↑	↑	↑	?	↑	–	?
Pressure (gas density)	↓	↑	↑	↓	↑	?	↓

Composed using data from: Kundu et al. (2003), Larachi et al. (1999), Al-Dahhan & Dudukovic (1995), Al-Dahhan et al. (1997), Lakota & Levec (1990), Saroha et al. (1998), Wang et al. (1999), Piche et al. (2002), Dudukovic et al. (2002).

This table has been compiled from reported trends in the references cited at the end of the table. In rare instances, contradictory trends were reported and the more commonly accepted one is shown in the table. Green arrows indicate that an increase in the operating condition (first column) results in an increase in the hydrodynamic parameter. Red arrows and yellow bars indicate an inverse relation and a negligible effect respectively. A question mark indicates that there is no conclusive data. For example, examining the first row of this table we see that increasing the bed porosity decreases the holdup (first row,

second column), but increases the axial dispersion coefficient (first row, seventh column). This table excludes a few issues that bear mentioning:

- It is desirable is to have the *bed diameter to particle diameter ratio* larger than 25 (Prchlik et al., 1975) or 20 (Sie & Krishna, 1998) in order to avoid the fact that wall-flow effects alter the bed-averaged parameter values. This is difficult to achieve in practice (Al-Dahhan et al., 1995b) and other authors have suggested that values between 12 and 18 are satisfactory (Gierman, 1988, Herskowitz & Smith, 1983). For single phase flow a value of 10 is considered sufficient (Nemec & Levec, 2005a).
- *Bed height* similarly influences the hydrodynamics only if too short a bed is used. However, if a uniform liquid distributor is used at the top of the bed, a bed length larger than 200 mm ensures that entrance effects are negligible (using the correlation in Gianetto et al., 1992 for typical trickle flow conditions).
- More than one *packing method* exist (including sock, dense and loose loading). However, there is little evidence that it impacts the hydrodynamics apart from its effect on bed porosity. Nemec et al. (2005b) recently showed that the *shape of the particles* (spheres, cylinders, extrudate) has little effect on the hydrodynamics, except when hollow cylinders are used. Larachi et al. (1999) incorporated a sphericity factor into their artificial neural network equations. Keeping all other operating variables constant (including effective diameter), both pressure drop and liquid holdup increase with a decrease in sphericity.
- The top-of-bed *liquid distribution* drastically influences the flow pattern (Ravindra et al., 1997b), but a drip-point-density exceeding 5000 points per m^2 is sufficient to negate the initial maldistribution (Burghardt et al., 1995).
- The liquid-solid *contact angle* affects the way that the liquid spreads over the solid and therefore impacts the hydrodynamics indirectly. In general, porous particles are considered to have contact angles close to zero (Ravindra et al., 1997b).

- The trickle-to-pulse flow *regime transition* shifts to higher gas and liquid velocities when the pressure (or gas density), particle diameter, porosity or surface tension is increased and to lower velocities for higher liquid density. The fluid viscosity has little effect in the typical ranges (Larachi et al., 1999, Al-Dahhan et al., 1997). Enlarging the trickle flow regime makes hydrodynamic multiplicity more important.
- There is no indication that the operating *temperature* has any influence on the hydrodynamics apart from changing the fluid properties and possible liquid vaporization effects (Dudukovic et al., 2002).

In addition to the trends mentioned so far, the hydrodynamic parameters themselves are obviously inter-connected. For example, a higher wetting efficiency is obviously associated with increased liquid-solid mass transfer area and therefore a higher volumetric mass transfer coefficient. However, this assumes that whatever mechanism that was responsible for the increased wetting has not also influenced k_{LS} as well (which is unlikely in general). A cause-effect diagram (as used by Kundu et al., 2003) is misleading. For example, wetting efficiency increases with increasing holdup. Now, it is true that increased holdup results in better spreading and therefore higher wetting efficiency. It is also true that higher wetting corresponds to increased liquid-solid drag force area which in turn results in increased holdup. Wetting and holdup therefore have a symbiotic relationship that is more complex than a cause-effect diagram can indicate. There are many such complexities involved here and they are the motivation behind presenting Table 4 without the inter-connections between the hydrodynamic parameters themselves.

This concludes a brief overview of trickle flow hydrodynamics that serves as the background for an investigation into hydrodynamic multiplicity. The trends reported in this section will be re-examined (and to a fair degree explained) in connection with the hydrodynamic models of section 2.3.

2.2 Experimental Investigations into Multiplicity

Hydrodynamic multiplicity was first noticed by Kan & Greenfield (1978) and has since enjoyed ample attention from various researchers. This section presents the data of all previous experimental studies that incorporate hydrodynamic multiplicity in the broadest sense of the word. This excludes the well-known but unrelated phenomenon of temperature induced hysteresis that is due to the thermal capacity of the solid in a non-isothermal reaction (Watson & Harold, 1993). Recall that the term hydrodynamic multiplicity is taken to include both hysteresis loops and the effects of pre-wetting. It is first important to explore the relationships between hysteresis loops, pre-wetting procedures and periodic operation.

2.2.1 Hysteresis and Pre-wetting

There are two major concepts involved in previous experimental studies: hysteresis loops and pre-wetting procedures. Hysteresis loops involve increasing and then decreasing some operating variable (like liquid flow rate) during operation, whereas pre-wetting refers to some procedure (like flooding and/or draining) that is applied to the bed before operation commences. Hysteresis loops were the first manifestations of hydrodynamic multiplicity and judging from recent literature it remains the preferred way of thinking about hydrodynamic multiplicity. A recent review from Maiti et al. (2006) summarizes the early major works on hysteresis loops. A hysteresis loop is shown schematically in Figure 4. For illustrative purposes pressure drop is shown as a function of liquid velocity. The hysteresis loop is obtained as follows:

- Starting from a low (or zero) liquid velocity, the liquid flow rate is increased incrementally. The pressure drop increases accordingly (following the blue line) and reaches points A, B and C at liquid velocities $u_{L,1}$, $u_{L,2}$ and $u_{L,pulse}$ respectively.
- Further increasing the velocity beyond the trickle-to-pulse flow boundary also increases the pressure drop (following the grey line).

- When the velocity is decreased, the pressure drop decreases along the same path (grey) until $u_{L,pulse}$ is reached. Further decreasing u_L sees the pressure drop decreasing along the black line (which may be several times higher than the corresponding values on the increasing blue leg). At $u_{L,1}$ the pressure drop reaches point D. Note that all the operating conditions at this point are identical to those at point A – the only difference between the upper and lower legs is the history of the flow rate.

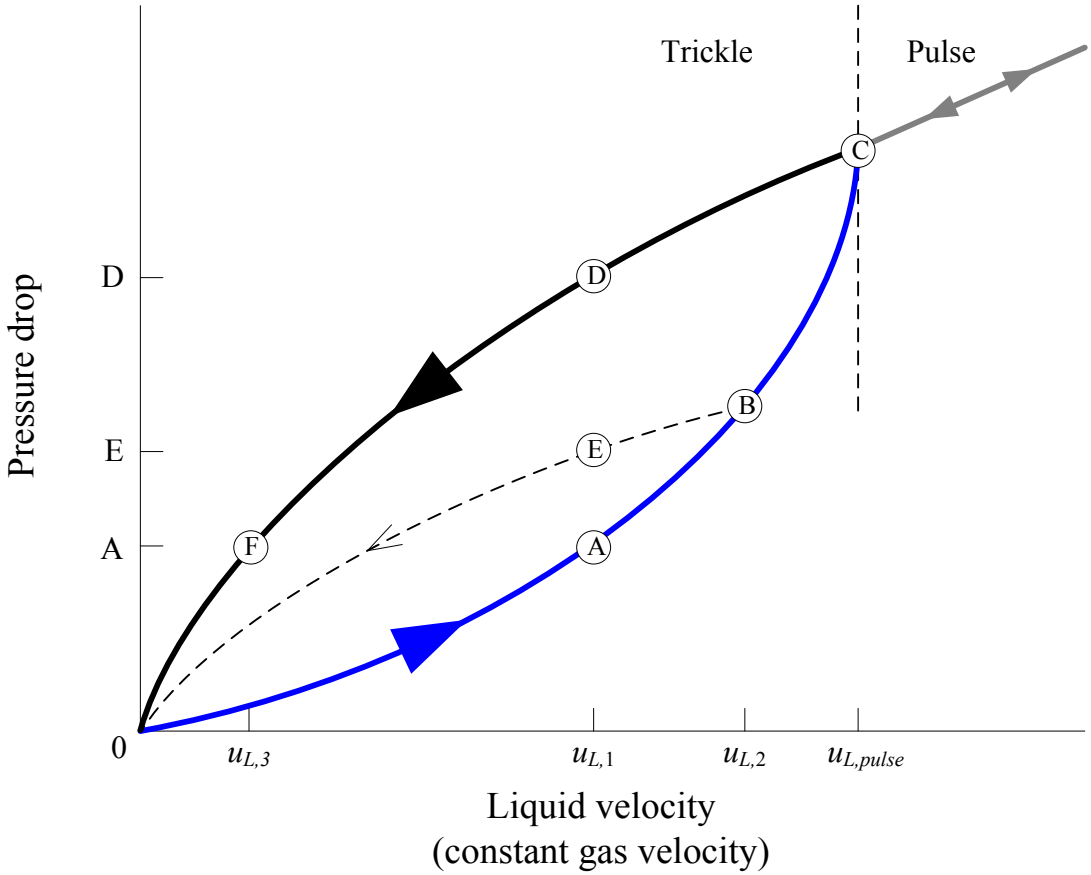

Figure 4. A schematic hysteresis loop (based on Levec et al., 1986)

Interestingly, when the liquid velocity is increased from zero to $u_{L,2}$ (which is smaller than $u_{L,pulse}$) and then decreased, the pressure drop follows the dashed line and reaches point E at $u_{L,1}$. This means that at $u_{L,1}$, any pressure drop between that of points A and D can be attained. It is important to note that all of these observations are at steady state, i.e.

when the flow rate is increased from zero to $u_{L,1}$, the pressure drop stabilizes at point A and when the flow rate is decreased from $u_{L,pulse}$ to $u_{L,1}$, pressure drop stabilizes at point D. Figure 4 depicts a *liquid flow rate variation induced hysteresis loop* because the liquid flow rate was manipulated in order to achieve a change in the hydrodynamic state. There can also be *gas flow rate variation induced hysteresis loops* (where the liquid flow rate is kept constant and the gas flow rate is manipulated to get hysteresis) or *surface tension change induced hysteresis* (where the surface tension is changed momentarily before returning it to the original value).

Hysteresis loops are not the only manifestations of hydrodynamic multiplicity. Since the hydrodynamic state of the bed depends critically on earlier conditions within the bed, it can also be altered by adopting a different pre-wetting procedure. For example, Kan & Greenfield (1978) first performed a liquid flow rate variation induced hysteresis loop (to get to point D on Figure 4) and then performed gas flow rate variation induced hysteresis. Levec et al. (1986), on the other hand, first pre-flooded and drained their bed and then performed liquid flow rate variation induced hysteresis loops. Of course, there are many combinations of pre-wetting procedures and hysteresis loops that can be performed. For example, if we have a bed pre-wetted according to the procedure in Levec et al. (1986) and once operation has been established on the upper branch of the hysteresis loop (say point D in Figure 4), the lower branch (point A) can again be reached by draining the bed and increasing the flow rate from a low value. However, if the bed had not been pre-wetted, draining the bed and re-establishing the flow will result in a pressure drop somewhere between A and D (this will be explored experimentally in Chapter 4). This can obviously become very complicated and it is necessary to define a conceptual framework by which the literature on hydrodynamic multiplicity can be interpreted. This is the first objective of this thesis and is presented next. Afterwards, all previous literature is summarized within this framework.

2.2.2 Framework of Limiting Cases

In the discussion around Figure 4, it was mentioned that the pressure drop can take any value between points A and D. Points A and D are therefore limiting cases for pressure drop variation as a result of liquid flow rate manipulation. A thorough examination of all literature indicates that there are five potential limiting cases of hydrodynamic multiplicity, as defined in Table 5. These procedures will result in one (or more) of the hydrodynamic parameters adopting a maximum (upper limit) or minimum (lower limit) value. The limiting cases are also referred to as *modes*.

Table 5. The five limiting cases (modes) of hydrodynamic multiplicity

Name	Description
Non-pre-wetted mode	Dry particles are loaded into a dry reactor. Gas and liquid flow rates are increased from zero to the operating values.
Levec pre-wetted mode	Dry particles are loaded into a dry reactor. The reactor is flooded completely for several hours and then drained under gravity until only the residual liquid holdup remains in the bed. The liquid and then the gas flow rates are increased from zero to the operating values. (It was observed that draining under gas flow at the operating velocity had a negligible effect on the hydrodynamic state).
Super pre-wetted mode	Dry particles are loaded into a dry reactor. The reactor is flooded completely for several hours and then drained. However, liquid is introduced at the operating velocity the moment that draining commences. Gas is introduced at the operating velocity a few moments after the liquid.
Kan-Liquid pre-wetted mode	Dry particles are loaded into a dry reactor. The reactor is flooded for several hours and then drained. The gas flow is introduced at the operating velocity. Keeping the gas flow rate constant, the liquid flow rate is increased from zero to a value greater than the pulsing velocity and the pulsing regime is maintained for several seconds. The liquid flow rate is then reduced to the operating value.
Kan-Gas pre-wetted mode	Dry particles are loaded into a dry reactor. The reactor is flooded for several hours and then drained. The liquid flow is introduced at the operating velocity. Keeping the liquid flow rate constant, the gas flow rate is increased from zero to a value greater than the pulsing (or spray flow) velocity and the pulsing (or spray) regime is maintained for several seconds. The gas flow rate is then reduced to the operating value.

The importance of this framework is in the fact that it makes it possible to identify categorical differences between the results of different investigators (as will be seen later in this chapter). Also, it suggests that the *extent* of hydrodynamic multiplicity and the major *trends* by which multiplicity manifests itself can be studied experimentally by looking at these five modes. Note that the identification of a conceptual framework is one of the major steps in the strategy outlined in Figure 1.

A few other pre-wetting procedures may be possible. For example, loading the particles into a flooded bed or operating in a liquid up-flow fluidized mode before establishing gas-liquid trickle flow at the operating rates. There is no indication that these procedures will influence the hydrodynamics apart from changing the bed structure and they are of little practical significance.

2.2.3 Holdup and Pressure Drop

Holdup and pressure drop are the two most studied hydrodynamic parameters in literature (Dudukovic et al., 2002). This is because a high value for holdup is generally associated with a large gas-liquid interfacial area and high liquid-solid wetting efficiency (i.e. large liquid-solid area and high particle effectiveness factors). A high pressure drop indicates a high degree of gas-liquid interaction and pressure drop is roughly indicative of the operating cost of the reactor (Kan & Greenfield, 1978).

The behaviour of holdup and pressure drop with gas and liquid flow rate variation in each of the modes is shown qualitatively in Figure 5. It represents an amalgam of the data of the references listed in the figure. The extent has been defined as the area between the upper and lower branches of the pressure drop hysteresis loop obtained by variation of the gas or liquid velocities (Maiti et al., 2005). Such numbers (in units of $\frac{kPa}{m}\frac{m}{s}$) are appropriate when the effects of different operating or system conditions on hysteresis is being examined (Maiti et al., 2006), but do not give us an intuitive feel for the extent and

applies only to pressure drop hysteresis. A simpler measure that most authors report, is the increase (at the same conditions) that is achieved in the value of the hydrodynamic parameter (e.g. pressure drop) when the operating variable (e.g. liquid velocity) is manipulated to its maximum extent. This then is the same as moving from one multiplicity mode to another as shown in Figure 4. **Error! Not a valid bookmark self-reference.** reports such values and is intended to provide a rough indication of how sensitive pressure drop and holdup is to hydrodynamic multiplicity, i.e.:

$$\text{Hysteresis Extent} = \frac{[\text{Value on upper branch}]}{[\text{Value on lower branch}]} \qquad (1)$$

These should be interpreted as the follows: for changes in gas velocity at constant liquid velocity starting from the Kan-Liquid mode (i.e. as shown in Figure 5q), the pressure drop can be *up to 2 times lower* after a gas velocity loop has been completed. This is equivalent to jumping from the Kan-Liquid to the Kan-Gas mode (as studied by Kan & Greenfield, 1978). From Table 6 we see that the pressure drop in the Kan-Liquid mode is up to 2 times higher the pressure drop in the Levec mode (data from Christensen et al., 1986 and Wang et al., 1995). Note also that it is easier to manipulate holdup by changing the liquid flow rate than by changing the gas flow rate. This has also been observed by Christensen et al. (1986) and Levec et al. (1988).

Note that the effect of gas velocity variation induced hysteresis is different in the Levec and Kan-Liquid modes (Figure 5m and Figure 5q). This is attributable to the major flow pattern differences between these modes (Wang et al., 1995) and will be returned to in later chapters.

Table 6 gives a rough indication of the *extent* of multiplicity in pressure drop and holdup as reported by the investigators referenced (the exact values obviously depend on other factors as well). Various definitions exist for expressing the extent of hysteresis.

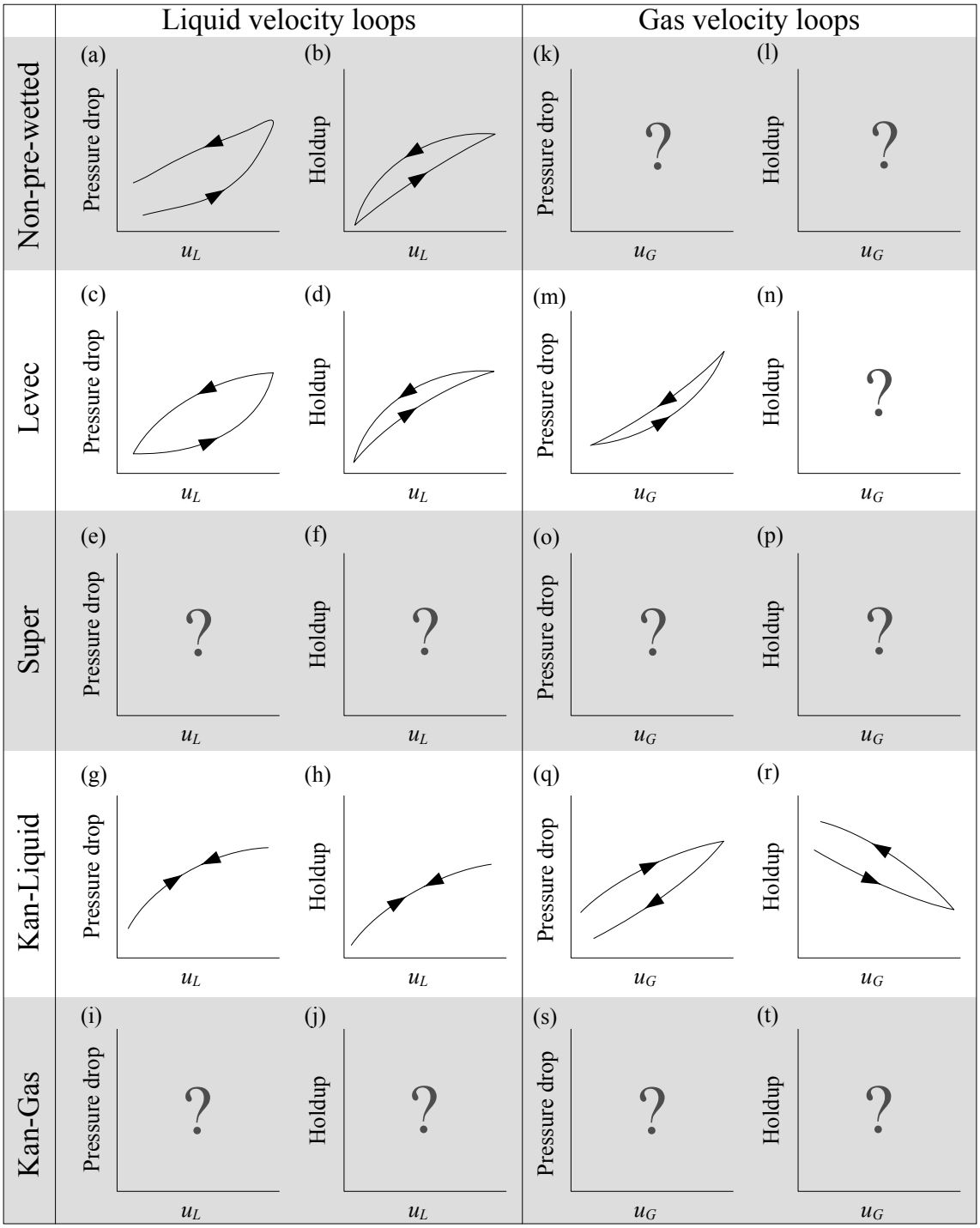

Figure 5. Single loop hysteresis for pressure drop and liquid holdup as functions of liquid (a-j) and gas (k-t) velocities (based on Kan & Greenfield, 1978, Kan & Greenfield, 1979, Levec et al., 1986, Levec et al., 1988, Christensen et al., 1986 and Wang et al., 1995)

The extent has been defined as the area between the upper and lower branches of the pressure drop hysteresis loop obtained by variation of the gas or liquid velocities (Maiti et al., 2005). Such numbers (in units of $\frac{kPa}{m}\frac{m}{s}$) are appropriate when the effects of different operating or system conditions on hysteresis is being examined (Maiti et al., 2006), but do not give us an intuitive feel for the extent and applies only to pressure drop hysteresis. A simpler measure that most authors report, is the increase (at the same conditions) that is achieved in the value of the hydrodynamic parameter (e.g. pressure drop) when the operating variable (e.g. liquid velocity) is manipulated to its maximum extent. This then is the same as moving from one multiplicity mode to another as shown in Figure 4. **Error! Not a valid bookmark self-reference.** reports such values and is intended to provide a rough indication of how sensitive pressure drop and holdup is to hydrodynamic multiplicity, i.e.:

$$\text{Hysteresis Extent} = \frac{[\text{Value on upper branch}]}{[\text{Value on lower branch}]} \qquad (1)$$

These should be interpreted as the follows: for changes in gas velocity at constant liquid velocity starting from the Kan-Liquid mode (i.e. as shown in Figure 5q), the pressure drop can be *up to 2 times lower* after a gas velocity loop has been completed. This is equivalent to jumping from the Kan-Liquid to the Kan-Gas mode (as studied by Kan & Greenfield, 1978). From **Error! Not a valid bookmark self-reference.** we see that the pressure drop in the Kan-Liquid mode is up to 2 times higher the pressure drop in the Levec mode (data from Christensen et al., 1986 and Wang et al., 1995). Note also that it is easier to manipulate holdup by changing the liquid flow rate than by changing the gas flow rate. This has also been observed by Christensen et al. (1986) and Levec et al. (1988).

Note that the effect of gas velocity variation induced hysteresis is different in the Levec and Kan-Liquid modes (Figure 5m and Figure 5q). This is attributable to the major flow

pattern differences between these modes (Wang et al., 1995) and will be returned to in later chapters.

Table 6. Typical differences in pressure drop and holdup due to multiplicity

Modes changed from:	**Illustration**	**Manipulated variable:**	**Extent: Pressure drop**	**Extent: Holdup**
Non-pre-wetted to Super	Figure 5(a-b)	*pre-flooding*	< 3.5	?
Levec to Kan-Liquid	Figure 5(c-d)	u_L	< 2	< 1.4
Levec to Kan-Gas	Figure 5(m)	u_G	< 1.5	?
Kan-Liquid to Kan-Gas	Figure 5(q-r)	u_G	> -2	< 1.1

Data from: Kan & Greenfield (1978), Kan & Greenfield (1979), Levec et al. (1986), Levec et al. (1988), Christensen et al. (1986), Lazzaroni et al. (1989), Ravindra et al. (1997), Wang et al. (1995). **Note:** These data were not generated on the same systems – an issue addressed in Chapter 4.

Other operating variables affect hydrodynamic multiplicity in pressure drop and holdup as listed below. Although these operating variables likely influence the other hydrodynamic parameters as well, no experimental data have been reported.

- *Particle size* – Several authors (Kan & Greenfield, 1978, Levec et al., 1986, Wang et al., 1995, Ravindra et al., 1997b, Gunjal et al., 2005) have shown that an increase in particle size (with little change in porosity) reduces the extent of hysteresis. This is one trend that has not been explained satisfactorily to date (and will be returned to in Chapter 7).
- *Liquid properties* – The major factor is surface tension and has been studied by several authors (see Table 7). Lutran et al. (1991) reports that lowering the surface tension in a Non-pre-wetted bed has the effect of preserving filament/rivulet flow but the rivulets meander less. In the Super mode, lower surface tension resulted in more filament-type flow, although it is unclear what constitutes a filament. In more quantitative terms, Kan & Greenfield (1978), Christensen et al. (1986) and Wang et al. (1995) report that lowering the surface tension increases the pressure

drop but had little effect on the extent of pressure drop hysteresis, while Levec et al. (1986) showed that holdup hysteresis is less pronounced at lower surface tension values.

- *Gas properties* (pressure) – The effect of pressure (or gas density) on the extent of hydrodynamic multiplicity has not been addressed. The general expectation is that increased gas density would result in less hysteresis. This is based on the argument that increased gas density results in increased gas-liquid shear that helps to distribute the liquid (Al-Dahhan & Dudukovic, 1995). Uniform liquid distribution in the bed is in turn associated with less hysteresis (Wang et al., 1995). This is yet to be validated or refuted by experiment (see Chapter 4).
- Levec et al. (1986) investigated the difference in holdup and pressure drop between the Levec and Super modes as *gas velocity* is increased. The results for holdup are shown in Figure 6. Apart from reducing the trickle-to-pulse flow transition liquid velocity, higher gas velocities do not alter the extent of hysteresis except at very high gas velocity.

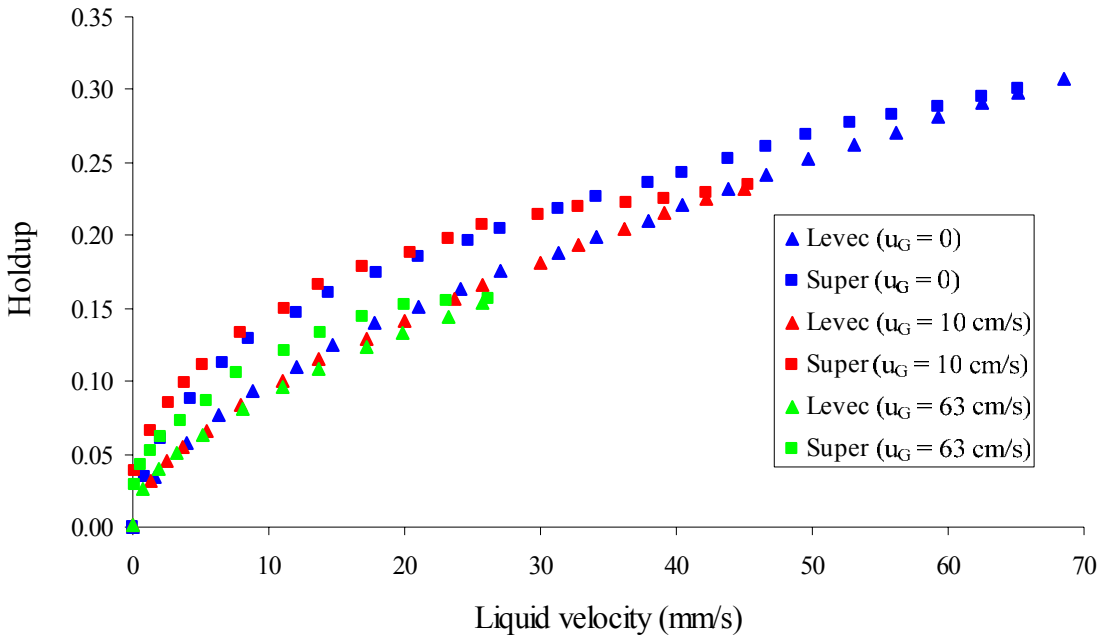

Figure 6. Effect of gas velocity on the difference between Levec and Super modes (data from Levec et al., 1986)

One major drawback in all of these analyses is the fact that none of the authors investigated all the multiplicity modes for their chosen systems. Quantitative comparisons are therefore very difficult to make. See section 4.1 for such quantitative comparisons in all the modes for a single system.

2.2.4 Mass Transfer Coefficients

The volumetric gas-liquid mass transfer coefficient also exhibits multiple hydrodynamic states, as shown by physical desorption/absorption methods. Wammes et al. (1991) reported that the gas-liquid mass transfer area in the Kan-Liquid mode is higher than that in the Levec mode. Wang et al. (1994) and Wang et al. (1997) showed that the volumetric gas-liquid mass transfer coefficient in the Kan-Liquid mode is up to 2.3 times higher than in the Levec mode, while it is up to 1.45 times higher in the Kan-Gas mode than in the

Levec mode. They found that gas velocity variation induced hysteresis starting from the Kan-Liquid mode (i.e. going from Kan-Liquid to Kan-Gas) had little effect on the transfer coefficient. Single loop hysteresis trends are illustrated in Figure 7.

Only one study has reported hydrodynamic multiplicity for the liquid-solid volumetric mass transfer coefficient. Sims et al. (1993) measured averaged particle scale liquid-solid mass transfer coefficients using an electrochemical technique with solid and hollow cylinders. They first established steady flow in the Kan-Liquid mode (i.e. pulse pre-wetting) and then performed liquid flow rate variation induced hysteresis loops. They found that the coefficient on the decreasing leg was up to roughly 1.5 times higher than on the increasing leg (see Figure 7h for a schematic diagram). Note that a similar procedure results in *no hysteresis* of either pressure drop or holdup (refer back to Figure 5).

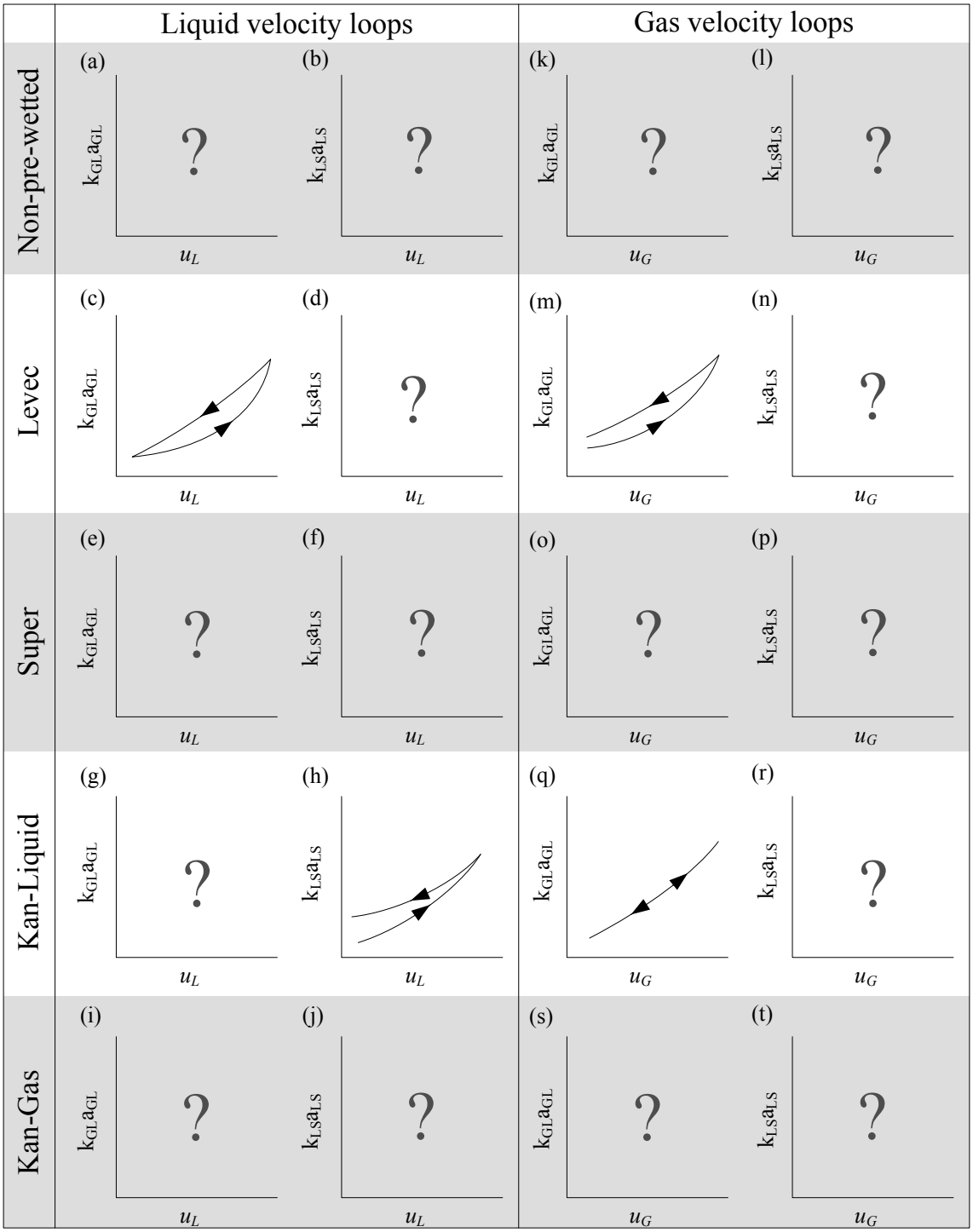

Figure 7. Single loop hysteresis for mass transfer coefficients as functions of liquid (a-j) and gas (k-t) velocities (based on Wammes et al., 1991, Wang et al., 1994, Wang et al., 1997 and Sims et al., 1993)

2.2.5 Wetting Efficiency

Since wetting efficiency impacts the gas-solid and liquid-solid mass transfer areas as well as the particle effectiveness (through the internal diffusion boundary conditions), it is of paramount importance in trickle bed reactor design. This is particularly true for low liquid velocities where hydrodynamic multiplicity can be expected to play a major role. Using colorimetric methods, Lazzaroni et al. (1988 and 1989) showed that the Super mode has larger wetting efficiencies than the Non-pre-wetted mode (up to 3 times higher). They also showed how the wetting is maldistributed over the bed cross-section. Starting from the Super mode, an increase in gas velocity decreased the wetting efficiency (contrary to the results of Al-Dahhan & Dudukovic (1995) who used tracer methods). Ravindra et al. (1997b) later confirmed these results (also using a colorimetric method and different particle sizes and distributors).

Most recently, Van Houwelingen et al. (2006) showed a 16-25% increase in wetting efficiency in going from the Levec to the Kan-Liquid modes and found that gas velocity increases had little effect on the wetting efficiency and the particle wetting distributions. Sederman & Gladden (2001) used magnetic resonance imaging to determine the wetting efficiency and found that the Levec mode had 2.9-3.6 times higher wetting than the Non-pre-wetted mode, and that the Kan-Liquid mode had twice the wetting efficiency of the Levec mode.

2.2.6 Liquid Distribution

The distribution of the liquid over the cross-section has been linked to all of the observed trends mentioned thus far. Originally, Christensen et al. (1986) identified two types of flow: film flow and rivulet or filament flow. Although difficult to quantify, the existence of multiple flow morphologies have been confirmed through other techniques. After extensive experimental work, Wang et al. (1999) concluded that the hydrodynamic multiplicity trends observed in pressure drop, holdup and axial dispersion can be

attributed to hysteresis of the liquid distribution. However, this issue has not received adequate attention in literature (Kundu et al., 2001). It is therefore necessary to review this topic in greater detail.

Liquid maldistribution (M) is usually quantified as the second moment of the distribution of some hydrodynamic parameter (x) around its mean (x_{mean}):

$$M = \sqrt{\frac{1}{N(N-1)}\sum_i \left(\frac{x_i - x_{mean}}{x_{mean}}\right)^2} \qquad (2)$$

Here x can be any of the hydrodynamic parameters listed in Table 2 or it is often taken as the volumetric flow rate of liquid (or gas) through an annular collector cell (Ravindra et al., 1997b, Wang et al., 1998c). An example is given in Figure 8(a). It is imperative to note that the values of M calculated from such data depend critically on how the cross-sectional area is divided (i.e. the area of each cell). Values of M are therefore only meaningful for a specific collector design. When tomography is used, holdup is often chosen as x (see Figure 8(b), Marcandelli et al., 2000). Other approaches have also been followed. Christensen et al. (1986) defined the fraction film flow as the ratio of the velocities in the Kan-Liquid and Levec modes for the same pressure drop (i.e. in Figure 4 the fraction film flow at a pressure drop of A is equal to $u_{L,3}$ divided by $u_{L,1}$), and showed that this fraction increases with liquid velocity (implying that the Levec mode tends more and more to the Kan-Liquid mode as velocity is increased, see Figure 8f). Liquid distribution is generally better at higher liquid velocity (Marcandelli et al., 2000). Lazzaroni et al. (1988) measured wetting in three concentric zones and showed that these follow the local liquid flow rates in these zones. This data was later extended to include other system conditions (non-porous packing and different distributor types) by Ravindra et al. (1997b). Wang et al. (1997) showed how the local liquid flow rate and gas-liquid mass transfer coefficient distributions are related. Later, Wang et al. (1999) showed that pressure drop hysteresis and liquid flux distribution hysteresis are also correlated (the better the liquid flux distribution the higher the pressure drop).

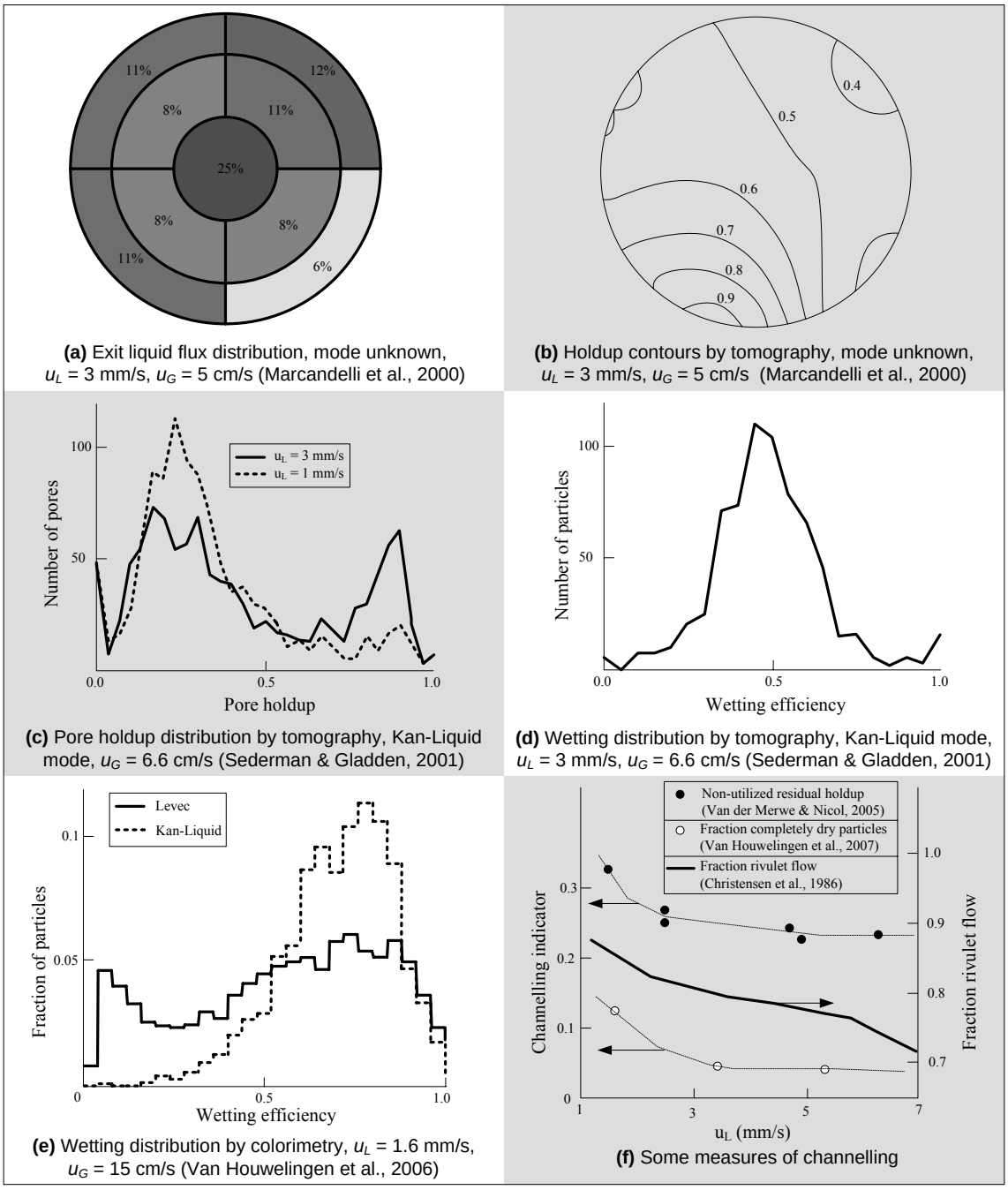

(a) Exit liquid flux distribution, mode unknown, u_L = 3 mm/s, u_G = 5 cm/s (Marcandelli et al., 2000)

(b) Holdup contours by tomography, mode unknown, u_L = 3 mm/s, u_G = 5 cm/s (Marcandelli et al., 2000)

(c) Pore holdup distribution by tomography, Kan-Liquid mode, u_G = 6.6 cm/s (Sederman & Gladden, 2001)

(d) Wetting distribution by tomography, Kan-Liquid mode, u_L = 3 mm/s, u_G = 6.6 cm/s (Sederman & Gladden, 2001)

(e) Wetting distribution by colorimetry, u_L = 1.6 mm/s, u_G = 15 cm/s (Van Houwelingen et al., 2006)

(f) Some measures of channelling

Figure 8. Recent liquid distribution results. (a) Annular collector liquid flux results, (b) Capacitance tomography holdup contours, (c) Pore holdup distribution for two velocities by tomography, (d) A particle wetting distribution (PWD) by tomography, (e) PWDs by colorimetry showing uni-modal and bi-modal character in Kan-Liquid and Levec modes respectively, (f) Levec mode channelling.

Sederman & Gladden (2001) obtained tomographical images of the Non-pre-wetted, Levec and Kan-Liquid modes. They further partitioned the void space into pores and calculated pore holdup distributions (Figure 8c) as well as particle wetting distributions (Figure 8d). They found a bi-modal holdup distribution at higher velocities and took this to be indicative of the actual flow pattern adopting some mixture of film flow and rivulet flow. Basavaraj et al. (2005) used radiographical imaging in a two dimensional bed with non-pre-wetted packing and showed that the holdup is not uniformly distributed throughout the bed even after the liquid flow rate was increased (up to 1 mm/s from 0.2 mm/s) and decreased. In an earlier study (Van der Merwe & Nicol, 2005), the author of this thesis investigated the liquid distribution of the Non-pre-wetted, Levec and Super modes for zero gas flow (Figure 8f). The distribution was quantified in terms of the utilization of the residual liquid holdup. It was found that this utilization coefficient is higher in the Levec mode (values of 0.40-0.85) than in the Non-pre-wetted mode (0.2-0.8) and even higher (close to unity) in the Super mode. The utilization was incorporated into a hysteresis model capable of predicting holdup in each of the modes. Van Houwelingen et al. (2006) used a colorimetric technique to get particle wetting distributions in the Levec and Kan-Liquid modes (Figure 8e). They showed that in the Levec mode particles are either well wetted or very poorly wetted (bi-modal distribution) and took this to indicate rivulet flow. In the Super mode, all the particles were approximately wetted at the bed average, indicating film flow. Recently, Van Houwelingen et al. (2007) have suggested that the best measure of channelling is the fraction of particles that are completely non-wetted, i.e. $f = 0$.

It is imperative to note that these trends are aggravated when point or line distributors are used, but that a perfectly uniform distribution does not change the fact that different flow patterns persist in the different modes (Lutran et al., 1991). Figure 8 shows some of the results of the more recent investigations.

While it is clear that the liquid distribution is central to the understanding of hydrodynamic multiplicity (Wang et al., 1999), it remains unclear why the liquid

distributes itself in these ways and section 2.3 reviews some proposed mechanisms. Resolving this issue is one of the main objectives of this thesis.

2.2.7 Summary of Experimental Studies

Table 7 presents an exhaustive list of all published literature (to date) that investigated some aspect of hydrodynamic multiplicity *experimentally*. It is presented in chronological order. The major findings of these studies have already been summarized in the preceding sections and are not repeated here. Papers based on work in the present thesis have not been included.

Table 7. Summary of experimental studies of hydrodynamic multiplicity

Reference	System properties						Hydrodynamics investigated							Modes investigated				
	u_L (mm/s)	u_G (cm/s)	σ (mN/m)	d (mm)	Porous/ Non-porous	Dist.*	ε_L	$\Delta P/\Delta z$ (kPa/m)	$k_{GL}a_{GL}$ (1/s)	$k_{LS}a_{LS}$ (1/s)	f	D_{AX} (m^2/s)	M	NP	L	S	KL	KG
Kan & Greenfield (1978)	1-10	2-100	38, 70	0.5, 1, 1.8	Non-porous	U	**Y**	**Y**	**N**	**N**	**N**	**N**	**N**	**N**	**N**	**N**	**Y**	**Y**
Levec et al. (1986)	0.1-25	0-40	39-73	3, 6	Non-porous	U	**Y**	**Y**	**N**	**N**	**N**	**N**	**N**	**N**	**Y**	**Y♠**	**Y**	**N**
Christensen et al. (1986)	0-11	0-55	<70, 70	3	Non-porous	U, L	**Y**	**Y**	**N**	**N**	**N**	**N**	**Y**	**N**	**Y**	**N**	**Y**	**Y**
Levec et al. (1988)	0-20	0-21	70	3	Non-porous	U	**Y**	**Y**	**N**	**N**	**N**	**N**	**N**	**N**	**Y**	**Y♠**	**Y**	**Y**
Lazzaroni et al. (1988)	2-6	0-8	≈70	≈3	Porous	U	**N**	**N**	**N**	**N**	**Y**	**N**	**Y**	**Y**	**N**	**Y**	**N**	**N**
Lazzaroni et al. (1989)	0.8-8.4	2-8	≈70	3	Porous	U, P	**Y**	**Y**	**N**	**N**	**Y**	**N**	**N**	**Y**	**N**	**Y**	**N**	**N**
Lutran et al. (1991)	3, 6, 9	0	28-72	3, 6	Non-porous	U, L, P	**N**	**N**	**N**	**N**	**N**	**N**	**Y♣**	**Y♠**	**N♥**	**Y♠**	**N**	**N**
Wammes et al. (1991)	3-12	1, 2.5	?	3	Non-porous	U	**N**	**Y**	**Y**	**N**	**N**	**N**	**N**	**N**	**Y**	**N**	**Y**	**N**
Sims et al. (1993)	1-6	14	≈70	2 x 3	Non-porous	U	**N**	**N**	**N**	**Y**	**N**	**N**	**N**	**N**	**N**	**N**	**Y**	**N**

Y = Yes, **N** = No, * Distributor options: P = Point, L = Line, U = Uniform, Modes: NP = Non-pre-wetted, L = Levec, S = Super, KL = Kan-Liquid, KG = Kan-Gas.
♠ Only with no gas flow, ♣ Only qualitatively, ♥ Authors erroneously grouped Levec and Super modes together.

Table 7. Summary of experimental studies of hydrodynamic multiplicity (continued)

Reference	System properties						Hydrodynamics investigated							Modes investigated				
	u_L (mm/s)	u_G (cm/s)	σ (mN/m)	d (mm)	Porous/ Non-porous	Dist.*	ε_L	$\Delta P/\Delta z$ (kPa/m)	$k_{GL}a_{GL}$ (1/s)	$k_{LS}a_{LS}$ (1/s)	f	D_{AX} (m^2/s)	M	NP	L	S	KL	KG
Wang et al. (1994)	0-15	5-55	70	2.7, 4	Non-porous	?	**N**	**N**	**Y**	**N**	**N**	**N**	**N**	**N**	**Y**	**N**	**Y**	**Y**
Wang et al. (1995)	0-22	5-55	57, 73	2.7, 4, 8	Non-porous	U	**N**	**Y**	**N**	**N**	**N**	**N**	**N**	**N**	**Y**	**N**	**Y**	**Y**
Wang et al. (1997)	0-15	20.8	73	2.7	Non-porous	U	**N**	**N**	**Y**	**N**	**N**	**N**	**Y**	**N**	**Y**	**N**	**Y**	**N**
Ravindra et al. (1997a)‡	1-7	1.7	≈70	1.9	Porous	U	**N**	**N**	**N**	**N**	**N**	**N**	**N**	**Y**	**N**	**Y**	**N**	**N**
Ravindra et al. (1997b)	1-8	5	≈70	1.6/1.9, 3.5, 5.5/6.3	Both	U, L, P	**N**	**Y**	**N**	**N**	**Y♦**	**N**	**Y**	**Y**	**N**	**Y**	**N**	**N**
Rajashekharam et al. (1998) ‡	0.01-0.5	0.2-0.6	?	1, 2	Porous	P	**N**	**N**	**N**	**N**	**N**	**N**	**N**	**Y**	**N**	**N**	**N**	**N**
Wang et al. (1998)	0-17	0-23	≈70	3	Non-porous	U	**N**	**Y**	**N**	**N**	**N**	**N**	**Y**	**N**	**Y**	**N**	**Y**	**Y**
Wang et al. (1999)	0-13	0-23	≈70	3	Non-porous	U	**N**	**Y**	**N**	**N**	**N**	**Y♪**	**Y**	**Y**	**Y**	**N**	**Y**	**N**
Jiang (2000)	0.7-11	?	≈70	3	Non-porous	U, P	**N**	**N**	**N**	**N**	**N**	**N**	**Y**	**Y**	**Y**	**N**	**N**	**N**

Y = Yes, **N** = No, * Distributor options: P = Point, L = Line, U = Uniform, Modes: NP = Non-pre-wetted, L = Levec, S = Super, KL = Kan-Liquid, KG = Kan-Gas.
‡ Reaction study (see Chapter 8), ♦ Only qualitatively, ♪ Reduced second moments of RTD outputs reported.

Table 7. Summary of experimental studies of hydrodynamic multiplicity (continued)

Reference	System properties						Hydrodynamics investigated							Modes investigated				
	u_L (mm/s)	u_G (cm/s)	σ (mN/m)	d (mm)	Porous/ Non-porous	Dist.*	ε_L	$\Delta P/\Delta z$ (kPa/m)	$k_{GL}a_{GL}$ (1/s)	$k_{LS}a_{LS}$ (1/s)	f	D_{AX} (m^2/s)	M	NP	L	S	KL	KG
Sederman & Gladden (2001)	0.5-5.8	6.6-36	≈70	5	Non-porous	U	**Y**	**N**	**N**	**N**	**Y**	**N**	**Y†**	**Y**	**Y**	**N**	**Y**	**N**
Tsochatzidis et al. (2002)	1-20	14	≈70	3.2	Porous	U, HB♫	**N**	**Y**	**N**	**N**	**N**	**N**	**N**	**Y**	**N**	**N**	**Y**	**N**
Basavaraj et al. (2005)	0.2-1	0	?	3.8	Non-porous	L	**Y**	**N**	**N**	**N**	**N**	**N**	**Y**	**Y**	**N**	**N**	**N**	**N**
Gunjal et al. (2005)	0-10	11-44	70	3, 6	Non-porous	U‡‡	**Y**	**Y**	**N**	**N**	**N**	**N**	**N+**	**Y**	**N**	**N**	**Y**	**N**
Van der Merwe & Nicol (2005)	0-17	0	70	3	Non-porous	U	**Y**	**N**	**N**	**N**	**N**	**N**	**Y**	**Y**	**Y**	**Y**	**N**	**N**
Van Houwelingen et al. (2006)	1.6, 5.4	2, 15	≈70	2.5	Porous	U	**Y**	**Y**	**N**	**N**	**Y**	**N**	**Y§**	**N**	**Y**	**N**	**Y**	**N**

Y = Yes, **N** = No, * Distributor options: P = Point, L = Line, U = Uniform, Modes: NP = Non-pre-wetted, L = Levec, S = Super, KL = Kan-Liquid, KG = Kan-Gas.
♫ HB = Half-blocked, ‡‡ Spray and plate distributors used, + Wall pressure fluctuations measured, **§** Distribution inferred from particle wetting distribution, † Pore-scale holdup distribution.

2.3 Hydrodynamic Modelling

2.3.1 Hydrodynamic Modelling in General

There are three broad approaches to correlating or modelling trickle flow hydrodynamics (Dudukovic et al., 2002):

- *Empirical methods:* The relevant hydrodynamic parameters are correlated to dimensionless groups identified by dimensional analysis. These include well-known dimensionless numbers like the Reynolds, Froude, Weber, Lockhart-Matinelli, Eötvos (Bond) and Schmidt numbers. Each number represents the ratio of two forces, namely (Iliuta et al., 1999b) the inertial-to-viscous, inertial-to-gravity, inertia-to-capillary, gas-to-liquid inertia and gravity-to-capillary forces (the Schmidt number being the momentum-diffusivity-to-mass-diffusivity ratio). The physical basis for this type of correlation is that the liquid in the bed experiences the following forces (Fukutake & Rajakumar, 1982): gravitational, inertial, viscous, surface, solid-liquid interfacial and gas-liquid interfacial forces. A correlation usually takes a power-law form. For example, Specchia & Baldi (1977) found that holdup is roughly proportional to $Re_L^{0.55}$. Other commonly used empirical correlations are those of Turpin & Huntington (1967), Ellman et al. (1988), Ellman et al. (1990) and Larachi et al. (1991). However, the pinnacle of empirical correlations is the artificial neural networks (ANN) of the group at Laval University (Larachi et al., 1999, Iliuta et al., 1999a, Iliuta et al., 1999b) that rely on a large database of experimental values. Incidentally, the ANN approach has not been applied to hydrodynamic multiplicity. This thesis aims toward addressing hydrodynamics more fundamentally and the empirical approach is not pursued.
- *Fundamental simulation:* With the advent of increased processing power, several authors have attempted to solve volume-averaged versions of the Navier-Stokes

equations of fluid flow. This computational fluid dynamic (CFD) approach is potentially the most fundamentally sound and rigorous, but suffers from what is generally described to as the closure problem. This refers to the fact that the fluid-fluid and fluid-solid boundaries need closure relations that can at present only be specified empirically (Dudukovic et al., 2002) in order to properly deal with phase interaction and issues like turbulence. Another problem with CFD is the complexity of the pore space in a packed bed. This has led to the use of an ensemble of "representative cells" where each cell encapsulates several particles and is assigned a uniform porosity (see for example Gunjal et al., 2005). It is unclear at this stage how such a cell is to be defined and how its definition impacts the calculated result. CFD is therefore not yet free from some empiricism, but even so exhibits great potential in reactor scale simulation (Kuipers & Van Swaaij, 1997).

- *Phenomenological approaches:* In the phenomenological approach, hydrodynamics are modelled by applying the laws of the conservation of mass, momentum and energy to a postulated geometry that is simple enough so that expressions for each term in these balances can be obtained. The idea has been used with great success to capture hydrodynamic trends (Dudukovic et al., 2002). Nevertheless, phenomenological models always have some adjustable parameters that need to be determined experimentally. Unfortunately, the values of these parameters do not often have sound physical meanings.

The fundamental solution and phenomenological approaches start from the general conservation law (Dudukovic et al., 2002):

(nett rate of output by phase i)
- (nett rate of input by phase i)
+ (nett rate of transport into phase i) (3)
+ (nett rate of generation in phase i)
= (rate of accumulation in phase i)

This equation is written in terms of mass, momentum and sometimes energy conservation for different geometries and on different scales. On the bed-scale and for the case of no inter-phase mass transfer and no change of phase, Iliuta & Larachi (2005) provides a generic expansion for each term, yielding:

$$\frac{\partial}{\partial t}\varepsilon_\alpha \langle \psi_\alpha \rangle^\alpha + \nabla \bullet \varepsilon_\alpha \langle \mathbf{v}_\alpha \rangle^\alpha \langle \psi_\alpha \rangle^\alpha + \nabla \bullet \langle \xi_\alpha \rangle$$
$$= \nabla \bullet \langle \Omega_\alpha \rangle + \varepsilon_\alpha \langle \sigma_\alpha \rangle^\alpha + \frac{1}{V}\iint_{A_{\alpha\beta}} \Omega_\alpha \mathbf{n} dA + \frac{1}{V}\iint_{A_{\alpha\gamma}} \Omega_\alpha \mathbf{n} dA \qquad (4)$$

Accumulation + Inertia + Dispersion
= Surface flux + Source + Transfer from β to α + Transfer from γ to α

Below equation 4, each term has been given a descriptive name. α indicates the phase (i.e. either gas or liquid) and brackets indicate α-phase volume averaged values. Although seemingly complicated, the equation simply re-states equation 3. For example, a momentum balance on the α phase is obtained by setting $\langle\psi_\alpha\rangle^\alpha$ as the momentum vector ($\rho_\alpha \boldsymbol{u}_\alpha$), $\langle\sigma_\alpha\rangle^\alpha$ as the body (gravity) force ($\rho_\alpha \boldsymbol{g}$), $\langle\Omega_\alpha\rangle^\alpha$ represents the pressure and viscous stress, and the last two terms are simply the forces exerted by the gas and solid phases on the liquid (F_{GL} and F_{SL}). Now, assuming constant phase densities, steady, uni-directional (vertical) flow and that the macroscopic inertia is negligible (i.e. the flow is fully developed in the axial direction), the momentum balance (for phase α) further reduces to (Carbonell, 2000):

$$\varepsilon_\alpha \frac{dP_\alpha}{dz} + \varepsilon_\alpha \rho_\alpha g - F_{\alpha\beta} - F_{\alpha S} \qquad \alpha = g, l \quad \text{and} \quad \beta = l, g \qquad (5)$$

Note that we have not assumed full wetting in order to obtain equation 5. It is often easier to arrive at Equation 5 by applying the overall linear momentum balance in integral form to a control volume that includes all three phases (Welty et al., 1984:49). Carbonell (2000) states that the key to obtaining any prediction is in determining the drag forces ($F_{\alpha\beta}$ and $F_{\alpha S}$). While each drag force is nearly always expressed in the Ergun (1952) formulation as the sum of a viscous and an inertial term, various approaches have been

adopted. There are six major approaches to modelling hydrodynamics. They are listed in Table 8, illustrated in Figure 9 (where possible) and discussed thereafter.

Table 8. Six major approaches to trickle flow hydrodynamic modelling

Approach	Comments	References
Relative permeability	Relatively simple. No accounting for partial wetting. Wide applicability. Low level of empiricism.	Saez & Carbonell (1985) Levec et al. (1986) Lakota et al. (2002) Nemec et al.(2001b) Fourar et al. (2001) Nemec et al. (2005a)
Slit models	Range from simple to very complicated with varying degrees of empiricism. Wide applicability. More complicated approaches account for partial wetting.	Holub et al. (1992) Holub et al. (1993) Al-Dahhan et al. (1998) Iliuta et al. (1999c) Iliuta et al. (2000) Iliuta et al. (2002) Iliuta & Larachi (2005)
Fundamental force balance	Low level of empiricism. Fully wetted flow only. Relatively simple and good applicability.	Tung & Dhir (1988) Narasimhan et al. (2002) Attou et al. (1999)
Lattice-Boltzmann simulation	Early stages of development.	Manz et al. (1999) Mantle et al. (2001) Gladden et al. (2003b)
Pore-network models	Relative high levels of empiricism and very complex. Fully wetted flow only. Little experimental validation.	Crine et al. (1979) Chu & Ng (1989) Melli & Scriven (1991)
Computational fluid dynamics	Relatively complex and computationally expensive. Boundary conditions are empirical (closure problem). Capable of dealing with 2 and 3 dimensions. Cannot yet deal with particle scale phenomena.	Jiang et al. (1999) Propp et al. (2000) Souadnia & Latifi (2001) Jiang et al. (2002) Gunjal et al. (2005)

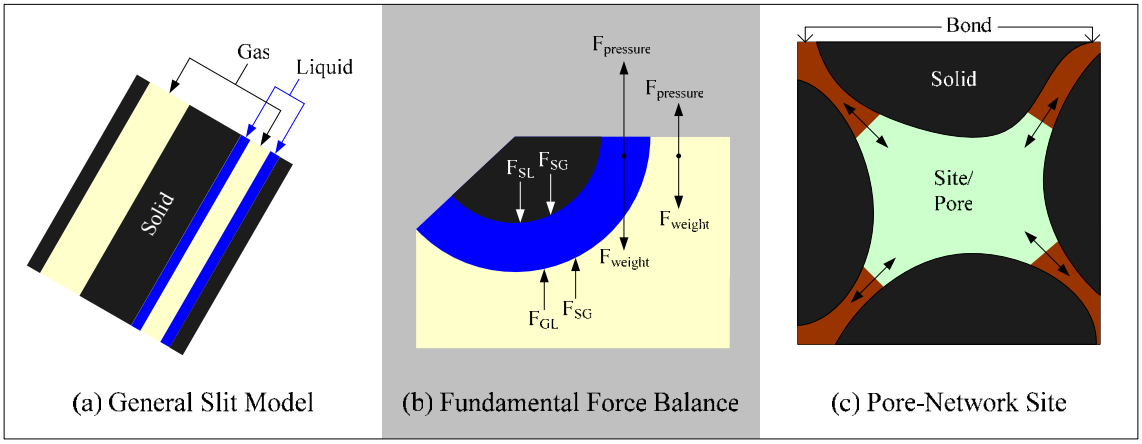

Figure 9. Geometries of three of the six modelling approaches. (a) Double slit model, (b) Fundamental forces, (c) Pore-network. See references in Table 8.

Relative Permeability Concept

The relative permeability idea starts from an Ergun-like equation for one-phase flow in a conduit (Saez & Carbonell, 1985):

$$\left(-\frac{\Delta P}{\Delta z}+\rho g\right)_{1-\text{phase}}=\frac{C_1\mu U}{D_h^2}+\frac{C_2\rho U^2}{D_h} \tag{6a}$$

The first term on the right-hand side is the Hagen-Poisseuille viscous term and the second is an inertial term derived from dimensional analysis. C_1 and C_2 are constants, U is the actual (interstitial) velocity and D_h is the hydraulic diameter (equal to 4 times the phase volume to wetted area ratio, Welty et al., 1984). The *relative* permeability concept now assumes that the two-phase flow pressure drop is equal to the one-phase flow pressure drop provided that the viscous term in equation 6 is divided by a factor k_α and the inertial term by a factor $k_{\alpha i}$:

$$\left(-\frac{\Delta P}{\Delta z}+\rho_\alpha g\right)_{2-\text{phase}}=\frac{C_1\mu_\alpha U_\alpha}{k_\alpha D_h^2}+\frac{C_2\rho_\alpha U_\alpha^2}{k_{\alpha i} D_h} \tag{6b}$$

Here α is again either gas or liquid. Usually, the viscous and inertial factors are assumed to be equal (Saez & Carbonell, 1985) and termed the relative permeability (one for each phase, i.e. k_L and k_G). They are further assumed to be functions of the phase saturations (holdups) only and correlated accordingly. Equation 6b is written for each phase (2 equations) and assuming that the pressure drop of each phase is equal to the other, these can be solved simultaneously for pressure drop and liquid holdup (2 variables). Saez & Carbonell (1985) applied this concept to the available trickle flow data and obtained best-fit expressions for the relative permeabilities in terms of the phase saturations. Similar investigations with equal success for additional low pressure data were conducted by Levec et al. (1986) and Lakota et al. (2002). Each of these studies report slight variations to the original Saez & Carbonell (1985) correlations. Recently, Nemec & Levec (2005b) generated a comprehensive set of experimental data and showed that very satisfactory predictions can be obtained for high pressure operation with a variety of systems (including differently sized spherical, cylindrical and tri-lobed particles). The most recent forms of the relative permeability equations are (Nemec & Levec, 2005b):

$$\frac{1}{k_L}\left[A\frac{\mathrm{Re}_L^*}{Ga_L^*}+B\frac{\mathrm{Re}_L^{*2}}{Ga_L^*}\right]\frac{\rho_L}{\rho_L-\rho_G}-\frac{1}{k_G}\left[A\frac{\mathrm{Re}_G^*}{Ga_G^*}+B\frac{\mathrm{Re}_G^{*2}}{Ga_G^*}\right]\frac{\rho_G}{\rho_L-\rho_G}=1 \tag{7}$$

$$-\frac{\Delta P}{\Delta z}\frac{1}{\rho_G g}=\frac{1}{k_G}\left[A\frac{\mathrm{Re}_G^*}{Ga_G^*}+B\frac{\mathrm{Re}_G^{*2}}{Ga_G^*}\right] \tag{8}$$

$$k_L=\begin{cases}\delta^{2.9} & \delta\geq 0.3\\ 0.4\delta^{2.1} & \delta<0.3\end{cases}\qquad \delta=\frac{\varepsilon_L-\varepsilon_{L,res}}{\varepsilon-\varepsilon_{L,res}} \tag{9a}$$

$$k_G=\begin{cases}0.4\beta_G^{\,3.6} & \beta_G\leq 0.64\\ \beta_G^{\,5.5} & \beta_G>0.64\end{cases}\qquad \beta_G=\frac{\varepsilon-\varepsilon_L}{\varepsilon} \tag{10}$$

The relative permeability model has proven to be well balanced between the level of detail (low) and the ability to capture the major hydrodynamic trends. However, it does

not make provision for partial wetting. Nemec & Levec (2005) showed that the assumption that $k_\alpha = k_{\alpha i}$ implies that the fluid-solid interfacial area in one phase flow and two phase flow is the same ($A_{\alpha S,1\text{phase}} = A_{\alpha S,2\text{-phase}}$), which can only be true when wetting efficiency is 1 and the liquid films are relatively thin. In such circumstances equation 9a can be derived theoretically to read:

$$k_L = \delta^3 \tag{11}$$

The power of the saturation (3) is close to the empirical value of 2.9. However, the same argument can be applied to the gas phase relative permeability and neither part of equation 10 corresponds. Levec et al. (1986) also suggested that altering the power in equation 9a from 2.9 to 2 gave a satisfactory correlation for the Levec mode. This issue will be returned to in section 2.3.2.

Closely related to the relative permeability concept is the F-function concept (Fourar et al., 2001). Starting from equation 6a, velocity is multiplied by a factor F_α to yield:

$$\left(-\frac{\Delta P}{\Delta z}+\rho_\alpha g\right)_{2-\text{phase}} = \frac{C_1 \mu_\alpha F_\alpha U_\alpha}{D_h^2} + \frac{C_2 \rho_\alpha \left(F_\alpha U_\alpha\right)^2}{D_h} \tag{12}$$

This approach is equivalent to the relative permeability approach for conditions of low effective velocity ($F_\alpha U_\alpha$), in which case $k_\alpha = 1/F_\alpha$. Interestingly, Fourar et al. (2001) then proceeds to make a case for the expression $F_\alpha = 1/\beta_\alpha{}^2$ which is valid for flow in a cylinder (Bacri et al., 1992) and which also happens to correspond to Levec et al. (1986)'s expression for the Levec mode. Unfortunately, Fourar et al. (2001) did not report their exact start-up procedure.

Slit Models

An extensive review of slit model approximations is given in Iliuta & Larachi (2005). Holub et al. (1992) postulated that gas-liquid trickle flow in a randomly packed bed behaves analogously to one-dimensional gas-liquid flow in an inclined slit. Writing

equation 4 for the slit for steady, non-interpenetrating fully wetted flow yields an expression that equates the pressure drop over a length of slit to the gas-liquid and liquid-solid shear stresses, which are in turn expressed as functions of the slit geometry and phase velocities in the usual Ergun (1952) formulation. They key to the slit approach is that the geometry of the slit can be mapped to the packed bed characteristics (namely the liquid holdup are related to the film thickness, the slit and the bed have the same solid surface area-to-volume, void-to-volume and liquid-to-solid volume ratios; pressure drop and the inclination angle is associated with the bed tortuosity or Ergun constants). Al-Dahhan et al. (1998) later extended the single slit model to account for discontinuities in the velocity and shear stresses at the gas-liquid interface (which introduces three additional empirical parameters – the velocity, f_v, and shear, f_s, slip factors and the interfacial liquid velocity). To account for partial wetting, Iliuta & Larachi (1999) introduced the double slit model that corresponds to the extended slit model together with a completely dry slit. The wetting is associated with the ratio of wetted slits to total slits. Its estimation requires another constitutive relation relating wetting efficiency with holdup and pressure drop. This can be attained from solving the liquid velocity profile in the wet slit in order to get an average velocity (Iliuta et al., 2000). This in turn is related to the other hydrodynamic parameters through a momentum balance (not unlike the Hagen-Poisseuille derivation). This then represents the state-of-the-art slit model approximation for co-current trickle flow (Iliuta & Larachi, 2005) and reduces to the other forms for a choice of simplifying assumptions (for example it reduces to Holub et al. (1992) single slit model for the assumptions of full wetting and no gas-liquid interaction, i.e. $f_s = f_v = 0$). As an interesting aside, there is a direct way of calculating the gas-liquid interfacial area from this kind of model, since it is directly proportional to the wetting efficiency. The generalized model equations are available in Iliuta et al. (2000) and are not repeated here. Additional refinements to the model were made by Iliuta et al. (1998), Iliuta et al. (2002a) and Iliuta et al. (2002b). Hydrodynamic multiplicity effects have not been incorporated into the general slit model.

Fundamental Force Balance

Tung & Dhir (1988) started from equation 5 but considered all the vertical force components acting on each phase for the geometry of two-dimensional film flow over a sphere (illustrated in Figure 9b). The force components are shown in Figure 9b. The force by which the gas pushes onto the particle through the liquid and the force by which the liquid pushes onto the particle (and their equal and opposite reactions) each have an interfacial drag and a pressure drag component. Note that here again complete wetting is assumed. Unsurprisingly, each force component is expressed in the Ergun formulation as the sum of viscous and inertial contributions. However, there are some subtleties to these formulations. For example, for the particle-gas drag the "diameter" of the particles are the sum of the particle diameter and the film thickness. Also, in expressing the gas-liquid interfacial force, a reference velocity at the gas-liquid interface has to be defined in order to account for slip. This is the same issue faced in the extended slit model formulation. Here, the reference velocity is taken as the saturation weighted average velocity. As before, the two Ergun constants appear in the equations. Attou et al. (1999) provided an equivalent derivation with the additional assumption that the tortuosity of each phase is inversely proportional to its holdup. Tung & Dhir (1988), Attou et al. (1999) and later Narasimhan et al. (2002) tested versions of this model for a miscellany of data produced by other investigators (including high pressure operation) and found it to be both accurate and robust.

Lattice-Boltzmann Simulation

The lattice-Boltzmann method is in principle a finite difference computational scheme of the Boltzmann equation. The Boltzmann equation describes the time evolution of a single-particle distribution in terms of a collision operator (Chen et al., 1994). The collision operator is in turn approximated by a single-time-relaxation process (with a relaxation time proportional to the kinematic viscosity). The particle distribution evolves toward an equilibrium distribution. Now, appropriately specifying the equilibrium distribution and taking the low flow velocity limit results in the method yielding a

computationally effective approximation of the incompressible Navier-Stokes equations (Chen et al., 1994). The lattice-Boltzmann method has been successfully applied to a variety of flow problems, including reactive flows in packed beds (Sullivan et al., 2005) and multi-phase hydrodynamics in packed beds (Manz et al., 1999, Gladden et al., 2003b), but excluding any hydrodynamic multiplicity effects.

Pore-Network Models

An alternative approach toward modelling trickle flow hydrodynamics is in viewing the void space in a packed bed as a set of interconnected pores bounded by the solid surface and the "pore necks" or constrictions, which can be thought of as the pore entrances and exits. Various definitions exist for defining these pore-to-pore connections and we will return to the issue in detail in Chapter 6. For the present discussion, it is sufficient to conceptualize the packed bed as an ensemble of pores such as the one depicted in Figure 9c (from Melli & Scriven, 1991). The pore itself is a capacity for which the gas and liquid competes (the pore therefore has a liquid holdup). Pressure drop due to drag forces are generally assigned to the pore-necks, who themselves can be occupied by gas, liquid or a combination of the two. Chu & Ng (1989) considered the pore structure of a tilted cubic packing of spheres. Each pore therefore has a coordination number of 6, i.e. six entrances/exists. The pore-to-pore connections are assumed to be cylinders with a length of 95.6% of the particle diameter. Their diameters are randomly assigned such that the diameter size distribution matches a computer-generated constriction size distribution generated in Chan & Ng (1988). The geometry thus set, it is further assumed that only four types of flow can occur in the cylinders: gas-phase gravity-viscous flow, liquid phase gravity-viscous flow, annular liquid-gas flow (for the film flow in the Kan-liquid mode) and stratified gas-liquid flow (for rivulet flow in the Levec mode). The final assumption is what is sometimes referred to as occupancy statistics, namely that a gas-liquid filled channel becomes completely liquid-filled when 86% of the cross-section is liquid filled (i.e. high channel holdup). An important additional observation is that because of the assumed symmetries, the liquid distribution is always regular, i.e. when

the liquid is to be divided at a pore exit into, say, 3 new channels, each channel takes one third of the flow rate.

Melli & Scriven (1991) used many of these concepts in the development of their pore-network model. However, they identify four types of bonds (instead of the four flow types in the cylinders of Chu & Ng, 1989), namely gas-continuous, liquid-continuous (flooded), liquid-bridged (no gas flow) and bubbling (gas bubbles in liquid flow). The sites (pores) have two variables, namely the volume of liquid in it and the pressure. Bonds (necks) have four variables: liquid saturation, liquid flow rate in and liquid flow rate out and the gas flow rate. The authors now introduce various *allowability* and *accessibility rules*. For example, a gas-continuous bridge is *allowed* to become a bubbling bridge if both the saturation and the liquid flow rate exceed pre-specified values. This does not mean that it necessarily will do so. To do so, either site connected to the passage must be *accessible* to the gas-continuous regime. Similar rules exist for all the other types of bonds. The issue of liquid distribution is again paramount. The authors assumed that when the liquid is faced with distributing to more than one passage, each passage gets a random fraction of the total flow (all the fractions adding up to 1). The drag terms in the passages are again taken as fully-wetted gravity-viscous flow in an assumed geometry of a bi-conical tube. This pore-network model is based on a thorough evaluation of the types of multi-phase flow that is encountered in porous media and makes a powerful argument that the macro-scale flow regimes are rooted in micro-scale phenomena. There are, however, two major drawbacks:

- It has a high level of complexity, which makes it both difficult to use (little or no follow-up work has followed its introduction) and difficult to validate experimentally (which has not been done). Extracting bed-scale trends that correspond to those in literature is relatively easy given the various aspects of the model that can be altered to do so. The model has not been applied to three-dimensional networks (possibly also because it would be computationally extraneous to do so).

- It has empiricism on multiple levels, including the specification of the allowability rules' critical values and the characteristics of the process by which the liquid is randomly distributed among potential outflow passages. Both of these drastically affect the calculated results and there is no fundamental way to specify them.

Another concern is that the level of detail with regards to the types of flow bonds and how they are created is not matched by an equivalent level of detail in the modelling of the drag forces in the assumed geometry of a bi-conical tube (for example, only viscous contributions are considered). It has not been tested how this latter assumption affects the results. In summary, while the model shows ample promise in capturing the micro-scale hydrodynamics, there are several critical issues that need further development. Its ability to capture multiplicity trends will be evaluated in section 2.3.2.

Computational Fluid Dynamics (CFD)

The computational fluid dynamics approach attempts to solve the volume averaged Navier-Stokes equations for two fluids. Drag forces are again expressed in the Ergun formulation with the difference in interstitial phase velocity as the characteristic velocity (U), full wetting again being assumed (Jiang et al. 1999). Ideally, the entire packed structure should be specified as the geometry (with boundary conditions imposed on every solid surface). This is computationally impossible at present. Instead, a meso-scale (cluster of particles) is viewed and it is then assumed that within such a meso-cell the porosity and holdup is uniformly distributed (Jiang et al., 1999). The cells are then randomly distributed throughout a two-dimensional bed in a way that ensures that the porosity distribution of the model bed matches that of an experimentally determined real packed bed. Constitutive mass and momentum balances are then solved in this geometry, usually by using a commercial CFD package. Propp et al. (2000) reformulated the mass and relative permeability-based momentum balances of Saez & Carbonell (1985) in terms of the total velocity (the sum of the gas and liquid velocities), yielding a one-dimensional

CFD model. The authors then proceed to give extensively detail on how to solve the resulting expressions numerically using the finite volume approach. Souadnia & Latifi (2001) applied this model (using a commercial CFD code) and showed that it agreed well with a limited set of experimental data. Gunjal et al. (2005) adopted Attou et al. (1999)'s formulation of the drag forces and Jiang et al. (1999)'s model two-dimensional bed and investigated various aspects of the model (including hysteresis and periodic flow). At present, indications are that CFD can develop into a powerful computational tool to represent hydrodynamics on the meso-scale. There are however, some areas of concern. Most notably is the fact that while the internal phase dynamics are modelled with relative ease, the boundary conditions are not (Dudukovic et al., 2002). This is termed the *closure problem* and introduces a significant amount of empiricism into the model (something that CFD was specifically trying to avoid). This is one reason why the 2D *model* bed is necessary. It is decidedly unclear whether this representation is valid, since once again there are many aspects to the model that can be tuned to yield results that match the limited experimental data on flow distribution. CFD in its present form deals with fully wetted beds, although hysteresis is dealt with by incorporating wetting efficiency in an empirical fashion (section 2.3.2). CFD's potential to be extended to the particle-scale will be evaluated in Chapter 6 in the context of new tomographical particle-scale imaging.

Other Approaches

Notable exceptions to the approaches summarized above are:

- The *partially-wetted particle model* (Zimmerman & Ng, 1986). These authors constructed a model 2D bed by dropping particles (disks) into a rectangle with liquid then introduced to the top layer. Liquid flows from sphere to sphere through contact points and the total flow rate to a sphere determines its degree of wetting (according to a de-wetting criterion, Ng, 1986). The model is similar to a pore-network except that spheres instead of pores are chosen as fundamental unit. The model has not seen further development, except in the conceptual interpretations of Maiti et al. (2005).

- Holub (1990) introduced the discrete cell model (DCM), where the minimum rate of mechanical energy dissipation is the governing principle and the bed geometry is the same as the one used for CFD calculations. Jiang et al. (1999) extended the approach to incorporate capillary pressure and showed that it agreed well with the results of the CFD approach for the same assumed geometries. Hysteresis is dealt with in the same manner as in the CFD approach (section 2.3.2). One major advantage of DCM is that it offers a good balance between the ease by which problems are formulated and the level of detail regarding the flow pattern that can be extracted from it.
- Several conduit models have been proposed (Biswas et al., 1988, Saez et al., 1986, Pironti et al., 1999 and Boyer & Fanget, 2002). The basis of these models is that the flow in a packed bed can be represented as a bundle of vertical tubes that can be straight or constricted. The drag forces in equation 5 are expressed in terms of an actual (interstitial) velocity and a hydraulic diameter. Another form of this model is the multi-zone model of Wang et al. (1995), where the bed is divided into gas-filled, liquid-filled and two-phase flow zones. The relative fractions of flow assigned to each of these zones are indicative of the flow uniformity. However, the model is not predictive since there is no way to determine these fractions a priori.

2.3.2 Hydrodynamic Multiplicity Modelling

Not all of the approaches discussed above have been extended to include the impact of hydrodynamic multiplicity. That hydrodynamic multiplicity is a neglected issue in hydrodynamic modelling is apparent from an evaluation of the hydrodynamic literature for approximately the last 3 decades (as reported in Dudukovic et al., 2002). Of the 28 recommended pressure drop and holdup models, none can deal with the issue of hydrodynamic multiplicity. This is a major concern for two reasons:

- Form an academic point of view, it does not make sense to model path variables as state-variables. Models that take only one hydrodynamic mode into account can at best succeed in predicting only that one mode. However, it is desirable to have a single mathematical framework by which all modes (and the states in-between modes) can be treated and where the distinction is based on a fundamental physical principle.
- Form an application point of view, there are a plethora of hydrodynamic states with different hydrodynamic characteristics that remain unexplored. Since hydrodynamics has a significant impact on the performance of the reactor, filter or absorption column, the different hydrodynamic options presented by multiplicity can be exploited to yield optimum performance.

An argument that is often aired as to why hydrodynamic multiplicity is relatively unimportant, is that the Kan-Liquid mode is the obvious optimum. This is based on the idea that since it has the highest pressure drop of all the modes (and therefore the highest degree of gas-liquid interaction), it must be the optimum. This is true for gas-liquid mass transfer limited systems, which are widely found, but there is no reason to believe that this mode must be the optimum for other equally common applications (like liquid-solid mass transfer limited systems). A hint that it might not be is the fact that the Kan-Gas mode has a higher holdup (and therefore presumably a higher wetting efficiency) than the Kan-Liquid mode. The idea of a hydrodynamic optimum is explored in Chapter 8.

Some of the approaches alluded to above have been extended to incorporate some aspects of hydrodynamic multiplicity. These are summarized in Table 9 and are discussed next.

Kan & Greenfield (1978) studied the evolution of a Kan-Liquid mode into a Kan-Gas mode with gas velocity changes. Later (Kan & Greenfield, 1979), they adopted the Turpin & Huntington (1967) empirical pressure drop model and introduced a maximum gas flow rate Reynolds number to account for the lower pressure drop in the modes between the Kan-Liquid and Kan-Gas modes. The model does not consider holdup. They

also speculated that the increased gas flow reduced the gas flow path tortuosity and then quantified this reduction. The empirical nature of this model makes it undesirable. In particular, one needs 9 fitted parameters for the Kan-Liquid mode, as well as another one that has to be introduced when gas velocity changes are used.

Table 9. Hydrodynamic multiplicity modelling in literature

Reference	Approach	Comments
Kan & Greenfield (1979)	Empirical	Deals only with gas flow rate variation induced hysteresis, but not just for the limiting cases. Highly unsatisfactory because of the high degree of empiricism.
Levec et al. (1986)	Relative permeability	Deals only with Levec and Kan-Liquid/Super modes. Multiplicity introduced externally by specifying a different permeability correlation. Predicts holdup well at low u_L.
Chu & Ng (1989)	Pore-network	Deals only with liquid flow rate variation induced hysteresis. Multiplicity introduced by externally specifying flow type. Good predictive capability.
Melli & Scriven (1991)	Pore-network	Very complex model. Applied to liquid flow rate variation induced hysteresis only. Multiplicity emerges naturally from flow history. Highly empirical. Not validated.
Wang et al. (1995)	Multi-zone model	Not predictive, but rather indicative of extent of flow uniformity.
Jiang et al. (1999) Gunjal et al. (2005)	CFD and DCM	Only meso-scale 2D beds. Deals only with non-pre-wetted and "pre-wetted" beds. Wetting and hysteresis introduced empirically through capillary pressure. Under-predicts multiplicity.

Levec et al. (1986) suggested that hysteresis is due to the differences in advancing and receding contact angles (increasing liquid flow rate legs being associated with advancing contact angles and decreasing legs with receding contact angles). Receding contact angles are lower, implying more liquid spreading. However, Levec et al. (1986) adopted the relative permeability approach and introduced hysteresis into the power of the liquid phase relative permeability. Whereas equation 9a accounts for the Kan-Liquid (and Super) modes, a new equation is introduced for the Levec mode (the power of the saturation being 2):

$$k_L = \delta^2 \qquad (9b)$$

This equation is especially valid for low velocities and cannot account for the states in-between the Levec and Kan-Liquid modes. Since this model is the only practical alternative for obtaining quantitative predictions for the Levec mode, it is informative to plot the model's performance for the original data (Figure 10). Note that for the Levec mode satisfactory predictions are only achieved at low liquid velocity – at higher velocities (u_L > 10 mm/s) the functional dependency is clearly different from the adopted power law expression. At the pulsing boundary (u_L ≈ 18 mm/s) the holdup is equal in both modes but the correlation still predicts a large difference. Evidently, the gas phase relative permeability-gas saturation relationship also needs adjustment in the Levec mode.

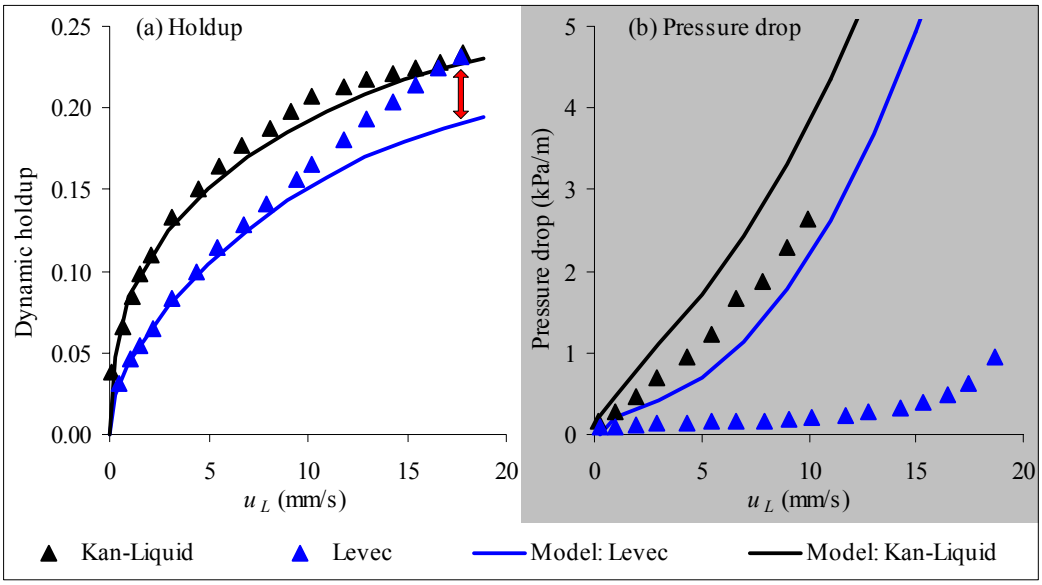

Figure 10. The inapplicability of the power law form for the Levec mode's permeability-saturation relationship at high u_L. Model and data from Levec et al. (1986).

Chu & Ng (1989) introduced hysteresis in their pore-network model by assuming that the cylinders that connect pores are in the annular flow regime for the Kan-Liquid mode and in the stratified flow regime for the Levec mode. Although the authors state that these two regimes correspond to film and rivulet flow, there seems to be little physical basis for

these assumptions. Melli & Scriven (1991) also showed that their pore-network model exhibits hysteresis with liquid flow rate. The hysteresis is derived from the fact that the allowability and accessibility criteria are asymmetrical with flow rate (they are functions of saturation among other things). The result is that different bond types prevail depending on whether the flow is increasing or decreasing. Although the criteria are set empirically, they are not changed according to the mode (i.e. the empirical part is the same for both the Non-pre-wetted and Kan-Liquid modes). This is the only hysteresis model that has this quality. To re-iterate, for an increase in liquid flow rate, the local pore saturations increase. As liquid flow rate is decreased, the high saturations allow different types of bonds (bubbling and flooded) to persist at the reduced flow rate where they were impossible before. This results in the observed liquid flow rate variation induced hysteresis. This mechanism has not been tested for gas flow rate variation induced hysteresis (Kan-Gas mode), nor for pre-flooding under irrigation (Super mode).

As mentioned before, Wang et al. (1995) conceptually divided the bed into three zones and showed that the different modes correspond to different fractions of flow in each of the modes. Again, there is no a priori method of determining these fractions for the different hydrodynamic conditions.

The CFD approach has seen attempts to extend it to incorporate hysteresis. Jiang et al. (1999) suggested that an empirical wetting efficiency be incorporated into the capillary pressure expression:

$$P_G = P_L + P_C\left(1 - f\right) \tag{13}$$

The capillary pressure (P_C) can be formulated as suggested by Grosser et al. (1988). The expression reduces to the absence of capillary pressure when the wetting is complete ($f = 1$). Jiang et al. (1999) suggested that the wetting be set to zero for Non-pre-wetted beds and one for pre-wetted beds (no distinction is made between Levec, Kan-Liquid, Kan-Gas or Super modes). Both the CFD and DCM models exhibit liquid flow rate variation induced hysteresis under this assumption. Gunjal et al. (2005) also adopted

equation 13 and compared CFD predictions to their own pressure drop and holdup liquid flow rate variation induced hysteresis data. While the trends are qualitatively represented, they found that the extent of hysteresis for both parameters were severely under-predicted (the Non-pre-wetted mode pressure drop is over-estimated). Considering that *f* is taken as either 0 or 1, it an be concluded that this assumed capillary effect *as formulated* cannot alone explain hysteresis. Moreover, the framework allows no way of dealing with gas velocity variation induced hysteresis. Assuming full wetting for pre-wetted beds and zero wetting for non-pre-wetted beds is a questionable practice.

Using the advancing/receding contact angle idea, Khanna & Nigam (2002) and later Maiti et al. (2005) presented an in depth analysis of spreading dynamics on porous and non-porous surfaces and conclude that hysteresis (liquid flow rate variation induced) is attributable to the concept of participating and non-participating particles. At low velocity, the liquid flows predominantly in "favourably clustered" particles. As the flow rate is increased, the liquid spreads out from this core. A subsequent decrease results in previously non-participating particles now also participating. The idea is reminiscent of that of Christensen et al. (1986) who visualized the Levec mode as consisting of liquid-filled cores surrounded by film flow. Interestingly, tomographical techniques can be used to validate these ideas. Sederman & Gladden (2001) reported that the number of rivulets increased as the liquid velocity is increased in the Levec mode. At higher velocity the number of rivulets did not increase but the rivulets instead swelled. In their analysis, the Kan-Liquid mode had more rivulets than the Levec mode, suggesting that more particles participate. However, it is possible to literally count the number of participating particles by tomographical means and this has not been done. This issue is returned to in Chapter 6, where it is posed that the number of participating pores is a better evaluation. The Maiti et al. (2005) framework does not account for gas flow rate variation induced hysteresis.

In the early stages of this study, Van der Merwe & Nicol (2005) adopted the conduit flow model of Boyer & Fanget (2002) and incorporated a "volumetric utilization coefficient"

into the drag force terms. This is equivalent to conceptually partitioning the bed into two regions: one that experiences fully wetted liquid flow and another that experiences no liquid flow. The only notable aspect of this model is the fact that (unlike other hysteresis models) the utilization coefficient can be determined independently as the residual holdup utilization. As such, it is a measure of the degree of spreading of the liquid in the bed. Using this coefficient, we were able to predict the holdup in the Non-pre-wetted, Levec and Super modes for the case of no gas flow (and a limited data set). The model is yet to be extended to pressure drop prediction and needs further validation.

2.3.3 Outstanding Issues

One major unresolved issue that has in fact received only empirical and statistical attention is the issue of the *mechanism of liquid distribution* and how this results in different hydrodynamic modes. It is generally well established that the different hydrodynamic modes are associated with different gas and liquid flow patterns. However, there has been little speculation and even less evidence as to how these flow patterns come about. Levec et al. (1986) suggested that the multiple states are the result of the hysteresis in the gas-liquid-solid contact angle when a liquid front is advancing and receding over the particle surfaces. Wang et al. (1995) associated the multiplicity with non-uniformity and developed a multi-zone model that measured this post priori. Van der Merwe & Nicol (2005) used the same idea, but quantified the uniformity in terms of a residual holdup utilization. Jiang et al. (1999) attributed hysteresis to differences in the capillary pressure expression. Maiti et al. (2005) ascribed it to the fraction of participating and non-participating particles but gave no indication of how this should be determined. This begs the question: *What is the fundamental mechanism that causes hydrodynamic multiplicity and how should it be incorporated into the already successful phenomenological models?*

2.4 Conclusions

The following conclusions are drawn from the literature evaluated in this chapter:

- **Hydrodynamics are difficult to model** owing to the complexities of gas-liquid-solid interactions, but not as difficult to understand qualitatively. This is evident in that the basic trends are more or less intuitive (for example, a higher liquid flow rate yields a higher holdup and therefore higher pressure drop). As a result, there are numerous different phenomenological approaches that attain a fair measure of success. Hydrodynamic multiplicity, however, is far less intuitive, has not received as much attention and is relatively poorly understood.
- **The hydrodynamic parameters are *all* influenced by hydrodynamic multiplicity and the extent of variability is large.** Adopting the modes interpretation introduced herein, it is clear that no single investigator studied all the modes (see Table 7). Also clear is the fact that the hydrodynamic behaviour is very complex, i.e. that different hydrodynamic states can be achieved in different ways (pre-flooding and/or hysteresis) and that the modes are different in character (flow pattern, liquid morphology and interfacial areas). The lack of an experimental framework that incorporates all the various combinations of pre-wetting and flow rate changes has led modellers to consider only some aspects of the phenomenon. This is a question of problem definition and is addressed as the first objective of this work.
- **It is unclear what the root cause of hydrodynamic multiplicity is.** Suggested mechanisms include contact angle hysteresis (Levec et al., 1986), the dynamics of a spreading film over porous/non-porous substrates (Maiti et al., 2004), flow uniformity (Wang et al., 1995), participating and non-participating particle clusters (Maiti et al., 2005), imperfect wetting (Lazzaroni et al., 1988), the flow differences between rivulet and film flow (Christensen et al., 1986) and the change in tortuosity of the gas channels (Kan & Greenfield, 1979).

- **Hydrodynamic models do not capture multiplicity trends.** Those that have attempted to incorporate multiplicity have generally done so for only one of the two manifestations thereof (namely liquid flow rate variation induced hysteresis loops and pre-wetted vs. non-pre-wetted modes). Moreover, multiplicity has only been incorporated into models *empirically* and with little quantitative success.

However, considerable experimental work has been done on this topic. Returning to Figure 1, note that a major objective of evaluating the literature was to identify characteristic multiplicity trends with the aim of providing a basis from which the proposed fundamental mechanism can be tested. These trends are:

(A) There are different flow patterns in the different modes: rivulet-type flow in the lower limiting cases and film-type flow in the upper limiting cases. New rivulets are created as u_L increases.

(B) Liquid flow rate variation induced hysteresis causes increases in pressure drop and liquid holdup in the Non-pre-wetted and Levec modes.

(C) Gas flow rate variation induced hysteresis causes increases in pressure drop and holdup in the Levec mode, but an increase in holdup and a decrease in pressure drop in the Kan-Liquid mode.

(D) The extent of pressure drop hysteresis is diminished when particle size is increased.

(E) The Levec mode *wetting efficiency* is lower on average and shows a bi-modal particle wetting distribution, whereas the Super mode shows a Gaussian distribution.

This list will be extended and modified throughout the remainder of the experimental investigations (Chapters 4, 5, 6 and 7).

Chapter 3. Objectives

This chapter summarizes the motivations and objectives of this study. It is also a guide to the subsequent chapters and an overview of the contributions made in this work.

3.1 Objectives

The overriding objective of this study is to advance the understanding of trickle flow hydrodynamics, with specific emphasis on the phenomenon of hydrodynamic multiplicity. This can be broken down into three objectives:

Objective 1. The establishment of a **conceptual framework** by which the phenomena alluded to in the previous chapter can be studied experimentally. The limiting cases of hydrodynamic multiplicity introduced in Table 5 are proposed as such a framework.

Objective 2. Closely coupled with this, is the objective of attaining further **experimental insight** into the role of bed and system conditions and their (possible) influence(s) on the extent of hydrodynamic multiplicity. This involves clarification of the relationship between the bed structure and flow multiplicity. Central to this issue are the questions of the temporal stability, spatial liquid distribution and reproducibility of the flow pattern, as well as the roles of surface tension and particle characteristics. Here, the idea is not to investigate all possible permutations of operating variables but rather to extract the fundamental trends (in accordance with the strategy in Figure 1).

Objective 3. The identification of the probable **mechanism responsible for hydrodynamic multiplicity**. An improved understanding of this mechanism should account for both manifestations of multiplicity: hysteresis loops and pre-wetting modes, and an outline of how the mechanism is to be incorporated in existing hydrodynamic models should be clear.

A further illustration of the impact of hydrodynamic multiplicity on trickle bed reactor performance is given in Chapter 8. First, experimental verification of pressure drop hysteresis in an industrial reactor is reported. Second, an experimental reaction case study (α-methyl styrene hydrogenation) is presented that illustrates the impact of multiplicity on conversion.

3.2 Thesis Structure

The objectives outlined above are addressed in subsequent chapters as outlined in Table 10. Together with Figure 1, this table is both a guide to the thesis and a list of the major contributions of this work.

Table 10. Thesis structure

Section	Issues Addressed
Chapter 2	Re-interprets literature in terms of proposed framework (section 2.2.2) and identifies multiplicity trends
Chapter 4	Experimental investigations into bed-scale hydrodynamics, identifying further multiplicity trends
Chapter 5	Preliminary experimental investigation into cluster-of-particles scale hydrodynamics using established radiographic and tomographic techniques (further multiplicity trends identified)
Chapter 6	Advances the image processing strategy of the tomographic data in order to yield high definition volume images that are again used to identify the nature (and trends) of hydrodynamic multiplicity.
Chapter 7	Interpretation of all experimental results and multiplicity modelling at the pore scale
Chapter 8	Experimental verification of pressure drop multiplicity in an industrial reactor. Impact of hysteresis on reactor performance, proving the concept that multiplicity can be used to enhance reactor performance

Chapter 4. Bed-Scale Phenomena

This chapter addresses hydrodynamic multiplicity at the bed-scale through measurements of bed-averaged hydrodynamic parameters. This forms part 1 of the Additional Experimental Insights block in Figure 1 and partially satisfies Objective 2 (achieving further experimental insight into hydrodynamic multiplicity - as outlined in Chapter 3). This chapter starts with the experimental details and then presents the results in three sections: those obtained in beds of non-porous particles, those obtained in beds of porous particles and the effect of increased operating pressure on hydrodynamic multiplicity. In accordance with the strategy in Figure 1, the list of characteristic multiplicity trends are confirmed and extended by the work in this chapter. The updated list is given at the end of the chapter.

4.1 Experimental

The perennial problem of investigating trickle flow hydrodynamics is the inherent complexity. In this work, like all others, the amount of experimental data is limited to what is practically possible. The emphasis here is placed on augmenting the literature data where Chapter 2 and the conceptual framework have identified the need to do so. The focus is on uncovering the mechanism of hydrodynamic multiplicity through identifying the characteristic trends.

The experimental setup that was used to generate the bulk of the data in this chapter is shown in Figure 11 and experimental details are given in Table 11.

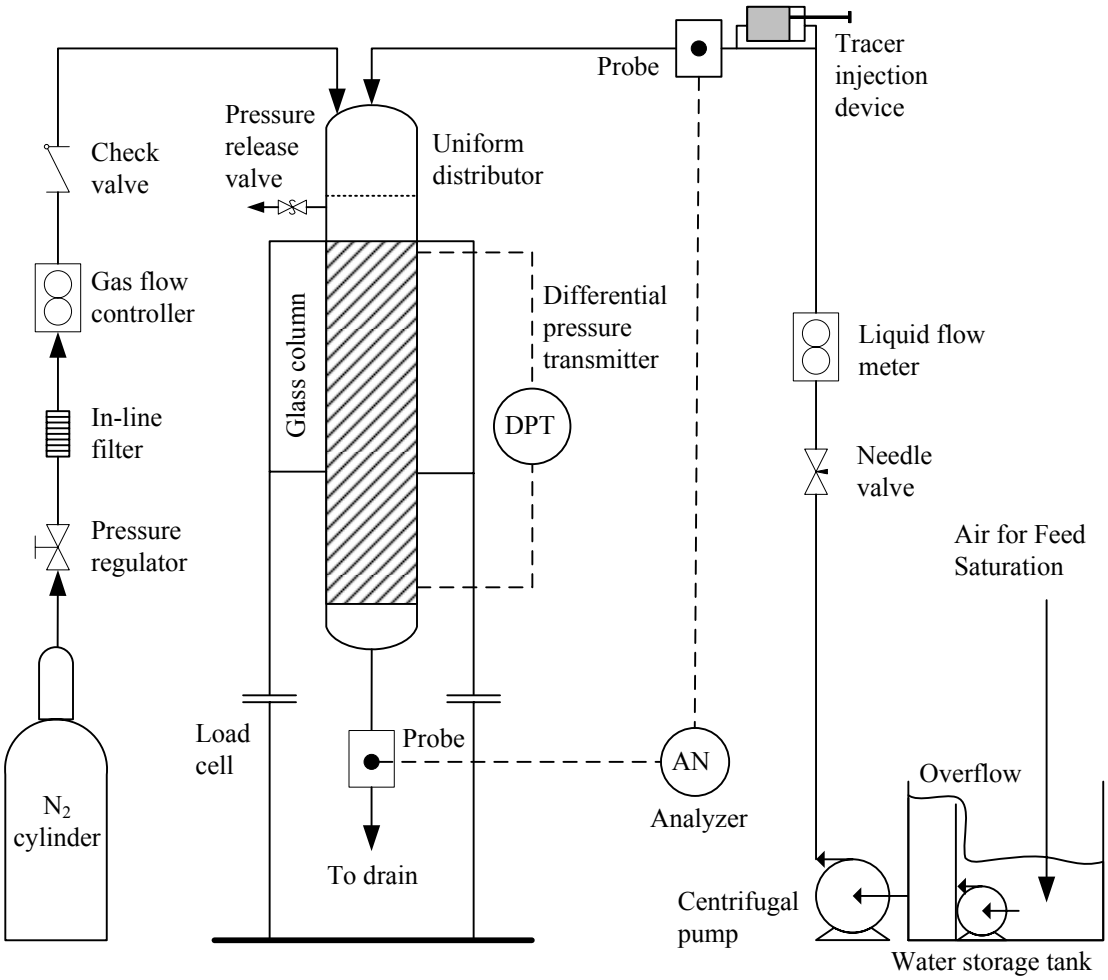

Figure 11. Experimental setup for bed scale experiments.

4.2 Multiplicity in Beds of Non-Porous Particles[1]

Table 7 shows that there has been no investigation into all five multiplicity modes for a single bed. It is imperative to confirm that the trends reported in literature are indeed due to flow peculiarities and not because of differences in the individual bed structures and experimental conditions.

[1] Data from this section was published in Chemical Engineering Science, Vol. 61, pg 7551-7562, 2006.

Table 11. Experimental details

Liquids	Water Water + Ethanol (20 %)
Gas	Nitrogen (87 kPa)
Surface tension	0.02-0.03 N/m, 0.07 N/m
Particles	3 mm non-porous glass spheres 3 × 3 mm porous extrudate 2.5 mm porous alumina spheres
Column diameter	68 mm
Bed length	850 mm
Liquid velocity	1.0 – 9.0 mm/s
Gas velocity	2.0 – 9.0 cm/s
Load cell	Revere Transducers Europe (accuracy: ±4 g)
Differential pressure transducer	Rosemount 3051CD (accuracy: ±10 Pa)
Dissolved oxygen probes	Rosemount 499ADO (resolution: 0.1 ppm)
Conductivity probes	Eutech PC5500 (accuracy: 0.1%)
Distributor drip point density	16000 points per m^2

For this reason, a set of experimental data was produced for the most common system in literature: 3 mm glass spheres, with water and low pressure nitrogen as fluids. Each multiplicity mode was established according to the framework introduced in Table 5. In addition to the pressure drop, the liquid holdup and the volumetric gas-liquid mass transfer coefficient were measured by the gravimetric method and the physical desorption of dissolved oxygen respectively over a range of gas and liquid velocities. All reported values are at steady state (no change in any of the hydrodynamics was observed after about 5 minutes at each operating condition). Additional experimental concerns are dealt with in detail in Loudon et al. (2006); here the emphasis is on interpreting the results. Figure 12 to Figure 14 show the pressure drop, holdup and mass transfer results as functions of liquid velocities. Figure 15 shows these parameters as functions of gas velocity at the highest liquid velocity (the highest liquid velocity is chosen because it was

not possible to achieve gas flow rate induced pulsing at lower liquid velocities). Note that each point represents the average of three experiments. Error bars are not shown since they coincide with the symbols themselves. Instead, the reproducibility for each parameter for each mode is reported in Table 12. The total average relative standard deviation is 4%, and this is considerably lower than the differences between the modes.

Table 12. Reproducibility of results

Parameter	**Average relative standard deviation (%)**					
	NPW	Levec	Super	Kan-Liquid	Kan-Gas	All modes
$\Delta P/\Delta z$	4.1	2.5	5.0	3.9	10.5	5.2
ε_L	2.9	1.5	1.7	1.5	0.6	1.6
$k_{GL}a_{GL}$	14.1	3.3	6.6	3.5	2.1	5.9

Several important conclusions can be made from this data. In Figure 12 there are two very clear regions, the upper branch consisting of the Kan-Liquid and Super modes and the lower branch consisting of the Non-pre-wetted and Levec modes. It is for this reason that several investigators (for example Jiang et al., 2000) only distinguish between “non-pre-wetted” and “pre-wetted” conditions. Figure 13 and Figure 14 however dispels this framework. In fact, Figure 15 shows that there are indeed five distinct multiplicity modes. In general, the present data confirm the trends that were extracted from literature in Chapter 2. Note that the data represents the average of three re-packings and that the reproducibility was good. This means that some general conclusions can be drawn about the hydrodynamic behaviour in each multiplicity mode and that all the different modes can be compared directly for the first time (since previous investigators did not investigate all the modes for the same system). A list of these conclusions follow.

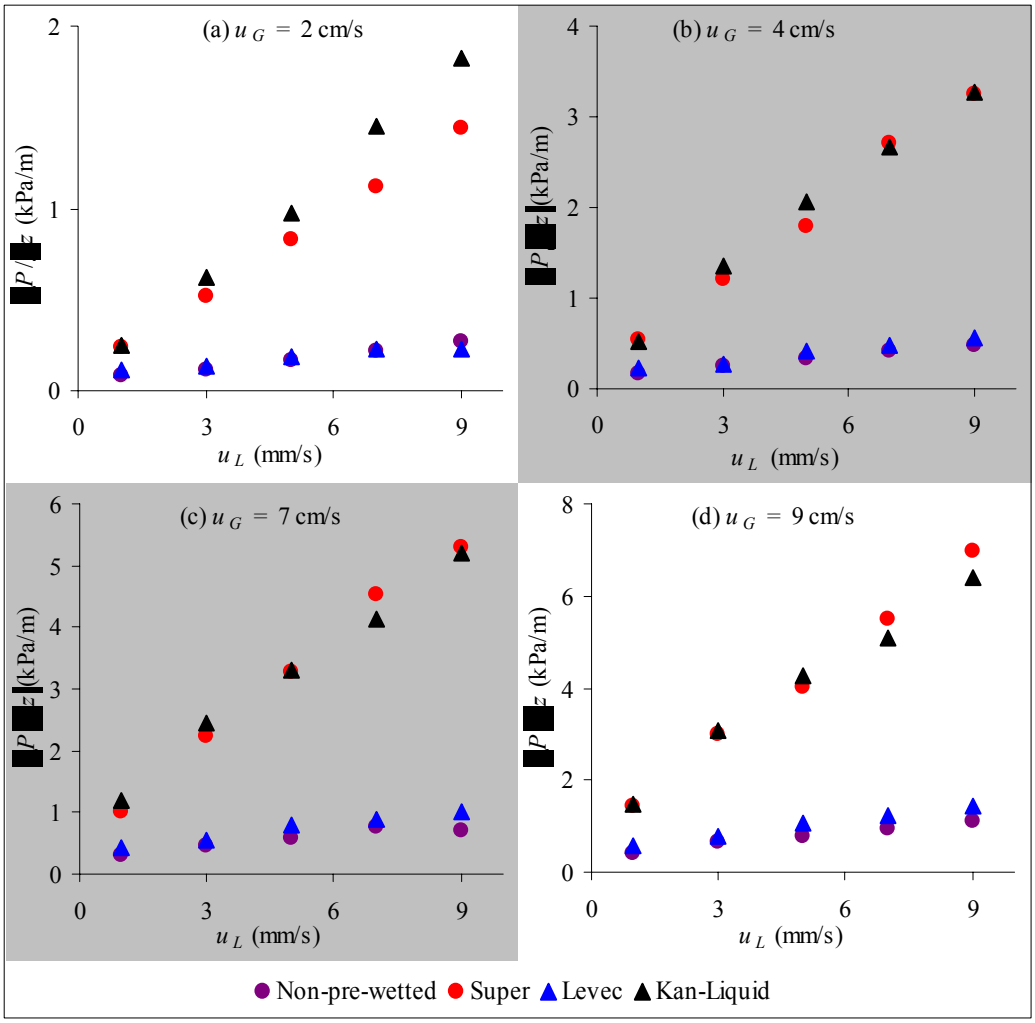

Figure 12. Pressure drop as a function of gas and liquid velocity

- The absolute upper limit of *pressure drop* is achieved in the Kan-Liquid/Super modes and the absolute lower limit is the Levec and Non-pre-wetted modes. The absolute upper limit for *holdup* is the Kan-Gas mode and the absolute lower limit is the Non-pre-wetted mode. The Levec mode is the lower limit for holdup that can be achieved in a pre-wetted bed, while the Super mode represents the upper limit for holdup and pressure drop where no flow rate above the operating rates were used. All five cases are therefore significant.

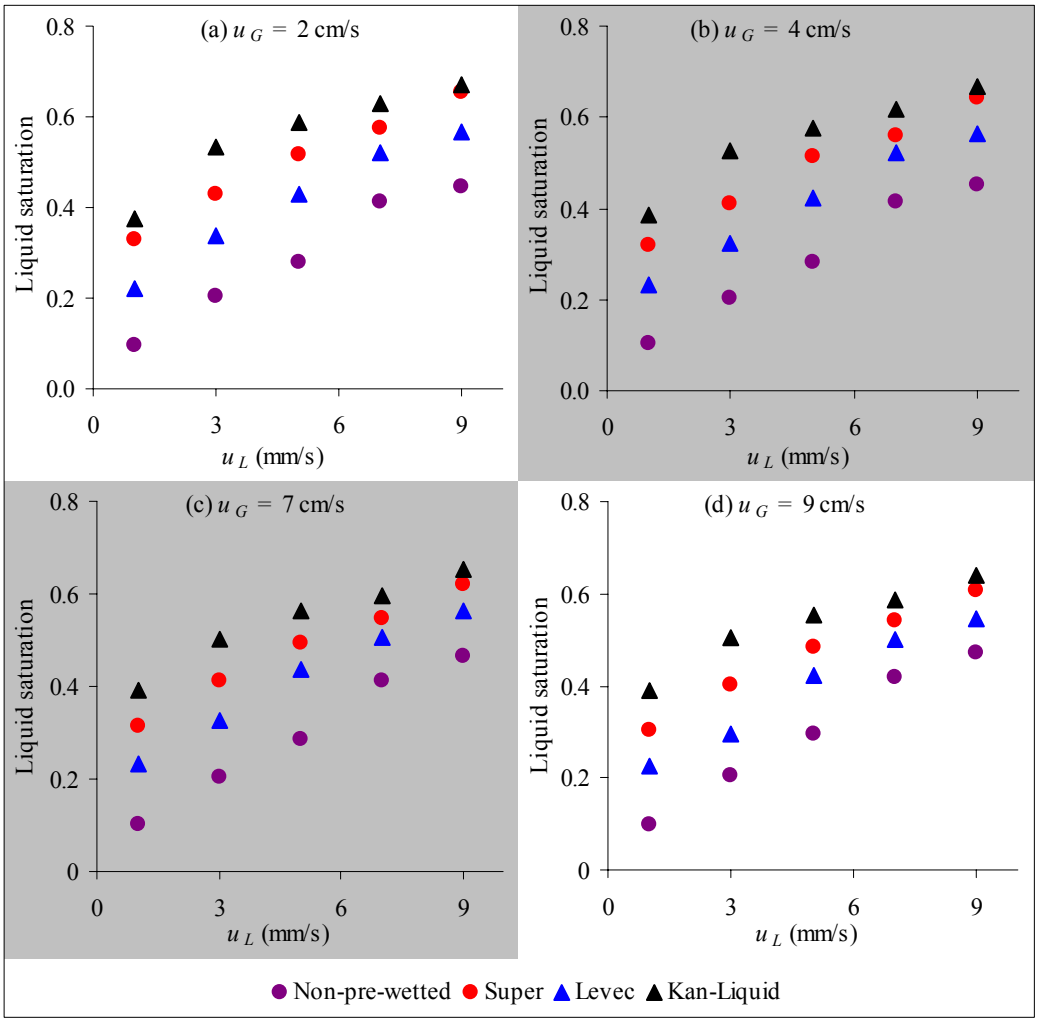

Figure 13. Liquid saturation ($\varepsilon_L/\varepsilon$) as a function of gas and liquid velocity

- The pressure drop in the upper limiting mode is between 2 and 8 times higher than that in the lower limiting mode. The holdup in the upper limiting case (Kan-Gas) can be up to 8 times higher than in the lower limiting case (Non-pre-wetted) and up to 4 times higher than the lower limiting case for pre-wetted beds (Levec mode). The gas-liquid mass transfer coefficient is up to 6 times higher in the upper limiting case (Super mode) than in the lower limiting case (Non-pre-wetted) and up to 2.4 times higher than the lower limiting case for pre-wetted beds (Levec mode). This emphasizes not only the importance of pre-wetting, but also the importance of the exact operating procedure and the flow history.

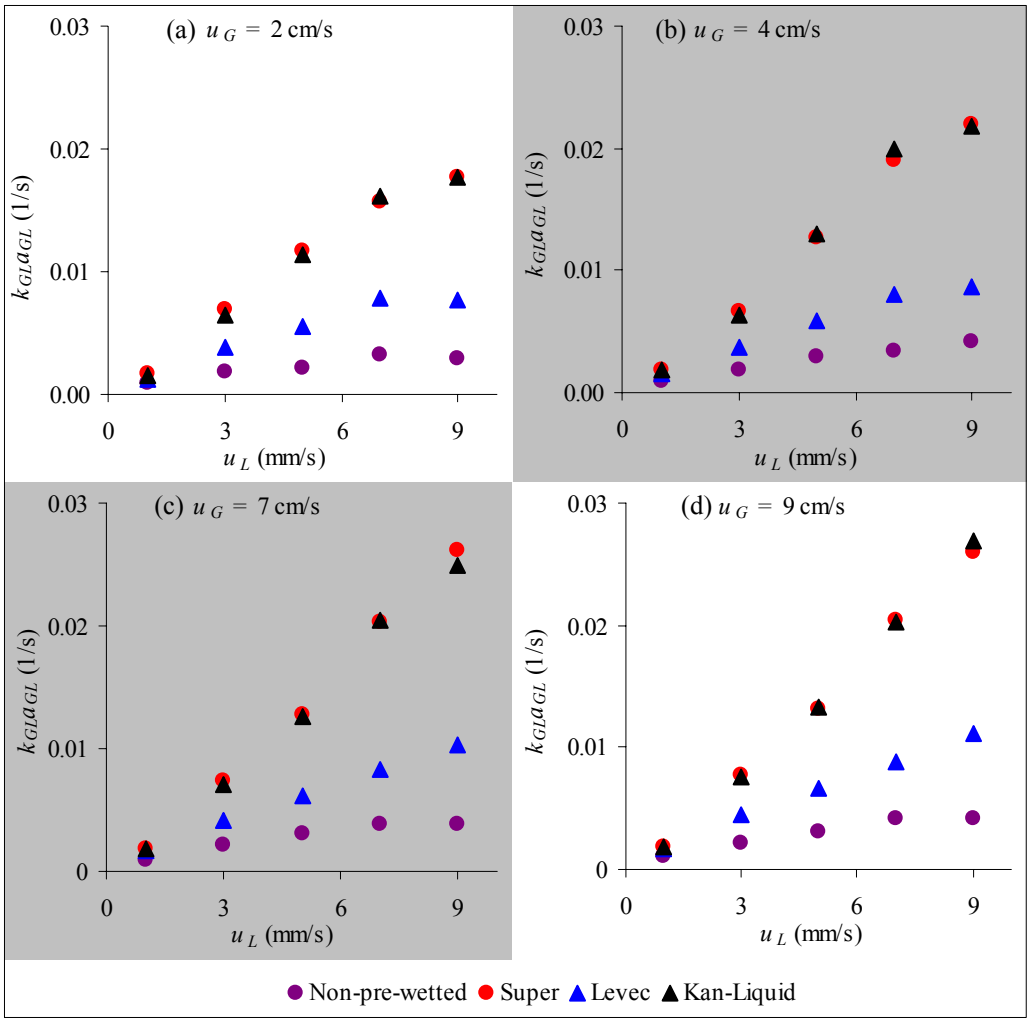

Figure 14. Volumetric gas-liquid mass transfer coefficient as a function of gas and liquid velocity

- In all the modes pressure drop, liquid holdup and gas-liquid mass transfer always increase with an increase in liquid velocity as expected from the increased liquid-solid drag that result in higher holdup. Pressure drop and gas-liquid mass transfer also increases with gas velocity and liquid holdup decreases with gas velocity in the Kan-Liquid, Kan-Gas, Super and Levec modes (as expected from the increased gas-liquid drag), but liquid holdup increases in the Non-pre-wetted mode as u_G increases. This is indicative of a second effect, namely that the increased gas-liquid drag serves to spread the liquid over the packing (and

therefore results in higher liquid-solid drag). Here, we see again the importance of liquid distribution in determining the hydrodynamics of the system.

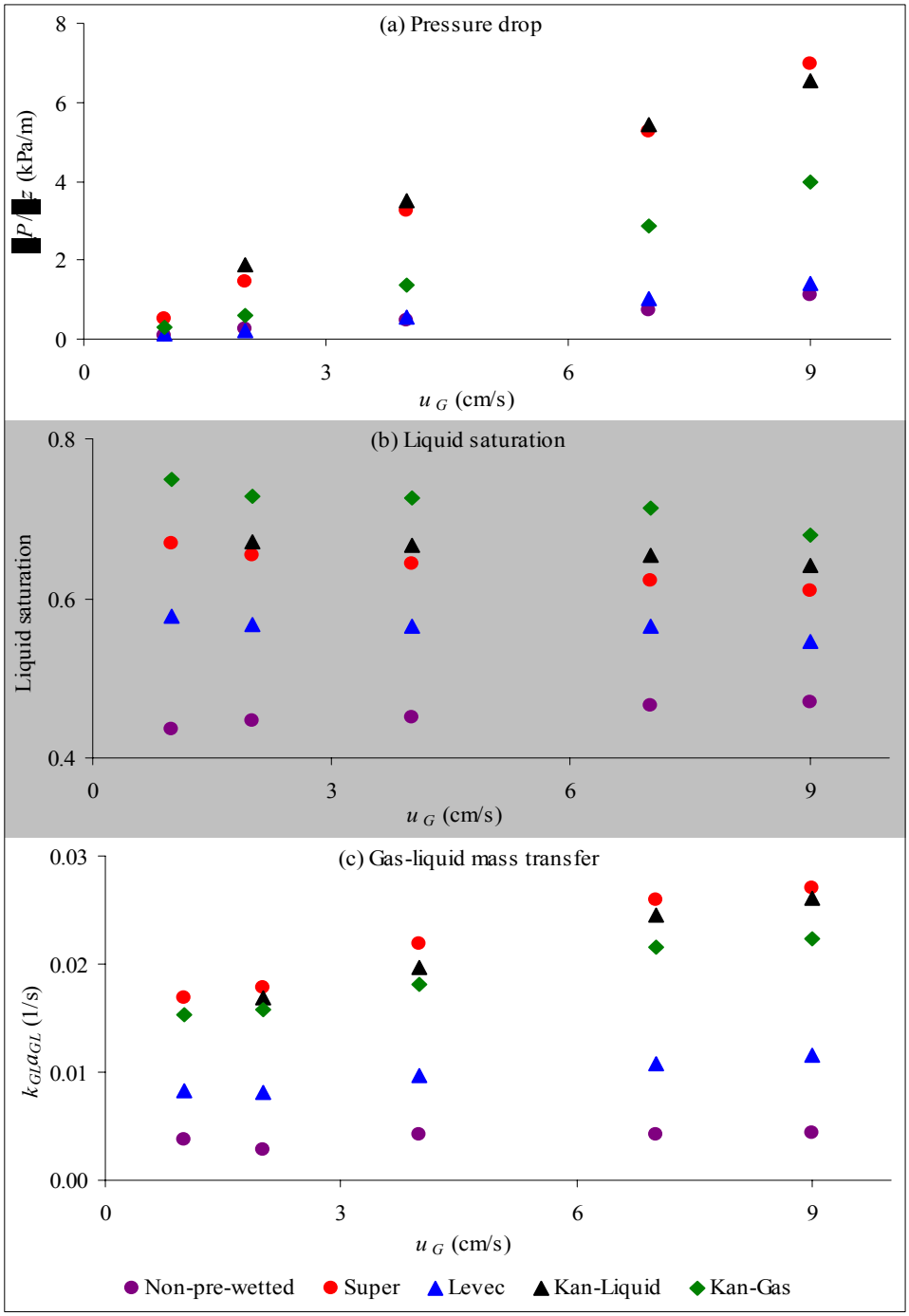

Figure 15. Pressure drop, liquid saturation and volumetric gas-liquid mass transfer coefficient as a function of gas velocity at u_L = 9 mm/s.

- The gas-liquid mass transfer coefficient is an indication of the "spreadedness" of the liquid. A uniform film that covers all the particles will have a much larger gas-liquid interfacial area than a rivulet that encompasses clusters of particles. This supports the idea of rivulet and film flow introduced by Christensen et al. (1986).
- The Non-pre-wetted and Levec modes show interesting behaviour in that their pressure drops are equal, but both holdup and gas-liquid mass transfer differ significantly. This means that pressure drop is a poor choice for distinguishing these modes. From Figure 12, Figure 14 and Figure 15 it appears that the Super and Kan-Liquid modes are very similar. This is a significant result because these modes are obtained through vastly different procedures (flooding vs. pulsing).
- An important result that will re-surface in Chapter 8 is the fact that the Kan-Liquid mode has a significantly higher $k_{GL}a_{GL}$ value than the Levec mode.
- The Kan-Gas mode presents a peculiarity: it has a higher holdup than any other mode (Figure 15b) but not the highest pressure drop (Figure 15a). This is very much against the conventional understanding (that is based mostly on the other modes).

The observations listed above are the essential features that a hydrodynamic multiplicity model should incorporate and form part of the list of multiplicity trends.

It is also informative to evaluate present data through the relative permeability approach, since Levec et al. (1986) showed some success in incorporating multiplicity into this model (see Chapter 2). Figure 16 shows the liquid and gas phase relative permeabilities as functions of the reduced liquid and gas phase saturations. In this figure, the experimental pressure drop values were inserted into equations 7 and 8 to obtain k_L and k_G. These are then plotted against their associated holdups (reduced liquid saturation) for each mode. The functional dependencies of relative permeability on phase saturation compare well with those obtained by Levec et al. (1986) for k_L in the Levec (2.0 vs. 2.0)

and Kan-Liquid (3.5 vs. 2.9) modes. Likewise, for k_G, the powers of β_G for the Kan-Liquid/Super modes also compare well (3.3 vs. 3.6).

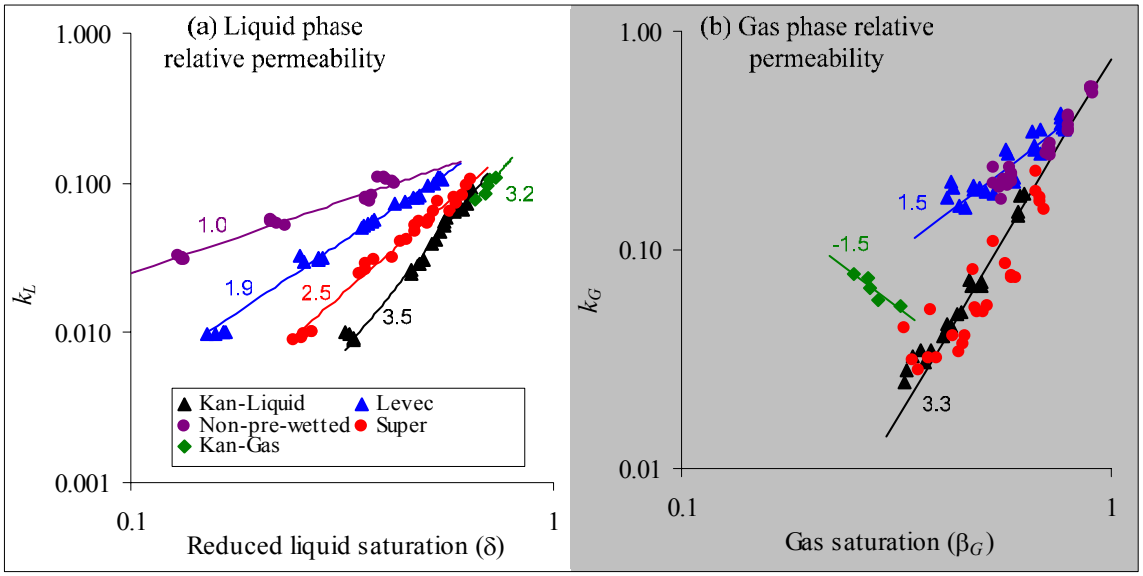

Figure 16. Liquid and gas relative permeabilities as functions of the phase saturations. Numbers on the lines indicate approximate slopes that correspond to the power of the saturation in equations 9 and 10.

The peculiarity of the Kan-Gas mode is apparent in Figure 16b where the negative slope indicates that lower pressure drop is associated with lower gas saturation (i.e. higher holdup). Figure 16 suggests that the relatively simple way used by Levec et al. (1986) to model multiplicity can be extended to incorporate the additional modes as well by writing expressions analogous to equations 9 and 10 for each mode. There are two problems with this. The first is that there are (at least) two equations per mode (one for liquid and one for gas relative permeability) and that each of these has two fitted parameters (the power of the saturation which determines how permeability changes with velocity and the coefficient that determines the basis from which it changes). To model all 5 modes there are 2×2×5 = 20 fitted parameters. In attempting to obtain such a model for the present data, it was found that these 20 parameters were all different and could only be determined empirically. The second problem is that the functional form of the equation (power law), only works well at the lower end of velocities. This cannot be seen from Figure 16 because a log-scale is used, but was illustrated in Figure 10. For these reasons

relative permeability is used here only in a qualitative sense. From Figure 16a it is seen that the slope increases in the order Non-pre-wetted, Levec, Super, Kan-Gas and Kan-Liquid. Now, two other slopes are well known, namely a slope of 3 for a uniformly wetted packed bed (Nemec et al., 2005b) and a slope of 2 for flow in a vertical cylinder (Fourar et al., 2001). Flow in the Levec mode therefore corresponds closely to flow in a cylinder (which is again reminiscent of "rivulet" flow), while flow in the Kan-type modes corresponds to more uniform, fully wetted flow in a packed bed. The slopes of these lines can therefore be seen as a measure of the flow uniformity (but does not in itself describes how the specific flow type is established). This issue is returned to in Chapter 7.

Appropriateness of the Limiting Cases Framework

Another major issue requires experimental validation, namely the appropriateness of the limiting cases framework that was introduced at the start of this work. In Figure 5, gas and liquid flow rate variation induced hysteresis loops were reported for some of the modes. Using the same setup as before, additional gas and liquid flow rate loops were conducted after the bed had been put into each of the five multiplicity modes. The experimental details are given in Van der Westhuizen (2006) and the results are shown qualitatively in Figure 17. The results were generated by establishing steady state at $u_L = 5$ mm/s and $u_G = 2$ cm/s, and then increasing liquid velocity to 7 and 9 mm/s followed by decreasing it back to 7 and 5. The gas loops were conducted by establishing steady state at $u_L = 5$ mm/s and $u_G = 2$ cm/s, and then changing gas flow as follows: 2, 4, 7, 4, 2 cm/s. The data support the idea of using the limiting modes because flow rate variation simply results in moving around *in-between* the 5 modes (no limits crossed). For example, the maximum pressure drop is obtained in the Kan-Liquid mode and conducting gas or liquid flow rate loops does not cross this boundary – the Kan-Liquid mode is therefore the absolute upper limit of pressure drop that can be achieved through manipulation of the hydrodynamic state.

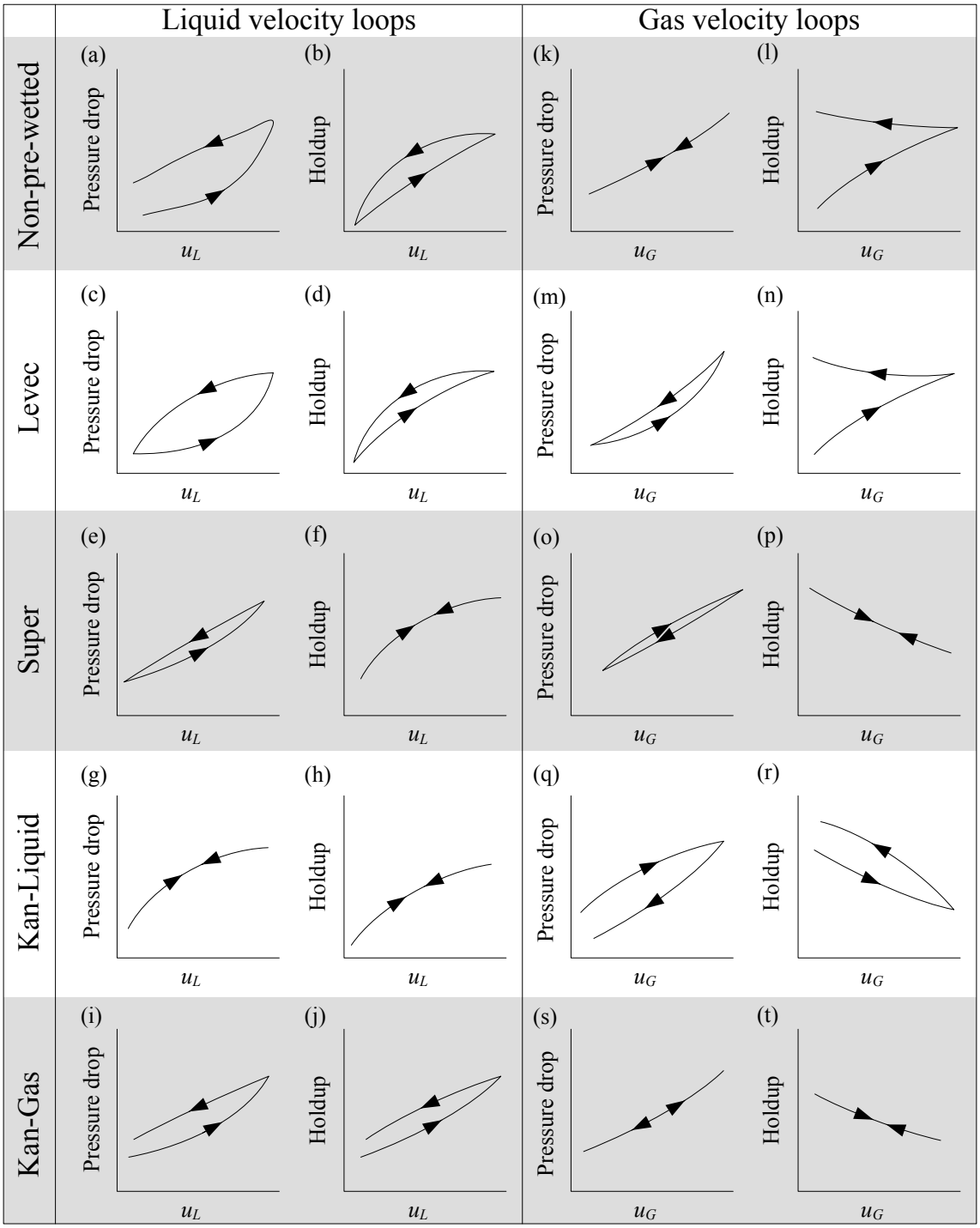

Figure 17. Gas and liquid flow rate induced hysteresis loops in all the hydrodynamic modes (a complete version of Figure 5).

An additional example is the fact that no flow rate manipulation (gas or liquid) can cross the lower boundaries (the minimum cases are still the Non-pre-wetted and Levec (for pre-wetted beds) modes. See Figure 17a to Figure 17d, as well as Figure 17k to Figure 17n.

The robustness of the limiting cases framework can be tested by conducting repeated loops (of gas or liquid) and to see whether there is any drift to the base value of the hydrodynamic parameter. This is akin to the experiments of repeated loops done by Ravindra et al. (1997b) and discussed in detail by Maiti et al. (2005). Some results are shown in Figure 18, where 10 liquid (Figure 18a) and gas (Figure 18b) flow loops were conducted in each mode.

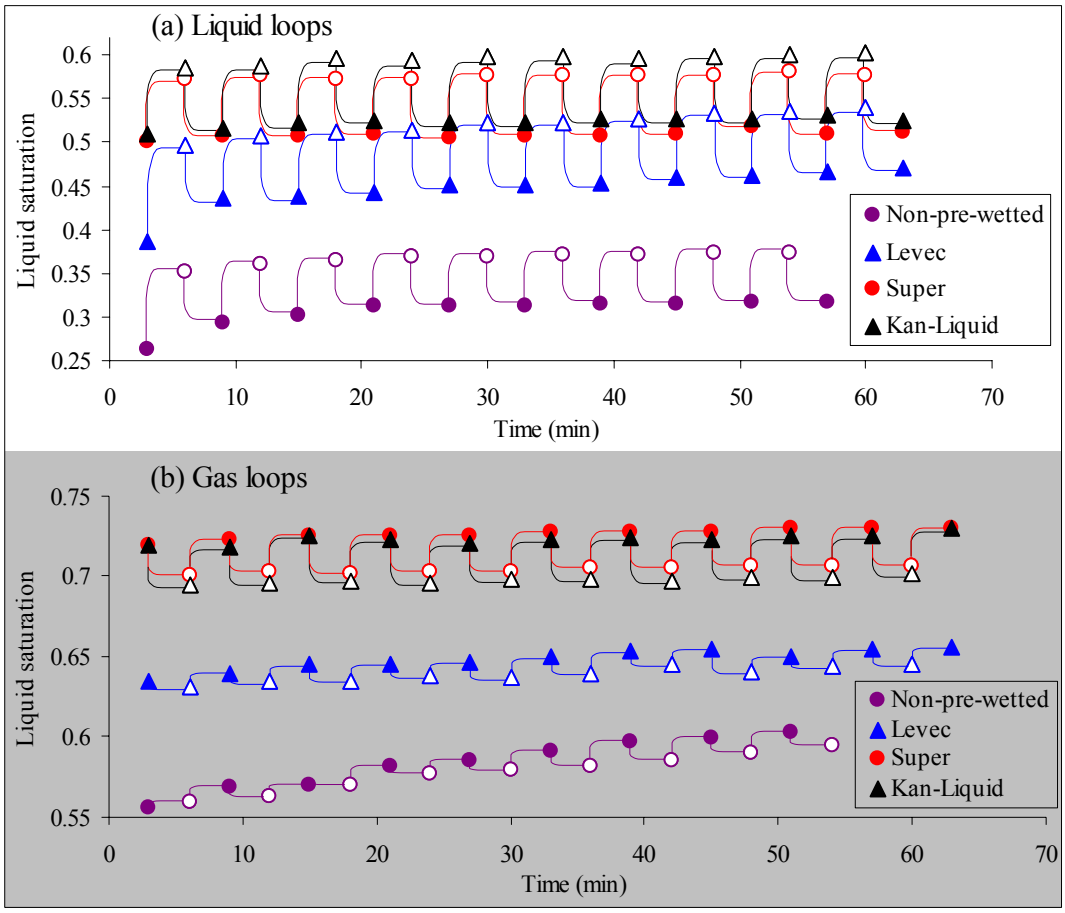

Figure 18. Effect of repeated flow rate variation loops on liquid saturation. In most cases little drift is observed after 2 loops (a) Filled symbols: u_L = 5 mm/s, open symbols: u_L = 7 mm/s. (b) Filled symbols: u_G = 2 cm/s, open symbols: u_G = 4 cm/s.

The liquid loops were performed by establishing steady state in the desired multiplicity mode and then increasing and decreasing the liquid velocity (from 5 to 7 back to 5 mm/s) at one minute intervals, all at a constant gas velocity of 2 cm/s. Similarly, during the gas loops the gas velocity was changed from 2 to 4 and back to 2 cm/s while keeping the liquid velocity at 5 mm/s. The modes are somewhat insensitive to repeated small perturbations of the fluid flow rates. As a specific example, examine the behaviour of the Non-pre-wetted mode at 5 mm/s (Figure 18a): The initial liquid saturation is approximately 0.26. After one liquid loop, the saturation has increased to approximately 0.30 (as expected). On completion of the second loop, it has risen to 0.31 and then stays roughly equal to that upon completion of loops 3 to 10. Importantly, the so-called lower branches (Non-pre-wetted and Levec modes) do not rapidly evolve into the upper ones (Kan-Liquid and Super) over time because of small liquid flow rate changes. The Levec mode also shows no drift with gas flow rate perturbations, although the Non-pre-wetted mode does.

A further aspect of hydrodynamic multiplicity that can be investigated at the bed scale is the impact that a lowering of the surface tension has on the extent of multiplicity. This is presented in two ways in Figure 19. In Figure 19a a liquid flow rate variation induced pressure drop hysteresis loop (starting from the Levec mode) *with a low surface tension liquid* (0.02-0.03 N/m) is compared to the same loop with a high surface tension liquid (0.07 N/m). Gas flow loops show similar behaviour. Experimental details are again reported in Van der Westhuizen (2006) and the present discussion is limited to the evaluation of the data. As noted by several other investigators (Kan & Greenfield, 1978, Levec et al., 1986, Wang et al., 1995), the result is simply that the pressure drop in each mode is now higher, but the hydrodynamic multiplicity is still there. Clear from this figure is the fact that the pulsing boundary is reached at lower liquid velocity for the low surface tension liquid, meaning that the range of liquid velocities where multiplicity is encountered is reduced (from 0-15 mm/s to 0-7 mm/s). Here again is another trend to be included into the list that will be rationalized in terms of the multiplicity mechanism

proposed in Chapter 7. In Figure 19b the effect of a temporary lowering in the surface tension is illustrated. After steady state had been established in the applicable mode, the liquid feed was switched from water to the low surface tension liquid for 3 minutes before it was switched back to water again. Figure 19b shows that the hydrodynamic state of the Kan-Liquid mode is not altered by the temporary reduction in surface tension, while the Levec mode advances toward the upper modes. One way to interpret this is that the temporary reduction in surface tension results in irreversibly increased liquid spreading for the Levec mode but not for the Kan-Liquid mode (since there the liquid is already well spread). This is yet another multiplicity trend that will be re-examined in Chapter 7.

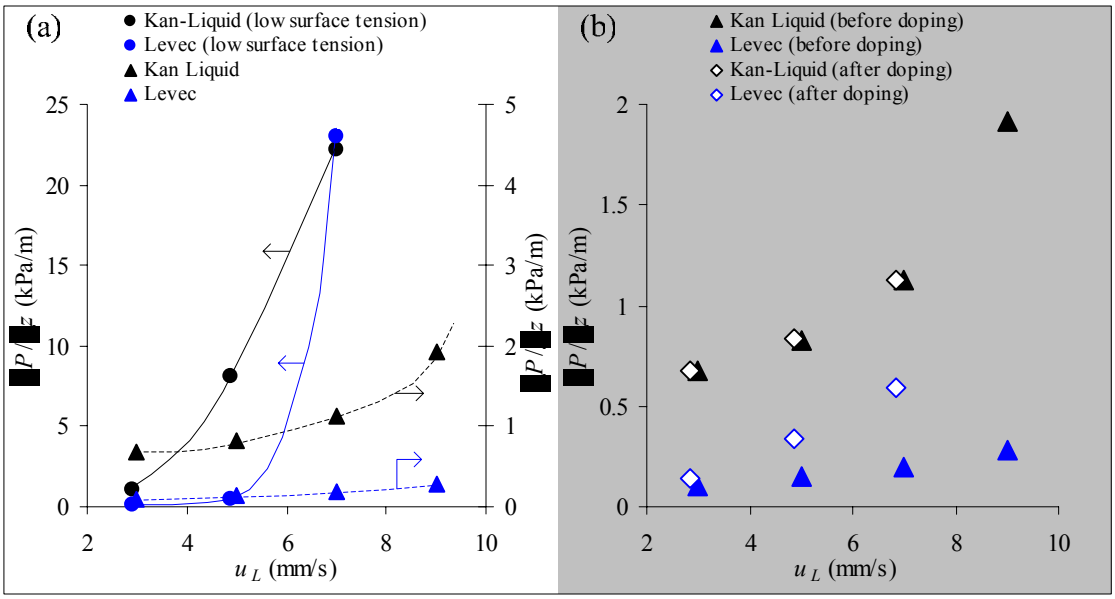

Figure 19. The effect of surface tension changes on hydrodynamic multiplicity. (a) A liquid velocity hysteresis loop with a low surface tension liquid at u_G = 2 cm/s (note that two y-axis scales are used) (b) The effect of surfactant doping, i.e. a surface tension change induced hysteresis loop.

It is concluded from these discussions that the limiting cases framework is both applicable to and useful for the investigation of hydrodynamic multiplicity. The reasons are:

- The 5 modes are distinct and all 5 are important limiting cases.

- *Major* changes in hydrodynamic parameters (at specific conditions) can *only* be brought about by changing from mode to mode.
- Flow rate or surface tension manipulation cannot result in conditions *outside* those of the limiting modes. This is true even for repeated loops.
- It is possible to switch from any mode to any other mode if appropriate procedures are followed.

Figure 20 is presented as a guide to these five modes of hydrodynamic multiplicity and the processes that can be adopted to alter the hydrodynamic state from one mode to any other.

4.3 Multiplicity in Beds of Porous Particles

The wettability of the solid is generally expected to play a big role in determining the hydrodynamics of trickle flow. In the previous section, glass beads were used exclusively in investigating hydrodynamic multiplicity. The equilibrium liquid-solid contact angle at the glass-liquid-solid contact line for glass-air-water is equal to 32 degrees (Van der Merwe et al., 2004). In industrial trickle bed reactors porous particles are predominantly used and the equilibrium contact angle can be expected to be close to zero. Using only the pressure drop hysteresis data of Ravindra et al. (1997b), Maiti et al. (2005) presented a detailed analysis of the differences between hysteresis loops in porous and non-porous beds and paid particular attention to the behaviour of the pressure drop with repeated gas or liquid flow rate cycles. In their work, the idea of "open" and "closed" hysteresis loops is introduced, the former being a hysteresis loop where the pressure drop on the decreasing leg is higher than that of the increasing leg *at the lowest velocity tested*. Since the choice of this lowest velocity is arbitrary (Ravindra et al. chose 1 mm/s) it is unclear exactly what the value of this distinction is. More specifically, *all* hysteresis loops in pre-wetted beds are ultimately closed if this lowest liquid velocity is chosen close enough to zero (at which point the holdup converges to the residual holdup).

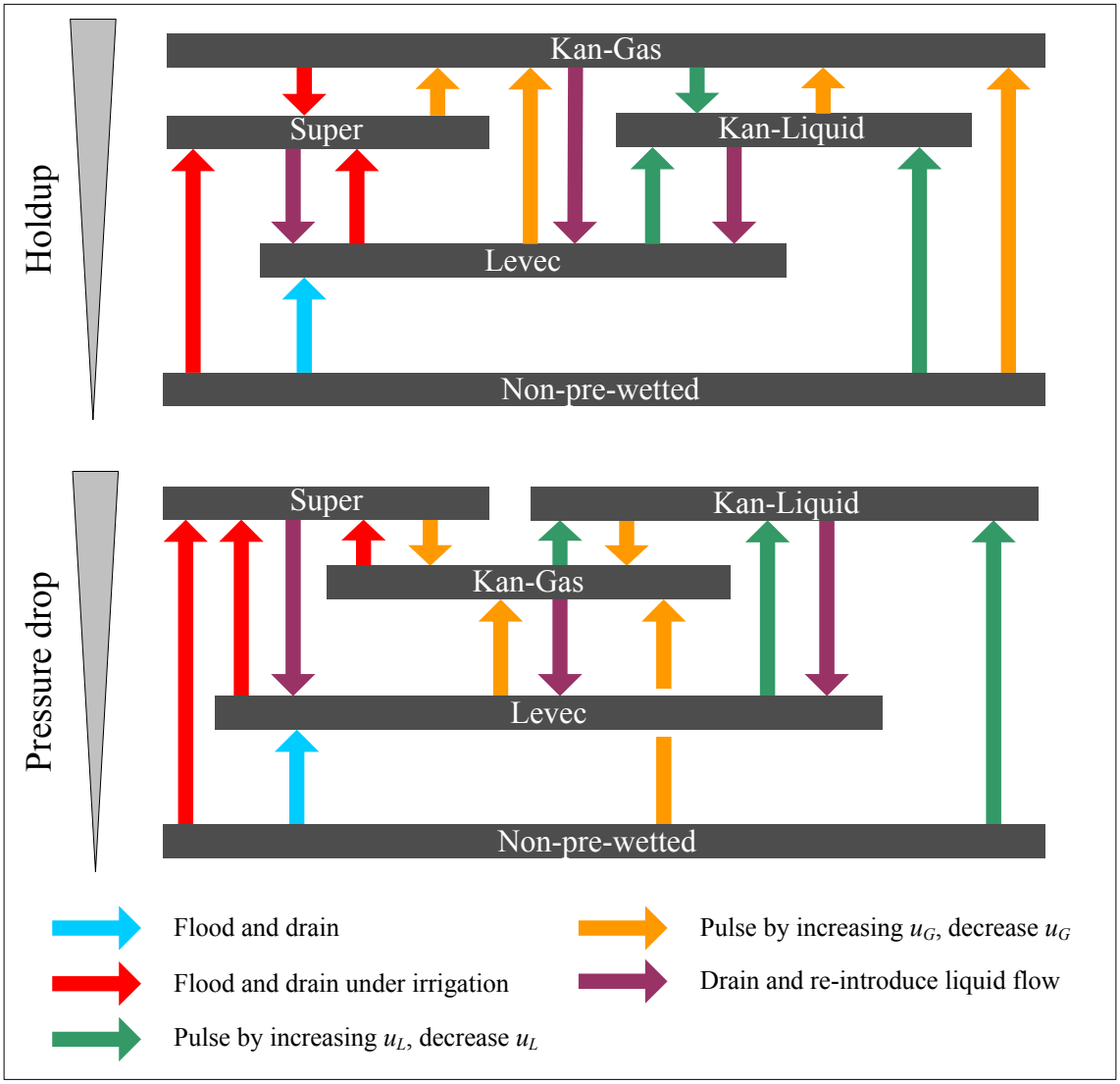

Figure 20. The limiting cases of hydrodynamic multiplicity and their inter-relationships. The limiting cases for gas-liquid mass transfer are the same as those for pressure drop.

However, Maiti et al. (2005) presents two very important ideas:

- The liquid spreading mechanism is different for porous and non-porous particles. In porous particles, there is an additional "pinning force" that keeps liquid films from retracting as severely as they do in non-porous packing. This obviously impacts the receding contact angle.

- Hysteresis is attributable to the different ways that liquid spreads inside the bed. The authors associates “participating and non-participating particles” and “favourable particle clusters” with this idea.

Because porous and non-porous particles show some differences in hydrodynamics, it is necessary to evaluate porous beds through the framework adopted in this work. For this purpose, this section introduces pressure drop, liquid holdup (saturation) and gas-liquid mass transfer multiplicity data generated for a bed packed with 2.5 mm porous alumina spheres for all the conditions examined in the previous (non-porous) section. Figure 21 shows steady state pressure drop, liquid saturation and gas-liquid mass transfer coefficients for the porous bed at a gas velocity of 4 cm/s. The other gas velocities showed comparable trends. For the porous case, the data is the average of two runs and reproducibility was comparable to the non-porous case. The non-porous data is also shown on these figures for comparison. The functional behaviour of all tested parameters remains the same, as well as the limiting cases that have been defined previously. The pressure drop (Figure 21a) in the bed of porous particles is higher than in the non-porous particles (even more than expected from the smaller particle size, 2.5 vs. 3 mm). The extent of pressure drop multiplicity between the Levec and Kan-Liquid/Super modes appear to be similar to the non-porous case. Holdup evidently does not differ as much as a result of hydrodynamic multiplicity in the porous case, although higher holdup is still achieved in the Super/Kan-Liquid mode than in the Levec mode. The gas-liquid mass transfer coefficient extent of multiplicity is also reduced but is still present. To illustrate this, Figure 22 compares the extent of multiplicity for pre-wetted beds (defined as the ratio of the values in the Kan-Liquid and Levec modes, equation 1) in each of the hydrodynamic parameters at u_G = 4 cm/s and u_L = 5 mm/s. Note that the other gas and liquid velocities showed similar behaviour but is not shown here for the sake of brevity.

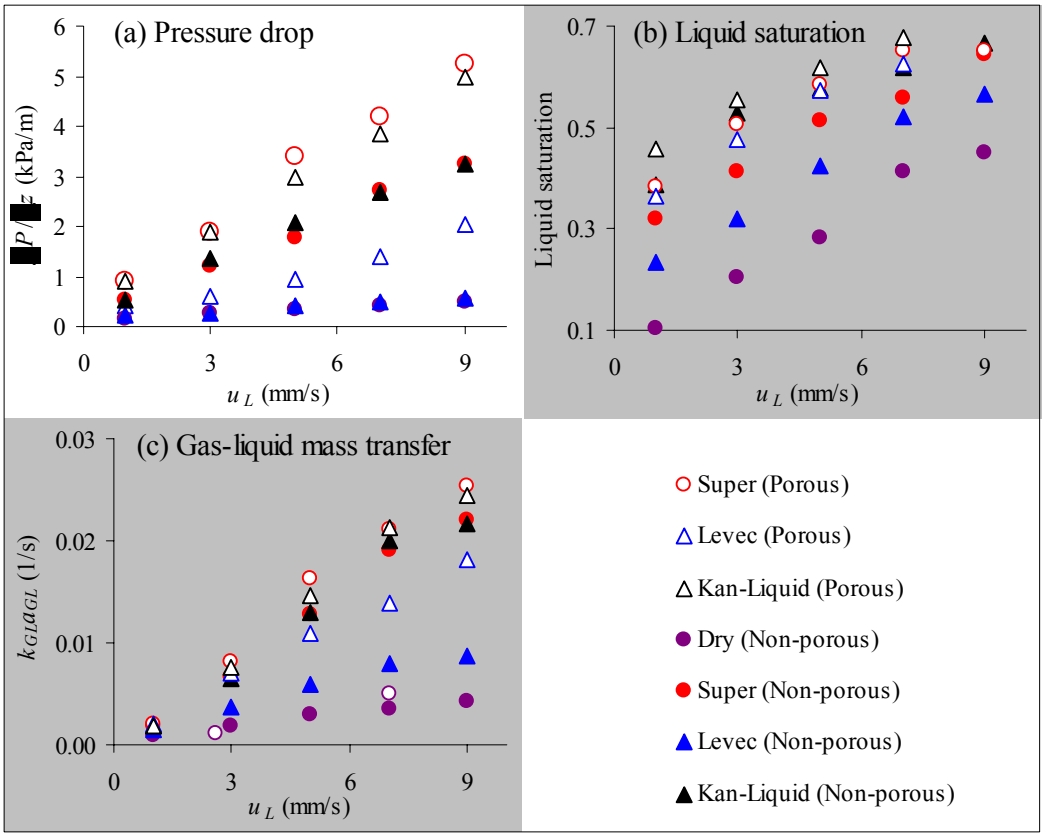

Figure 21. Comparison between porous and non-porous data at $u_G = 4$ cm/s.

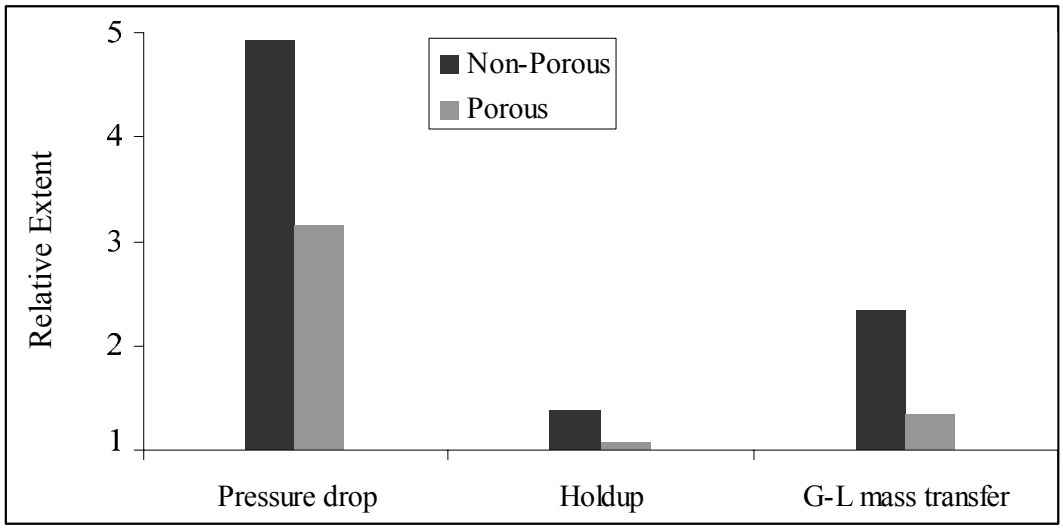

Figure 22. Comparison between the extent of hydrodynamic multiplicity (between the Kan-Liquid and Levec modes) for porous and non-porous packing (at $u_G = 4$ cm/s and $u_L = 5$ mm/s).

Evidently, the porous nature of the packing in the second case serves to aid liquid distribution - but not to the extent of destroying the hydrodynamic multiplicity. The limiting cases framework is valid for porous packing as well. Movement from one mode to another occurs through an irreversible change in the liquid distribution that is caused by either pre-wetting or large liquid or gas flow rate variation. Note that the repeated loop experiments of Ravindra et al. (1997b) is a sub-class of such movement in between modes: the first time a liquid flow rate loop is conducted in a Non-pre-wetted bed, the hydrodynamic state moves upward (see Figure 20) irreversibly and subsequent loops then work off this new base. The same behaviour is seen in Figure 18. Using a porous packing simply changes the extent of hydrodynamic multiplicity, but it is still present and has the same functional behaviour as in beds of non-porous packing.

The effect of particle shape on the hydrodynamic behaviour in the different modes is also of interest because catalyst shapes range from spherical (as used thus far) to cylinders and tri-lobes of very low sphericity. Figure 23 presents some pressure drop multiplicity results for porous alumina cylinders (3×3 mm, sphericity = 0.41) at two gas velocities and different liquid velocities. It is evident that the pressure drops for the extrudate were higher than for the spheres (which corresponds to the trend listed in Chapter 2 - pressure drop is higher when sphericity is lower) and that the pulsing regime is reached at lower liquid velocities for extrudates (the pressure drops in the Levec and Kan-Liquid modes nearly being equal at the top liquid velocity). Apart from these observations, the hydrodynamic multiplicity seems unaffected. The average extent (the average ratio of pressure drop in the two modes for all the liquid velocities at a gas velocity) for a gas velocity of 2 cm/s is 1.9 in both cases, but at u_G = 6 cm/s it is 1.5 for the spheres and 0.7 for the extrudates. This means that hydrodynamic multiplicity is somewhat diminished for the extrudates at high gas velocity compared to the spheres. The rapidity with which the pulsing boundary is reached upon increasing the liquid velocity is clearly associated with the extent of multiplicity (another trend to add to the Trends list). This was also seen in Figure 6 with respect to the effect of gas velocity.

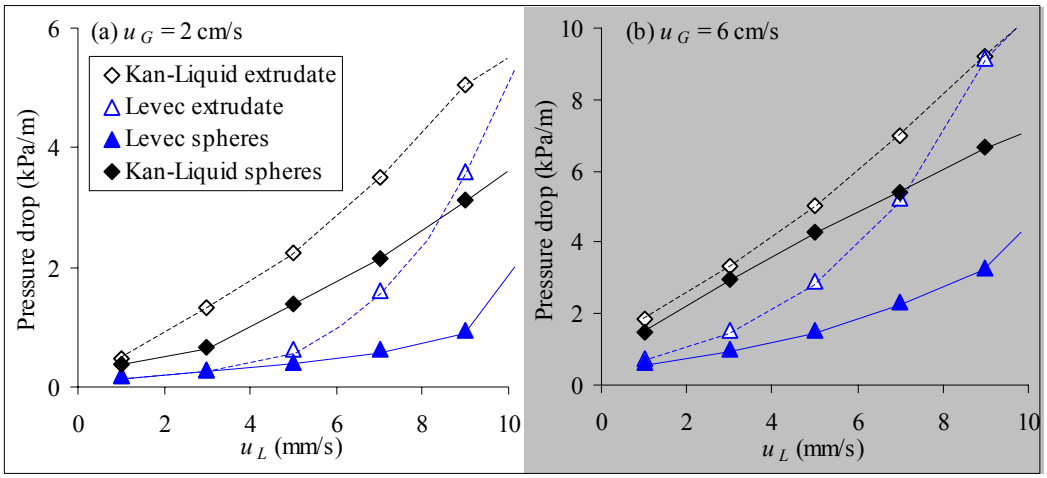

Figure 23. Pressure drop multiplicity as a function of liquid velocity for porous spheres and porous extrudate at two gas velocities.

4.4 The Effect of High Pressure Operation on Hydrodynamic Multiplicity[2]

Insofar as wetting efficiency, holdup and pressure drop in the Kan-Liquid mode is concerned, Al-Dahhan et al. (1995a) showed that an increase in the operational pressure is equivalent to an increase in the density of the gas phase. An important conclusion reached by the same authors is that the increased pressure therefore results in increased gas-liquid drag which in turn causes the liquid to spread more uniformly over the packing surface. This manifests as a simultaneous increase in wetting efficiency and decrease in holdup. Insofar as hydrodynamic multiplicity is concerned, it has been repeatedly mentioned throughout Chapter 2 that the liquid distribution is critically linked to the phenomenon.

If an increased pressure results in increased liquid distribution, it is likely that it will reduce the extent of hydrodynamic multiplicity. For trickle bed reactors specifically, the relevant range of gas densities can be calculated from typical operating conditions. The

[2] The work in this section was conducted at the Chemical Reaction Engineering Laboratory (CREL) at Washington University in St Louis, USA. It is to be published shortly following presentation at the annual AIChE meeting (2007).

conditions range from atmospheric pressure to several MPa. In hydroprocessing (H_2 as gas phase), the pressures range from 1 to 20 MPa at temperatures of 300 to 400 degrees Centigrade (Kundu et al., 2003), putting the gas density approximately in the range 0.4 to 7 kg/m^3. Following Al-Dahhan et al. (1997), these densities can be simulated by air at room temperature at pressures of 30 to 660 kPa (absolute). At low gas density the gas drag effect is negligible (Al-Dahhan et al., 1997). As a consequence, it is the pressures between atmospheric and 0.7 MPa that warrant further investigation. This section presents such data for the experimental conditions listed in Table 13. Additional detail on the construction of the experimental setup is discussed in Lanfrey (2006). Note that the column diameter is larger than what has been previously used. This was an unfortunate experimental constraint that could not be avoided.

Table 13. Experimental details of high pressure experiments

Fluids	Water, Air
Gas pressures	0.1, 0.3, 0.5, 0.7 MPa (absolute)
Gas densities	1.1, 3.3, 5.5, 7.7 kg/m^3
Particles	3 mm non-porous glass spheres
Column diameter	163 mm
Bed length	686 mm
Liquid velocity	1.9, 3.6, 6.7 and 9.5 mm/s
Gas velocity	3.5, 5.7 and 9.2 cm/s
Scale	Resolution: 50 g, maximum load: 220 kg
Differential pressure transducer	Validyne DP15-30 (accuracy: ±20 Pa)
Bed porosity	0.41
Distributor drip point density	11500 points per m^2

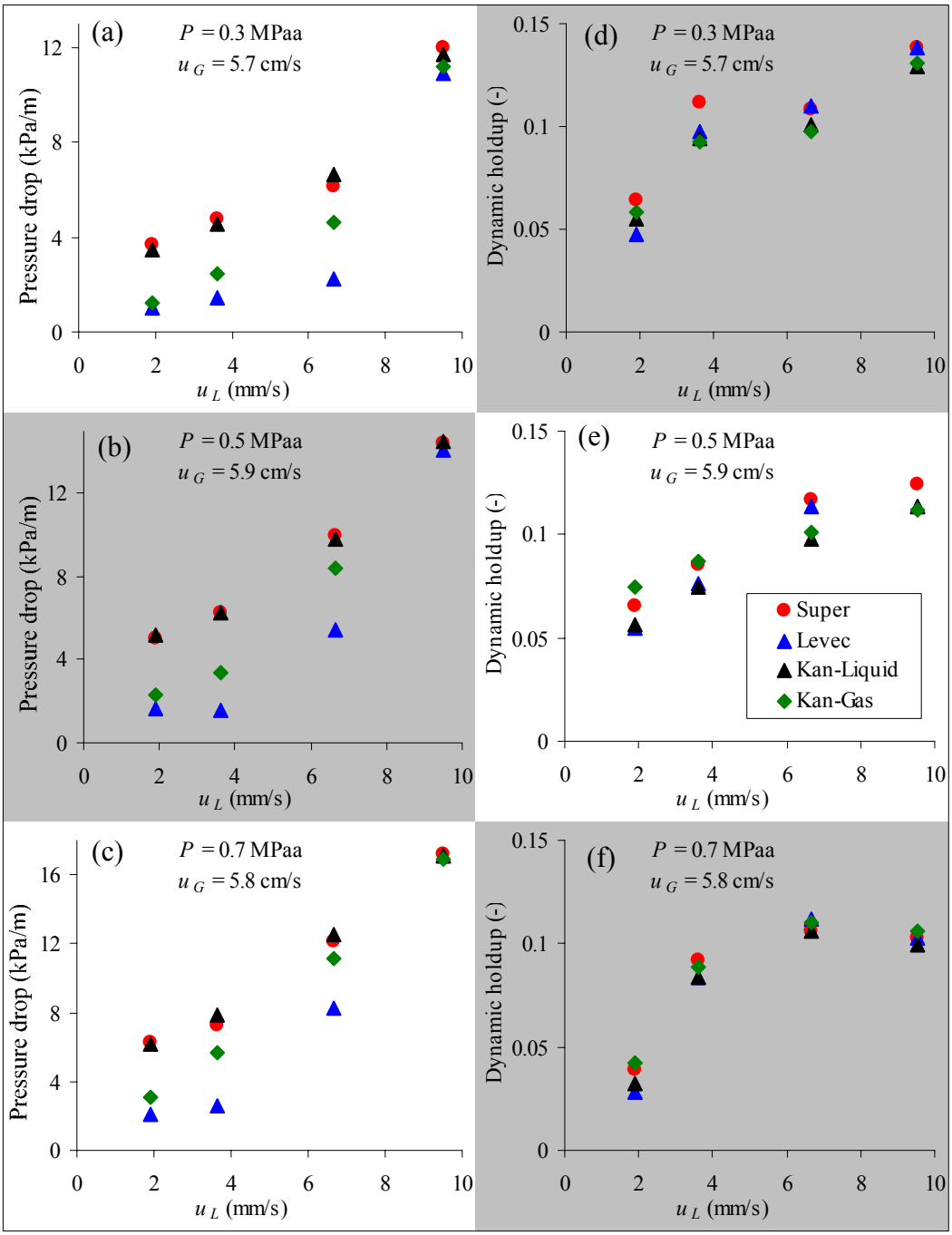

Figure 24. Pressure drop (a-c) and dynamic holdup (d-f) data at increasing pressure ($u_G \approx 5.7$ cm/s)

Results are presented in Figure 24 and Figure 25. The results are shown for u_G = 5.7 cm/s; the other gas velocities showed similar trends. In these figures, each data point is

the average of 2 measurements. Reproducibility was generally within 12-15%, with the pressure drop in the Levec mode being an exception (differences between successive runs were as high as 40%). The Non-pre-wetted mode could not be as extensively studied because of difficulty in loading and unloading the reactor. The results show that the holdup appears to be very similar to one another in the four modes regardless of the pressure. It should be stated that there are severe difficulties in making accurate weight measurements on the scale employed here. Not only is the objective to measure relatively small changes in weight from a large base, the end effects like the weight of the fluid supply lines and the collector installed at the bottom of the column are difficult to compensate for. In each case, a run at equivalent conditions but without the packing was subtracted from the data in an attempt to minimize these effects. The pressure drop measurements do not suffer from these uncertainties and are therefore preferred in subsequent analyses.

From Figure 24a to Figure 24c it is seen that the same trends are followed as the atmospheric pressure case discussed earlier (the limiting cases remain the same). Some additional information is presented in Figure 25, where the pressure drop in each mode is shown for all four pressures as a function of liquid velocity. An increase in pressure results in an increase in pressure drop for all hydrodynamic modes, although this effect is more pronounced in the Levec mode (Figure 25d).

Figure 26 shows the pressure drop ratio of Levec to Kan-Liquid (i.e. 1/Extent) as a function of the gas mass flux for different liquid velocities (Figure 26a) and as a function of the liquid velocity for different gas mass fluxes (Figure 26b). Figure 26a shows the importance of the liquid velocity – increasing the gas mass flux at low velocity has no effect on the extent of multiplicity. Figure 26b clearly shows that an increase in the gas mass flux at medium to high liquid velocity decreases the extent of hydrodynamic multiplicity.

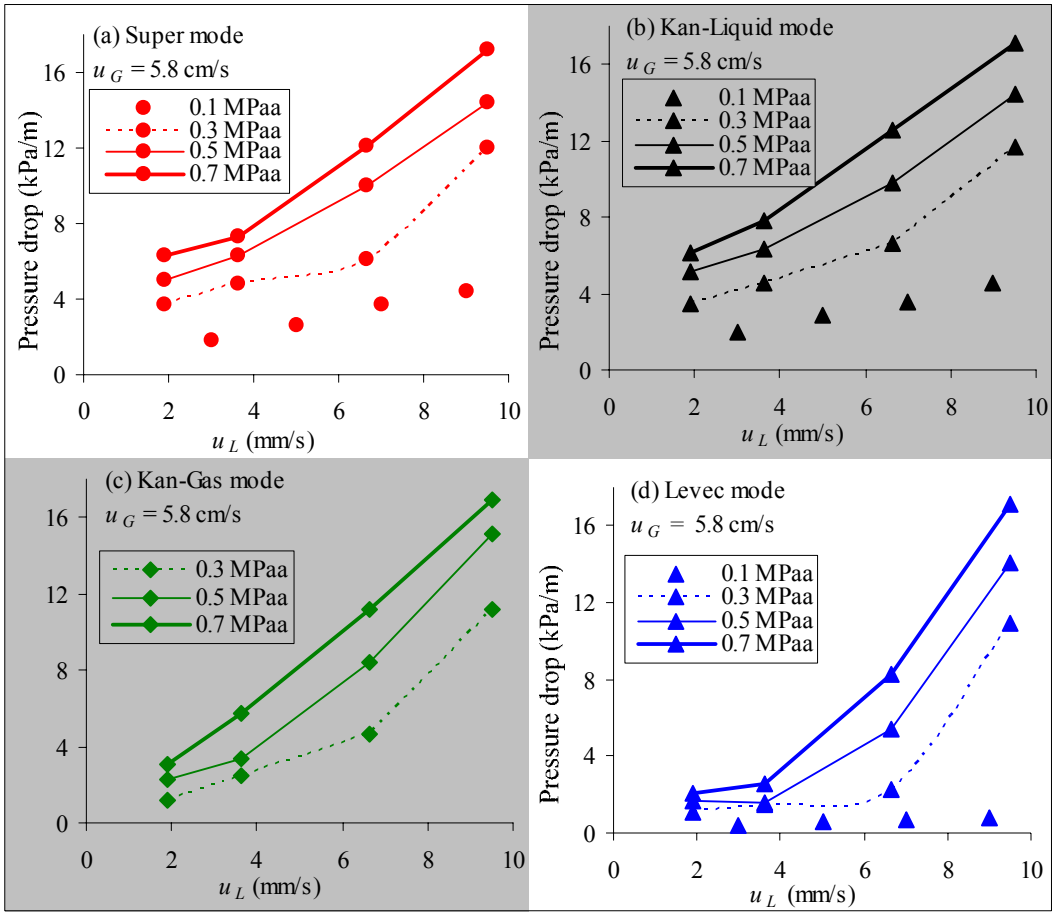

Figure 25. Pressure drop data at increasing pressure per mode (u_G = 5.8 cm/s)

Note that:

- Hydrodynamic multiplicity persists at low liquid velocities even at the highest gas velocity and highest pressure. Increasing either the gas velocity or pressure at low liquid velocity does not decrease the extent of multiplicity.
- At high liquid velocity there is little multiplicity (the pressure drop being equal in both modes).
- At medium to high liquid velocity an increase in gas velocity at constant pressure decreases the extent of multiplicity. Conversely, at medium to high liquid velocity an increase in operating pressure at constant gas velocity also decreases the extent of multiplicity.

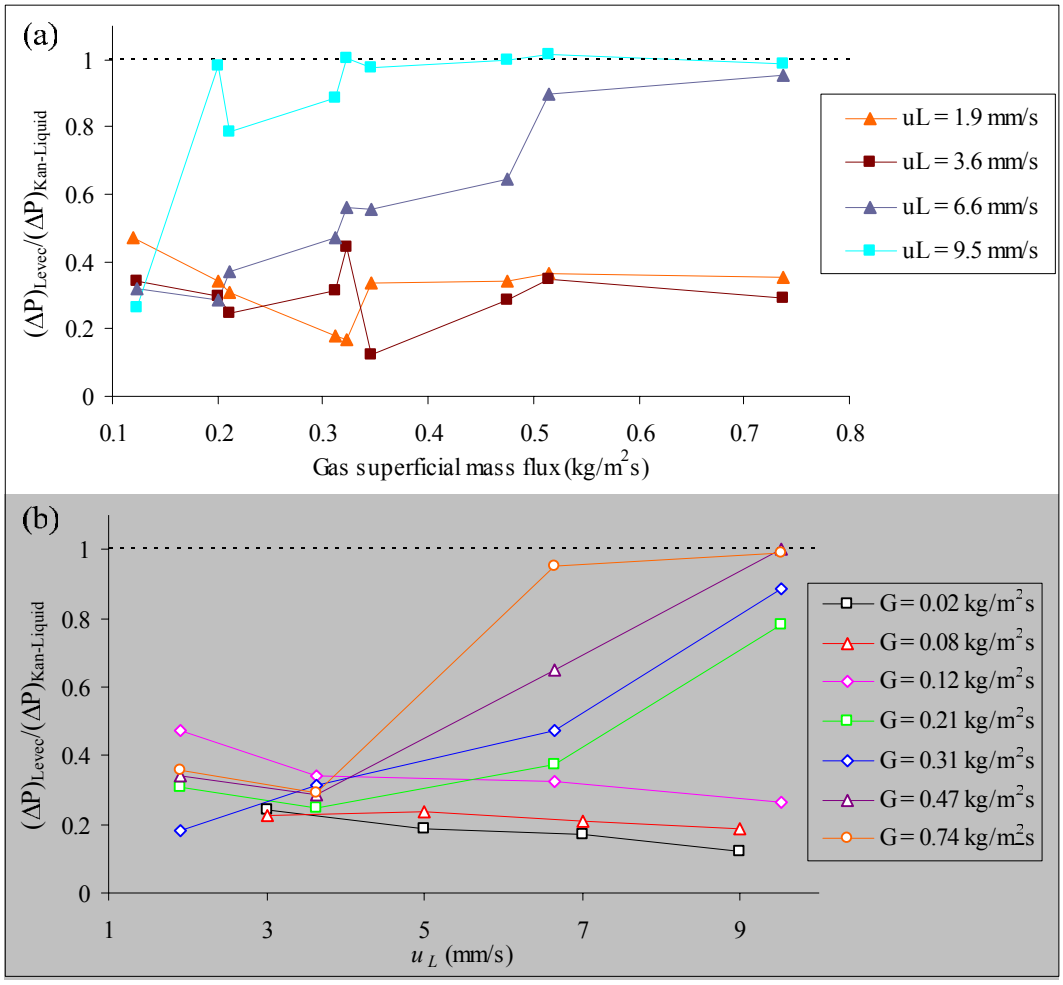

Figure 26. The ratio of Levec to Kan-Liquid pressure drops as a function of (a) gas superficial mass flux liquid and (b) liquid velocity.

The implications of these observations are that the *pressure drop* itself is the governing variable, since whenever pressure drop is high, the multiplicity extent is low and whenever it is low the extent is high. Figure 27 shows the ratio (inverse of extent of multiplicity) against the pressure drop in the Levec mode. Note that all the different conditions fall on one line. This means that for a specific bed, the pressure drop in the Levec mode determines the extent of hydrodynamic multiplicity.

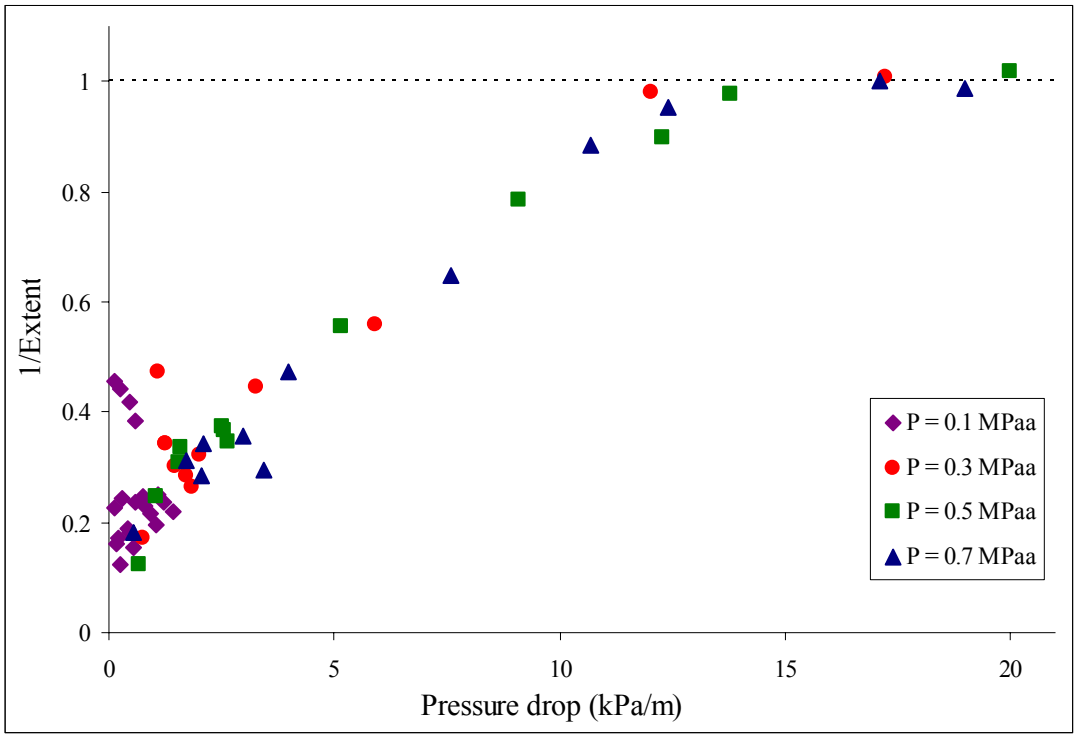

Figure 27. The ratio of Levec to Kan-Liquid pressure drops as a function of pressure drop in the Levec mode. Note that a ratio of 1 (black dashed line) implies that there is no difference in the pressure drop and therefore no hydrodynamic multiplicity.

It is concluded therefore that an increase in operating pressure for the range of industrially important pressures (gas densities) decreases the extent of hydrodynamic multiplicity provided that the liquid velocity is high. At low velocities, the operating pressure has little effect on the extent of multiplicity. High pressure operation therefore causes two major effects: *pressure drop is comparatively much higher (especially in the Levec mode) and multiplicity is less severe at high pressure drop*.

4.5 Conclusions

In this chapter, hydrodynamic multiplicity was investigated at the bed scale through pressure drop, liquid holdup and volumetric gas-liquid mass transfer measurements at conditions that included low and high pressures, porous and non-porous packing elements

and high and low surface tension liquids. This chapter also evaluated the proposed limiting cases of hydrodynamic multiplicity (the conceptual framework) and found them to be a handy framework by which to study pre-wetting and hysteresis in trickle flow. The existing bed-scale literature data are encompassed within this framework.

In accordance with the strategy in Figure 1, a number of trends were identified from new hydrodynamic data in terms of the behaviour of the various hydrodynamic parameters in each limiting mode, as well as how the modes are related to each other. In addition, some of the trends already identified in Chapter 2 were confirmed: **(A)** to **(D)**. The updated list of multiplicity trends is:

(A) There are different flow patterns in the different modes: rivulet-type flow in the lower limiting cases and film-type flow in the upper limiting cases. New rivulets are created as u_L increases.

(B) Liquid flow rate variation induced hysteresis causes increases in pressure drop and liquid holdup in the non-pre-wetted and Levec modes.

(C) Gas flow rate variation induced hysteresis causes increases in pressure drop and holdup in the Levec mode, but an increase in holdup and a decrease in pressure drop in the Kan-Liquid mode.

(D) The extent of pressure drop hysteresis is diminished when particle size is increased.

(E) The Levec mode *wetting efficiency* is lower on average and shows a bi-modal particle wetting distribution, whereas the Super mode shows a Gaussian distribution.

(F) The liquid *holdup* increases by mode in the order Non-pre-wetted, Levec, Kan-Liquid/Super and then the Kan-Gas mode.

(G) The *pressure drop* for the Non-pre-wetted and Levec modes are the same and lower than the Kan-Liquid/Super mode pressure drop. The Kan-Gas pressure drop is in between these despite it having a *larger* holdup.

(H) The *volumetric gas-liquid mass transfer coefficient* shows the same functional behaviour as the pressure drop.

(I) The *Super and Kan-Liquid modes have similar behaviour*, both in the uniformity of the flow distribution and in the nearly identical values in all the hydrodynamic parameters - despite having been established with different operating procedures.

(J) *Small flow rate changes* have little effect on the hydrodynamic multiplicity after the first or second cycle.

(K) A *decrease in surface tension* brings the pulsing boundary to lower liquid velocity, but hydrodynamic multiplicity still persists in the trickle regime.

(L) A temporary decrease in the surface tension (*surface tension change induced hysteresis*) has no effect on the pressure drop in the Kan-Liquid mode but increases the pressure drop in the Levec mode.

(M) Beds of porous particles have a lower extent of multiplicity compared to beds of non-porous particles.

(N) The extent of multiplicity is associated with the pulsing boundary; *hysteresis is diminished if the pulsing boundary velocity is lowered* (by changing surface tension or particle shape).

(O) An increase in liquid or gas velocity in the *Levec mode drastically increases the pressure drop* at high pressure (gas density), while the increase in the other modes is far less drastic.

(P) High pressure operation (or high gas mass flux) has little effect on multiplicity at low liquid velocity, but decreases the extent of multiplicity at high liquid velocity. The *pressure drop determines the extent of multiplicity*.

Note that these trends all refer to bed-scale averages of the hydrodynamic parameters. However, as discussed in section 2.3.2, several authors have suggested that the bed-scale observations are the results of phenomena that occur at the micro-scale (pore-scale). Therefore, there is reason to expect the governing mechanism for hydrodynamic

multiplicity to be easier identifiable at the pore-scale. This requires pore-scale hydrodynamic data, which is obtained through radio-imaging in the next two chapters.

Chapter 5. Preliminary Visualizations[3]

This list of characteristic multiplicity trends given at the end of the previous chapter is already extensive, but a major deficiency is the fact that all these trends are bed-scale and it is not possible to extract the localized characteristics from them. Additional insights into the distribution of liquid and gas at the local (pore) scale is necessary in order to discern the fundamental mechanism responsible for the multiplicity behaviour. The next two chapters addresses the cluster-of-particles (pore) scale characteristics of hydrodynamic multiplicity (it is Part 2 of the Additional Experimental Insights block in Figure 1). The technique by which this is accomplished is X-ray radio-imaging, of which two variants are employed: temporal radiography (2D) and 3D tomography. Here again, the objective is to identify the nature of hydrodynamic multiplicity at a smaller scale through the extension of the characteristic trends list, i.e. Objective 2 as identified in Chapter 3. In Chapter 7, these insights lead to the proposal of a multiplicity mechanism.

5.1 Background

The main visualization techniques used to study the micro-scale characteristics of trickle flow are colorimetry and non-intrusive imaging (including radiography and computed tomography). In recent years, both techniques have provided insights into the localized behaviour of trickle flow at the cluster-of-particles scale (Lazzaroni et al., 1988, 1989, Ravindra et al., 1997b, Van Houwelingen et al., 2006, Lutran et al., 1991, Toye et al., 1998, Mantle et al., 2001, Sederman & Gladden, 2001, Boyer & Fanget, 2002, Marchot et al., 2001, Anadon et al., 2005, Gladden et al., 2003a, Kantzas, 1994, Reinecke & Mewes,

[3] The work reported in this Chapter was published in Chemical Engineering Journal, Vol. 132, pg 47-59, 2007.

1996, Schmit, et al., 2000, Yin et al., 2002, Gladden et al., 2003b, Basavaraj et al., 2005). In particular, the structure of packed beds and the distribution of the fluid phases in these beds on various scales and under differing circumstances have been given considerable attention. Brief overviews follow.

The colorimetric technique involves colouring the catalyst particles at the locations where the liquid is in contact with the particle surface. The flow is brought to steady state before the feed is switched to a dye solution for either 5 or 20 minutes (Lazzaroni et al., 1988, Ravindra et al., 1997b). The wetting efficiency is calculated directly from the (partially) coloured particles, while the liquid distribution can be inferred from such data (Van Houwelingen et al., 2006). The validity of the technique is dependent upon the assumption that the liquid distribution remains stable throughout the period of dye irrigation. Any flow path deviations during this time will result in non-uniformly coloured particles and probably an over-estimation of the wetting efficiency and the flow uniformity. A further drawback of this method is its intrusive nature. The feed properties are changed by the dye and there are flow rate disturbances that influence the flow stability (Gladden et al., 2003a) and potentially the liquid distribution.

Radiography involves subjecting the trickle bed to some form of radiation (γ-, X- or neutron) and then recording the interaction between the different phases and the radiation (usually in the form of an intensity image). The technique relies on the fact that the different phases attenuate (absorb) the radiation to varying degrees. In computed tomography (CT), the bed is subjected to the radiation at several angles of rotation. From these images a three-dimensional reconstruction of the entire volume under consideration can be made. CT has emerged as a valuable tool for the non-invasive imaging of opaque systems in the chemical and process industries (Chaouki et al., 1997). In terms of trickle flow CT, the liquid distribution has been successfully investigated (for selected conditions) by several authors (Lutran et al., 1991, Toye et al., 1998, Sederman & Gladden, 2001, Gladden et al., 2003a, Kantzas, 1994, Reinecke & Mewes, 1996, Schmit,

et al., 2000, Yin et al., 2002 and Gladden et al., 2003b). However, most of these reports have been mainly concerned with proving the utility of the technique and only to a lesser degree with using the technique to investigate the underlying physical phenomena. CT investigations also assume that the flow remains stable during the acquisition of the images required for the volume reconstruction. These acquisition times can be very short (milliseconds) if one is prepared to accept either relatively poor spatial resolution (millimetres, MRI) or reconstruction artefacts in the final volume image (for example "streak lines" in X-ray tomography). For a greater resolution MRI image of a dry bed (micrometers), Anadon et al. (2005) used an acquisition time of 11.5 hours, but they do not report such high resolution images for trickle flow conditions. Gladden et al. (2003a) conducted a stability analysis of trickle flow using 2D images with acquisition times of 30 seconds per image and an in-plane resolution of 352 μm per pixel. For radiation-based CT, longer acquisition times will be required for larger diameter beds. A summary of CT and radiography investigations (with pertinent experimental conditions) into the trickle flow regime is given in Table 14. The trade-off between spatial resolution and acquisition time means that sufficiently high frequency flow path deviations can either not be detected (for the radiation-based CT. i.e. long acquisition times) or cannot be detected with a resolution smaller than a few millimetres per voxel (for example MRI). Note that there are three beam geometries for X- or γ-ray tomography. If fan beam geometry is used, it is possible to acquire rapid 2D cross-sectional images, but the question remains whether these are representative of the entire bed. Parallel beam geometry allows relatively rapid acquisition of radiographs, but no geometric enlargement of the sample. Cone beam geometry allows rapid radiograph acquisition as well as geometric enlargement of the sample, but introduces an element of inaccuracy called unsharpness. Some representative results form literature are reproduced in Figure 29.

Table 14. Trickle flow CT and radiation studies in literature

Reference	Type	Bed size (cm) D x H	Packing	Modes	Spatial resolution (μm)	TSS (min)	Acquisition time (s)
Lutran et al. (1991)	X-ray	6.03 x 19.05	Glass spheres	NPW, Kan-Liquid	500	n/r	26 (2D)
Kantzas (1994)	X-Ray	4.5 x 45	Glass spheres	NPW	400 x 400 x 3000	n/r	450 (3D*)
Reinecke & Mewes (1996)	Capacitance	12 x 200	Celcore spheres	N/A	6000-12000	n/r	0.01 (2D)
Toye et al. (1998)#	X-ray	80 x 200	Polypropylene wheels	n/r	880	n/r	150 (3D*)
Schmidt et al. (2000)	X-ray	20 x 25	Ceramic spheres	NPW, pre-wetted	400	n/r	900 (3D*)
Mantle et al. (2001)	MRI	4 x 55	Extrudate, spheres	NPW	313	160	n/r
Sederman & Gladden (2001)	MRI	4 x 50	Glass ballotini	NPW, Levec	328	n/r	21600 (3D*)180 (2D)
Marchot et al. (2001)#	X-ray	60 x 200	Polypropylene packing	n/r	1000	n/r	160 (2D)
Yin et al. (2002)	γ-ray	60 x 60	Pall rings	n/r	n/r	n/r	n/r
Boyer & Fanget (2002)	γ-ray	60 x n/r	Alumina extrudate	n/r	n/r	n/r	2700 (2D)
Gladden et al. (2003a)	MRI	70 x 4.5	Porous cyllinders	n/r	352	n/r	30 (2D)
Gladden et al. (2003b)	MRI	4 x 50	Alumina extrudate	Wetted	156	n/r	1500 (2D)
Basavaraj & Gupta (2004), Basavaraj et al. (2005)	X-ray	17 x 6 (rectangular) 75 (height)	Polystyrene spheres	NPW	757 x 757 x 60000	15	900 (2D)
Anadon et al. (2005)	MRI	4.3 x 70	Porous extrudate	Levec	3750 x 3750 x 1870 175 x 175 x 175	n/r	0.28 (3D*) 41400 (3D*)

n/r: not reported, TSS: Time to reach Steady State, NPW: Non-pre-wetted, * 3D images are obtained by stacking 2D images (obtained at several axial locations) on top of one another, # These authors investigated structured packings.

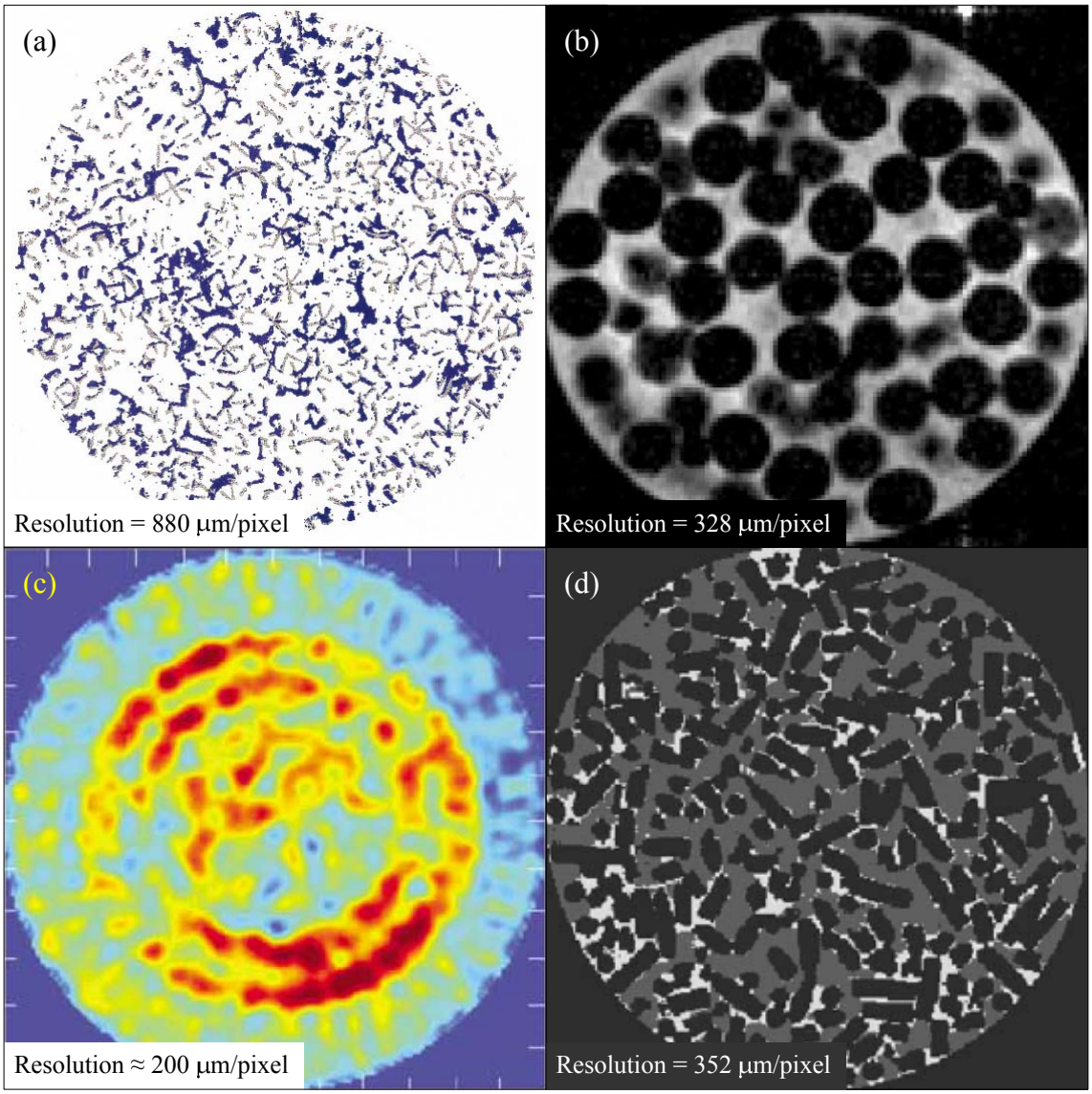

Figure 28. CT results from earlier investigators - representative of various techniques, (a) γ-ray: Toye et al. (1998) – liquid in blue, solid in grey, (b) MRI: Sederman & Gladden (2001) – solid in black, liquid in white, (c) X-ray: Boyer & Fanget (2002) – liquid saturation intensity image, (d) Processed MRI: Gladden et al. (2003a) – solid in black, liquid in white. Additional detail in Table 14. Also see Figure 8b for a representative capacitance tomography image.

5.2 Introduction

The aim of any (including the present one) particle-scale CT investigation is to establish the spatial locations and temporal behaviour of the three phases. It is evident from the preceding discussion that there is a need for determining the stability of trickle flow with high spatial and temporal resolutions. However, the objectives of both high spatial and high temporal resolution are mutually exclusively. For this reason, *radiography* is used here to obtain high temporal resolution 2D images of a section of the bed, while *tomography* is used to obtain high spatial resolution 3D images of the bed. The high temporal resolution 2D images is necessary because a proper interpretation of computed tomographical reconstructions is dependent upon the knowledge of whether or not the volume images are time-averaged representations of liquid and gas distributions or in fact a stable phase distribution configuration. The high spatial resolution 3D images then form the basis of an investigation into the local flow structures in the various multiplicity modes.

In the first part of this study, cone beam X-ray *radiography* is used to study the temporal stability of trickle flow. Radiography is better suited to the investigation of liquid saturation in porous media because it does not require exact phase-border distinction in order to attain phase saturations. X-ray radiography has been used successfully to study both liquid saturation and distribution in trickle flow packed beds (Basavaraj & Gupta, 2004, Basavaraj et al., 2005). In simple terms the focus here is to:

- Compare radiography and gravimetry as tools for a hydrodynamic investigation of trickle flow.
- Visualize the flow patterns encountered in different hydrodynamic states. The radiographic technique employed here provides visualisations of the overall liquid distribution in the bed for different fluid velocities and pre-wetting histories, the importance of which has been emphasized by Sederman & Gladden (2001),

Basavaraj & Gunjal (2004), Basavaraj et al. (2005), Marcandelli et al. (2000), Wang et al. (1995), Hoek et al. (1986) and Toye et al. (1995).

- Determine whether trickle flow is stable locally in the bed. In particular, to illustrate the usefulness of rapidly acquired radiographs to analyse the liquid distribution and its dynamic behaviour. There is some discrepancy as to the time it takes (from start-up) to reach steady state. This start-up time appears to vary considerably depending on the pre-wetting procedure (Ravindra et al., 1997b). The start-up dynamics are therefore also investigated.
- Establish whether the flow distributions and liquid saturations are reproducible provided that the same pre-wetting procedure was followed.

This first part of the radio-imaging (radiography) illustrates how a relatively simple technique can provide new insights into trickle flow phenomena. X-ray radiography has the potential to be scaled up to larger applications with relative ease (Boyer & Fanget, 2002), although the presence of steel reactor walls in industry diminishes this scaling ability.

The second part of the radio-imaging study is to obtain 3D *computed tomographic* images of the various hydrodynamic modes. These images are to provide the experimental basis for a pore scale evaluation of hydrodynamic multiplicity. One objective of such a highly detailed visualization is to obtain the interfacial areas (gas-liquid, liquid-solid and gas-solid), since these areas impact the external mass transfer (Wu et al., 1996), the particle effectiveness (Dudukovic, 1977), the residence time distribution characteristics (Iliuta et al., 1999) and the hydrodynamics in general (Pironti et al, 1998). This objective requires each phase to be properly distinguished in the processed tomograph. For CT studies of high resolution (where individual particles can be observed), the state-of-art method of distinguishing phases is by the method of thresholding (Sederman & Gladden, 2001, Gladden et al., 2003, Toye et al., 1998), whereby a range of image intensities is assigned to each phase. Section 5.4.2 will show the inadequacy of the thresholding technique for the present X-ray CT data.

5.3 Experimental

Radiograph Acquisition

A comprehensive description of the experimental facility as pertains to the acquisition of radiographs is given elsewhere (De Beer, 2005). Figure 29 is a schematic of the setup. The 40 mm (inner diameter) polypropylene column is mounted on a stand. The column is packed with spherical porous γ-alumina catalyst particles of diameter 2.5 mm. Air and water (atmospheric conditions) at controlled flow rates are fed co-currently downward into the bed. These fluids are used for ease of implementation and are the most common fluids found in the trickle bed literature. Experimental gas and liquid flow rates were chosen to represent a wide range of conditions within the trickle flow regime. Liquid superficial velocity varied from 1.3 to 8.0 mm/s and gas velocity from 0 to 16 cm/s. The liquid is distributed uniformly at the top of the bed through 16 equally sized and equally spaced holes; resulting in a drip point density in excess of 10 000 points per square meter. This ensures that the liquid distribution in the bed is independent of the distributor (Burghardt et al., 1995). A uniform initial distribution has been shown to be crucial to achieving proper liquid distribution inside the bed (Ravindra et al., 1997b). The gas enters the bed through a separate ¼" tube located in the centre of the distributor head. For the pre-wetted modes, the bed was flooded for 5 hours prior to experimentation to ensure complete internal saturation of the catalyst spheres (Van der Merwe et al., 2006).

Experimental considerations with regards to the acquisition of X-ray radiographs are the amplitude of the X-ray source, the focal point size, the source-detector distance and the presence of inorganic species in the liquid phase (Toye et al., 1998, Basavaraj & Gupta, 2004, Toye et al., 1995). Extensive testing during the course of this investigation revealed that the experimental conditions listed in Table 15 yield satisfactory results. Note that adequate phase distinction was achieved without the need to add $BaCl_2$. This ensures that the liquid properties were not changed from that of water, reduces beam hardening and reduces deviations from the Beer-Lambert Law (as discussed later).

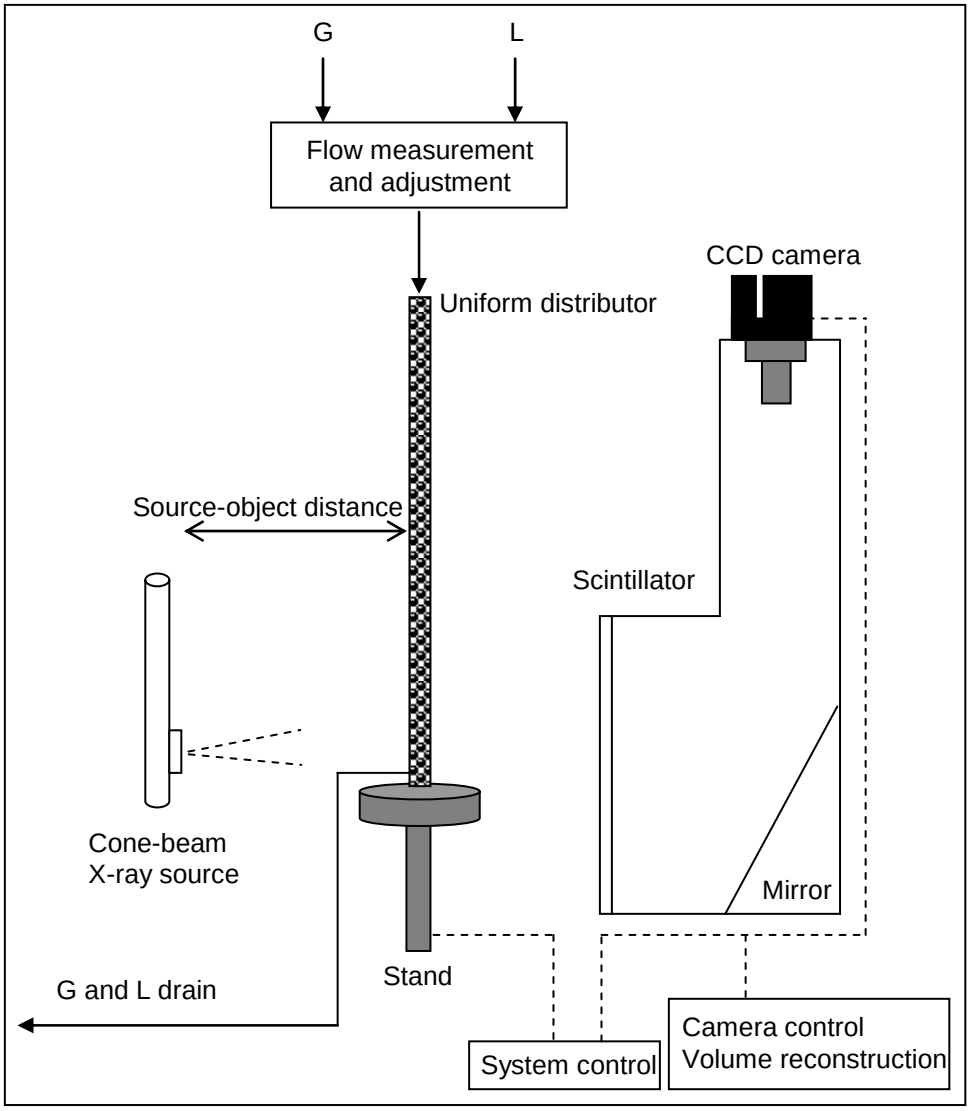

Figure 29. Experimental setup for radio-imaging study

Using these settings, a radiograph of 61 mm of the bed was obtained. The top of the radiographed section was located 539 mm below the top of the bed. This was done specifically to avoid the calming zone at the top of the bed where the liquid distribution is not representative of the entire bed (Gianetto & Specchia, 1992).

Table 15. Experimental parameters for radiography study

X-ray source	Tungsten filament
X-ray amplitude	100 keV (at 6 mA)
Packing	2.5 mm γ-alumina spheres (porous)
Packing height	900 mm
Exposure time	1.5 seconds per radiograph
Delay time (between successive acquisitions)	Approximately 0.5 seconds
Image size (binning)	512 X 512 pixels (2)
Spatial resolution	120 μm/pixel (approximately)
Focal point opening	1 mm
Source object distance (SOD)	610 mm

As in Basavaraj & Gupta (2004), the beam hardening effect is minimized by two measures:

- A low inorganic concentration (in the present study no salt was added to the liquid).
- A hardware filter (in the present study the 5 mm polyethylene column walls acted as a filter for the incoming X-rays).

Representative radiographs are shown in Figure 30. These images were filtered using a 3 × 3 low pass filter in order to remove experimental noise (white spots). In Figure 30a, the column had not been placed in the X-ray beam. The cone beam geometry is evident from the fact that the image intensity is higher in the centre of the image and decreases towards the sides. Figure 30b is the radiograph of the column packed with dry particles. Note that the X-rays traverse the entire diameter (50 mm) of the column only in the centre of the image. As one moves away from the central vertical axis, the intensity increases because the X-rays pass through less material (because of the cylindrical shape of the column) and are therefore not as severely attenuated. The reduction in intensity in the image is related to the thickness of material transverse to the viewing plane. Figure

30c is the same column after the introduction of liquid (Non-pre-wetted mode). The darkening of the image is indicative of the beam being attenuated by the water in the bed. Similarly, radiographs of a pre-wetted and drained bed (no flow) and a bed in the different pre-wetting modes were obtained once the flow had stabilized. There is a geometrical error in these radiographs that stem from the cone geometry of the X-ray beam. X-rays travelling to the top (and bottom) of the image section has a slightly longer path length (and therefore diverges more than those travelling in the plane of the focal point). This results in the top (and bottom) of the image appearing slightly larger than the middle. In the present investigation, this error is negligible because the source-object distance greatly exceeds the size of the sample. The apparent size of the top (and bottom) of the column is approximately 0.5% larger than the apparent size of the middle.

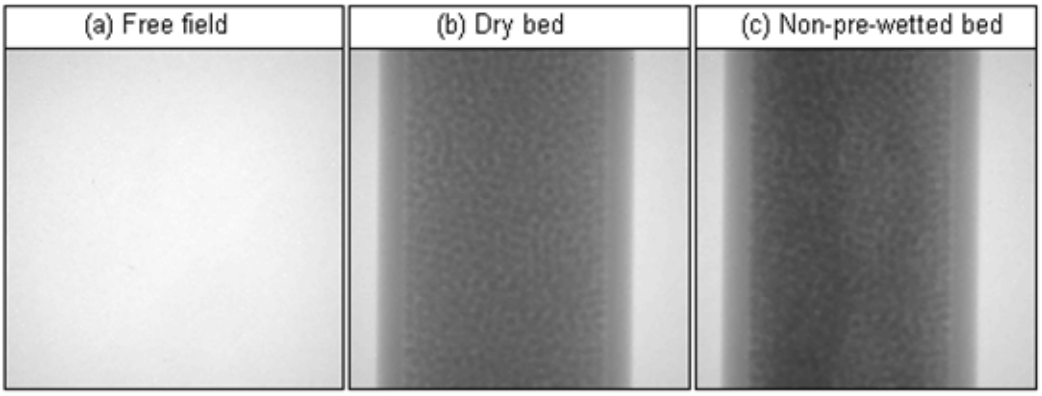

Figure 30. A selection of radiographs

Experimental: Tomography

With a few modifications, the experimental setup can be used to obtain sufficient data for a tomographic investigation. The column is mounted on a computer controlled rotating desk. Two-dimensional radiographs are taken at 1 degree intervals for a full 360 degree rotation. The distributor rotates with the column, thereby ensuring that the top-of-bed distribution is not affected by the rotation. The rotational acceleration is set at a very low value to curb the effects of any centrifugal forces acting on the liquid. For high definition radiographs, utilising the full 16 bit dynamic range of the CCD camera, the total

acquisition time is 16 minutes for the whole volume. The data acquisition frequency therefore is 0.38 images/s, meaning that each radiograph takes 2.6 s to acquire (1.5 s exposure time and 1.1 s to rotate 1 degree). The source-object distance remains at 610 mm, allowing the same geometric enlargement that proved useful in the radiographic imaging. A height of 61 mm of the bed located 539 mm from the top of the bed was imaged. This is in order to avoid the "calming zone" located in the top part of the bed and ensures that the flow pattern is well-established in the imaged section. The bed and operating conditions were the same as in the radiographic study. A set of radiographs was also taken for a drained bed (no liquid flow) to provide a reference for the liquid flow experiments. Preliminary investigations indicated that the Non-pre-wetted mode flow pattern takes at least 8 hours to stabilize (because of the slow internal saturation of the catalyst particles). For this reason, experimental constraints unfortunately dictated that the Non-pre-wetted mode could not be investigated to the same degree as the pre-wetted modes. Tomographic reconstruction is discussed at the end of this chapter.

5.4 Results

5.4.1 Two Dimensional Radiographs

This section is concerned only with the result of the first part of this radio-imaging study, namely radiography.

Radiograph Processing

The intensity of the attenuated image (I) relates to the intensity of a free field image (I_0) according to the Beer-Lambert Law (Toye et al., 1998, Basavaraj et al., 2005):

$$I = I_0 e^{-Ex} \tag{14}$$

Here x is the thickness of the attenuating material and E is the attenuation coefficient (assumed to be independent of x). For a given fluid, E is a function of the intensity of the

X-ray source. At 100 keV its value is 17.07 per meter for water (NIST database). Several processing combinations are possible. Using Figure 30(a) as the free field image (I_0) and Figure 30(b) as the intensity image (I), the solids content in the bed is isolated. Alternatively, setting Figure 30(b) as I_0 and Figure 30(c) as I, the water content in the bed at the time of acquisition is obtained. This however, includes the internal holdup. For pre-wetted beds, the pre-wetted and drained bed is set as I_0 and the irrigated bed as I, yielding the dynamic (more accurately the free-draining) holdup in the bed during operation at the time of acquisition. An example of a Levec mode of operation is shown in Figure 31a. Here, the (dark) intensity of the image is proportional to the thickness of water transverse to the viewing plane. Since the exposure time for such an image is equal to 1.5 seconds, the image actually shows the average water thicknesses in the preceding 1.5 seconds. However, for practical purposes it can be thought of as a snapshot of the liquid in the bed at the time of acquisition.

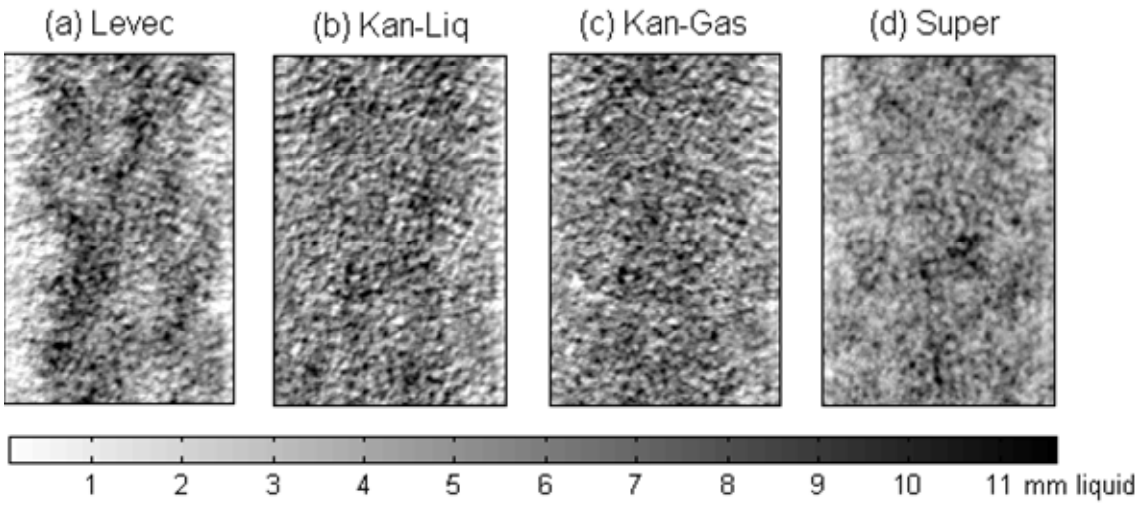

Figure 31. Liquid distribution in the various pre-wetting modes (u_L = 8 mm/s, u_G = 16 cm/s).

Images similar to that shown in Figure 31 were generated for all times (at intervals of 2 seconds), fluid velocities and operating modes. They are used to characterise the stability and uniformity of the flow. Note that any changes in the total amount of liquid in the column or in the distribution of the liquid in the column will register on these images. To

re-iterate, the dark intensity in Figure 31 is the thickness of liquid transverse to the viewing plane. It represents the entire bed and not just the wall flow or a vertical slice of the bed as one would get from a tomographical reconstruction (as originally reported in Lutran et al., 1991).

Liquid Saturation from Radiographs

The liquid saturation (holdup divided by the external porosity) in the field of view of the radiograph is determined from images analogous to those in Figure 31 by summation of the water thickness at each location, i.e.:

$$\text{Dynamic saturation} = \frac{\sum_{\text{all pixels}} x_i . \Delta s^2}{V_{\text{section}} \varepsilon} \qquad (15)$$

The saturation obtained through this radiographic technique may be inaccurate because of:

- The presence of several processing steps (in arriving at Figure 31 and in particular the assumption of a constant attenuation coefficient (E). Improved saturation values can be obtained through a calibration technique (Basavaraj et al., 2005), but the subsequent qualitative investigations into flow stability are not expected to be affected by assuming E to be constant).
- The liquid saturation is only applicable to a section of 61 mm of a 900 mm bed.
- Any high frequency oscillations that occur within the 1.5 seconds of exposure time will register as averaged intensity values.

With regards to liquid distribution, the draw-back of radiography (as opposed to tomography) is evident from equation 14. While the amount (thickness, x) of the liquid in the direction transverse to the image can be obtained (by solving for x in equation 14), all the information on how the liquid is distributed in that direction is lost. Nevertheless, the different flow patterns can still be distinguished (compare Figure 31a to Figure 31b-d). Note also, that any flow fluctuation will be registered as an increase (darkening -

increased saturation) or decrease (lighting – decreased saturation) in the intensity at a location.

Gravimetric Saturation Determination

It is imperative to compare the radiographic interpretation presented here to gravimetric saturation measurements. Since there is a considerable scatter in liquid saturation measurements in literature due to system and operating differences, liquid saturation was measured under conditions similar to those under which the radiographs were taken. Due to practical constraints, the liquid saturation measurement was not done during the actual radiography experiment. Instead, the setup was moved to another location where the column was mounted on an Ohaus Pro 22001 balance that is capable of registering intervals of 0.1 gram in mass. Identical operating procedures were followed for the radiographic and gravimetric experiments. The procedure for determining liquid saturation by gravimetric means involves subtracting the weight of the drained bed from an irrigated bed and is discussed in detail elsewhere (Nemec et al., 2001). Gravimetric saturation measurements were found to be satisfactorily reproducible. Unfortunately, the bed had to be re-packed between the two sets of experiments. However, the bed porosity was found to be very reproducible with re-packing (a value of 0.41 is used throughout this study). Additionally, it was necessary to correct the measurements for significant hysteresis in the amount of water retained in the distributor. In order to properly evaluate the temporal evolution of the liquid saturation, the weight of liquid present in the bed was recorded every second from start-up to steady state (and beyond) for each mode of operation.

Possible inaccuracies in the gravimetric method of holdup determination described here are:

- End effects (including the liquid in the distributor and retained on top of the sieve at the bottom of the bed).

- The gravimetrically determined liquid saturation is a bed-averaged value and therefore includes the non-representative calming zone holdup that may well encompass the first 200 mm of the bed (Gianetto & Specchia, 1992).

The gravimetric liquid saturation measurements serve as a check of the radiographic technique employed here. One would expect the two methods to give similar liquid saturation values at steady state. A selection of results is shown in Figure 32a to Figure 32c. Note that both techniques indicate that liquid saturation increases with liquid flux (Figure 32a to Figure 32b) and decreases with gas flux (Figure 32c). Figure 32d is a parity plot of the liquid saturation at all fluid velocities and all pre-wetting modes as determined by the radiographic and gravimetric techniques. An average absolute relative error (AARE) of 5.5 % indicates that there is excellent agreement between the two techniques, especially considering that a constant attenuation coefficient was used.

Liquid Configuration Variation with Fluid Fluxes

The radiographic technique is suitable for a visualisation of the liquid flow pattern. Figure 33 shows processed radiographs of the bed at steady state for different liquid and gas fluxes. Note that the higher fluxes reported do not imply that the bed was operated at the low flux and that the flux was then increased. Instead, for the Levec mode, the bed was pre-wetted and drained and then the operating fluxes were introduced. If a higher operating value was required, the whole procedure was repeated. For the Kan-Liquid mode the operating fluxes were set, the liquid flow was increased and then decreased to the operating value – again repeating the whole procedure if higher fluxes were required. Similarly, the Super bed was flooded between flow rate changes and the Kan-Gas bed was pulsed (with increased gas flow) between flow rate changes (their results were similar to the Kan-Liquid mode and are not shown). Examination of Figure 33a suggests that in the Levec mode the liquid is improperly distributed through the volume (areas of dark and light) while in the Kan-Liquid mode the liquid is relatively uniformly distributed.

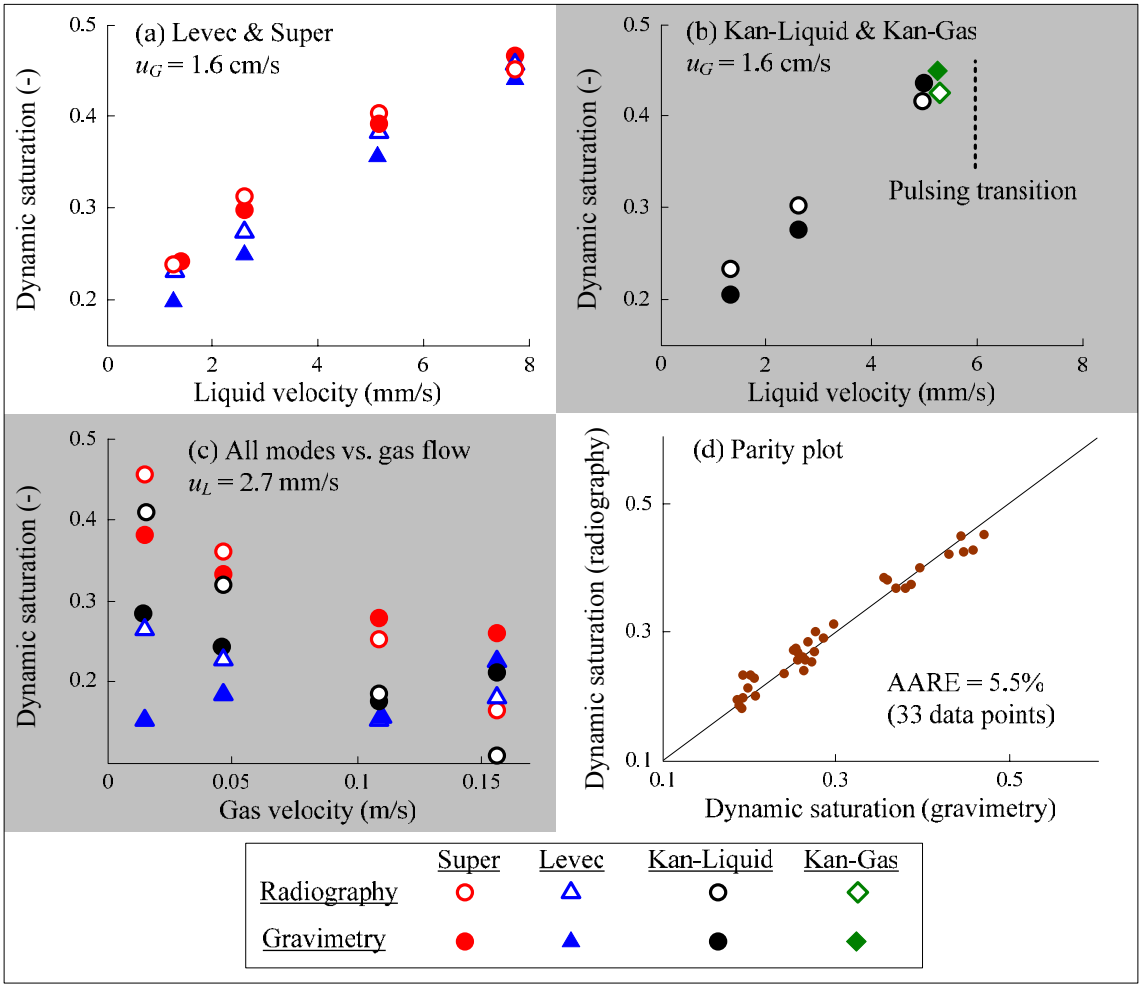

Figure 32. Gravimetric and radiographic saturation comparisons

Moreover, the improper distribution in the Levec mode persists at high liquid velocities. Finally, it appears as though the there are completely dry zones at the low u_L (see for example the lower left corner of the image). Although there is still improper distribution at high u_L, the completely dry zone is absent. This is in agreement with Sederman & Gladden (2001) who reported that there is new rivulet creation as u_L is increased up to 2 mm/s, as well as Van der Merwe & Nicol (2005) and Van Houwelingen et al. (2006) who report completely dry zones at low u_L. From Figure 33b it is not clear what the effect of gas flow is on the liquid morphology. It is apparent however, that the improper liquid distribution in the Levec mode persists at high gas velocity and even appears to increase as a result of the higher gas flux. This is contrary to the expectation that high gas fluxes

will serve to spread the liquid more evenly over the packing. Unexpectedly, there are several dark spots (local volumes of high liquid saturation) in the Kan-Liquid mode at high u_G that are not as apparent at lower u_G. Here the gas may indeed have the expected effect of increasing the liquid spreading (Al-Dahhan & Dudukovic, 1995). In accordance with this, a higher total liquid saturation is registered at this higher u_G (Figure 32c). It is noted that an increased wetting efficiency as a result of increased gas flux was reported for this pre-wetting mode by Al-Dahhan & Dudukovic (1995), which certainly indicates better liquid spreading (although their saturation decreased with gas velocity). However, present results pertain to low pressure conditions (although the gas density is 1.1 kg/m^3).

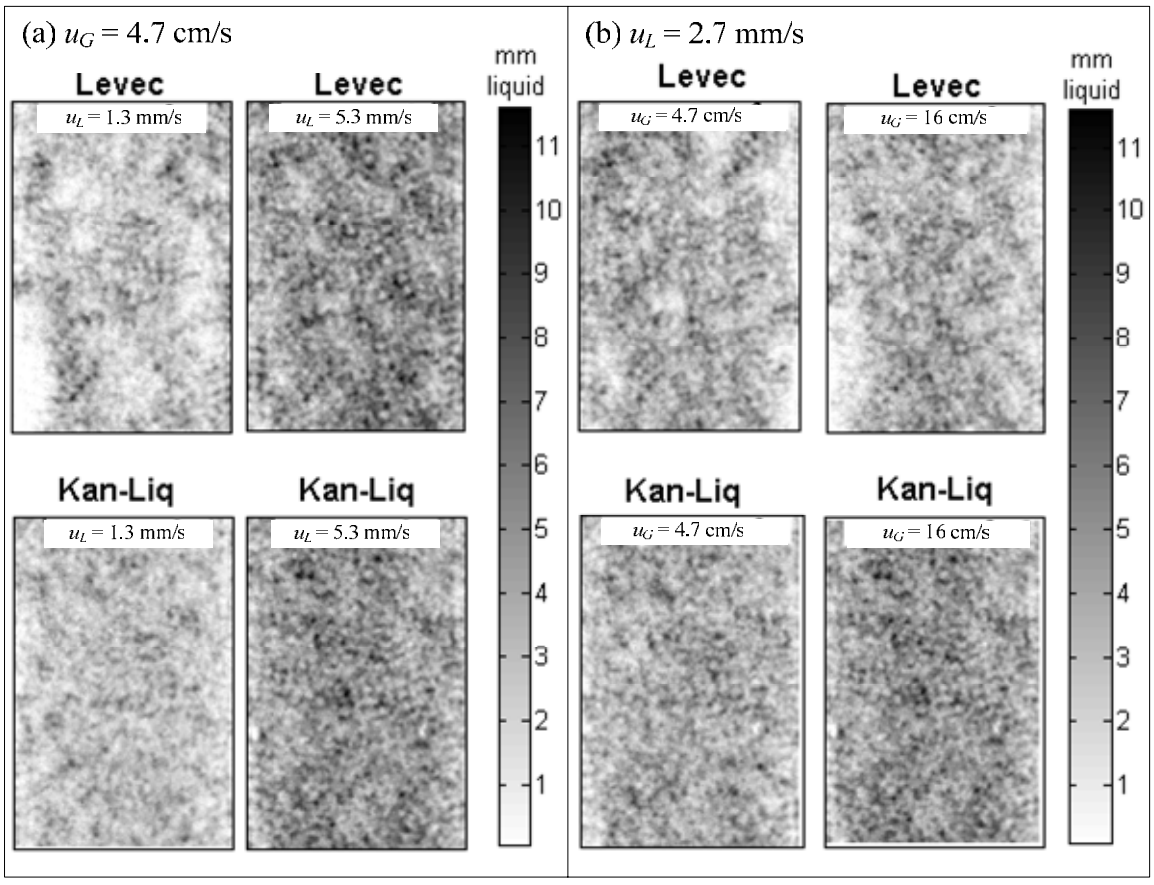

Figure 33. Flow patterns with increased fluid fluxes.

A mathematical analysis based on the calculation of maldistribution factors for these radiographic images is inappropriate. This is because all the information regarding the

liquid distribution transverse to the viewing plane is lost. The maldistribution factor would therefore be insensitive to changes in liquid morphology in that direction. In addition, due to the cylindrical column shape, a small change in the liquid morphology close to the wall (in the viewing plane) will drastically affect the factor, while even a substantial change to the flow morphology close to the centre of the column (in the viewing plane) will fail to affect it significantly. Maldistribution is therefore better investigated in quantitative terms by computed tomography.

Start-Up Dynamics

Little attention has been given to the time required (from start-up) for the liquid saturation to reach its steady state value (see Table 14). Ravindra et al. (1997b) reported that the time-to-steady-state (TSS) can vary from 10 to 360 minutes depending upon the start-up procedure, the nature of the packing and the inlet distribution. However, they only considered the Non-pre-wetted and Super pre-wetted modes of operation. Figure 34a shows the temporal evolution of liquid saturation as registered by both the gravimetric and radiographic techniques employed in this study. Note that both techniques register the same dynamic behaviour of the liquid saturation shortly after start-up in each mode. Also evident from Figure 34a is the fact that in these pre-wetting modes the saturation stabilized within 50-150 seconds. The Non-pre-wetted mode failed to reach steady state even after 4 hours of operation. Therefore Non-pre-wetted mode results are not reported elsewhere in this chapter. The differences in saturation for the different modes are in agreement with numerous studies on hydrodynamic hysteresis as summarized in Chapter 2 and extended in Chapter 4.

The rapidity of the saturation stabilization in the Levec, Kan and Super modes is further illustrated in Figure 34b. It shows successive radiographs of Levec and Kan-Liquid pre-wetted beds. Based on these, it appears that the Levec bed reaches a stable configuration within 10 seconds after the first liquid appears in the field of view. The Kan-Liquid bed reaches its stable configuration approximately 70 seconds after the liquid flow rate was

reduced from its high value. The Super and Kan-Gas modes had similar dynamics to that of the Kan-Liquid mode and are not shown for the sake of brevity. These trends form part of the characteristic trends list and are revisited in Chapter 7.

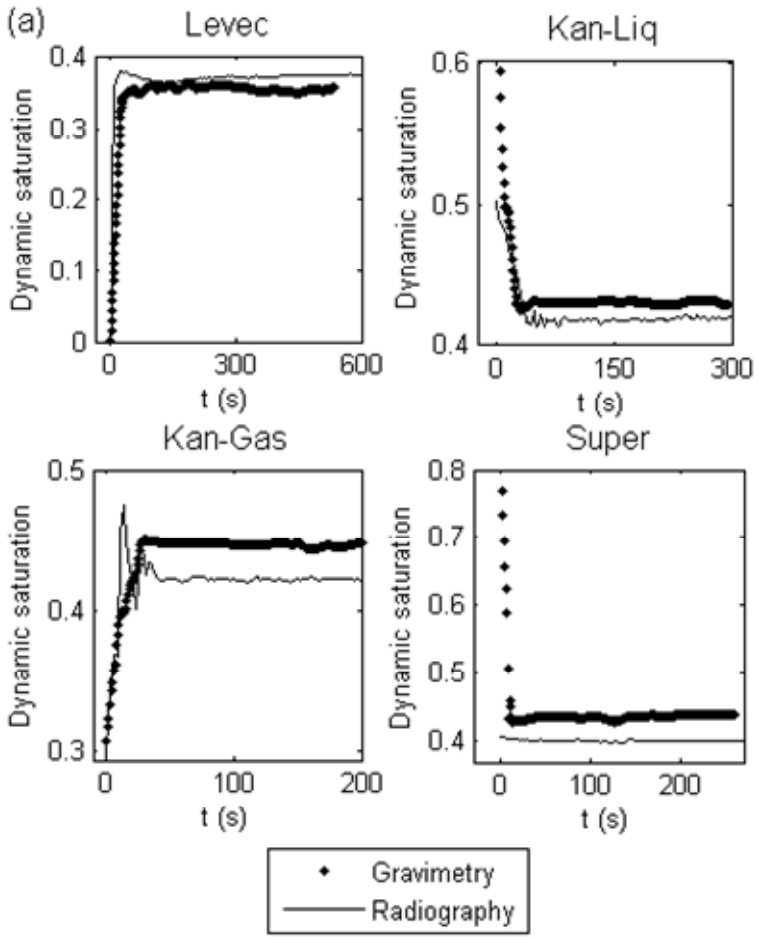

Figure 34a. Temporal saturation behaviour (saturation)

Temporal Stability at "Steady State"

The stability of the liquid configurations in the various pre-wetting modes over longer times can now be tested using the radiographic technique. Although the term steady state implies no change with time in any variable, it is interesting to investigate whether it is possible to have liquid path variations without necessarily changing the global parameter values.

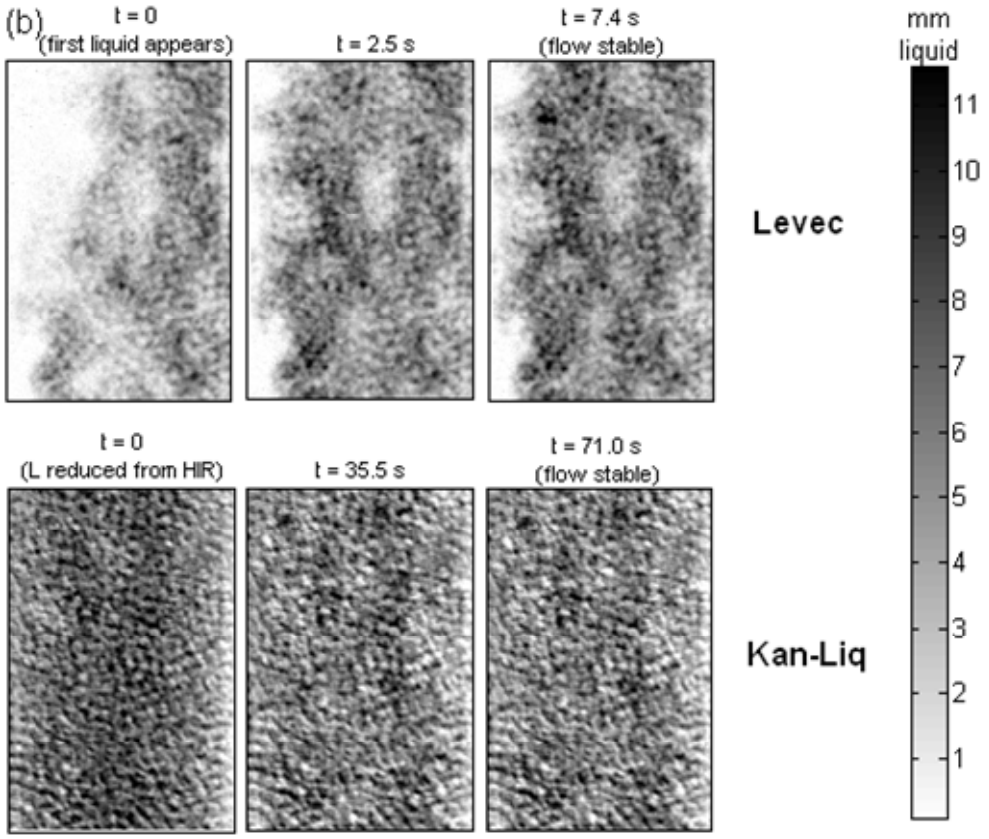

Figure 34b. Temporal saturation behaviour (images)

For each of the operating points, 200 consecutive radiographs approximately 2 seconds apart (spanning a total of 8 minutes of operation) were monitored for flow path changes. The 8 minutes were taken from a period where the bed-averaged liquid saturation showed no substantial change. In order to more clearly show local saturation changes, the first image is subtracted from the last - yielding a difference map (i.e. difference map = steady state image #200 – steady state image #1). These are shown in Figure 35. The dark areas in these images indicate locations where the saturation had a nett increase during the 8 minutes, while the light (white) areas indicate a nett decrease. Several millimetres (maximum of 3.4 mm) of change register at multiple locations in the Levec pre-wetted bed. Considering that there is a maximum of approximately 12 mm water at any given location (Figure 31) at these flow rates, this represents a large change in local saturation. Interestingly, there are almost no such saturation changes in the other pre-wetting modes.

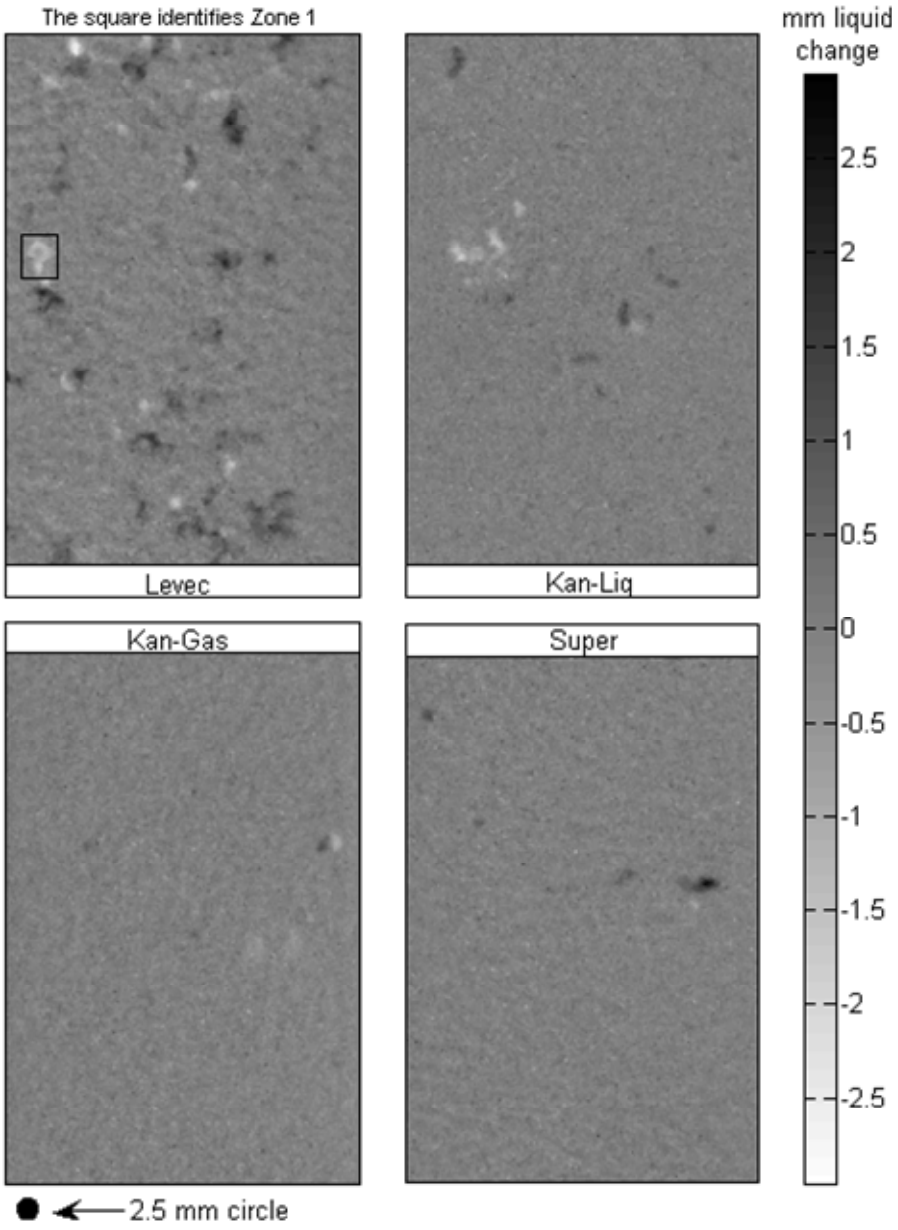

Figure 35. Difference maps (u_L = 8.0 mm/s, u_G = 1.6 cm/s)

Very similar difference maps are obtained at other liquid and gas flow rates (not shown). Additional characteristics of the saturation perturbations in the Levec mode are revealed by the difference maps. The length scale appears to be very close to one particle diameter (a single particle diameter is shown at the bottom of Figure 35 in direct proportion to the radiograph), although the shape is not spherical. There are both increases and decreases

in local saturation and these seem to cancel each other out so that the bed-average value remains nearly constant. In the Kan-Liquid, Kan-Gas and Super modes the flow pattern remains stable. The locations of temporal instability in the Levec mode are subsequently referred to as unstable zones. Having established the locations of these unstable zones, they can be monitored by examining consecutive radiographs (2 seconds apart) to establish when the liquid saturation change(s) occurred, how long such a change takes and whether it is a single change or multiple oscillations at that location. One way of illustrating this is to plot the total liquid thickness in an unstable zone against time. Figure 36a, zone 1, is such a plot for the unstable zone marked in Figure 35, clearly showing that there was one sudden de-saturation (at approximately 250 seconds). Figure 36 also includes such plots for other unstable zones (also at other gas and liquid fluxes). Zones are numbered consecutively for convenience. Their exact locations are not important apart from the fact that they were all present only in the Levec pre-wetted mode. In these plots, step changes indicate sudden increases or decreases in local saturation.

From all the timed data generated in this study, the following conclusions can be drawn:

- An increased saturation in one zone is sometimes (but not always) accompanied by a decreased saturation at another (close by). See for example Figure 36a zones 2 and 3 and Figure 36c zones 9 and 10. This suggests that the liquid had moved from one zone to the other.
- The change in saturation never takes longer than 5 seconds to complete (regardless of the flow velocities).
- The frequency of changes is very low (there are hundreds of seconds between changes).
- The same unstable zone sometimes experiences more than one saturation change (see zones 4 and 8 in Figure 36a and Figure 36c respectively). This suggests that there is some underlying aspect to the bed that can be associated with these saturation changes. However, at different flow rates it is not these same zones that undergo saturation changes (not shown).

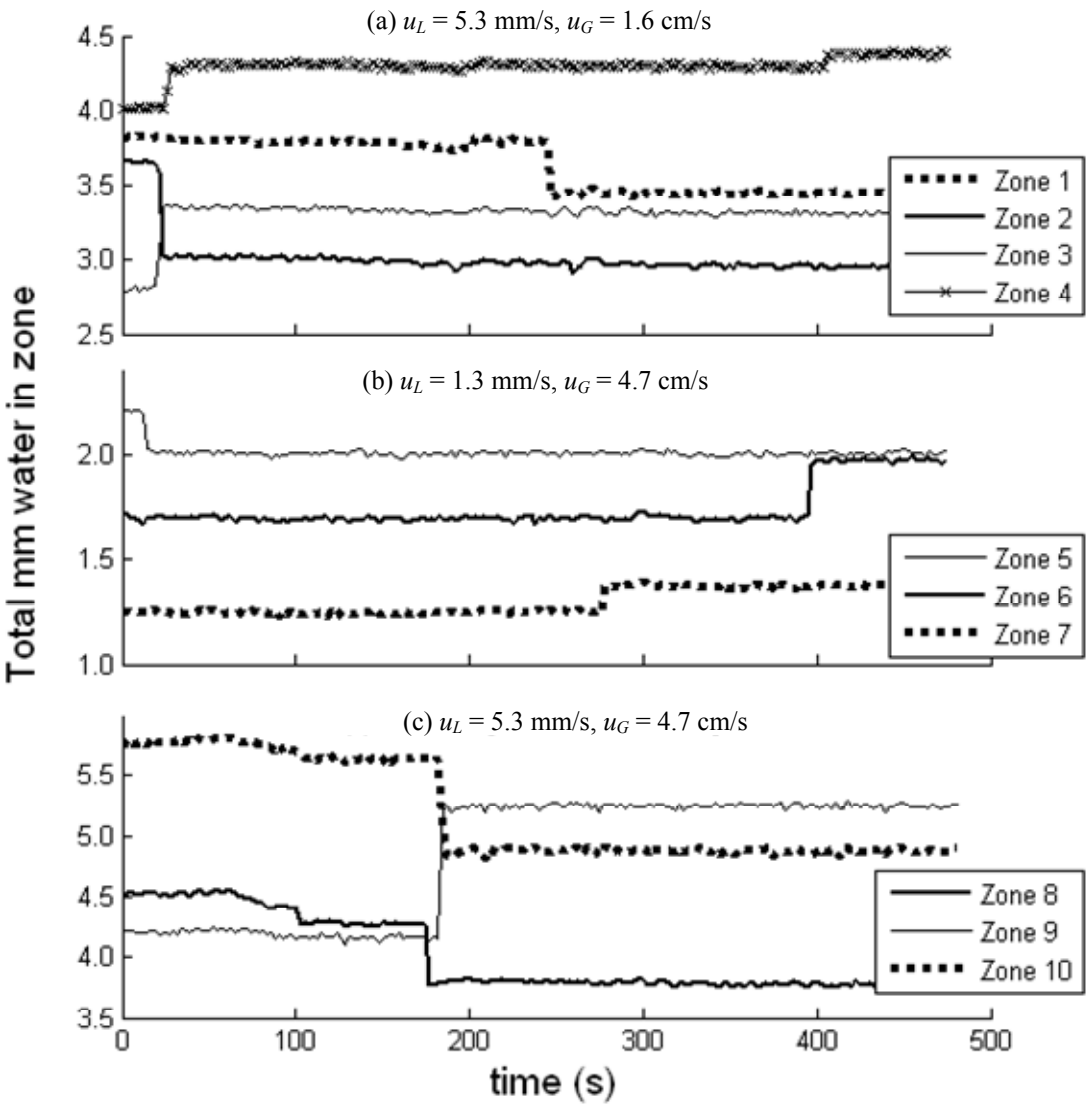

Figure 36. Liquid saturation changes in different zones showing the size and frequency of changes

- It cannot be concluded that either the frequencies of saturation changes or their magnitudes are linked to the liquid or gas flow rates.
- The local saturation changes in the Levec mode does not serve to increase the distribution uniformity and the flow pattern remains far removed from the Kan-Liquid mode (at least for the longest time under investigation here: 2.5 hours).

It is important to note that the difference maps employed here only shows the difference between the 200th and first images. As such, a difference map is incapable of registering saturation changes that cancel themselves out in the interval between the images used for its generation. That is, should a saturation increase somewhere in the bed be followed by a saturation decrease of the same magnitude within the 8 minutes it would not show on the difference map. However, such double (or multiple) changes do show on a standard deviation map which uses all of the images in the interval. These are calculated analogously to those of Anadon et al. (2005). Figure 37 shows a comparison between a difference map and a deviation map for the Levec pre-wetted mode shown in Figure 35. In every case presently under examination, the standard deviation maps and difference maps identified the same zones as unstable for the Levec mode.

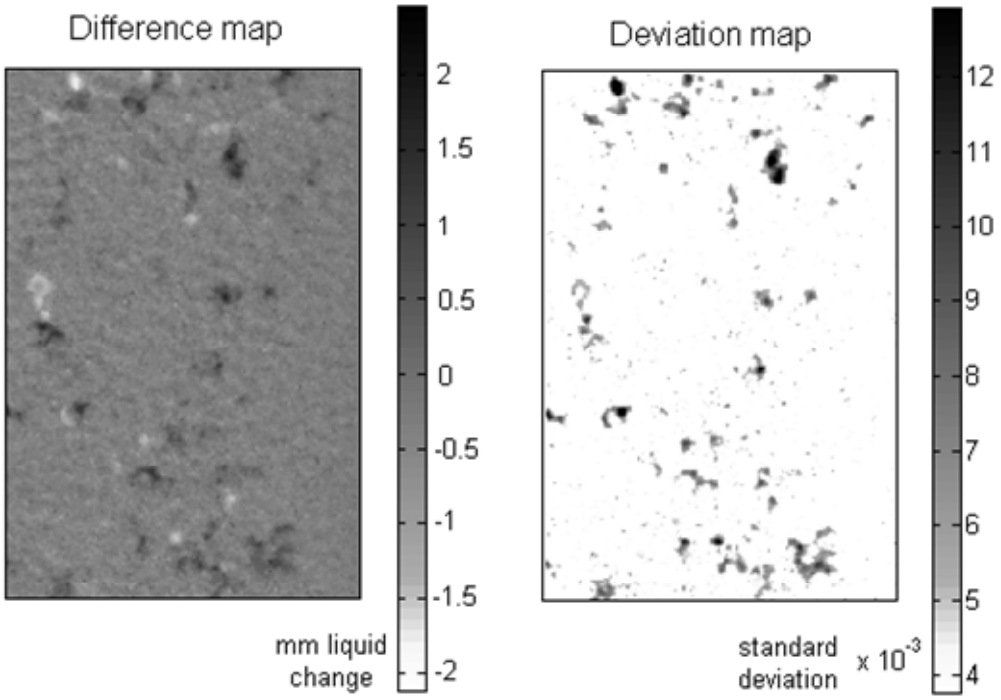

Figure 37. Comparison between a difference map and a deviation map (u_L = 8.0 mm/s, u_G = 1.6 cm/s)

This means that there where no zones that had double changes of opposing sign and equal amplitude in the time period under investigation. In the other modes both the difference and the deviation maps indicate no dynamic changes in flow pattern. Consequently, difference maps are preferred because they are capable of showing whether an increase or

a decrease in saturation had occurred while the standard deviation maps are not. It should be noted that the saturation changes reported here are not equivalent to those of Anadon et al. (2005). In their work, high frequency (several per second) localized saturation changes occurred in the Kan-Liquid mode close to the trickle-to-pulse flow transition boundary. It was shown how these instabilities are to be considered the precursors of the pulsing regime. In contrast, the low frequency instabilities reported in this study are inherent to the Levec mode in the trickle flow regime and occur at all velocities, but not in the Kan-Liquid, Kan-Gas and Super modes.

Saturation and Flow Pattern Reproducibility

For one set of gas and liquid flow rates, repeat runs for the Levec and Kan-Liquid modes were conducted. These two modes are the most commonly employed in literature. Figure 38a shows that in both pre-wetting modes the *total liquid saturation* had completely reproducible temporal behaviour with little difference between the steady state saturation values. However, close examination of the processed radiographs at steady state reveals that the liquid is not located at the same positions in the bed. This can be more clearly seen when the difference of two liquid saturation radiographs are taken (i.e. Run 1 radiograph – Run 2 radiograph) as shown in Figure 38b. Note that these runs were conducted directly after one another on exactly the same bed without moving it. Moreover, the same pre-wetting and operational procedures were followed. It is concluded that the *liquid morphology* is not exclusively determined by the bed structure and the pre-wetting method. However, both the total external saturation values and the general flow type are. This is true for both the Levec and Kan-Liquid pre-wetted beds, although it is more apparent for the former. Lutran et al. (1991) concluded that the flow pattern was reproducible given that the same pre-wetting procedure had been followed. However, examination of their figure 21 shows that although the general flow pattern was reproducible, the liquid was not located at exactly the same locations. It is therefore concluded that present results agree with those in Lutran et al. (1991).

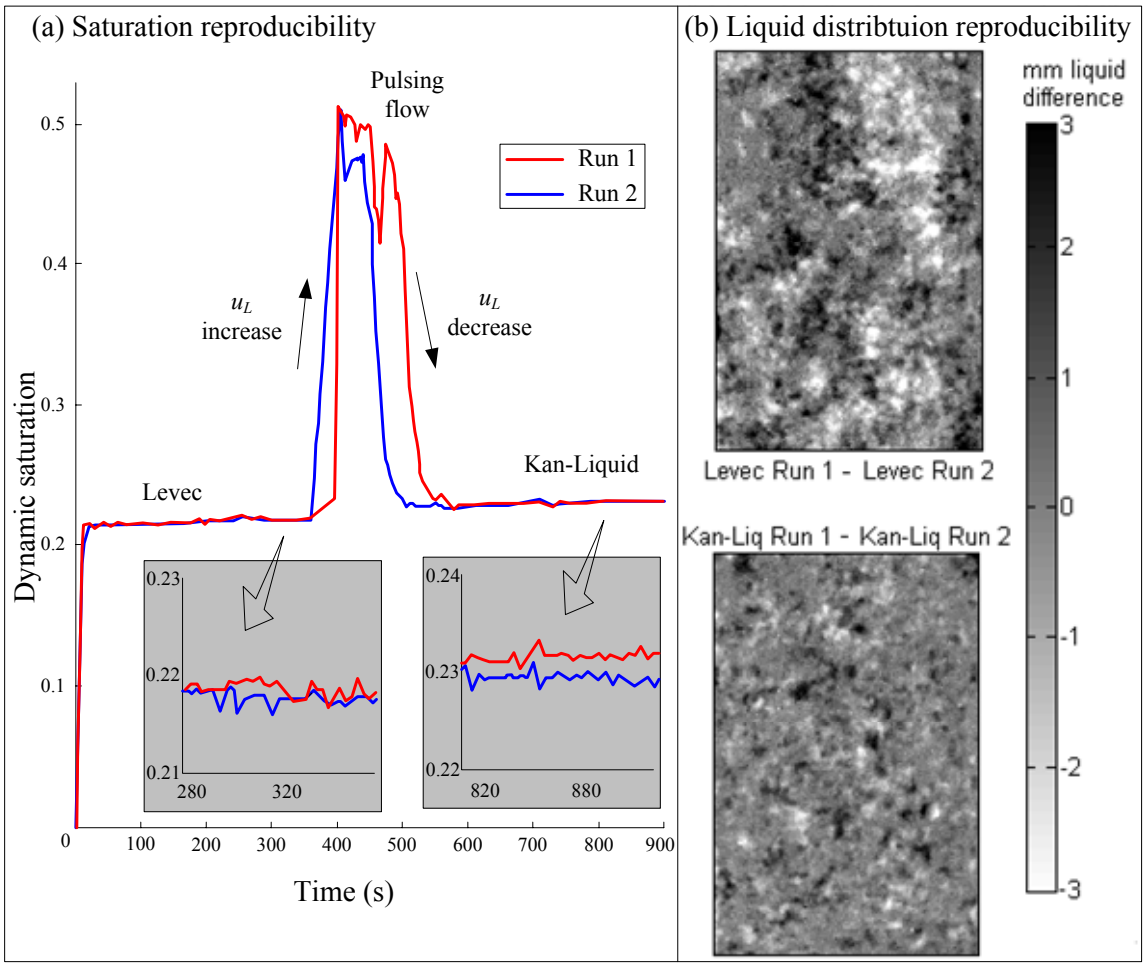

Figure 38. Flow pattern and liquid saturation reproducibility. (a) The overall saturation is reproducible (b) The flow pattern is not reproducible - dark and light intensities indicate areas where the saturation of runs 1 and 2 were different (u_L = 1.3 mm/s, u_G = 1.6 cm/s).

Radiography Conclusions

Radiographic imaging of trickle flow liquid saturation and distribution as a function of time, pre-wetting procedure and liquid and gas velocities is presented. A procedure to isolate the dynamic (free-draining) liquid from such images is introduced. The liquid saturation determined from these images is shown to agree with gravimetric liquid saturation measurements. This is encouraging since large diameter reactors are easier to radiograph than to weigh. The radiographic images indicate that the liquid saturation stabilizes shortly after the end of the start-up procedure for all pre-wetting modes except

non-pre-wetted beds. Present results agree with previous investigators in that Levec beds have lower saturations and are dominated by non-uniform flow. These flow non-uniformities persist at high liquid and gas flow rates. Although the bed-averaged liquid saturation and general flow type (sometimes referred to as rivulets for Levec pre-wetted beds and films for Kan and Super beds) are completely reproducible, the exact location of the liquid in the bed appears to have a stochastic nature. It has been established that there are local saturation changes (without changing the bed-averaged values) in the Levec mode, but not in the Kan-Liquid, Kan-Gas or Super modes. These changes are sudden but with a low frequency, occur at both high and low liquid and gas flow rates and do not appear to alter the general flow type. Apart from these *small, low frequency* perturbations in this one mode the overall flow structure remains stable for several hours, suggesting that the different modes of operation will prevail for long operating times. These observations form the basis of the computed tomography part of the radio-imaging study of trickle flow in the various pre-wetting modes, since the flow distributions obtained from the CT investigation will represent the actual (not time-averaged) flow patterns.

In summary, the capabilities of X-ray radiography (in particular its high temporal resolution) have been used to provide new insights into the stability and uniformity of trickle flow in several hydrodynamic states. This provides the basis for the detailed tomographic analysis of trickle flow multiplicity at the particle scale in the next section.

5.4.2 Three Dimensional Tomography Results

This section presents the preliminary results of the three dimensional tomographic investigation.

Tomography Reconstruction

Note that 2D radiographs of the bed (at steady state) were obtained for different rotations of the bed. A volume image (in three dimensions) can be reconstructed from the digitally recorded two dimensional radiographs by application of Beer-Lambert's law through the

Feldkamp-Davis-Kress (FDK) algorithm for cone beam reconstruction (details of which can be found in Feldkamp et al., 1984). Before applying the algorithm, a "white spot" filter is employed to remove individual pixels with exceedingly high intensity. In addition, a ring filter is employed to minimize reconstruction artefacts due to the rotation of the sample. The Octopus reconstruction package developed at the University of Ghent, Belgium, was used for this purpose (Dierick et al., 2004). A cross-section of the resultant volume image (trickle flow conditions) is shown in Figure 39.

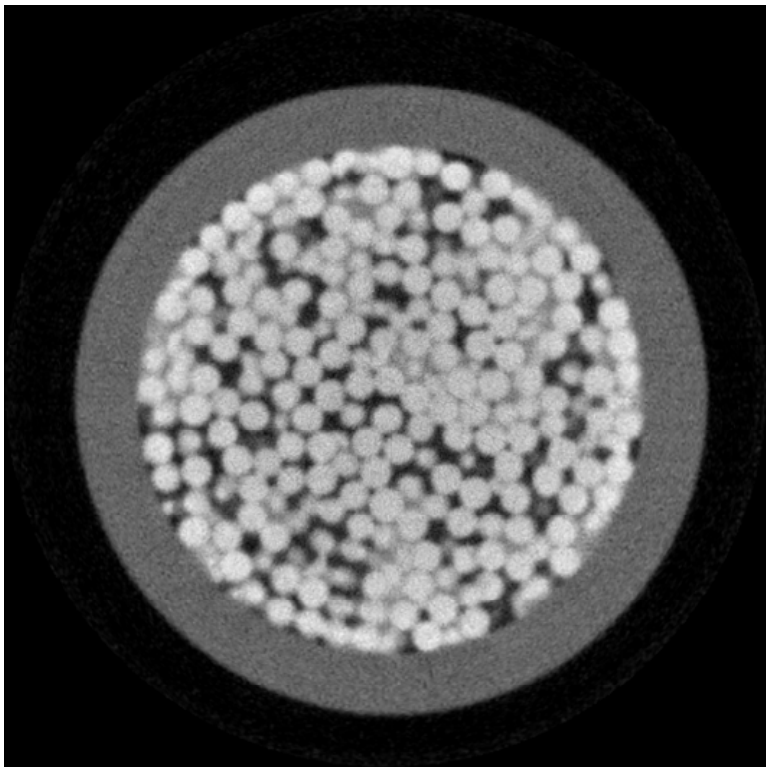

Figure 39. Cross-section of a raw reconstruction. Note the difficulty in clearly distinguishing the three phases.

It should be clear that it is very difficult to distinguish the three phases from this image. The reason for this is the presence of numerous "artefacts" in the image that are due to the following possible reconstruction errors (Boyer & Fanget, 2002):

- The *statistical error* in assuming a single photon energy as opposed to a distribution of energies (and the related phenomenon of beam hardening).

- Errors associated with the *accuracy of the acquisition instrumentation*.
- The *dynamic error* associated with phase instabilities during the image acquisition (i.e. if the local flow paths of the phases change with time).
- *Beam scattering* and *geometrical unsharpness* (because of the fact that the "point" source of the cone beam is in fact not an exact point) resulting in the inaccurate capturing of sharp phase distinctions (for example the solid-gas interface).

In fact, comparing various aspects of the radiography results (section 5.4.1) and the attributes of the raw reconstruction, estimates for some of these errors can be made:

- The dynamic error (flow path changes) is usually assumed to render the reconstructed image only valid in a time-averaged sense, i.e. as a representation of the flow patterns averaged over a period of time. However, the previous section has shown that trickle flow patterns are to be considered mostly stable (even the Levec mode flow pattern changes were small and of low frequency). This means that the dynamic error in the reconstructed images is small and that the patterns observed are stable flow configurations. This is the case only for the relatively low liquid velocities under investigation here, since the unstable nature of the flow pattern at high velocities is well known.
- By comparing the reconstructed image with the physical dimensions of the column and the particles, estimates for the geometrical and scattering effects can be made. Firstly, the inner diameter of the column (40 mm) spans 339 pixels, indicating that the spatial resolution is 118 μm/pixel. Examination of a single particle intensity profile through its centre (Figure 40), reveals that the geometrical unsharpness impacts approximately 4 pixels, i.e. 2 to each side of the interface. For comparison, the entire particle profile is approximately 20 pixels, i.e. one particle diameter is roughly captured by 20 pixels. Secondly, there is an apparent graininess to the inter-particle void space. This is a reconstruction artefact attributable to the scattering of X-rays that produces false signals from void space.

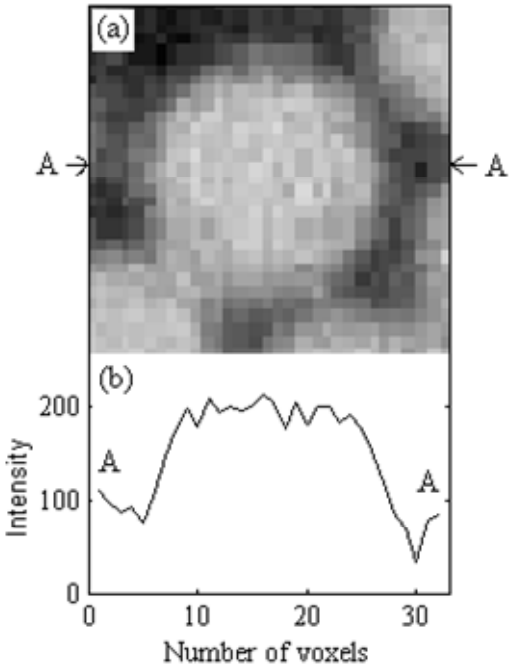

Figure 40. (a) Single particle reconstruction (cross-section). (b) Intensity line profile through section A-A showing the edge effect.

- Beam hardening is apparent in that the particles closer to the column wall have higher intensities than particles closer to the central axis (Figure 39). This is because the X-rays are initially absorbed (attenuated) non-linearly with material thickness. The beam hardening is reduced by the presence of the column wall which acts as a hardware filter (Basavaraj et al., 2005), although it was found to be very difficult to remove it entirely. Beam hardening is particularly undesirable because it makes the operation of thresholding ineffective (as discussed later).

Every effort was expended to tailor the FDK reconstruction algorithm to produce optimal reconstruction results for the system under investigation. These steps include the relatively thick wall to act as radiation (hardware) filter (Basavaraj et al., 2005), the optimal adjustment of the acquisition parameters (source-object distance, X-ray focal point, exposure time, number of rotations) and the reconstruction parameters (like the degrees of white spot and ring filtering). For example, the white spot filter compares each pixel value to the mean of its eight neighbours and sets the pixel value equal to this mean

only if the intensity exceeds the mean significantly, thereby preserving sharp edges (as compared to a regular median filter). Although the effectiveness of reconstruction algorithms has received some attention in recent years, there invariably remain some of the above mentioned inaccuracies in the final image. Some techniques are more prone to reconstruction errors than others. X-ray CT is particularly prone to beam hardening and scattering. As a result, some processing of the raw reconstruction is inevitable.

Image Processing According to the Thresholding Method

The objective of the processing steps is to obtain a ternary volume image where each spatial location in the bed is occupied by one of the liquid, solid or gas. Note that the reconstruction and processing steps are in fact not separate (a considerable deal of "image processing" has already gone into producing the raw reconstruction). Nevertheless, it is convenient to separate these operations conceptually, especially since the first has received considerable attention in literature and the second very little.

To start, consider that the usual way of identifying the three phases in an image like Figure 39, is to associate each phase with a range of intensities. This is done as follows:

1) The drained bed is thresholded at a value that yields a bed porosity equal to the independently measured bed-average value (0.41).
2) The drained bed image is then subtracted from the trickle flow image and this image is thresholded, yielding an image of the liquid only.
3) The result of step 2 is superimposed on the result of step 1, yielding the ternary gated image presented in Figure 41.

Clearly, the standard processing procedure fails to capture the detail of the bed structure and the flow pattern. An obvious way to see this is from examination of the particle contact points, where an artificial "neck" appears between the particles. This is understood in terms of the edge effect that results from the inaccurate capturing of particle edges (see Figure 40).

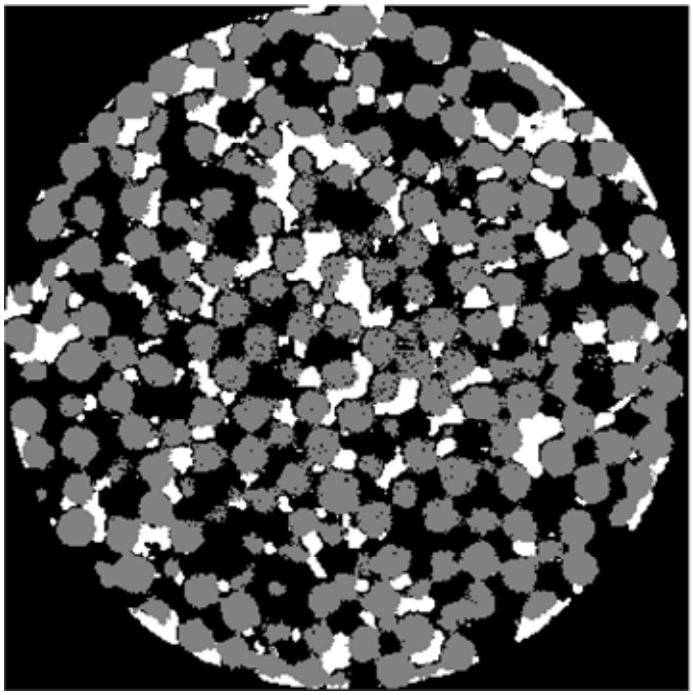

Figure 41. Ternary gated image processed according to the thresholding method

For illustrative purposes, it is shown schematically (in two dimensions) in Figure 42. For two nearly touching particles (Figure 42a), the reconstructed image will be similar to Figure 42b. The line profile through the contact point is shown directly next to each image. The thresholding procedure with the porosity target causes the particles to appear smaller than they are except for close to the contact point where additional phantom solid appears. Thresholding is seen to be poor at identifying edges when the intensity values on the outside of the particle differs from place to place (it is higher when there is another particle in close proximity). Liquid that is located close to particle contact points do not register on the ternary gated map generated by this procedure. Note also that this procedure is incapable of providing the bed porosity since its value has to be known in order to set the threshold level. Finally, thresholding is also very susceptible to beam hardening (which is why particles close to the centre of Figure 41 are only partially captured while excessive “necking” is observed close to the wall).

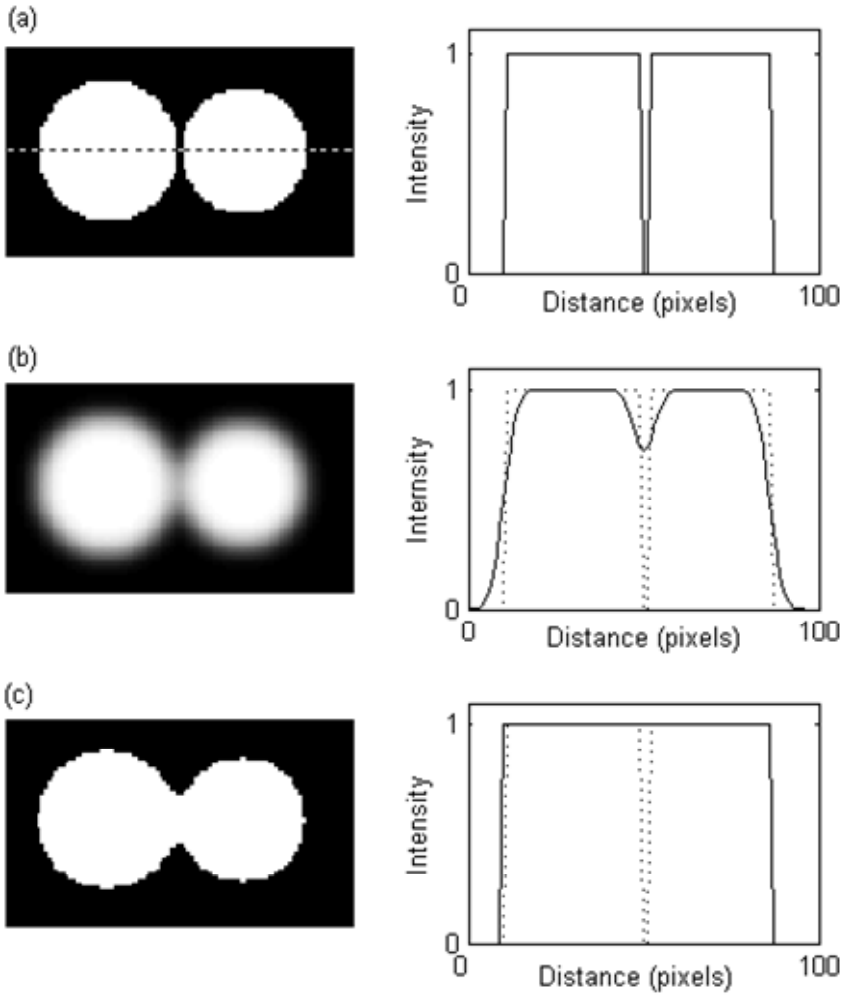

Figure 42. Schematic of how the edge effect creates "necks" when thresholding is used (a) true image (b) reconstructed image (c) thresholded reconstructed image.

As a first approximation, the radially averaged intensity, $\boldsymbol{I}_{avg}(r_c)$, can be corrected so that the average image intensity is the same at all distances from the central axis:

$$\boldsymbol{I}_{avg}(r_c) = \boldsymbol{I}_{avg}(r_c \to 0), \quad \text{where the subscript } avg \text{ refers to radial averages} \qquad (16)$$

However, this implicitly assumes that the local porosity is not a function of the distance from the central axis. Unfortunately, it is well established that the porosity decreases toward the wall (de Klerk, 2003). The peculiarities of a packed bed porosity distribution therefore make the beam hardening effect difficult to remove. Note that Figure 41 can be

used to once again investigate averaged properties of the flow. For example, it is possible to calculate a cross-sectional maldistribution factor by applying a form of equation 2 to the liquid in the image. One can then show that the Levec mode has a much larger maldistribution factor that any of the other pre-wetted modes and that the maldistribution factor decreases with velocity. However, these two important observations are clear from the images themselves (see Figure 50 in Chapter 6) without having to quantify them numerically (recall that the numerical value of the maldistribution factor has only relative significance). In fact, the radiographic images already showed these same trends (Figure 31). Figure 41 also provides a motivation for an improved image processing strategy because the particle scale phenomena cannot be obtained from this image. This includes interfacial areas and pore-scale statistics which will prove vital to the development of a multiplicity mechanism in Chapter 7.

5.5 Conclusions

This chapter introduced new experimental data on the localized behaviour of trickle flow in the various pre-wetted multiplicity modes. Using a 2D radiography technique, it was established that the trickle flow patterns are approximately stable over the longest period of time investigated (2 hours). This implies that CT visualizations yield the actual flow patterns and not time-averaged liquid distributions. Some of the hydrodynamic multiplicity trends already identified at the bed-scale were confirmed, while 2 major new trends were identified:

(Q) *Time to steady state*: the Kan-Liquid mode takes longer to reach a steady flow pattern than the Levec mode.

(R) There are *particle scale low frequency flow pattern changes* in the Levec mode, but not in any of the other pre-wetted modes.

In a second application of radio-imaging, 3D computed tomographic images of the different modes were produced and processed according to the usual method. The

resultant ternary image is inadequate to provide the necessary level of detail, and more advanced processing is required to establish the locations of the gas, liquid and solid in the bed. The development of such a processing strategy is the objective of the next chapter.

Chapter 6. Advanced Visualizations

This chapter reports the results of applying a novel image processing strategy (capable of identifying the three phases) to the raw reconstruction. The first section introduces the new processing strategy. The second presents the results in various forms that reveal the nature of trickle flow multiplicity. Thereafter, the void space is partitioned into distinct pores according to an established method. This allows the determination of pore-scale statistics which provide further insight into the nature of hydrodynamic multiplicity.

In reference to the overall strategy of this investigation, this chapter forms part of Part 2 (cluster-of-particles scale) of the Additional Experimental Insights block in Figure 1, and addresses Objective 2 from Chapter 3. At the end of this chapter, the list of characteristic multiplicity trends will be completed and the experimental investigation concluded.

6.1 Novel Image Processing Strategy[4]

6.1.1 Introduction

Note that in this discussion the objective is to obtain a high definition ternary image of the section of the bed under investigation where each voxel is associated with gas, liquid or solid. The new image processing strategy takes as its input the raw reconstruction, the origin of which is unimportant provided that the spatial resolution is sufficient to distinguish individual particles. Although cone beam geometry is used in this study, the proposed image processing techniques are equally applicable to tomographical

[4] The work in this section has been accepted for publication in Chemical Engineering Science, doi:10.1016/j.ces.2007.08.009, 2007.

reconstructions derived from fan or parallel beam geometries or magnetic resonance techniques.

The key toward improving upon thresholding is in realizing that it is a scalar operation where the assigned value of the voxel depends only on its intensity. It does not draw any information from the surrounding voxels. The alternative procedure developed here addresses this deficiency in two ways:

- First, by taking information from the surrounding environment into account in deciding whether the voxel is solid, liquid or gas.
- Second, by using the a priori knowledge of the particle shape in identifying solid voxels.

The methodology is to first identify the particle locations using all the available information (in three dimensions) from the drained bed. The inspiration for using all local information in deciding the value of a voxel is drawn from edge finding techniques in two-dimensions. Canny (1986) showed that faint edges in an image can be detected by recognizing that edge pixels usually appear along lines. A "faint" edge pixel is detected by using the "strong" edge information of the surrounding pixels.

The mathematical basis of the majority of steps in the proposed procedure is the (discrete) convolution operation, defined as:

$$C_{m,n,p} = \sum_{i=1}^{a1+b1-1} \sum_{j=1}^{a2+b2-1} \sum_{k=1}^{a3+b3-1} A_{i,j,k} B_{i-m+1,j-n+1,k-p+1} \qquad (17)$$

Here, entries into matrices are indicated by subscripts starting from 1. In computational terms, the $a1 \times a2 \times a3$ matrix $\boldsymbol{A}$ (in this case the reconstructed volume image) is acted upon by a $b1 \times b2 \times b3$ matrix $\boldsymbol{B}$ (called a convolution kernel) to yield a $a1+b1-1 \times a2+b2-1 \times a3+b3-1$ matrix $\boldsymbol{C}$, of which the innermost $a1 \times a2 \times a3$ matrix corresponds in position to $\boldsymbol{A}$ (i.e. $\boldsymbol{C}_{m,n,p}$ is located at the same physical position as $\boldsymbol{A}_{m-a1+1,n-a2+1,p-a3+1}$). One last aspect to consider is the values of $\boldsymbol{A}$ at the index values outside of $\boldsymbol{A}$ (i.e. $a1+1,$

a1+2, .. a1+b1-1 and similarly for the other dimensions and for ***B***). By equation 17, these values are required to compute the values of ***C*** at locations close to the boundary of matrix ***A***. These are assumed to be zero (i.e. ***A*** and ***B*** are zero-padded) which is appropriate since there is no image intensity outside of the bed. The convolution operation is written in shortened form as:

$$\boldsymbol{C} = \boldsymbol{A} \otimes \boldsymbol{B} \tag{18}$$

Here it is understood that ***C*** is resized (by neglecting its outermost shell) to correspond in size with ***A***. That is, entries into ***C*** therefore correspond in physical position to those in ***A***.

6.1.2 Image Processing Steps

The first objective is to distinguish the particles in an image without liquid flow. The processing of the CT image of a drained bed into a binary (solids-gas) image is done following the steps illustrated schematically in Figure 43 and discussed below. Figure 44 shows results of applying the steps to the image in Figure 40b (a two dimensional slice plane is shown although the procedure is applied in all three dimensions).

Filter

The first step toward identifying the solid in the tomography image is to apply a 3 × 3 × 3 median filter to the image. This is accomplished by specifying:

- ***I*** = original reconstructed intensity image (337 × 337 × 150 voxels)
- ***B*** = 3 × 3 × 3 matrix with 3^{-3} in each position (i.e. equal weight to each of the surrounding voxels)
- ***F*** = the filtered image (337 × 337 × 150 voxels)

F is simply the convolution of ***I*** with ***B*** (Figure 44a, to be compared to Figure 39). The purpose of the filter is to remove high intensity noise. Equally important, filtering smoothes the intensity transition from gas to solid. Smooth transition profiles are required for the next processing step. The filtering also removes some of the grainy quality to the

inter-particle void, and "flattens" the interior solid intensities (more uniform solid interiors reduce the number of "false edges" that register in the next processing step).

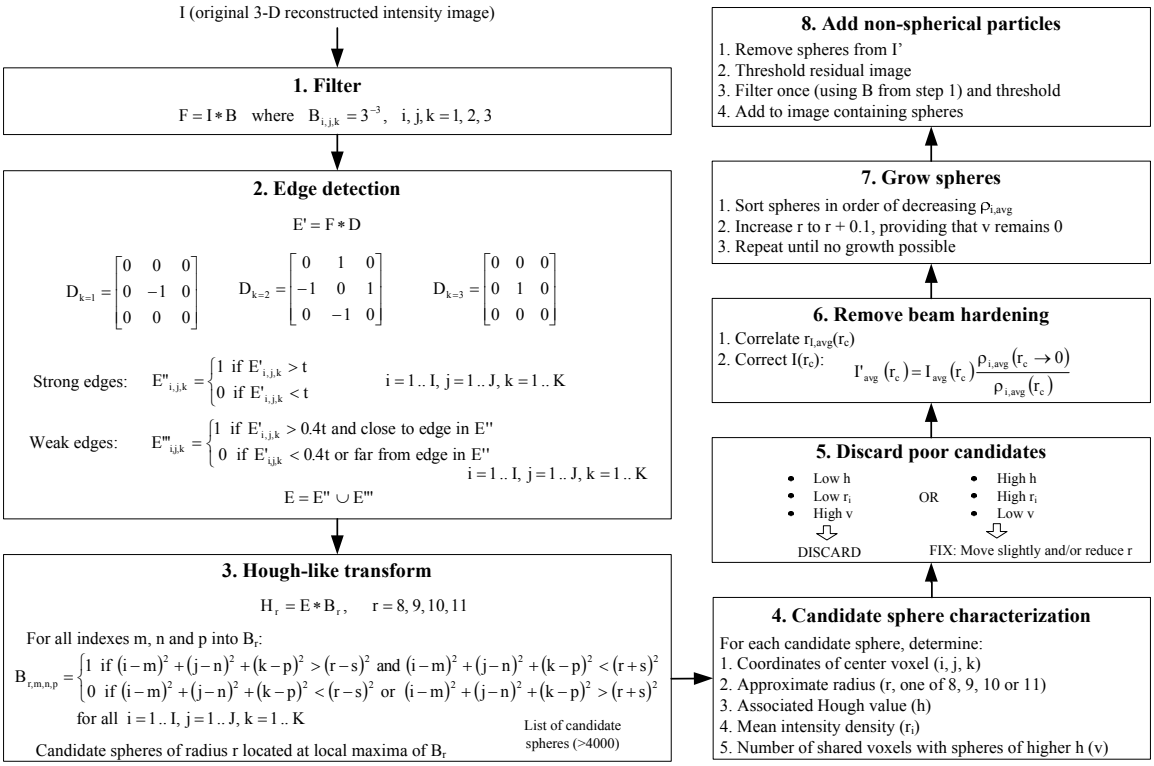

Figure 43. Image processing steps

Edge Detection

Edges are detected in images by identifying the locations of inflection in the intensity profiles (Van der Merwe et al., 2006), i.e. finding the values of *u* that satisfy:

$$\frac{\partial^2 \boldsymbol{I}}{\partial u^2} = 0\,,\ \text{where } u \text{ is the direction normal to the edge being detected.} \qquad (19)$$

The fact that the second derivative appears in this equation signifies the importance of the filtering step. Without pre-filtering the second derivative cannot be evaluated accurately due to the presence of high frequency noise. Ideally, the edges should be detected in directions normal to the particle surfaces, but the locations of the particles are not yet established.

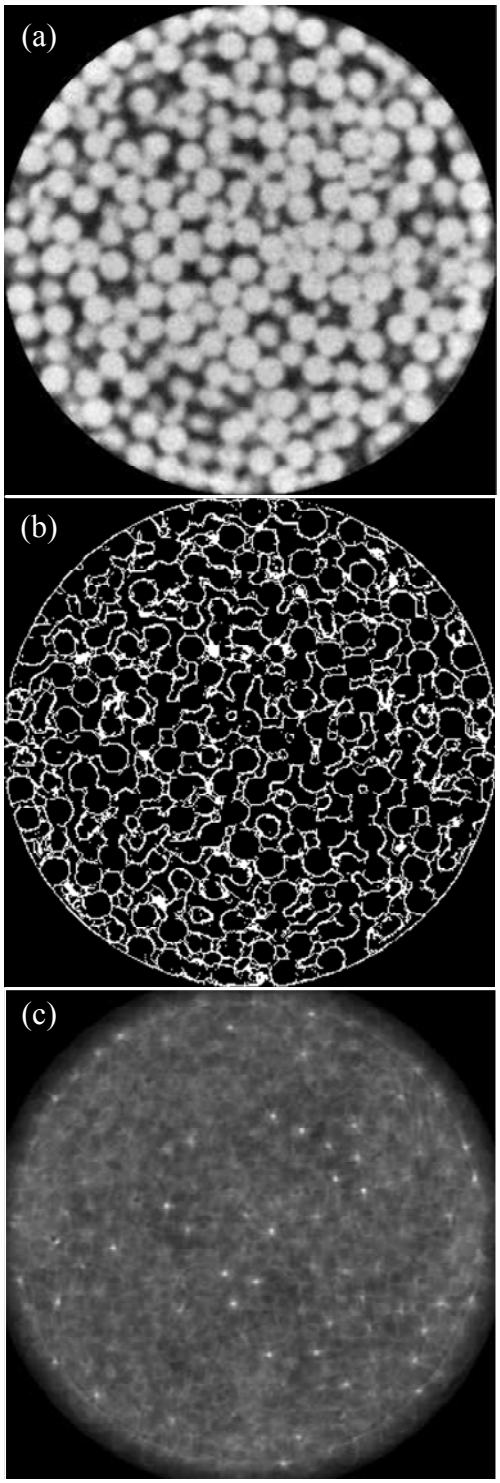

Figure 44. Cross-sections of a (a) Filtered image, (b) Edge image, (c) Hough-like transform

Therefore, the edges are detected in each of the three Cartesian directions that coincide with the image discretization (i.e. in each of the matrix directions). This is easily accomplished using convolution. A three-dimensional analogue of the Canny method (Canny, 1986) was found to yield superior results. It is a two-stage detection algorithm that finds first strong and then weak edges. A cross-section of the edge image ($\boldsymbol{E}$) is shown in Figure 44b. Large white patches in this image are instances where the slice plane coincides with an edge plane (e.g. near the top of a sphere).

Hough-like Transform

Examination of Figure 44b reveals that the edges of the spheres are neither smoothly nor explicitly accurately captured. Nevertheless, the (three dimensional) edge image can be used to identify likely coordinates in the volume that correspond to sphere centres. This is done by postulating a sphere radius (in this case 8, 9, 10 and 11 pixels were used; around 1.25 mm) and then "searching" for locations in the volume where edge voxels often appear approximately that distance from the location (the actual spheres are not exactly uniform in size so provision has to be made for spheres of different sizes). Computationally, this is accomplished by convolving the edge image ($\boldsymbol{E}$) with a convolution kernel ($\boldsymbol{B}_r$) that is constructed with 1's at a radius r from the centre of the image and zeros elsewhere. In practice, $\boldsymbol{B}_r$ is constructed with 1's whenever the distance from the central voxel is within $\pm s$ pixels of r. This is necessary because of two reasons. First, the digital cubic array (matrix) representation of a volume image means that spherical objects are inaccurately captured. Second, the particles can be expected to have small deviations from exact spherical shapes. In this way, $\boldsymbol{B}_r$ resembles a spherical "egg-shell" configuration with a "shell thickness" of $2s$ pixels (after some experimentation a value of $s = 1$ was adopted in this study). The original inaccurate edge image ($\boldsymbol{E}$) is convoluted with the "mask" of an accurate spherical shell yielding the Hough-like transformed image. The likely particle centres can be identified as the coordinates where the Hough-like image exhibits local maxima. The two-dimensional cross-section of the Hough-like image (with $r = 10$) is illustrated in Figure 44c. In this figure, the white spots

mark locations where one is likely to find a particle centre. With each Hough-like transform there is a radius associated, since the specification of $\boldsymbol{B}_r$ requires a postulated radius. A list of candidate spheres with their radii approximated to one of 8, 9, 10 or 11 pixels is therefore attained. There are more than 4000 such candidate spheres with normalized Hough-like transform values above 0.35 in the volume under consideration. A rough estimate of the real number of spheres in the volume can be obtained from the bed porosity (0.41, measured independently) and the approximate particle radius (1.18 mm):

$$N = \frac{V(1-\varepsilon)}{V_p} \approx 1545 \ particles \tag{20}$$

Many of the candidate spheres are computational artefacts or overlap with other candidate spheres. These need to be removed. An alternative to the Hough-like transform is the distance transform, where the convolution kernel of a solid sphere is used together with the filtered image $\boldsymbol{F}$. While the convolution of these two also yields maxima at potential sphere centres, the intensity profile through the centre has a slope approaching zero. In using the edged image, the Hough-like transform also identifies the sphere centres and the line profile slopes are very large at the centre. This means that the proposed procedure is more sensitive to the exact position of the sphere centre than the distance transform.

Candidate Sphere Characterization

The candidate spheres are characterized by:

1. Position and approximate radius.
2. Hough-like value (normalized) at centre of sphere (h, indicates the correlation with identified edges)
3. Mean intensity density (ρ_i)

4. Number of overlapping voxels (v) with candidate spheres of higher h (since candidate spheres with higher h values are more likely to correspond with the actual spheres).

Discard Candidate Spheres Unlikely to Correspond to Actual Spheres

Roughly speaking, the candidate spheres could be divided into two groups:

- Relatively low h, relatively low ρ_i or relatively high v
- Relatively high h, relatively high ρ_i and relatively low v

Sometimes phantom spheres are identified when there is a good correspondence with the edges of a combination of actual spheres. These spheres have low intensity densities and fall in the first group. In other cases, actual spheres are identified multiple times at one location but with different radii. Of these the larger ones (larger radius) generally have high v values and are removed on the basis that the spheres cannot physically overlap. Removal of the first group (low h, low ρ_i, high v) leaves a good approximation of the actual spheres in the bed. Some of these overlap ($v > 0$) with spheres of higher h values. In those cases where v is small ($v < 10$), visual inspection indicate that there is an actual sphere approximately in that position. In order to remove the overlapping, the sphere is moved locally (by no more than 2 voxel distances) to maximize the value of ρ_i. In all but a few cases, this reduced the value of v to 0. In the few remaining cases, the sphere radius was reduced by 1 voxel and then the value of ρ_i was maximized by translation. After these operations, 1526 spheres remained in the volume (which compares well with the approximate value of 1545).

Correct Beam Hardening

It can be observed that the average intensity density (ρ_i) of a sphere toward the centre of the column is lower than that of spheres at the wall. This restates the beam hardening effect and can be quantified as illustrated in Figure 45. The beam hardening effect is removed by adjusting image intensities as a function of the radial distance according to:

$$\boldsymbol{I}'_{avg}(r_c) = \boldsymbol{I}_{avg}(r_c)\frac{\rho_{i,avg}(r_c \to 0)}{\rho_{i,avg}(r_c)} \tag{21}$$

The original and adjusted images are compared in Figure 45. The beam hardening effect has been successfully removed.

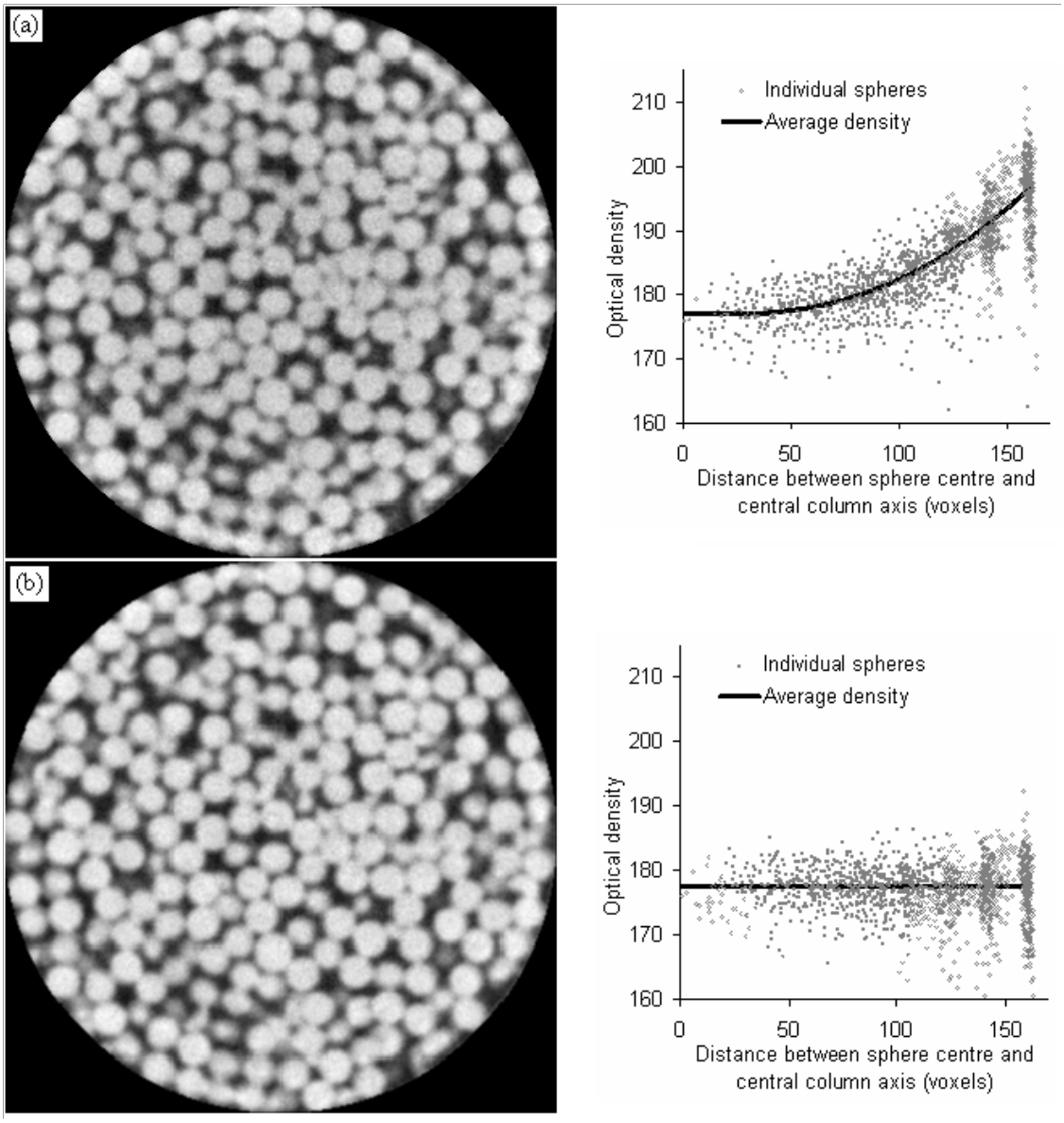

Figure 45. Beam hardening correction. (a) Uncorrected (b) Corrected.

Grow Spheres

The spheres identified thus far have approximate integer radii and do not overlap. In the previous steps, whenever two spheres with different radii at the same location were identified (by both having large Hough-like values), the smaller sphere was preferred. Inspection revealed that these spheres often do not touch any of their neighbours (a phenomenon which is again physically impossible since the spheres need to be supported against gravity). A simple way of correcting the radii is by growing the spheres in small increments until they touch. This is done by visiting a sphere, growing its radius by 0.1 voxels, evaluating whether the grown sphere overlaps with any existing spheres and only allowing the growth if it does not. The procedure is then applied to the next sphere in the list. Note that a single sphere cannot be grown until it touches the existing spheres, since this would not allow its neighbours to experience any growth. Note also that the order in which the growth process is applied determines which spheres are grown preferentially. It is necessary to appeal to the nature of computed tomography in order to determine which spheres to grow first. It is known that a sharp gas-solid transition reconstructs to a bi-directionally smoothed profile, schematically shown in Figure 46. In this one dimensional analogue, the mean intensity density of a candidate sphere of radius r is given by the area under the curve divided by r. If $r < r_{actual}$ (the actual radius), the intensity density will be high. Therefore, the candidate spheres with high ρ_i are those that should be preferentially grown. A cross-section of the resulting image that contains all the spherical particles is shown in Figure 47 (spherical particles shown in grey, ignore for the time being the white non-spherical particles).

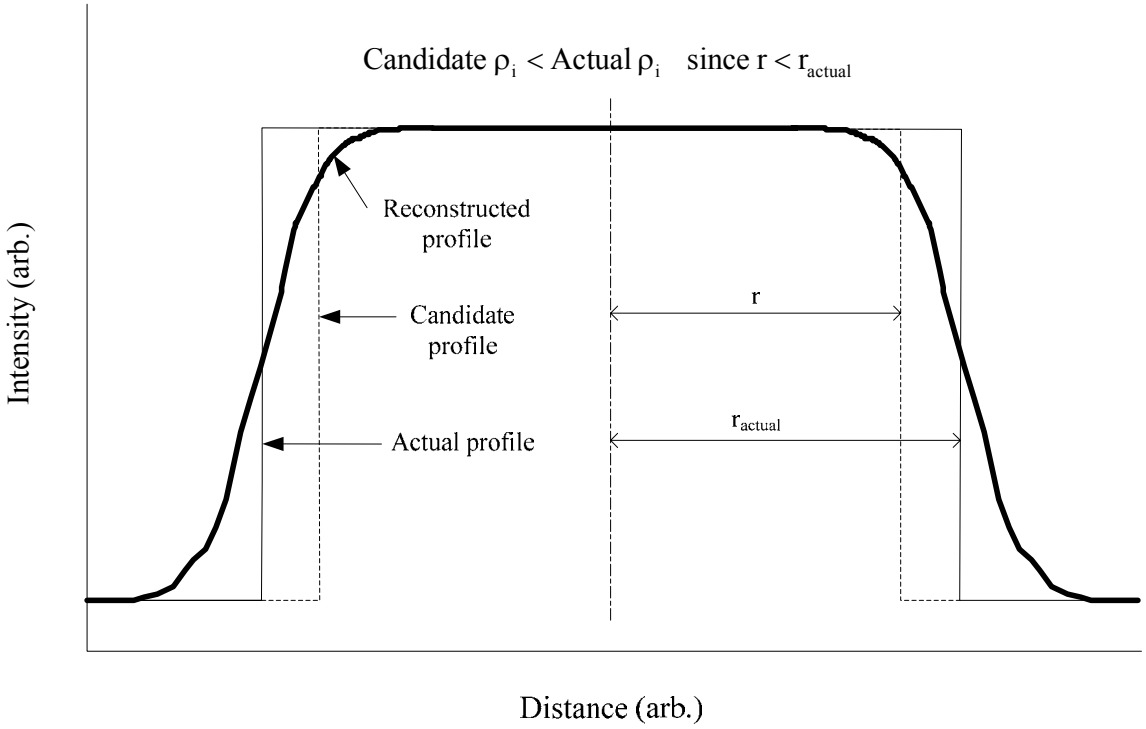

Figure 46. Motivation for the growth prioritizing

Procedure Generalization

The procedure stipulated above appears to correctly identify the locations and sizes of the spherical particles in the volume by using non-local information in establishing the nature of each voxel. A priori knowledge of the spherical shape of the particles was used in calculating the Hough-like transform (in particular in specifying $\boldsymbol{B}_r$). This step can be generalized to identify any particle of known shape by appropriate specification of $\boldsymbol{B}_r$. For example, if the bed had been packed with cylinders of different sizes, a Hough-like transform will be calculated for each size and orientation of the cylinders. This is equivalent to searching for cylinders of a certain size and a certain orientation in the bed (for each size and orientation a different $\boldsymbol{B}_{size,orientation}$ will be constructed). This expression is somewhat complicated for particles for which rotational symmetry does not hold. Nevertheless, although the procedure would be computationally expensive, it can be applied to any bed packed with particles of known shape and approximate size.

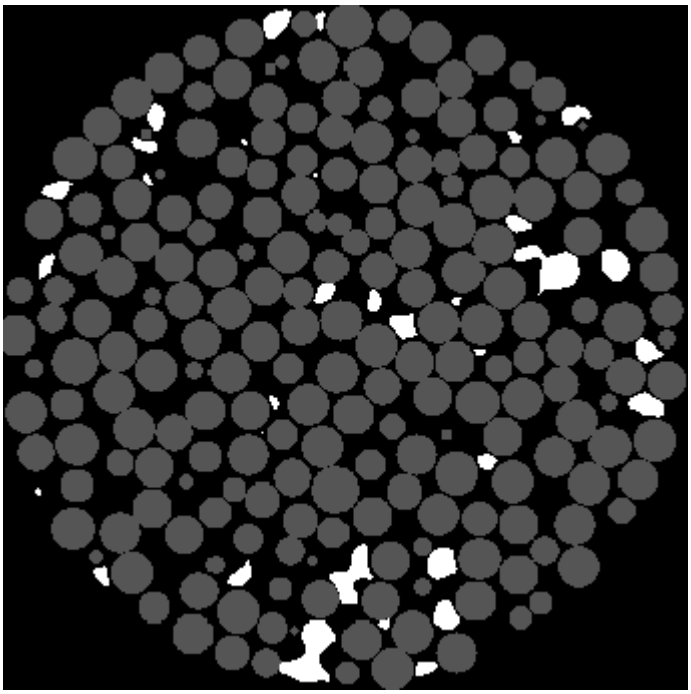

Figure 47. Solids image (non-sphericals shown in white)

Addition of Non-Spherical Particles

Although this procedure is effective for known shapes (in this case spheres), a significant fraction of the particles in the bed under consideration is not captured. Inspection reveals that these particles have arbitrary shapes (usually broken spheres). They are identified by taking all voxels with an intensity higher than some threshold, that is not already part of an identified sphere. While this is inaccurate there are relatively few non-spherical particles (as illustrated in Figure 47, non-spherical solid shown in white). In summary, the three dimensional volume image, $\boldsymbol{S}$, consists of a 3D matrix of voxels with a value of 1 if the voxel is located inside a particle and zero if it is not. In addition, the location and radius of each spherical particle is also known. This enables particle scale evaluations of the bed and flow structures. It is encouraging to note that the overall bed porosity

computed from this image (***S***) (0.41) compares well with that determined by gravimetric means (0.41).

Identifying the Fluid Phases

The liquid in the bed is isolated by subtracting the volume image of the bed under irrigation from the volume image of the bed without irrigation (Figure 48a). This image is then thresholded (at a value that removes an assumed Gaussian noise distribution) and the solids image (***S***) is superimposed onto it. Because the solid phase has been properly identified, the liquid located at particle contact points are now captured with greater accuracy. At some rare locations it was found that there is a slight gap (1 voxel in size) between the liquid phase and the solid. Based on visual examination of the original reconstructed images, these gaps are taken as computational inaccuracies and filled in with liquid. A cross-section of the final image (***T***) is shown in Figure 48b. The proposed procedure is recommended as a superior alternative to thresholding in CT image processing.

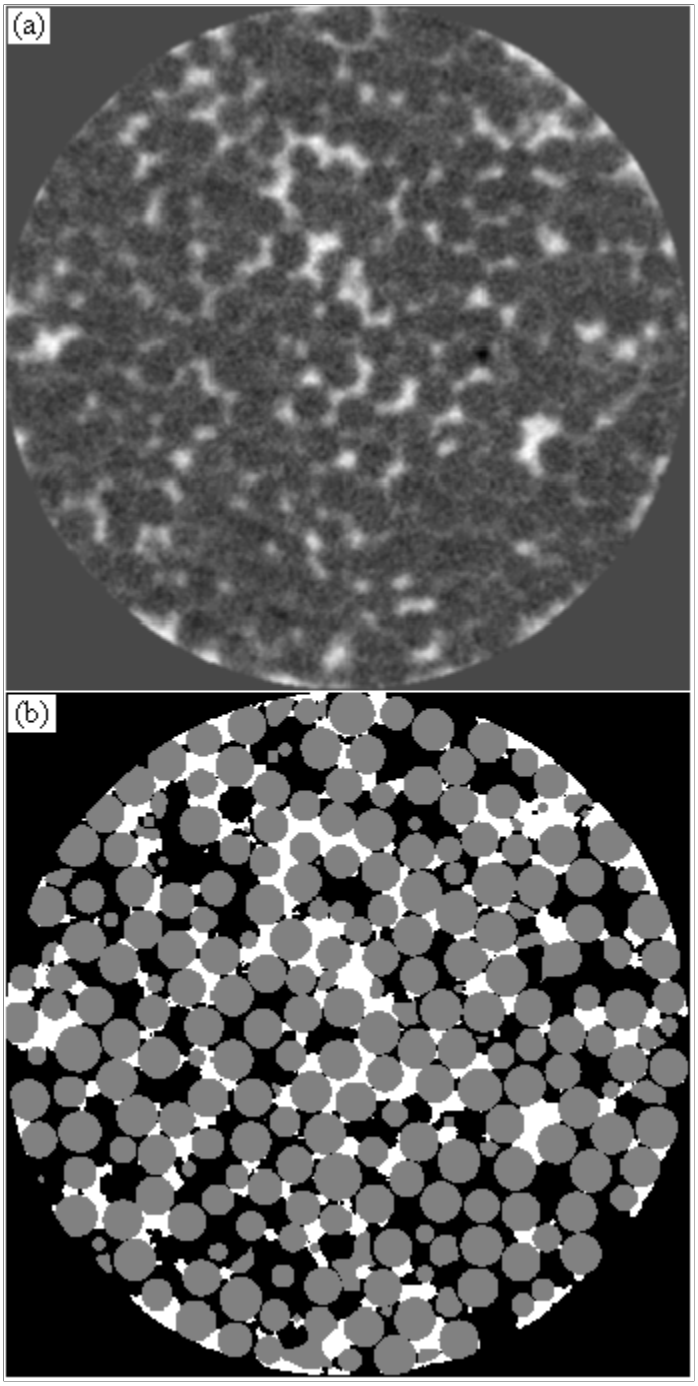

Figure 48. (a) Dynamic liquid in the bed obtained from subtracting the drained image from the flow image. (b) Ternary gated image (***T***) showing solids in grey and dynamic liquid in white.

De-Rectangularization

At this stage, the image (***T***) is a three dimensional matrix with each entry identified as either solid, liquid or gas. Most particles are approximately 10 voxels in radius. While volumes can be calculated in this representation by addition of voxel volumes, external surface areas cannot be calculated by addition of the areas of each external face. For example, a sphere with radius 10 voxels (i.e. 1.18 mm) has a real volume of 6.88 mm^3 and an external surface area of 17.5 mm^2. The sum of voxel volumes comes to 6.85 mm^3 (and approaches the real volume as the resolution becomes better), but the sum of external face areas is considerably higher than the real surface area (22.3 mm^2) and increases further as the resolution becomes better. That means that the external solid surface area as well as the liquid-solid surface area cannot be calculated by counting faces. Instead, the surface area is calculated as follows:

- The edge voxels are identified as voxels that share at least one face with gas or liquid (wet edge voxels share at least one face with a liquid voxel). Each edge voxel has associated coordinates (*ex, ey, ez*) taken at the centre of the voxel. From standard geometrical arguments, the rotational and azimuthal angels of that voxel (θ, ϕ) can be calculated. Note that the distance from the centre of the central voxel is not necessarily equal to the radius, *r* (it is less than one voxel size shorter).
- The solid external surface is then "paved" with squares (patches), with the centre of the patch located at (θ, ϕ, *r*). Larger spheres therefore comprise more of these patches because there are more edge voxels. The areas of these patches are approximately equal ($1.81 \pm 0.02 \times 10^{-8}$ m^2) because of the regular spacing of the edge voxels.
- The specific external surface area calculated from these patches (1461 m^2/m^3), compares well with the same area calculated using the porosity and the average particle radius (1446 m^2/m^3). The gas-liquid interface is handled in the same way.

- Whether or not an external solid surface patch is contacted by liquid is determined by matching the (θ, ϕ) values of the wet edge voxels to those of the patches. The fraction of these patches contacted by liquid is the wetting efficiency.

There is one apparent error in this method. This lies in determining whether an edge voxel is wet or dry. Edge voxels close to the dry-wet interface on the particle surface will very often have some of its external faces in contact with liquid and others contacted by gas. In these cases, the voxel has been counted as both wet and dry. An estimate of the error in doing this can be made by counting these voxels as either wet or dry and then calculating the change in gas-solid or liquid-solid surface area. These changes were typically below 3% and the error is therefore negligible. A similar situation arises for liquid voxels that contact both the solid and the gas. Because it is smaller than the other areas, the error in the gas-liquid area is estimated to be around 12%.

It is important to note at this stage that the wetting efficiency calculated in this way is the dynamic wetting efficiency (because the drained bed that was used as a subtractor includes the residual liquid holdup). It was found to be very difficult to distinguish the residual (sometimes referred to as static) liquid in the difference between a drained bed and a dry bed. This is because the pendular rings are very small for this system and because the internal holdup in the drained bed changes the magnitude of the edge effect discussed earlier (the operation of subtracting a dry bed from drained bed therefore yields a lot of noise at the particle contact points). Therefore, the residual liquid holdup (RLH) was added to $\boldsymbol{T}$ by an alternative approximate method. It is known that residual holdup accumulates at locations of close particle-particle contact, and that for this particular system the majority of RLH is in the form of pendular rings at the contact points. The RLH was measured independently for this system at 2.5% by the weighing method. The RLH image ($\boldsymbol{SL}$) is added to $\boldsymbol{T}$, by calculating it as $\boldsymbol{SL} = 1$ where $\left(\left[\boldsymbol{S} * \boldsymbol{F}\right] - \boldsymbol{S}\right) > t$. This yields artificial RLH at locations where the local solid density is high (e.g. contact

points). The filtering and thresholding parameters are set so that the average RLH equals the 2.5% previously measured. The final image showing the solid, gas, residual liquid and free-draining liquid is shown in Figure 49. This is a considerable improvement over Figure 41, and can now form the basis of a comprehensive investigation in trickle flow behaviour. A great deal of information is available from the three dimensional image of the bed where each phase has been more accurately identified, and is reported in the next section and explored further in Chapter 7.

6.1.5 Image Processing Strategy Conclusions

Computed tomography techniques offer unprecedented potential for detailed examinations of trickle flow hydrodynamics. This section showed how more advanced image processing techniques can be employed to extract valuable information from less than perfect tomography results. X-ray CT results of a pilot scale trickle bed under various different conditions are used to illustrate the procedure. Using the proposed approach, it is possible to investigate trickle flow hydrodynamics to a level of detail that has been impossible before.

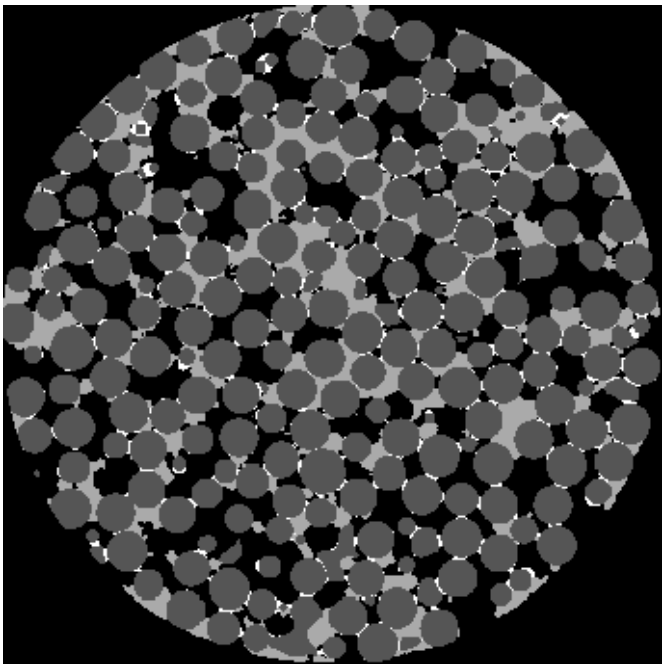

Figure 49. Addition of RLH (in white)

6.2 Tomography Results

It should be obvious now that a wealth of information can be extracted from the high detail tomographic images. This includes bed characteristics like porosity and its axial and radial distributions, particle coordination numbers, the fluid flow patterns, global and local holdup and its distribution, average and particle scale wetting efficiency and its relationship to bed and flow characteristics, gas-liquid interfacial area and the influence of velocity changes, pre-wetting and flow histories on the hydrodynamics. Some examples follow. These are all pertinent to the discussions in Chapter 7 and are intended to illustrate both the power of the experimental technique and the nature of hydrodynamic multiplicity.

Figure 50 shows cross-sections of the bed for three of the modes. Notice the differences in liquid distribution. Figure 51a shows the results of imaging the bed in three dimensions without any liquid present (4.7 mm of the reconstructed 18 mm are shown in the axial direction). If the liquid is imaged without the presence of the solid, the prevailing flow patterns become apparent (Figure 51b to Figure 51h). A careful examination of these figures reveals the following:

- There are un-irrigated volumes in the Levec mode at low liquid velocity, and these volumes become active at high velocity. The Kan-Liquid and Super modes show very good liquid distribution at both high and low velocities, but smaller scale un-irrigated volumes persist in the Levec mode at high velocity. There appear to be little difference in macroscopic liquid distribution between the Super and Kan-Liquid modes.
- An increase in velocity results in higher saturation and increased spreading of the liquid – a greater fraction of the bed volume is occupied by liquid.

Images like those in Figure 51 serve to illustrate global features, but it is necessary to augment them with quantitative analyses. From an image like that depicted in Figure 51a, the radial and axial porosity distributions can be calculated. They are shown in Figure 52 along with the trend predicted by the recent model of De Klerk (2003b) for similar systems. The radial porosity distribution was evaluated at different length scales, but no new information that relates to hydrodynamic multiplicity was gained from such analyses.

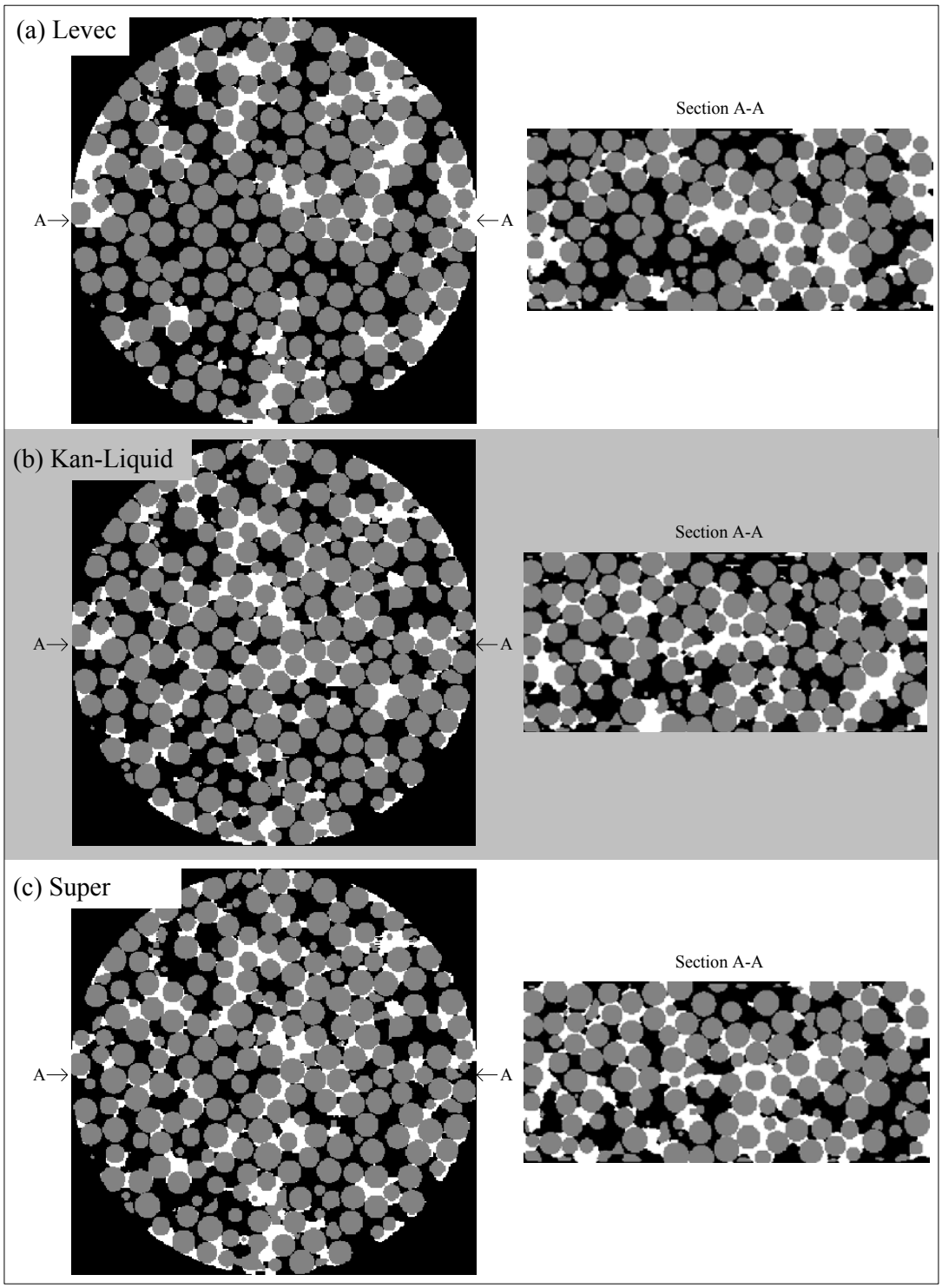

Figure 50. Tomography results at u_L = 2.7 mm/s and u_G = 4.7 cm/s

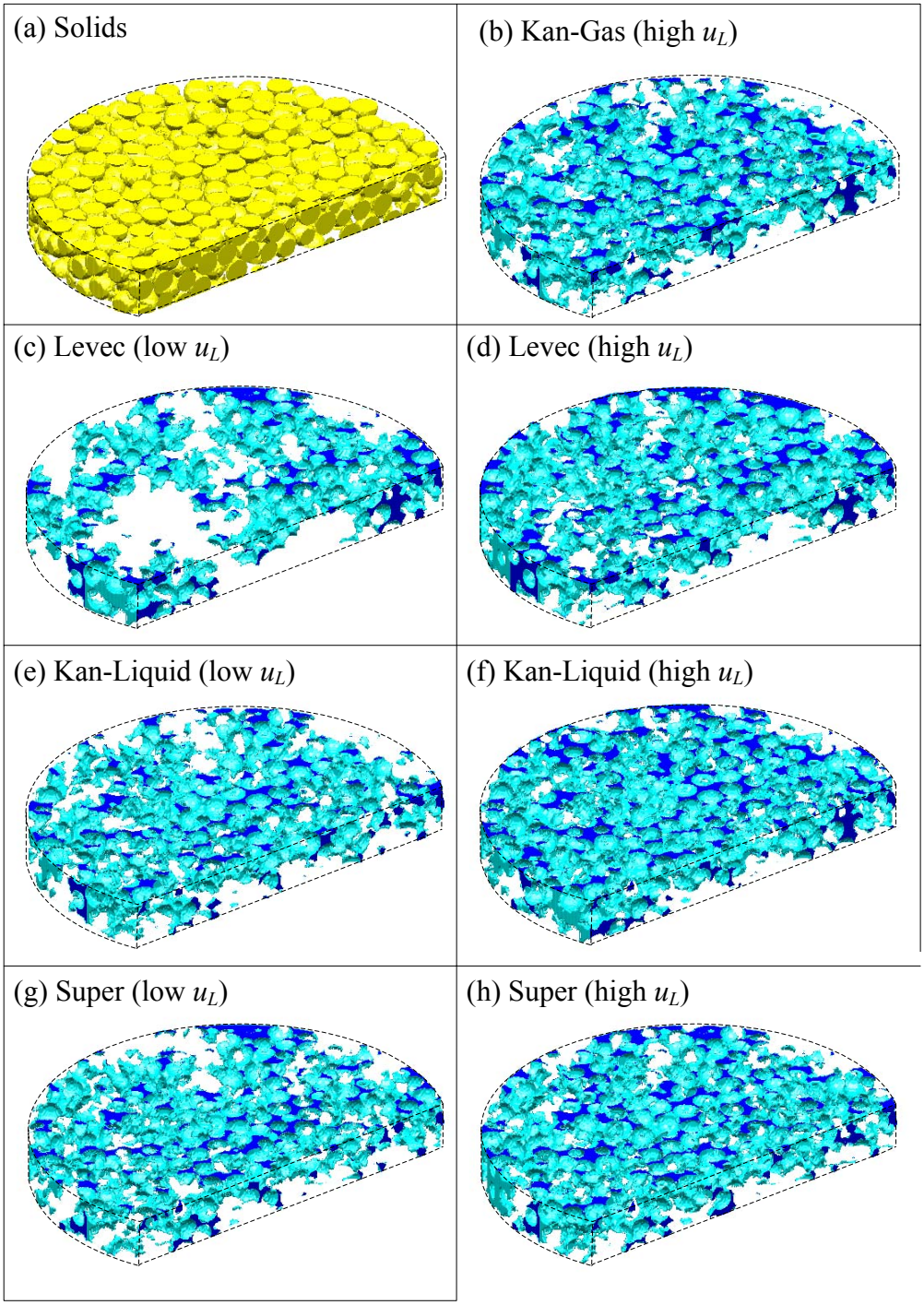

Figure 51. Three dimensional images of the (a) solid (yellow), and (b-h) the liquid (surface in light blue, slice plane in dark blue) in the bed in the different modes. High u_L = 5.3 mm/s, low u_L = 2.6 mm/s, u_G = 3.2 cm/s.

The axial porosity distribution is sinusoidal (not damped) with a relative standard deviation of 3.3%.

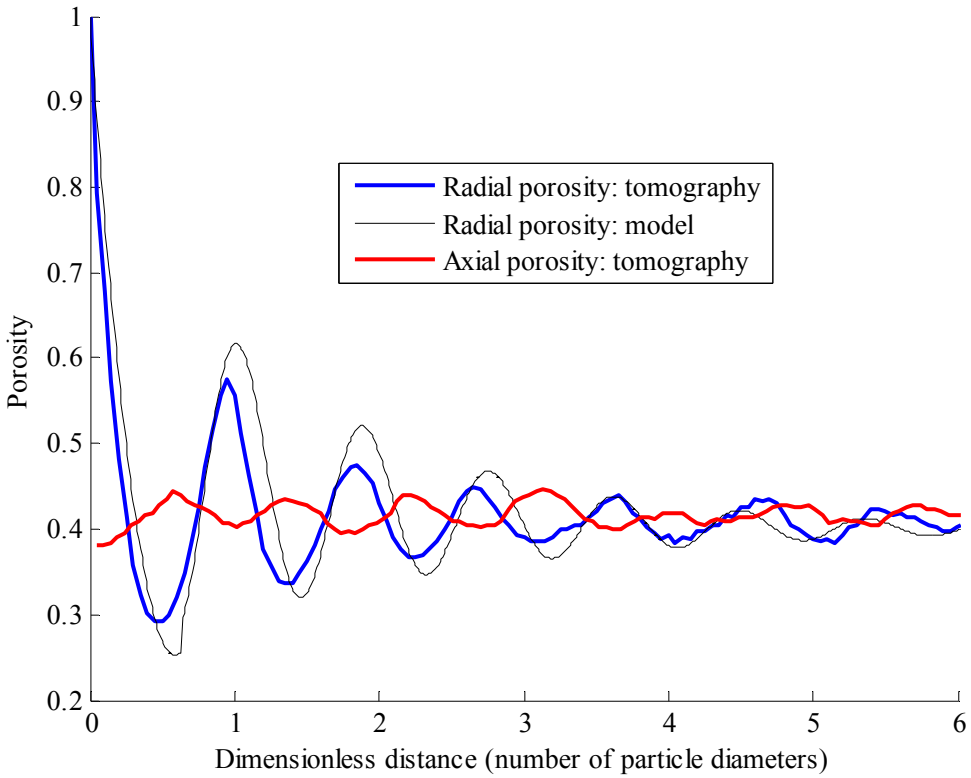

Figure 52. Porosity distribution in the radial and axial directions.

Other bed-scale properties that can be extracted from the three-phase images are the liquid holdup, wetting efficiency and gas-liquid mass transfer area (Figure 53). To keep the figures un-cluttered, only the Levec and Kan-Liquid modes are shown here (the Super and Kan-Gas modes data are available but is not shown). The data generally agree very well with the trends evaluated in Chapter 4. This instils the belief that the images are indeed representative of the hydrodynamics. The level of detail inherent in the processed tomographic images allows the determination of localized hydrodynamic phenomena, an example being the wetting geometry on individual spheres (Figure 54). However interesting these kind of visualizations are, the focus is now shifted specifically toward establishing what the mechanism of hydrodynamic multiplicity is, as well how it explains

the qualitative behaviour that has been observed so far. This issue is dealt with in context in Chapter 7.

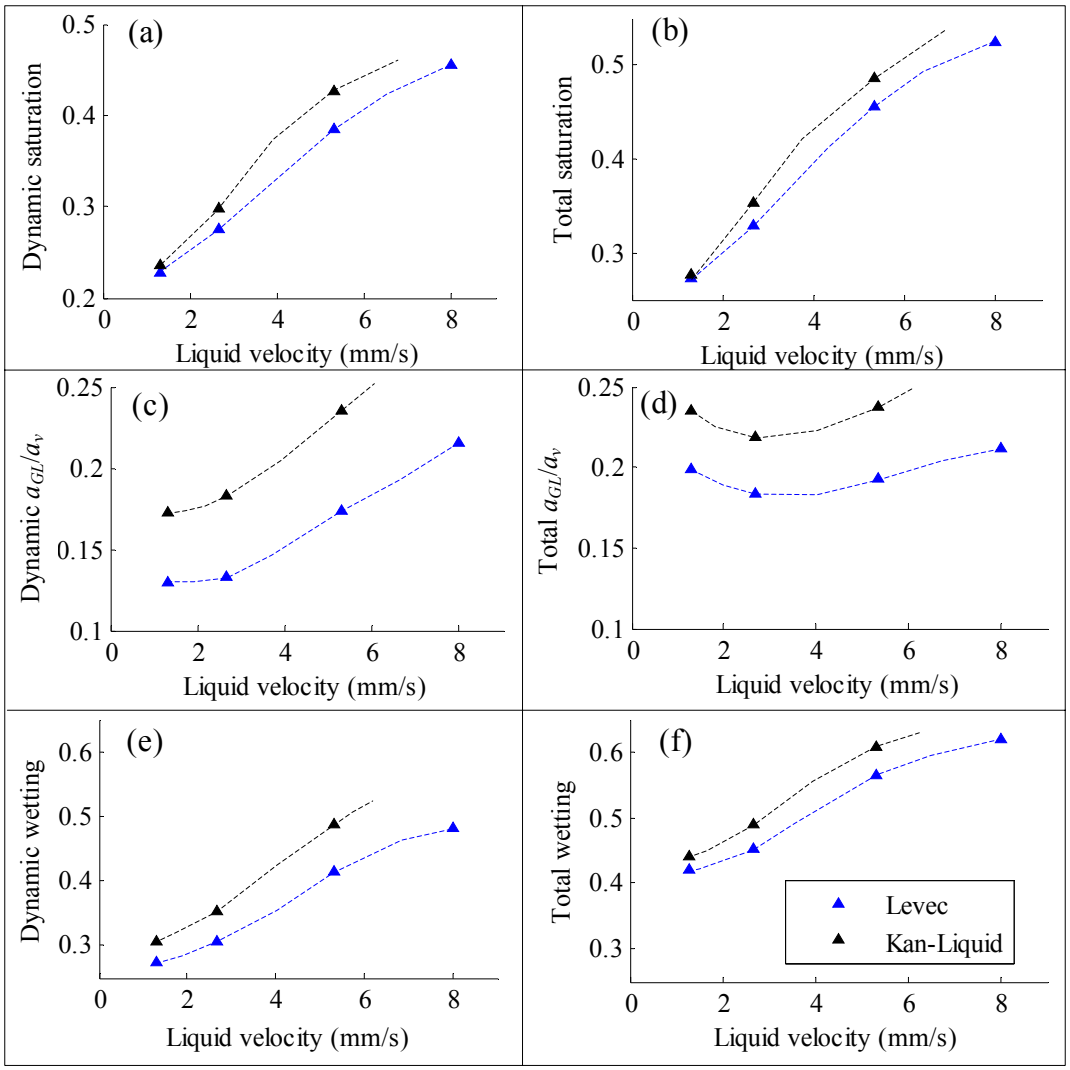

Figure 53. Bed-averaged hydrodynamic parameters computed by the method developed in this study (u_G = 1.6 cm/s). (a), (c), (e) is the dynamic saturation, gas-liquid area and wetting efficiency, (b), (d), (f) is the total saturation, gas-liquid area and wetting efficiency.

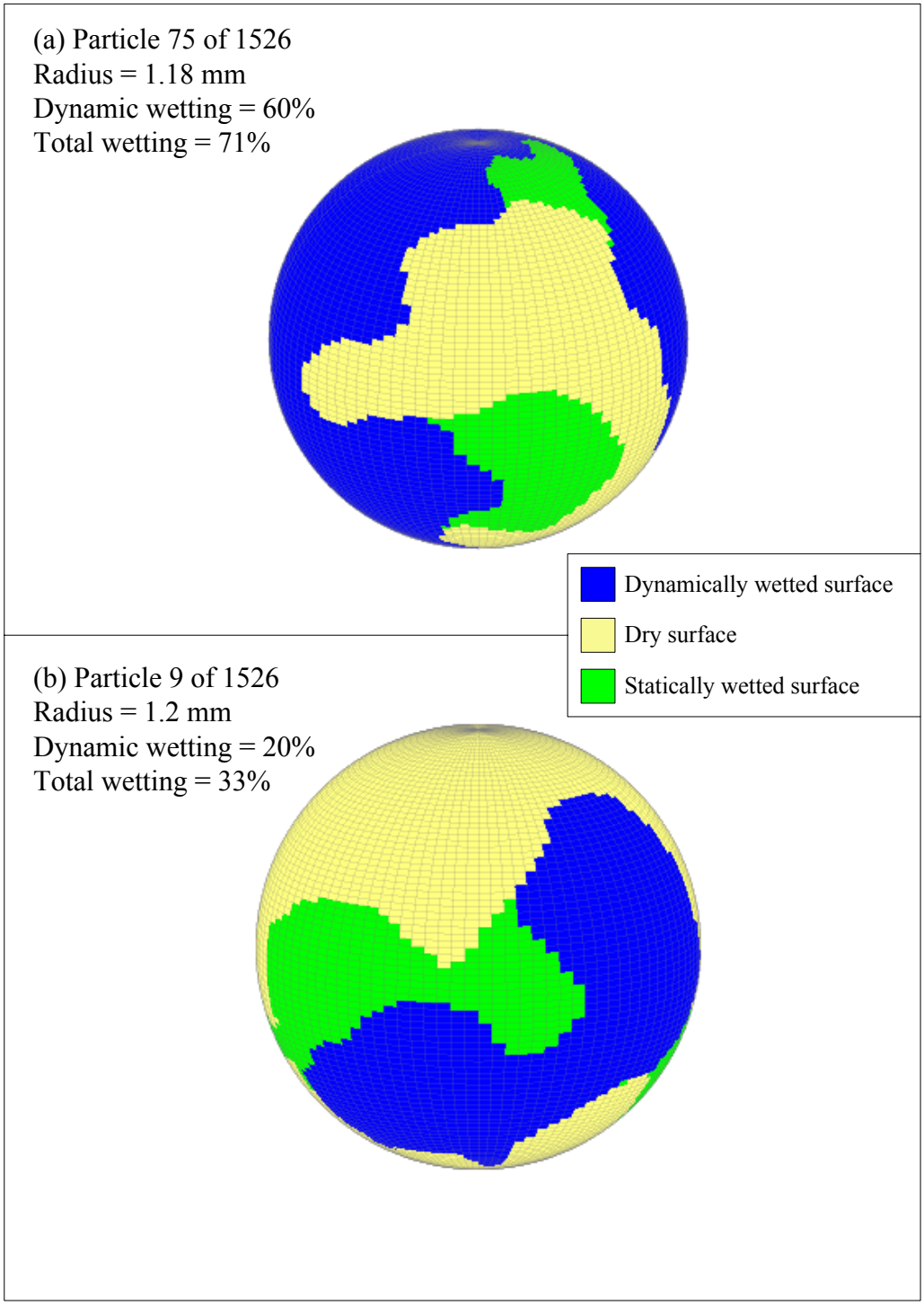

Figure 54. Three-dimensional images of typical partially wetted spheres (dry surfaces in yellow, dynamically wetted surface in blue, statically wetted surface in green).

6.3 Bed Structure and Flow Pattern Characterization

Additional information can be extracted from the high definition ternary image generated in section 6.1. This is done by partitioning the bed into "pores" according to the procedure developed by Baldwin et al. (1996). The details of this procedure are discussed in detail in literature and are only summarized here briefly. Pores are defined as relatively large void volumes bounded by solid surfaces and planes erected where the hydraulic radius is a minimum (Dullien, 1992). Starting from the three dimensional image where each voxel is identified as either gas or solid (***S***, no flow), the void space is "thinned" morphologically. This operation is basically the discrete version of the distance transform and yields high intensities at locations far from any solid (i.e. the potential centres of the pores). The pores are then grown from these local maxima sequentially, i.e. the largest pore centres (as identified by the value of the thinned image at the local maxima) are grown by one voxel in each direction outward from the centre, then the largest pore and the next largest is grown by one voxel and so on until the whole void space is filled. A pore stops growing when it reaches the solid surface or meets another pore. Two touching pores therefore always share an approximate plane of voxels (which is referred to as a pore neck or pore exit). These steps are illustrated in Figure 55 for a 2D section of the actual bed. A technical detail is that in each case the "connectivity" of voxels have to be chosen for the growth step. The three options are 6-connected (voxel faces touch), 12 connected (faces and edges touch) or 26-connected (faces, edges and corners touch). It was found that the resulting pore classification did not differ drastically with these options and 26-connection was used. Baldwin et al. (1996) states that this procedure results in an unambiguous pore classification, but there is some ambiguity in what exactly is meant by a "local maximum" in defining pore centres. As an example, Figure 56b shows a surface plot of the thinned image for the region shown in Figure 56a (the same region as used before). In this figure, the decision to view point 2 as a local maximum results in a smaller pore centred at point 1 (Figure 56c).

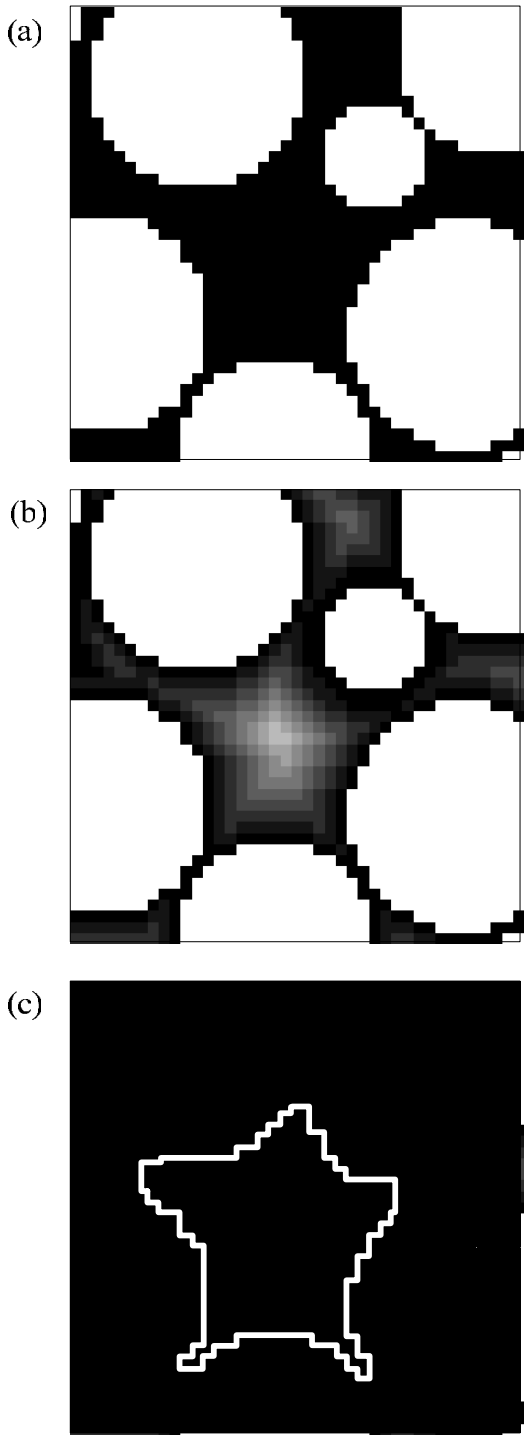

Figure 55. Pore space classification (a) Original image (b) Thinned image (c) Pore (white line shows pore boundary)

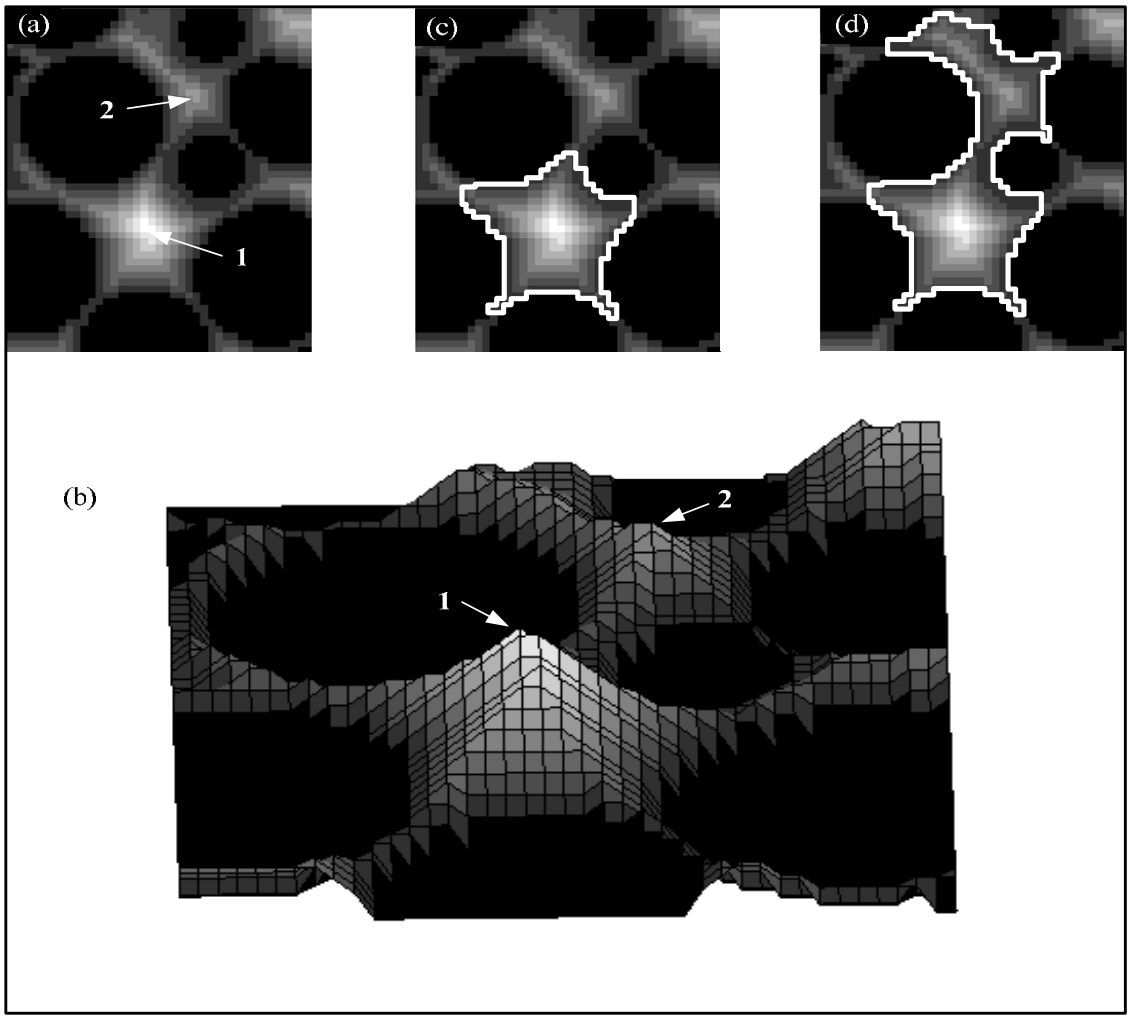

Figure 56. The ambiguity of pore classification. (a) Thinned image (b) Surface plot showing local maxima (labelled 1 and 2) (c) Pore classification with small window (b) Pore classification with large window.

If point 2 is not considered a maximum, the pore centred at point 1 is much larger and encompasses the region around point 2 (Figure 56d). One has to choose a window size that is to be considered in order to identify local maxima. If the window size is small, both points 1 and 2 will register as maxima. If it is large, only point 1 will register. For the remainder of this chapter, a window size of 10 voxels (i.e. one particle radius) is chosen as this yielded results that seemed intuitively correct. However, all calculations were repeated with smaller window sizes and while the data are obviously different, none of the conclusions drawn regarding hydrodynamic multiplicity were compromised.

An example of a three dimensional pore is shown in Figure 57 in relation to its neighbourhood. The figure also shows the liquid inside the pore. From this sort of analysis, a number of pore-scale statistics regarding the bed and the liquid distribution in the bed can be calculated. These pore-scale statistics include the following (as shown in Figure 58):

- The centroid of each pore
- The volume of each pore - the pore volume distribution
- The external surface area of each pore, including the pore-solid area and the pore-pore area. This allows the calculation of a pore hydraulic diameter (6 times the pore volume divided by the pore-solid area), which shows an approximate normal distribution (average = 1.8 mm, relative standard deviation = 14%).
- The coordination number of each pore (the number of pores each pore is connected to). Also included here is a list of which pores are connected and the characteristics (area, location and circumference) of each pore-pore interface (neck).
- The sphericity of each pore (while the particles are spherical, the pores are far from it).

When the liquid distribution in each pore is also considered, some additional statistics can be calculated (as shown in Figure 59):

- The holdup distribution (by pore) and its evolution with gas and liquid velocity in each multiplicity mode.
- The wetting distribution (by pore) and its evolution with gas and liquid velocity in each multiplicity mode.
- The gas-liquid area distribution (by pore) and its evolution with gas and liquid velocity in each multiplicity mode.

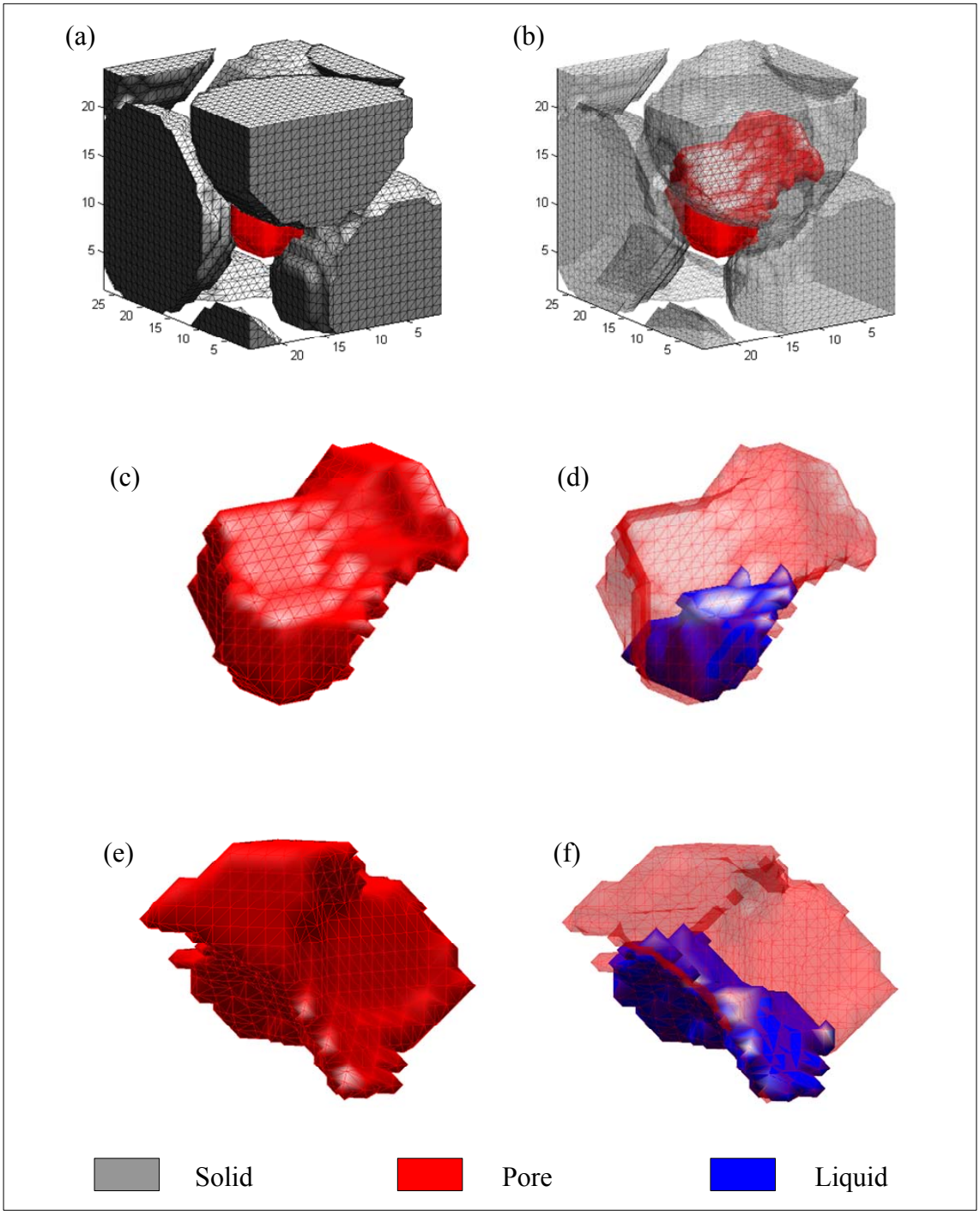

Figure 57. An example of a typical pore, (a) in relation to its neighbourhood (b) the pore nestled in the void space (c) the pore on its own (d) the liquid inside the pore (e) the pore from another angle (d) the liquid inside the pore from another angle.

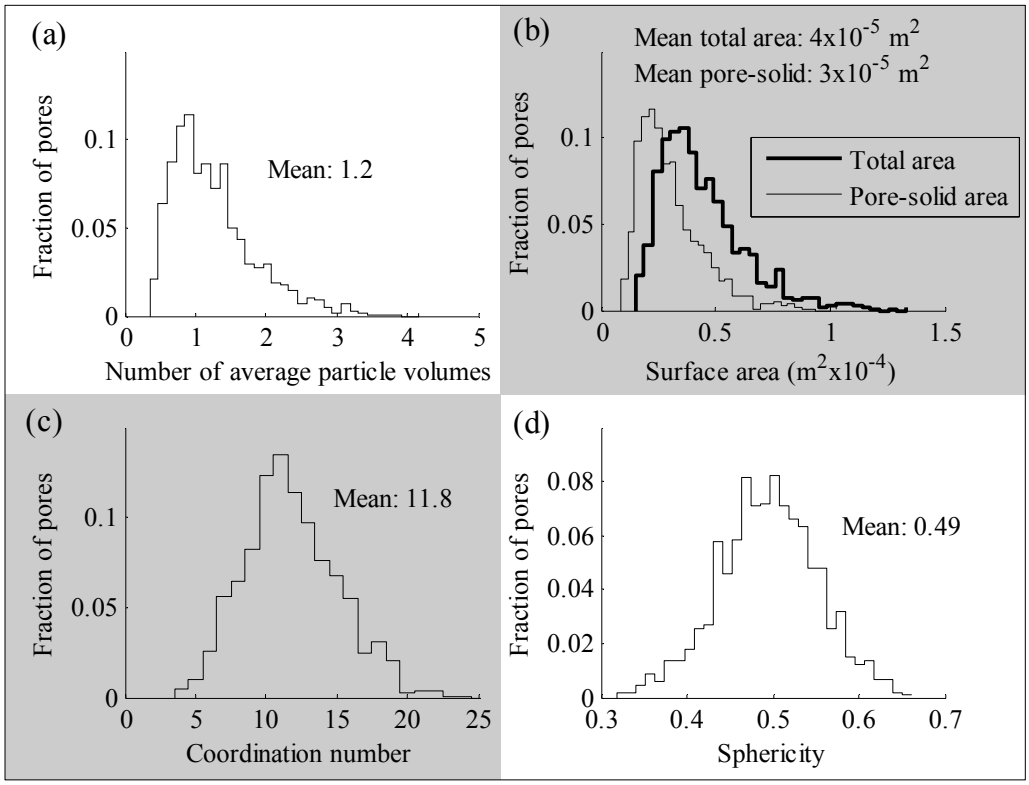

Figure 58. Pore-scale statistics of the packed bed. (a) Pore size distribution (b) Pore external surface area distributions (c) Pore coordination number distribution (d) Pore sphericity distribution.

Similar trends to those observed in Figure 59 were observed for the other gas velocities and they are not shown for the sake of brevity. The pore holdup distributions are of particular importance because they are indicative of the mechanism of liquid distribution (as will be discussed shortly). Two additional multiplicity trends are:

(S) The Levec mode holdup distribution is always bi-modal (and increasingly so as liquid velocity is increased). The Kan-Liquid mode is uni-modal at low velocity and bi-modal at the highest velocity. See Figure 59.

(T) The fraction of pores that contain no dynamic liquid in the Levec mode decreases from 12.7% to 5.5% and then to 0.2% as velocity rises from 1.3 to 2.7 to 5.3 mm/s. In the Kan-Liquid mode, this fraction is always approximately zero – even at low velocity (see Figure 60). Note also that increasing the gas velocity in the Levec mode results in a decrease in the fraction un-irrigated pores, despite also resulting in a decrease in holdup (as discussed in Chapter 4).

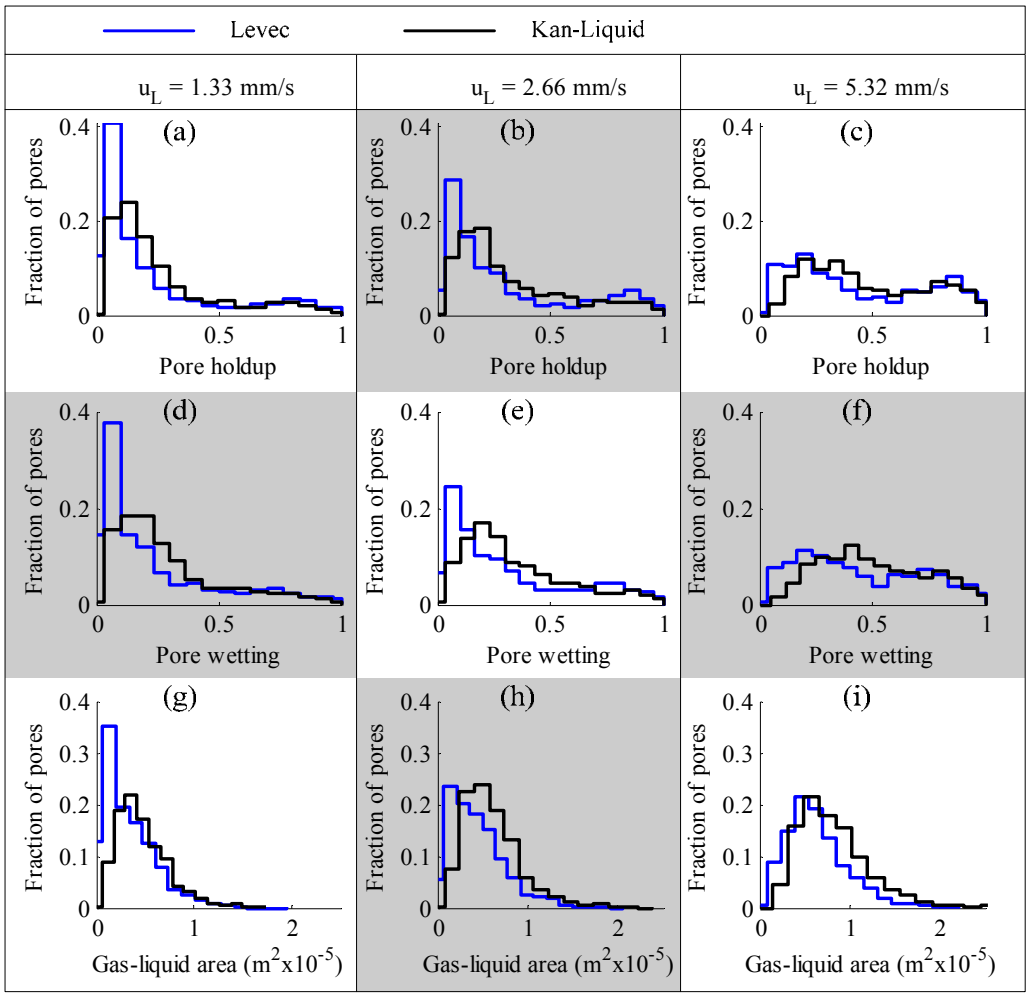

Figure 59. Pore-scale statistics of the flow pattern in the Levec (blue) and Kan-Liquid (black) modes. (a-c) Pore holdup distribution with increasing liquid velocity, (d-f) Pore wetting fraction distributions, i.e. the fraction of the solid surface exposed to the pore that is dynamically wetted, (g-i) Pore gas-liquid area distribution. u_G = 4.7 cm/s for all figures.

The trends listed in **(A)** to **(T)** in Chapter 2 to 6 are the fundamental features of hydrodynamic multiplicity as evaluated by the limiting case framework introduced in this work.

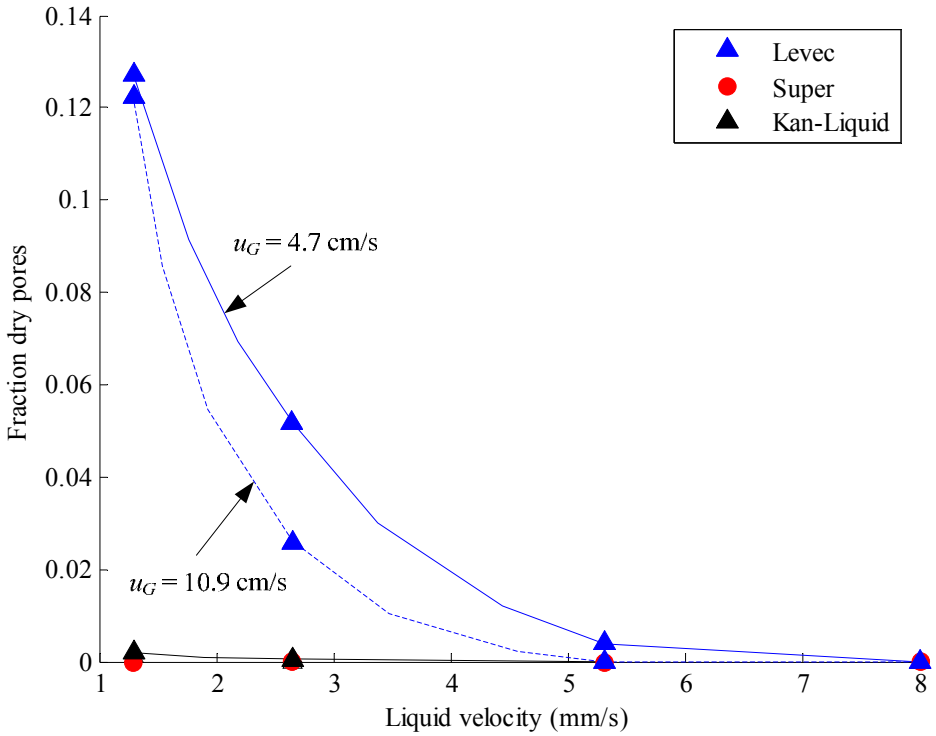

Figure 60. Fraction of pores without dynamic holdup in them (dry pores) as a function of gas and liquid velocity and hydrodynamic mode.

Chapter 7. Interpretations

This chapter combines the experimental insights of Chapters 2 to 6 and explains the hydrodynamic multiplicity trends in terms of a newly proposed multiplicity mechanism. In order to steer clear of empirical detail, the focus is firmly on a qualitative description of the observed trends. However, at the end of this chapter a clear strategy is outlined by which hydrodynamic multiplicity can be incorporated into existing hydrodynamic models. In terms of the overall strategy, this chapter addresses the Multiplicity Mechanism block in Figure 1 and Objective 3 of Chapter 3.

7.1 Introduction: Trends Revisited

In Chapters 2, 4, 5 and 6 a number of trends were pointed out that embodies the nature of hydrodynamic multiplicity and that should be described by a hydrodynamic multiplicity model. These were discussed in detail and the reader is referred to the many figures in these chapters. However, there are some issues and trends that are prominent in understanding hydrodynamic multiplicity. To recap, these are:

(A) There are different flow patterns in the different modes: rivulet-type flow in the lower limiting cases and film-type flow in the upper limiting cases. New rivulets are created as u_L increases.

(B) Liquid flow rate variation induced hysteresis causes increases in pressure drop and liquid holdup in the Non-pre-wetted and Levec modes.

(C) Gas flow rate variation induced hysteresis causes increases in pressure drop and holdup in the Levec mode, but an increase in holdup and a decrease in pressure drop in the Kan-Liquid mode.

(D) The extent of pressure drop hysteresis is diminished when particle size is increased.

(E) The Levec mode *wetting efficiency* is lower on average and shows a bi-modal particle wetting distribution, whereas the Super mode shows a Gaussian distribution.

(F) The liquid *holdup* increases by mode in the order Non-pre-wetted, Levec, Kan-Liquid/Super and then the Kan-Gas mode.

(G) The *pressure drop* for the Non-pre-wetted and Levec modes are the same and lower than the Kan-Liquid/Super mode pressure drop. The Kan-Gas pressure drop is in between these despite it having a *larger* holdup.

(H) The *volumetric gas-liquid mass transfer coefficient* shows the same functional behaviour as the pressure drop.

(I) The *Super and Kan-Liquid modes have similar behaviour*, both in the uniformity of the flow distribution and in the nearly identical values in all the hydrodynamic parameters - despite having been established with different operating procedures.

(J) *Small flow rate changes* have little effect on the hydrodynamic multiplicity after the first or second cycle.

(K) A *decrease in surface tension* brings the pulsing boundary to lower liquid velocity, but hydrodynamic multiplicity still persists in the trickle regime.

(L) A temporary decrease in the surface tension (*surface tension change induced hysteresis*) has no effect on the pressure drop in the Kan-Liquid mode but increases the pressure drop in the Levec mode.

(M) Beds of porous particles have a lower extent of multiplicity compared to beds of non-porous particles.

(N) The extent of multiplicity is associated with the pulsing boundary; *hysteresis is diminished if the pulsing boundary velocity is lowered* (by changing surface tension or particle shape).

(O) An increase in liquid or gas velocity in the *Levec mode drastically increases the pressure drop* at high pressure (gas density), while the increase in the other modes is far less drastic.

(P) High pressure operation (or high gas mass flux) has little effect on multiplicity at low liquid velocity, but decreases the extent of multiplicity at high liquid velocity. The *pressure drop determines the extent of multiplicity*.

(Q) *Time to steady state*: the Kan-Liquid mode takes longer to reach a steady flow pattern than the Levec mode.

(R) There are *particle scale low frequency flow pattern changes* in the Levec mode, but not in any of the other pre-wetted modes.

(S) The Levec mode *holdup distribution* is always bi-modal (and increasingly so as liquid velocity is increased). The Kan-Liquid mode is uni-modal at low velocity and bi-modal at the highest velocity. See Figure 59.

(T) The *fraction of pores that contain no dynamic liquid* in the Levec mode decreases from 12.7% to 5.5% and then to 0.2% as velocity rises from 1.3 to 2.7 to 5.3 mm/s. In the Kan-Liquid mode, this fraction is always approximately zero – even at low velocity (see Figure 60). Note also that increasing the gas velocity in the Levec mode results in a decrease in the fraction un-irrigated pores, despite also resulting in a decrease in holdup.

7.2 Proposed Mechanism

The proposed mechanism of liquid distribution is based on overcoming the surface forces at the pore necks (pore-to-pore connections). To start, consider the hydrostatic fate of a liquid droplet at the bottom end of a vertical conical capillary tube that is being filled with a liquid from the top (Figure 61a to Figure 61e). This discussion follows the simplified treatment of Middleman (1998:33-45). The forces on the liquid body are the gravitational body force and the surface tension forces at the top and bottom menisci. The liquid-solid surface tension is treated as a contact angle (defined as the angle between the

tangent to the liquid surface at the triple point and the solid surface, Ku et al., 1968). A force balance on the liquid volume yields:

$$\cos\theta' = -\frac{mg}{\sigma_{GL}\pi d} \qquad (22)$$

Now, when there is very little liquid in the tube, the gravitational force is small, and the top and bottom contact angles are equal (see Figure 61a). As the amount of liquid is increased, a droplet forms at the bottom of the capillary and the bottom contact angle increases to compensate for the additional weight (Figure 61b and Figure 61c). This continues until the contact angle reaches the *critical contact angle* (which may be as high as 180^{o} but is often taken as the *advancing* contact angle, Meister & Latychevskaia, 2006), at which point the drop detaches. This yields the familiar result that the droplet detaches when the gravity and surface forces are equal (ratio of 1) and the bottom contact angle is a maximum (Middleman, 1998:34). The shape of the droplet can be solved for from the Young-Laplace equation (Meister & Latychevskaia, 2006), but it is not important for the present purposes. If we continue to supply liquid to the top, a steady flow will be established (Figure 61d). If the liquid supply is then decreased, the contact angle decreases until it reaches the *receding contact angle*, at which point the flow stops. Now, it is well established that the receding contacting angle is smaller than the advancing one (see for example Bear, 1974). This means that the capillary exit acts like a gate that is blocked by capillary pressure and is only opened when the hydrostatic pressure exceeds the capillary pressure value associated with the critical/advancing contact angle: $(4\sigma/d)\cos\theta'_{crit}$. The gate closes when the hydrostatic pressure drops below $(4\sigma/d)\cos\theta'_{rec}$. For hydrostatic pressures in the range $(4\sigma/d)\cos\theta'_{rec}$ to $(4\sigma/d)\cos\theta'_{crit}$, the gate is either open (if the hydrostatic pressure had exceeded the critical value in its history) or closed (if it had not).

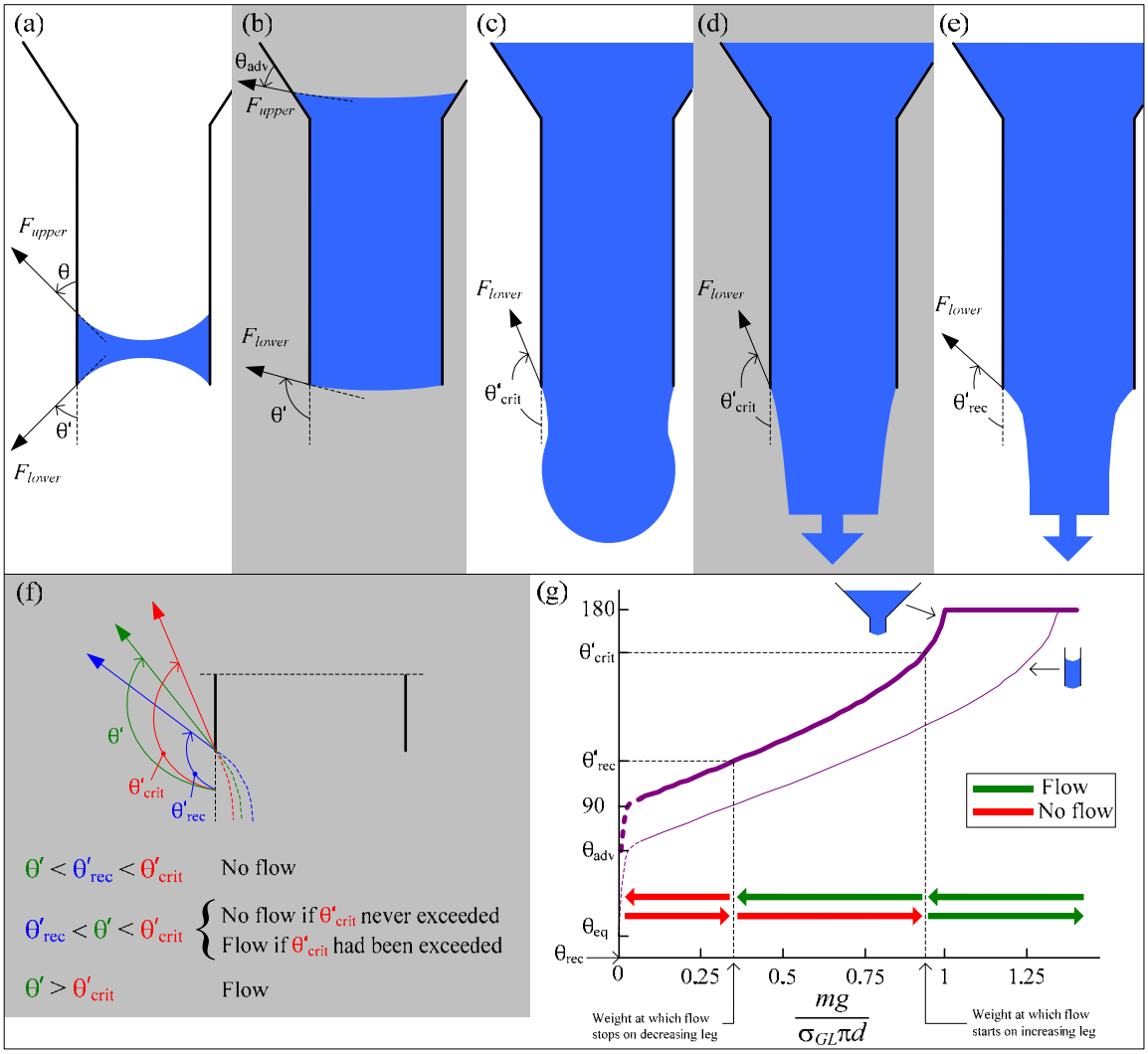

Figure 61. Liquid suspended by capillary force in a vertical conical capillary tube. (a)-(c) Menisci shapes as the weight in the tube increases (d) Just after the critical contact angle is exceeded (e) As flow rate is reduced θ' decreases until the flow stops at θ'$_{rec}$ (f) The fringe region enlarged (g) Bottom contact angle as a function of weight - showing the weight to capillary force regions where the gate is closed (red) and open (green).

See Figure 61f. This behaviour was observed qualitatively with a 1 mm capillary in the laboratory. This is the crux of the proposed mechanism. It is illustrated in another way by the coloured lines in Figure 61g. Note that this is reminiscent of the stick-slip behaviour of control valves as well as the phenomenon of a static and a dynamic friction coefficient in rigid body dynamics. In fact, it is possible to reformulate the equations in terms of a

"retardation" coefficient that is a type of static friction coefficient analogue (Ku et al., 1968).

There are a variety of complications that may arise. The geometry of the capillary greatly influences the values of the bottom contact angle and therefore the range of hydrostatic pressures that can either induce flow or not. For example, if the capillary is straight (as opposed to conical at the top), the upper surface force is not negligible and the bottom contact angle changes with the ratio of gravity to surface force as shown by the thin line in Figure 61g. The value of the critical contact angle is another contestable point, although the fact that it is larger than the receding angle is well established. Another complication arises when there is a substrate close to the exit of the capillary (Figure 62, Ku et al., 1968). At first, capillary action keeps the liquid from forming a bridge by keeping it inside the capillary. Once the drop touches the substrate, a bridge is formed and the liquid flows freely. As liquid flow is reduced, the liquid column is supported also by the vertical component of the force ($F_{sub}\sin\theta''$) at the substrate, which means that θ' will not need to reduce as much as it did when there was no substrate (it takes a lower static head for θ' to reach θ'_{rec}, meaning θ' is larger at the same flow rate than it was when the substrate was not present). All this means that flow will continue for even lower hydrostatic heads (i.e. there are lower flow rates that can be maintained without the "gate" closing). The orientation of the tube (assumed to be vertical before) of course also impacts the situation. Note that viscous forces are neglected in this treatment and that the full dynamic case is more complex and somewhat less understood. The concepts introduced here are based mainly on hydrostatic considerations and this should be considered the major limitation of the idea.

From this brief discussion, it is evident that a fundamental treatment of capillary phenomena in the complex environment of a packed bed is beyond present capabilities. The proposed mechanism is a *phenomenological* one that still needs to be mapped to the bed and flow characteristics.

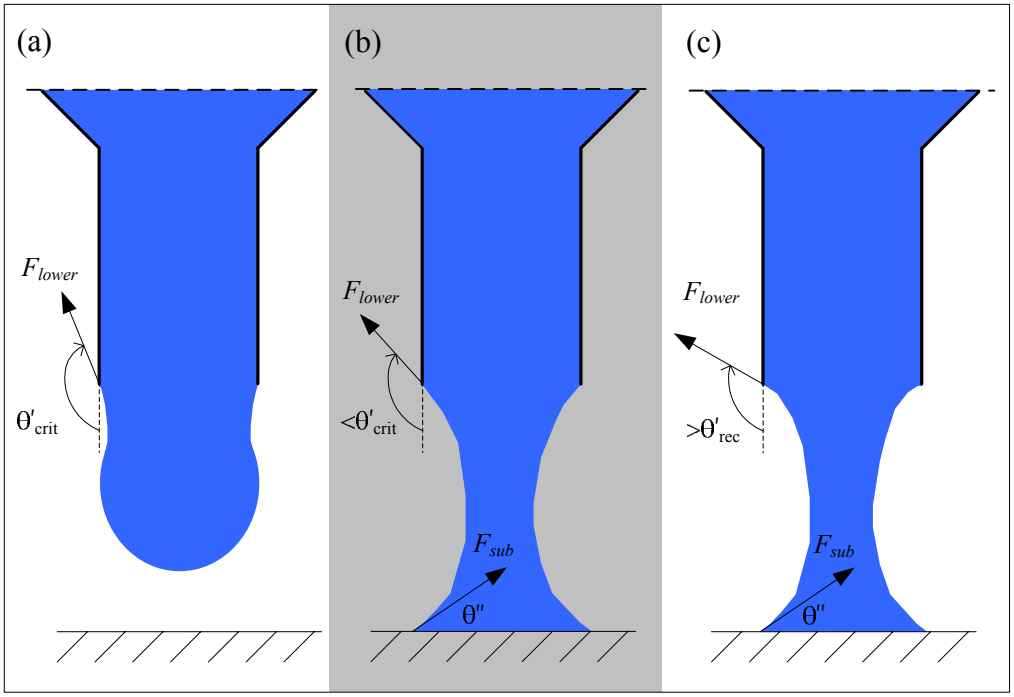

Figure 62. Liquid discharge from a vertical capillary in the presence of a substrate. (a) Droplet is critically poised (b) Just after liquid bridge was created (c) Liquid bridge at the weight where the flow in the substrate-less case stopped – flow persists down to smaller weights because the additional support allows θ' to take longer to reach θ'_{rec} as the weight is decreased.

Having considered these complexities, they are now reconciled with the desire to develop a simple yet effective model. It is proposed that adequate representation of this effect is the following:

- A capillary exit acts as a gate that is initially closed.
- The gate opens for flow when the pressure exceeds a critical value that is given by the capillary pressure at the advancing contact angle.
- When the pressure is reduced (by a reduction in the feed flow rate for example), the gate remains open until the pressure has dropped to below the capillary pressure at the receding contact angle.

7.3 Capillary Gate Model For Explaining Multiplicity Trends

In this section a capillary gate model based on the ideas of the previous section is developed. The objective is to apply a simplified version of the capillary effect to a simplified pore geometry in order to try to reproduce the multiplicity trends listed at the start of the chapter. An additional objective is that the model should also be able to capture hydrodynamic trends that are not specifically multiplicity related (as summarized in Chapter 2.1).

7.3.1 Model Development

The model is developed in three phases. First**,** the focus is on how the pores themselves should be represented (in particular the choice between viewing the pore as a tank or as a tube). In the next two phases the effect of capillary action on liquid flow and gas flow is considered.

Simplification of Pore Geometry: Tank vs. Tube

Note that there is no hysteresis for isothermal single phase flow. This suggests that hydrodynamic multiplicity is a consequence of interfacial surface forces. The first step toward understanding how these surface tension effects lead to the observed hydrodynamic multiplicity behaviour, is to recognize that each pore-pore connection or "neck" acts as a capillary exit or gate (and is therefore subject to the effect described in the previous section). A question that arises is whether a pore can be approximated by a *straight* capillary tube or a *conical* one. In the former, the exit diameter is comparable to the mean diameter, whereas for the latter the exit is much smaller than the mean. Note that this is also an important hydrodynamic question, namely whether the pores are to be represented as "tubes" (with pressure drop over its entire length – an approach adopted by most present hydrodynamic models) or "tanks" with constricted exits (with pressure drop

only over the exits because the fluid velocity in the pore is comparatively low). Consider the pressure drop over a tube with a constricted exit, where capillary actions have been neglected for the time being (it will be incorporated in the next two sections). As shown in Figure 63, the total pressure drop is the sum of the pressure drop over the length l and the pressure drop over the exit (which has an area of A_{exit}). If viscous laminar flow prevails in the tube, the pressure drop is given by the Hagen-Poiseuille equation (Welty et al., 1984), whereas the pressure drop over the exit can be deduced from a mechanical energy balance (Bernoulli's equation, where it is assumed that all the potential energy is converted to kinetic energy). This yields (subject to the assumptions of incompressible, steady Newtonian flow):

$$\begin{aligned}\left(\Delta P+\rho g l\right) &= \left(\frac{\Delta P}{l}\right)_{tube} l+\Delta P_{exit} \\ &= \left(\frac{32\mu u_{tube}}{d_t^2}\right) l+\frac{\rho u_{exit}^2}{2} \\ &= \frac{128\mu Q l}{\pi d_t^4}+\frac{\rho Q^2}{2A_{exit}^2}\end{aligned} \tag{23}$$

This equation closely resembles the Ergun (1952) equation for pressure drop in packed beds. The relative importance of the two contributions can be expressed in terms of their ratio (N):

$$N=\frac{256\mu l A_{exit}^2}{\pi d_t^4 \rho Q} \approx \frac{256\mu A_{exit}^2}{\pi d_t^3 \rho Q} \tag{24}$$

If $N << 1$ then most of the pressure drop is over the exit (and the geometry resembles a tank). If $N >> 1$ most of the pressure drop is over the tube length (and the geometry is that of a tube). Taking the hydraulic diameter (d_t) as the characteristic length (l) and substituting reasonable estimates for the physical parameters (A_{exit} is taken from tomography as ¼ of the mean pore-pore area per pore) and the flow rates, values of N for the gas and the liquid are calculated as ranging from 3.0 to 30 for gas and 0.15 to 1.5 for

liquid. The difference between gas and liquid is due to the differences in viscosity and density (equation 24). These estimates are based on average values in order to reduce the level of complexity. Although both the tube and the exit contributions are significant in both cases, this is some indication that the "tank" analogy is more appropriate than the "tube" analogy for the liquid phase, while the "tube" analogy is more appropriate for the gas phase. In the capillary gate model, liquid flow will therefore be modelled as though it takes place in a tank and gas flow as though it takes place in a tube.

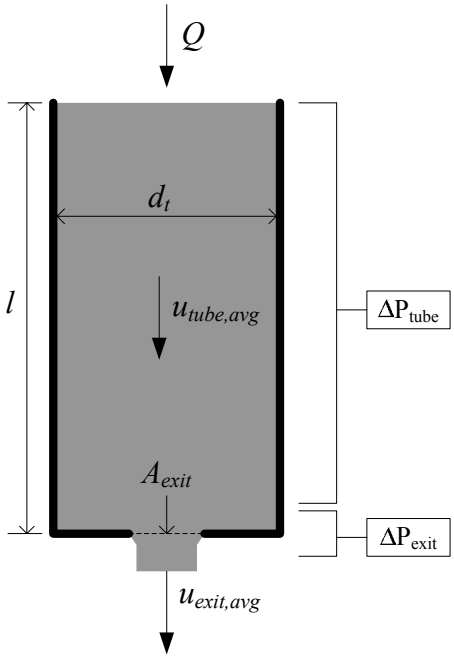

Figure 63. A pore can be approximated as a tube with a constricted exit

Effect of Capillarity on Liquid Flow

The focus is now shifted to how the phenomenological insights in preceding sections are mapped to the packed bed. To start, the effect that capillary action at pore exits have on the liquid flow is dealt with. Consider liquid flow only for a single tank with multiple entrances at the top and bottom (only one of each is shown) as illustrated in Figure 64a. The tank denoted as Tank i receives flow either from other tanks (numbered 1, 2.. K) or from an outside source ($Q_{L,i}$). Flow exits Tank i to tanks numbered 1, 2.. J.

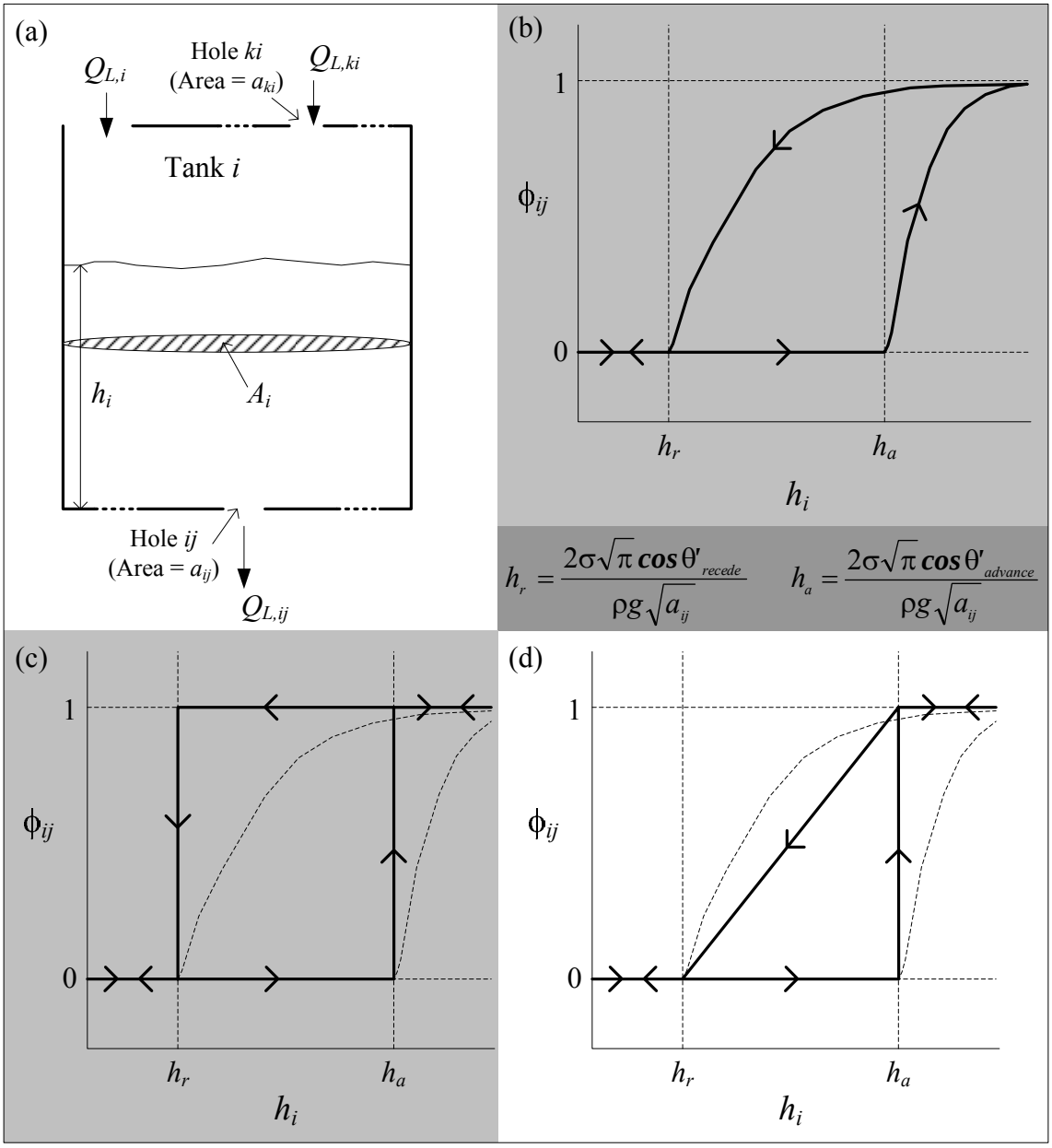

Figure 64. Applying the hydrodynamic multiplicity mechanism to a pore. (a) Single tank geometry, (b) Qualitative plot of the capillary correction factor as a function of liquid height, (c-d) Two approximations of the capillary correction factor as a function of liquid height.

A mass balance on the liquid in Tank *i* reads as (where the constant density of the liquid has been cancelled on both sides of the equation):

$$\frac{dh_i}{dt} = \sum_{k=1}^{K} \frac{Q_{L,ki}}{A_i} - \sum_{j=1}^{J} \frac{Q_{L,ij}}{A_i} + \frac{Q_{L,i}}{A_i} \tag{25a}$$

The relationship between the volumetric flow rate through an exit and the height in the tank is given by equation 23 (with the viscous terms neglected). However, it is now necessary to incorporate capillary action through a factor ϕ_{ij} as follows:

$$\begin{aligned} Q_{L,ij} &= a_{ij}\sqrt{2g}\sqrt{h_i} \quad \text{with no capillary effect} \\ Q_{L,ij} &= a_{ij}\sqrt{2g}\sqrt{h_i\phi_{ij}} \quad \text{with capillary effect included} \end{aligned} \tag{23b}$$

ϕ_{ij} is a factor that accounts for the capillary back-pressure that is present at the tank exit connecting Tank i with Tank j. For a capillary head $h_{c,ij}$ associated with hole ij, ϕ_{ij} is *defined* as:

$$\phi_{ij} = \frac{h_i - h_{c,ij}}{h_i} \quad \text{and} \quad h_{c,ij} = \frac{2\sigma\sqrt{\pi}\,\boldsymbol{cos}\,\theta'}{\rho g\sqrt{a_{ij}}} \tag{26}$$

Note that ϕ_{ij} is always between 0 and 1. In words, the real flow rate through a hole will be smaller than expected because of the presence of the capillary back-pressure. If the capillary back-pressure is greater than the pressure due to the liquid head, there will be no flow and ϕ_{ij} will be equal to zero. When ϕ_{ij} is equal to 1, there are no capillary effects. There are some complexities involved. For example, the angle θ' (in equation 26) evolves dynamically as a function of h_i. Most importantly, ϕ_{ij} fully incorporates the multiplicity effects described in the previous section. To see how, examine Figure 64b, where the relationship between ϕ_{ij} and h_i is shown qualitatively based on visual observations of actual flow through a 1 mm capillary exit. When the head is smaller than h_a (the capillary head associated with the advancing contact angle), there is no flow and ϕ_{ij} is 0. As the head is increased beyond h_a, the contact angle increases asymptotically up to 180 degrees an then stays there. ϕ_{ij} therefore increases gradually and approaches 1 asymptotically. When the flow rate is decreased (remember that flow and head is directly related), the

contact angle decreases gradually back to θ_{rec}, with ϕ_{ij} decreasing to 0 at h_r. It is not known what the exact shapes of these curves are, but two approximations are suggested in Figure 64c and Figure 64d. The first corresponds to neglecting capillary effects once flow is established, while the second assumes that ϕ_{ij} is linear with h_i for the decreasing flow rate leg in the appropriate range. Both approximations yield the same qualitative behaviour and the second approach is adopted because it is believed to be more accurate. ϕ_{ij} is therefore *correlated* as:

$$\phi_{ij} = \begin{cases} 0 \text{ if } h_i < h_r \\ \dfrac{h_i - h_r}{h_a - h_r} \text{ if } h_r < h_i < h_a \text{ and } \dfrac{dh_i}{dt} < 0 \\ 0 \text{ if } h_r < h_i < h_a \text{ and } \dfrac{dh_i}{dt} > 0 \\ 1 \text{ if } h_i > h_a \end{cases} \tag{27}$$

When equation 23b is substituted into the mass balance (equation 25a), it reads:

$$\frac{dh_i}{dt} = \sum_{k=1}^{K} \frac{a_{ki}\sqrt{2g}\sqrt{h_k \phi_{ki}}}{A_i} - \sum_{j=1}^{J} \frac{a_{ij}\sqrt{2g}\sqrt{h_i \phi_{ij}}}{A_i} + \frac{Q_{L,i}}{A_i} \tag{25b}$$

Note that this equation can just as easily be written with Hagen-Poisuielle-type drag terms instead of the Bernoulli terms shown here. Unfortunately, the dynamic behaviour of a single tank does not capture the hydrodynamic behaviour of a packed bed (because there is only one way for the liquid to distribute in the tank). However, consider a system of *three open* tanks as illustrated in Figure 65. Tank 1 has two exits with cross-sectional areas a_{12} leading to tank 2 and a_{13} leading to tank 3 and cylindrical geometry is assumed for both the tanks and the exits. Tanks 2 and 3 have one exit each, with areas of a_{2o} and a_{3o} respectively. The average pore exit area as determined from tomography is approximately 1.3×10^{-6} m^2 with a relative standard deviation of 0.88. We therefore set a_{13} and a_{3o} equal to the average pore exit area and choose a_{12} and a_{2o} to be one standard deviation smaller (i.e. 1.5×10^{-7} m^2). These values are therefore representative of the

packed bed (which is important because they greatly influence the hydrodynamic multiplicity behaviour). The values of the other parameters are given in Table 16 and they have been chosen to represent the system investigated in Chapter 6.

Equation 25b is now written for each tank (with ϕ_{ij} substituted from equation 27), resulting in three ordinary first order non-linear differential equations. Given appropriate initial conditions, the height of liquid in each tank is readily solved for by employing a numerical integration technique.

Table 16. Values of variables used in flow simulation

Variable	**Value(s) used**	**Variable**	**Value(s) used**
A_1, A_2, A_3	5×10^{-6} m^2	ρ	1000 kg/m^3
μ_G	1×10^{-5} m/s^2	P_o	0
θ'_{rec}	95^o (θ_{rec} = 5^o)	σ	0.07 N/m
h_T	0.14 m	$Q_{G,1}$	1×10^{-5} m^3/s (low flow) 13.5×10^{-5} m^3/s (high flow)
a_{small} a_{large}	1.5×10^{-7} m^2 1.3×10^{-6} m^2	$Q_{L,1}$	1×10^{-6} m^3/s (low flow) 2×10^{-6} m^3/s (high flow)
θ'_{crit}	160^o (θ_{adv} = 70^o)		

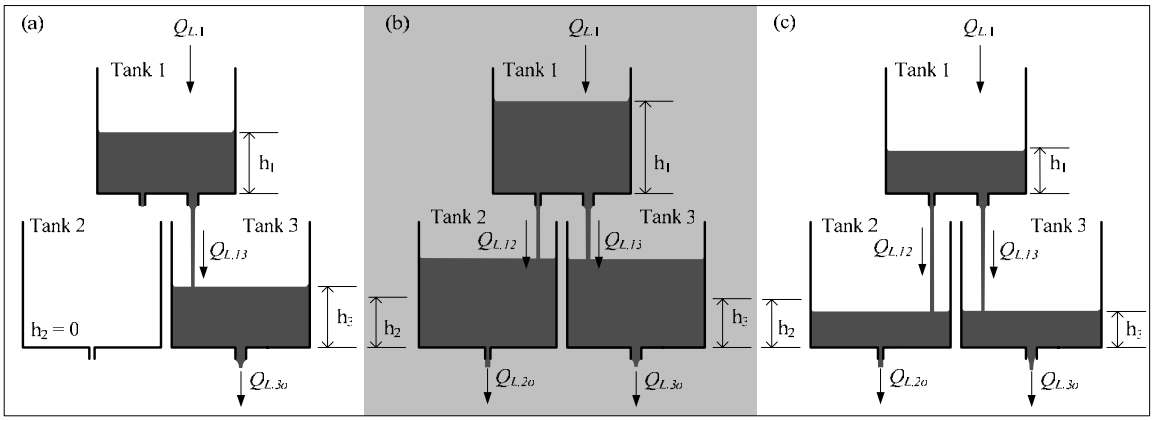

Figure 65. A system of three capillary tanks shows hysteresis akin to that of the packed bed. (a) Low flow condition – increasing leg (b) High flow rate condition (c) Low flow rate condition – decreasing leg.

Note that because the ϕ_{ij} parameter changes abruptly at different values of h_i, some numerical problems may be encountered when the usual solvers (e.g. Runge-Kutta) are used since these solvers do not expect such abrupt changes. Instead, it is recommended that an adaptive mesh be used for the temporal discretization, where smaller time steps are employed in the vicinity of detected ϕ_{ij} changes.

As an example of how a hydrodynamic multiplicity trend can be captured by this relatively simple model, a liquid flow rate variation induced hysteresis loop is executed – results shown in Figure 66. The initial h_i in each tank is specified as zero. The flow rate to Tank 1 is then increased to the low flow condition ($Q_{L,1}$=1×10^{-6} m^3/s) and steady state is established (point A). The flow is increased to the high flow condition ($Q_{L,1}$=3×10^{-6} m^3/s) and then decreased back to the low flow condition, and steady state is again established (point C). The numerical values of these flow rates were chosen for illustrative purposes because the actual flow rate through a pore is difficult to estimate.

Starting from time zero, when flow is introduced the level in Tank 1 rises. There is at this stage no flow through holes 12 or 13 to Tanks 2 or 3. When the height in Tank 1 (h_1) exceeds $h_{a,13}$ (the blue dashed line), hole 13 opens and liquid flows into Tank 3.

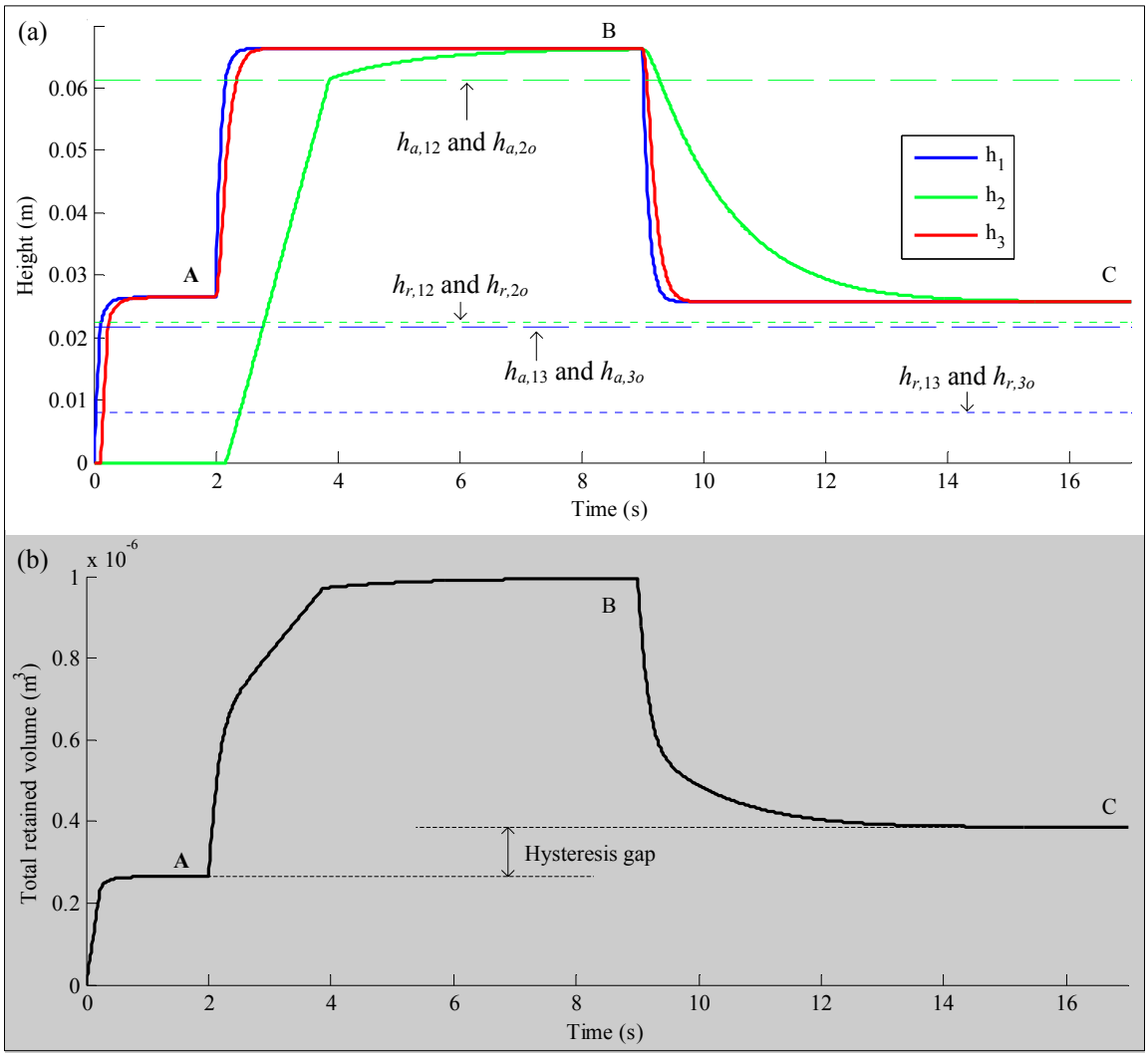

Figure 66. A liquid flow rate variation induced hysteresis loop for the model system. (a) Height in each tank. (b) Total retained volume. Point A corresponds to the illustration in Figure 65a, point B with Figure 65b and point C with Figure 65c. Note that the total retained volume (the analogue of holdup) is higher at point C than at point A.

As soon as h_3 exceeds the same value liquid starts draining from Tank 3 and steady state (point A) is reached within about 2 seconds. Note that h_1 does not exceed $h_{a,12}$ (the dashed green line) and so hole 12 does not open. Tank 2 remains dry. When the feed flow rate is increased, hole 12 does open (when $h_1 > h_{a,12}$) and shortly after (when $h_2 > h_{a,2o}$) so does hole 2*o*. When the flow rate is reduced again, all four holes remain open (because $h_1 > h_{r,12}$, $h_1 > h_{r,13}$, $h_2 > h_{r,2o}$ and $h_3 > h_{r,3o}$) and a different steady state is achieved (point C). Despite the fact that both h_1 and h_3 is smaller at C than they were at A (not apparent in

the figure), the additional volume retained in Tank 2 at point C causes the total retained volume to be higher at C than at A (Figure 66b). This is exactly what is seen in a liquid flow rate variation induced holdup hysteresis loop in trickle flow (when comparing the Kan-Liquid and Non-pre-wetted modes). Note that the fact that the three tank levels are equal at steady state is because holes 12 and 2*o* and holes 13 and 3*o* were assumed to be equal in size (this will not generally be the case). Before extracting the other hydrodynamic trends, it is prudent to incorporate the effects of gas flow first.

Effect of Capillarity on Gas Flow

The effect of capillarity in gas flow is handled similarly to that of liquid flow through the introduction of a correction factor (ψ_{ij}). However, some changes to the geometry of the three tanks first need to be made in order to properly evaluate the pressure drop (as shown in Figure 67). The tanks are closed off at a height of h_T and gas is fed at a flow rate of $Q_{G,1}$ to Tank 1. Some additional connections are made: Tank 1 is connected to Tank 2 and Tank 3 with holes of large diameter ($a_{G,12} = a_{G,13} = a_{L,13} = a_{L,3o} = 1.3 \times 10^{-6}$ m^2) and to the outside with a hole of small diameter ($a_{G,1o} = a_{L,12} = a_{L,2o} = 1.5 \times 10^{-7}$ m^2). Tanks 2 and 3 are connected with the outside with one large hole each ($a_{G,2o} = a_{G,3o} = 1.3 \times 10^{-6}$ m^2). Note that only two hole diameters are used, a large one equal to the average hole diameter as measured in Chapter 6 and one small one equal to the average diameter minus one standard deviation.

Recall that gas flow is to be treated as flow in a tube as governed by the viscous (Hagen-Poisuielle) drag term in equation 26. Neglecting the gas head, the flow rate of gas between two tanks are related to the difference in pressure as follows:

$$\Delta P = P_i - P_j = \frac{128\mu_G Q_{G,ij} l}{\pi d_t^4}, \text{ or}$$

$$Q_{G,ij} = \frac{(P_i - P)\pi d_t^4}{128\mu_G l} \approx \frac{(P_i - P)\pi d_t^3}{128\mu_G} \approx \frac{C(P_i - P)\pi(h_T - h_i)^3}{128\mu_G} \quad \text{no capillarity} \tag{28a}$$

$$Q_{G,ij} = \frac{C(P_i - P)\pi(h_T - h_i)^3 \psi_{ij}}{128\mu_G} \quad \text{with capillarity} \tag{28b}$$

Here, the characteristic length and tube diameters are both assumed to be the hydraulic diameter of the space above the liquid in the tank (C is a constant that depends on the value of A_i only – it is roughly equal to 5×10^{-8} for present conditions). Note that the gas capillary correction factor (ψ_{ij}) has been incorporated in equation 28b. It is there because for pre-wetted beds the gas exits will be clogged with liquid and a capillary threshold ($P_{crit,ij}$) will need to be crossed before gas flow can commence through the hole. Once the hole is open however, there is no capillary back-pressure and the hole never closes again. This means that unlike ϕ_{ij}, ψ_{ij} will be *either* 1 or 0. This corresponds to the "liquid-bridged" condition of Melli & Scriven (1991).

A small change to the liquid momentum relation (equation 23b) is also necessary once a pressure drop exists between the tanks. Note that the gas pressure in each tank adds an additional head to the liquid and should be included in the flow relations, i.e.:

$$Q_{L,ij} = a_{ij}\sqrt{\phi_{ij}\left[2gh_i + \frac{2(P_i - P_j)}{\rho_L}\right]} \tag{29}$$

For each tank, a mass balance is derived assuming incompressible flow and the momentum relations (equations 28b and 29) are substituted. The generic equations of the final model are:

Liquid :

$$\frac{dh_i}{dt} = \sum_{k=1}^{K} \frac{a_{L,ki}}{A_i} \sqrt{\phi_{ki}\left[2gh_k + \frac{2\left(P_k - P_i\right)}{\rho_L}\right]} - \sum_{j=1}^{J} \frac{a_{L,ij}}{A_i} \sqrt{\phi_{ij}\left[2gh_i + \frac{2\left(P_i - P_j\right)}{\rho_L}\right]} + \frac{Q_{L,i}}{A_i} \tag{30}$$

Gas :

$$-\frac{dh_i}{dt} = \sum_{k=1}^{K} \frac{C\pi\left(P_k - P_i\right)\left(h_T - h_k\right)^3 \psi_{ki}}{128\mu_G A_i} - \sum_{j=1}^{J} \frac{C\pi\left(P_i - P_j\right)\left(h_T - h_i\right)^3 \psi_{ij}}{128\mu_G A_i} + \frac{Q_{G,i}}{A_i} \tag{31}$$

Capillary Correction :

$$P_{crit,ij} = \frac{-2\sigma\sqrt{\pi}\cos\theta'_{crit}}{\sqrt{a_{L,ij}}}$$

$$P_{rec,ij} = \frac{-2\sigma\sqrt{\pi}\cos\theta'_{rec}}{\sqrt{a_{L,ij}}}$$

$$\phi_{ij}\left(t_{now}\right) = \begin{cases} 0 \text{ if } \left[\rho_L g h_i + \left(P_i - P_j\right)\right] < P_{rec,ij} \\ \dfrac{\left[\rho_L g h_i + \left(P_i - P_j\right)\right] - P_{rec,ij}}{P_{crit,ij} - P_{rec,ij}} \text{ if } P_{rec,ij} < \left[\rho_L g h_i + \left(P_i - P_j\right)\right] < P_{crit,ij} \text{ and } \dfrac{dh_i}{dt} < 0 \\ 0 \text{ if } P_{rec,ij} < \left[\rho_L g h_i + \left(P_i - P_j\right)\right] < P_{crit,ij} \text{ and } \dfrac{dh_i}{dt} > 0 \\ 1 \text{ if } \left[\rho_L g h_i + \left(P_i - P_j\right)\right] > P_{crit,ij} \end{cases} \tag{32}$$

$$\psi_{ij}\left(t_{now}\right) = \begin{cases} 0 \text{ if } \left(P_i - P_j\right) < \dfrac{-2\sigma\sqrt{\pi}\cos\theta'_{crit}}{\sqrt{a_{G,ij}}} \text{ and } \psi_{ij}\left(t < t_{now}\right) \neq 1 \\ 1 \text{ if } \left(P_i - P_j\right) \geq \dfrac{-2\sigma\sqrt{\pi}\cos\theta'_{crit}}{\sqrt{a_{G,ij}}} \text{ or } \psi_{ij}\left(t < t_{now}\right) = 1 \end{cases}$$

Model parameters are reported in Table 16. From these 6 equations it is possible to solve for the three tank heights (h_1, h_2 and h_3) and the three pressures (P_1, P_2 and P_3). The system's liquid saturation and system pressure drop can be calculated from these values. It is possible to specify various flow histories (to yield hysteresis loops) or initial conditions (to yield different pre-wetting modes). This model also captures the well known hydrodynamic trends that are not multiplicity related – namely that pressure drop

increases with both liquid and gas velocity, while holdup increases with liquid velocity but decreases with gas velocity.

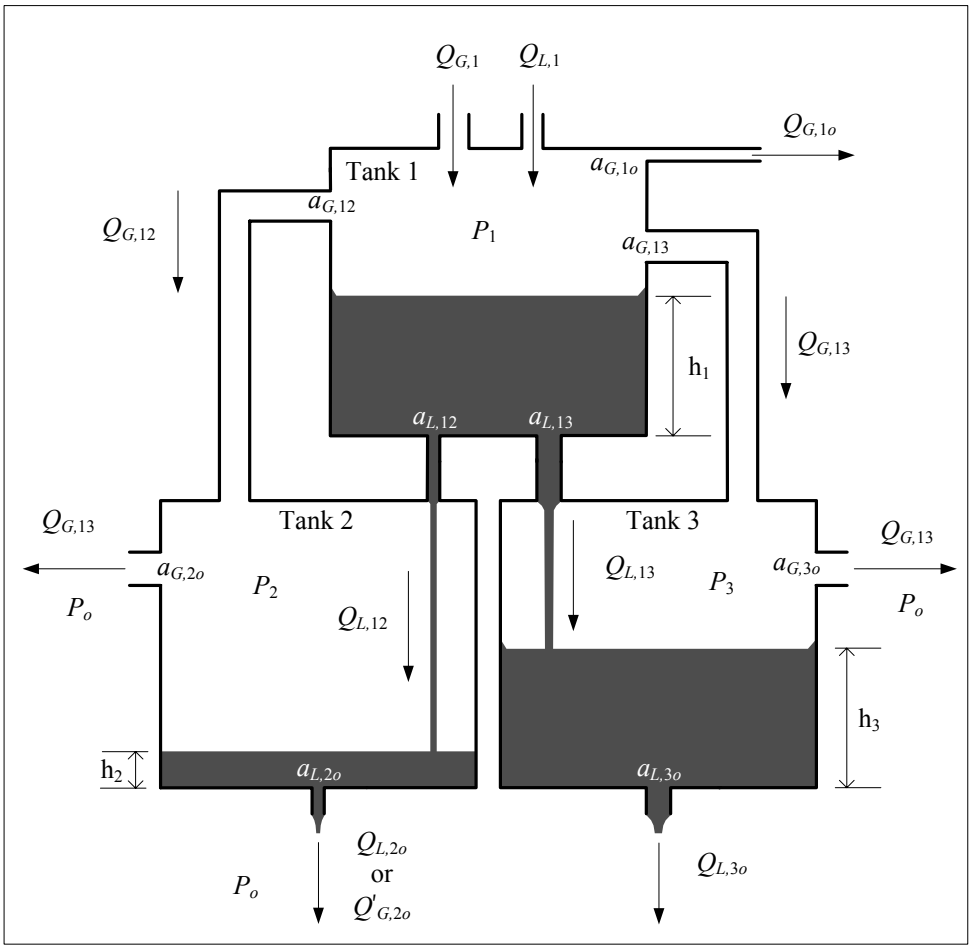

Figure 67. The proposed hydrodynamic model for gas and liquid flow.

7.3.2 Model Performance and Characteristics

The efficacy of the proposed model to qualitatively represent the hydrodynamic multiplicity trends is illustrated by instigating the following experimental plan on the model. Notice that this plan closely represents the actual experimental plan that was adopted to generate the data in earlier chapters according to the conceptual framework identified in Chapter 2. Model performance is illustrated in Figure 68 along with the calculated saturation and pressure drop values.

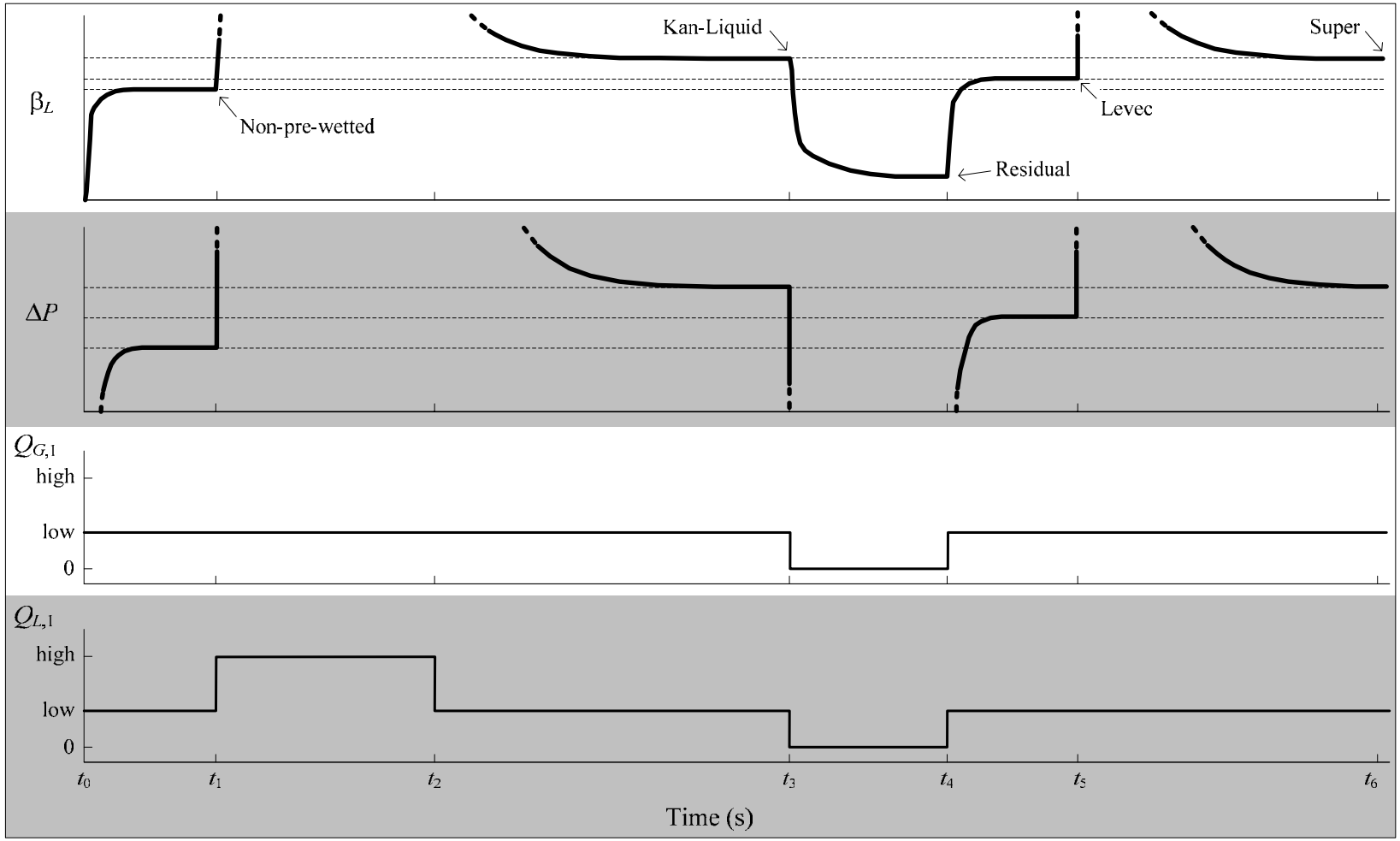

Figure 68. Model performance: dynamic evolution of saturation and pressure drop with liquid flow rate changes

(i) The initial values for all three tank heights are set to zero (i.e. zero saturation). The initial pressures in all three tanks are set to zero (t_0).

(ii) Gas and liquid flow is introduced at the *low* velocities and the simulation continues until steady state has been achieved. This corresponds to the Non-pre-wetted mode (t_1).

(iii) The liquid flow rate is increased to *high* while keeping the gas flow rate at *low* and steady state is achieved (t_2).

(iv) The liquid flow rate is reduced to *low* (gas flow rate still at *low*) and steady state is achieved. This corresponds to the Kan-Liquid mode (t_3).

(v) The liquid and gas flow rates are reduced to zero and the system drains under gravity – this yields the residual holdup (t_4).

(vi) The flow rates are increased back to the *low* value and steady state is achieved. This corresponds to the Levec mode (t_5).

(vii) The simulation is now restarted with flow rates set at *low*, but with the important difference of specifying the initial tank heights equal to 90% of their maximum values (i.e. $\beta_L = 0.9$). Draining now continues under irrigation until steady state is established, i.e. the Super mode (t_6).

The model performance closely resembles the actual experiment both in holdup and in pressure drop (refer back to Figure 34a). When liquid flow is initiated at t_0, the capillary threshold for flow through liquid hole 13 ($P_{crit,13}$) is quickly reached and steady state is established without liquid hole 12 being opened. When the liquid flow rate is increased to the *high* value at t_1, $P_{crit,12}$ is exceeded and liquid flows through both hole 12 and 13. When the flow rate is reduced back to low, the total pressure head is below $P_{crit,12}$ but above $P_{rec,ij}$, and both holes remain open. The new steady state is the Kan-Liquid mode and the total retained volume (saturation) is higher. Next, gas and liquid flow is shut off (at t_3) and the tanks drain. However, the holes close for flow when $P_{rec,ij}$ is reached and a height of liquid is retained at zero flow. This is the residual holdup. When flow is re-started at t_4, holes 13 and 3*o* soon open for flow but the pressure head in Tank 1 remains

below $P_{crit,12}$ and Tank 2 therefore does not receive any flow. The combined saturation of all three tanks is higher than the Non-pre-wetted mode but lower than the Kan-Liquid mode. This is the Levec mode. Lastly, when the saturation in each tank is set at a high value and drained under irrigation, both hole 12 and 13 are open and remain open because the steady state heights exceed $P_{rec,12}$. This is the Super mode. Note that flooding and draining under irrigation has exactly the same effect as increasing and decreasing the tank heights by increasing and decreasing the flow rate. This explains why the Kan-Liquid and Super modes yielded such similar results in Chapters 4, 5 and 6. Note also that most previous hydrodynamic models failed to converge to the residual holdup in the limit of zero liquid velocity. This is because these models do not take adequate account of the capillary effect. Figure 68 also illustrates the dynamics of establishing the different modes. The Levec mode reaches steady-state very quickly while the Kan-Liquid modes takes much longer (in the simulation above the Kan-Liquid mode took approximately 5 times as long as the Levec mode to reach steady state). Compare this with the results of Figure 34b. De-saturation (Kan-Liquid) takes longer than saturation (Levec) because the liquid leaves the tanks at slower rates than it enters the tank (before steady state is established).

A further illustration of the efficacy of the model is shown in Figure 69, where the liquid distribution in the three tanks is shown along with the discharge rates of Tanks 2 and 3. Note that the liquid distribution is bi-modal in the Levec mode (Tanks 1 and 3 have high holdup and Tank 2 has a low holdup) and uni-modal in the Kan-Liquid mode (all three tanks have the same holdup). Note that the idea of rivulet and film flow is also represented. A rivulet is a series of connected tanks (pores) with high holdup together with tanks (pores) with very low holdup (as seen in the Levec mode). Film flow corresponds to the fact that all tanks (pores) in the Kan-Liquid mode have a (lower) uniform holdup. These observations agree with those in the previous chapter and also with the similar investigations of Lutran et al. (1991) and Sederman & Gladden (2001). Cross-sectional holdup maldistribution is another manifestation of this effect.

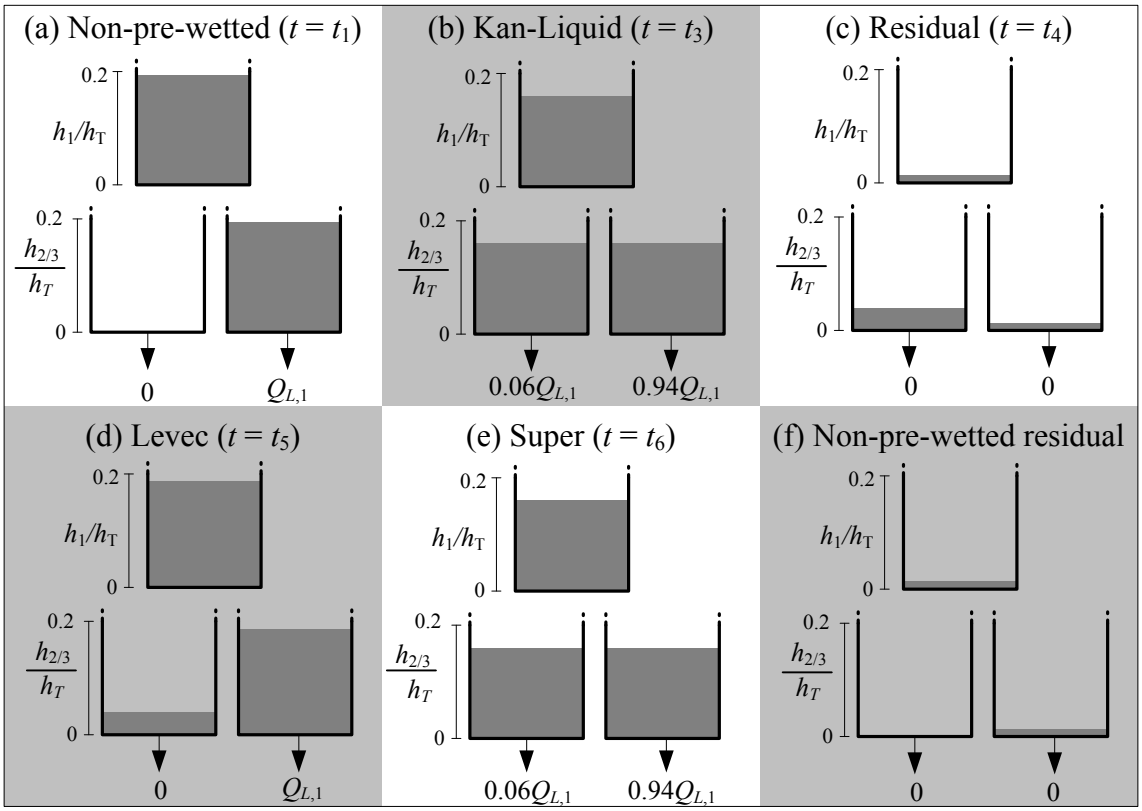

Figure 69. Liquid distribution by tank for the simulation shown in Figure 68.

The model also captures the liquid exit flux distribution differences between the modes, namely that the liquid exits more uniformly in the case of the Kan-liquid mode than in the Levec or Non-pre-wetted modes. This agrees qualitatively with the data of Ravindra et al. (1997b).

Note that this evaluation is not restricted to the limiting cases. In general, any incremental increase in liquid velocity will increase holdup and more and more holes will open for flow. This is the mechanism by which new rivulets are created.

As an interesting aside, the residual liquid distribution is shown in Figure 69c. Note that there is a lot of liquid in Tank 2 and very little in Tanks 1 and 3. The heights correspond to the capillary head for the exit. In an early study (Van der Merwe et. al., 2004), we showed by photography that the residual holdup is held in mainly two forms: small volume pendular rings (Tanks 1 and 3), and large volume "globules" at locations where

the local porosity is low (i.e. small pores, Tank 2). It is satisfying that the present model also captures these observations qualitatively. Secondly, note that when the liquid and gas flow is interrupted after operation in the Non-pre-wetted mode, the residual holdup will be much smaller and distributed as shown in Figure 69f. The fraction of residual holdup after the Non-pre-wetted mode to the residual holdup after flooding gives one a qualitative indication of the number of active pores. Similarly, the residual holdup in Tank 2 is not contacted by liquid in the Levec mode. In the Kan-Liquid and Super modes all the residual holdup is contacted. In a preliminary study (Van der Merwe & Nicol, 2005), we measured these "active residual" holdup fractions at different flow rates and found the same qualitative trends as exhibited by the present model. The fact that gates close at very low velocity was also seen in the fact that the volumetric utilization coefficient was below 1 in the Super mode only at very low velocities (< 2 mm/s) and increased with increasing liquid velocity.

It is equally important for the same capillary mechanism to represent the effect of changes in gas flow rate on the system. A major question that has not been addressed is the fact that a gas velocity variation induced hysteresis loop causes a Kan-Liquid mode to have a higher holdup but lower pressure drop, while it causes the Levec mode to have both higher holdup and higher pressure drop. The results of applying such gas flow rate changes to the model are shown in Figure 70. Consider that for pre-wetted beds before gas flow is introduced, the holes marked $a_{G,13}$, $a_{G,12}$, and $a_{G,1o}$ are all likely to be filled with liquid and are therefore closed by capillary action. When gas flow is turned on, the pressure in Tank 1 will rise until it exceeds the capillary threshold $P_{crit,13}$ at which point hole 13 will open and the liquid will be discharged. The hole then remains open since the liquid does not re-establish itself. Now, the same reasoning applies to the other large gas-carrying holes and these all open as well ($\psi_{12} = \psi_{12} = \psi_{2o} = \psi_{3o} = 1$). However smaller holes will only open when the pressure exceeds their capillary counter-pressures (that are higher than those of the large holes).

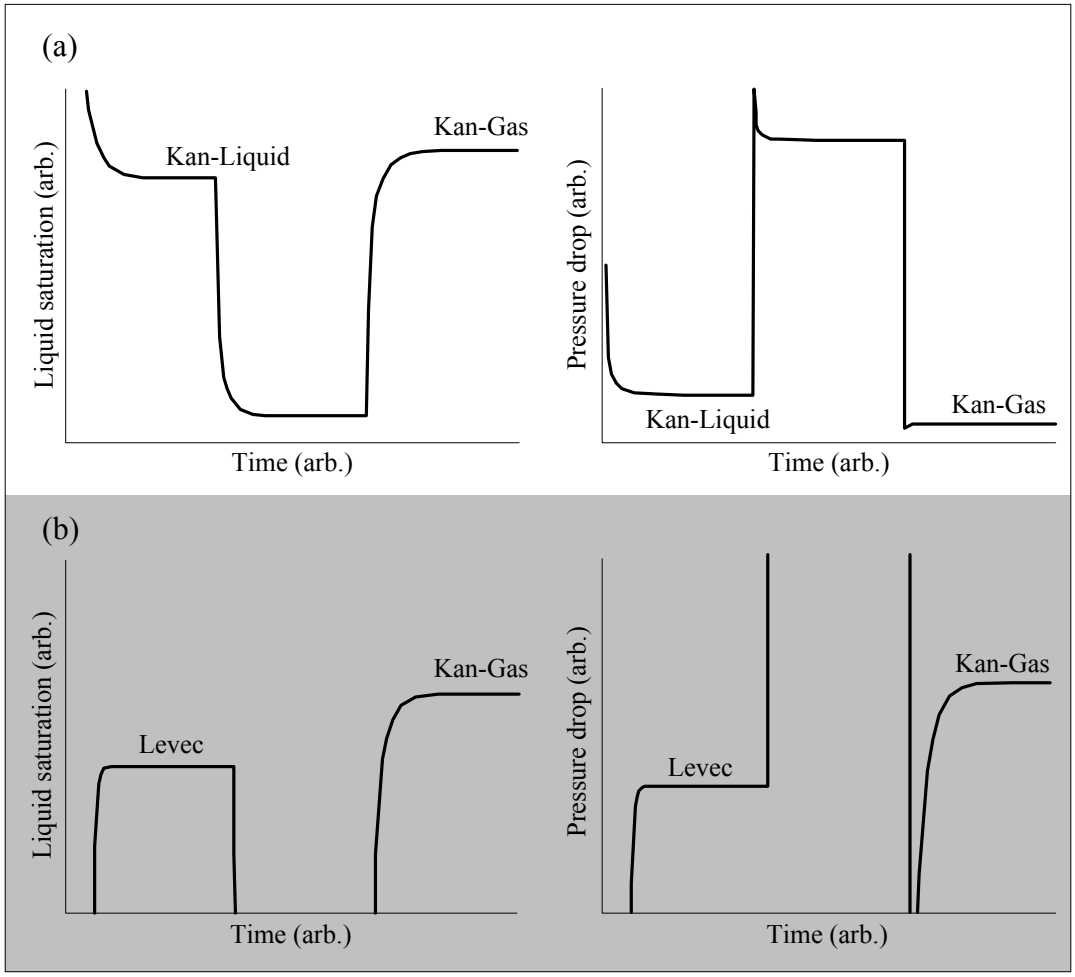

Figure 70. Gas flow rate variation induced hysteresis starting from the (a) Kan-Liquid mode and (b) Levec mode.

It was found that only one smaller hole (gas hole 1*o*) needed to be included in the model to account for gas flow rate variation induced hysteresis. Starting from the Kan-Liquid mode, the large gas holes are open for flow, but the small one is not. When gas flow is increased, a stage is reached where the pressure in Tank 1 exceeds the critical value for hole 1*o* to open for gas flow. When the gas flow is reduced, the hole remains open. At the original gas velocity, the gas now has an additional escape route and the pressure in Tank 1 is lower (total pressure drop is lower). Consequently, the pressure head on the liquid is also smaller resulting in higher saturations (higher holdup). The limiting case of this effect is the Kan-Gas mode. This corresponds closely to the original postulate of Kan &

Greenfield (1979) who suggested that the high gas velocity results in the creation of additional gas pathways (and a consequent decrease in the average gas tortuosity). Off course, the increased gas velocity has a second effect, namely that it results in higher pressure drops that add to the pressure head above the liquid exits. In the Levec mode hole $a_{L,12}$ was closed. A high gas velocity can cause the total pressure head (liquid head plus pressure difference between Tanks 1 and 2) to exceed the capillary threshold ($P_{crit,12}$) even though the liquid head has decreased. Hole 12 will open for liquid flow and remain open even as the gas velocity is decreased back to the original value (provided that the total pressure head exceeds $P_{rec,12}$). The result is that both liquid saturation and pressure drop is higher than before. The existence of different sized gas holes along with the capillary mechanism therefore sufficiently accounts for gas flow rate variation induced hysteresis.

The illustrations above have primarily addressed trends **(A), (B), (C), (F)**, **(G)**, **(I), (Q)** and **(S)**. However, the capillary gate model also provides rationalizations for the other trends as follows (they are not illustrated or discussed in as much detail for the sake of brevity):

- **(D)** Larger particles do not exhibit as much hysteresis because their pore exits are larger in size (despite the fact that porosity is the same) and therefore have lower capillary thresholds that are more easily crossed.
- **(E)** Wetting efficiency is lower in the Levec mode because the liquid is maldistributed.
- **(H)** The gas-liquid area follows the liquid holdup trends.
- **(J)** Small flow rate changes have little effect after the first cycle because the first cycle opens those holes that are near $P_{crit,ij}$. They do not close in the low flow condition because the total pressure head was near $P_{crit,ij}$ (i.e. higher than $P_{rec,ij}$).
- **(K)** Decreasing the surface tension lowers the pulsing boundary because the critical capillary threshold decreases – making it easier to cross.

(L) A temporary decrease in surface tension does not affect the Kan-Liquid mode because all the holes are already open for flow. It does however open up holes in the Levec mode that do not close again (because the total pressure head exceeds $P_{rec,ij}$ but not $P_{crit,ij}$).

(M) Porous particles show less hysteresis because the difference between receding and advancing contact angles are smaller.

(N) The pulsing boundary is associated with the extent of hysteresis because reaching the pulsing boundary at lower velocity means that it is easier to cross all the capillary thresholds (and hysteresis is therefore diminished).

(O) The pressure drop increases drastically with increasing gas or liquid velocity in the Levec mode (at high pressure) because more and more pores participate in liquid flow as holes are opened with increasing velocity. At lower pressures, the lower pressure drop means that holes are not as easily opened and the efect is smaller. In the Kan-Liquid mode, all the holes are already open and the effect of more participating pores is absent.

(P) At high pressures the pressure drop is high (it scales with the density of the gas) and it is easier to cross the capillary thresholds. This is especially true at high u_L, where the high holdup causes high pressure drop. The result is that the holes open at lower velocity and therefore a lower extent of multiplicity is observed at a given velocity. Note that both the experiments in Chapter 4 and the model indicates that pressure drop determines the extent of hydrodynamic multiplicity.

(R) The small saturation changes in the Levec mode are pores that are close to one of the capillary thresholds (P_{crit} for saturation and P_{rec} for de-saturation). Any small disturbance may cause the threshold to be crossed. Note that the scale of these changes were approximately 1 particle diameter – i.e. approximately the size of a pore (see pore size distribution), and similar in shape to the pores identified in Chapter 6. The difference maps of Chapter 5 are therefore a direct visualization of the capillary mechanism in action (pore heights crossing the capillary thresholds).

(T) The fraction dry (bar residual holdup) pores in the Levec mode decreases with both u_L and u_G because both these increase the total pressure head (u_G increases the pressure drop more than it decreases the holdup), which opens more holes.

7.3.3 Detractions, Limitations, Validations and Extensions

This model is intended as an example of how the capillary mechanism leads to the observed behaviour and not as a quantitative tool. The major limitation of the model therefore is its qualitative nature. The central idea here is that liquid distribution is governed by the requirement that a capillary threshold need to be crossed before liquid can flow from pore to pore and that this threshold exhibits hysteresis itself. It is not difficult to see that this idea can be incorporated into larger pore networks and most of the existing hydrodynamic models. For example, the slit model can be extended to a network-of-slits model where each pore is then represented as a slit. Liquid and gas access to slits can then be governed by the capillary mechanism. Similarly, Jiang et al. (1999) already proposed that capillary pressure be incorporated into a CFD or DCM type description. However, there is ample indication in this work that the fundamental unit of a trickle bed (by which the mass and momentum conservation equations are to be derived) is the pore (and not a homogeneous cell). In this regard, it is necessary to emphasize that hydrodynamic multiplicity through the proposed mechanism arises only because there are dissimilarities between the pores. More specifically, the pore exits vary in size. The tomographical analysis of Chapter 6 allows us to determine that this is indeed the case (Figure 71a).

Note also that the model assumes that all exits are either gas- or liquid-filled – there are no two-phase flow through any of the exits. This simplification is supported by the actual measured pore exit filling fractions shown in Figure 71b. It shows two clear peaks at 0 (gas-filled) and 1 (liquid-filled), although some two-phase flow also occur.

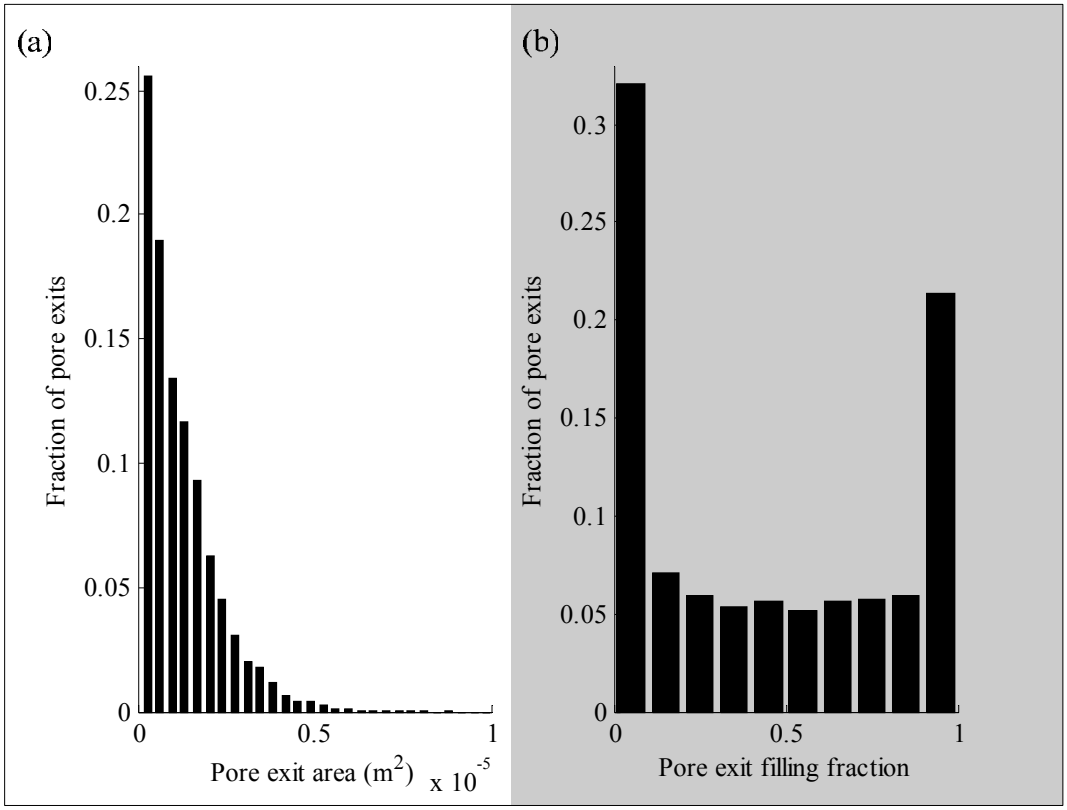

Figure 71. Pore exit statistics. (a) Pore exit area distribution (b) Pore exit filling fraction (Levec mode at u_L = 5.3 mm/s, u_G = 4.7 cm/s – other conditions look similar).

A further limitation of this study is that the dispersion characteristics of the model and the trickle bed have not been compared. Also, the interfacial areas cannot be calculated directly from the model. A possible exception may be wetting efficiency. Note that in adopting the cylindrical tank geometry, it was implicitly assumed that wetting efficiency is directly proportional to holdup (saturation). To see this, note that the wetting efficiency of the three tanks increases linearly with tank height. Again, the tomographical analysis can be used to support this approach (Figure 72).

A final observation regarding the validity of the assumed operating variable values in Table 16 is necessary. The volumetric flow rates and total tank height were chosen to illustrate the trends that can be extracted from the model, and not to represent the individual pores. The height is particularly large and physically unrealistic.

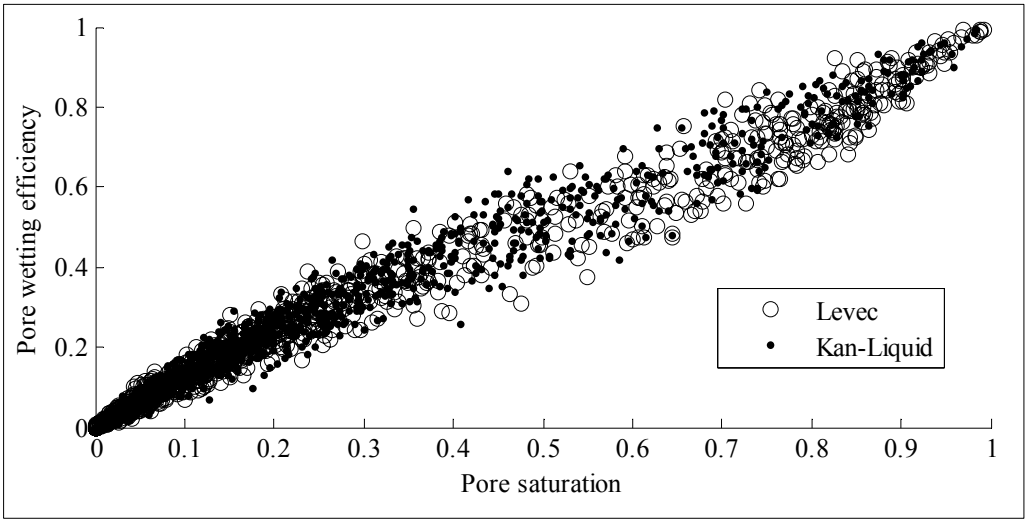

Figure 72. Pore wetting efficiency as a function of pore holdup from tomography. Note the nearly linear relationship (u_L = 2.7 mm/s, u_G = 4.7 cm/s). Other conditions show similar behaviour.

Of course, the total height necessary to illustrate the model performance is a function of the total pore exit area. For the real geometry, the pore coordination numbers are larger (mean of 11), which means that the liquid heights will all be much smaller. However, in the model a coordination number of 2 is chosen in order to keep it simple. Note also that, in reality, the capillary back-pressure at the pore exits is a function of the length of the gas-liquid-solid contact line, which is likely to be longer than the circumference of the hole (because of the geometry of the liquid held in the neck). This too will reduce the tank heights to more realistic values. These effects are severely complicated and are considered beyond the present scope.

In conclusion, the model has been developed based on the existing data in literature and the new experimental insights in Chapters 2, 4, 5 and 6. The model agrees qualitatively with all the observed trends and shows the potential to be incorporated into larger pore network models or alternative approaches like CFD or phenomenological models.

7.4 Conclusion

This chapter introduced a pore-scale capillary mechanism based on the original suggestion that contact angle hysteresis is the controlling phenomenon (Levec et al., 1986). The mechanism dictates which pores receive flow. When properly incorporated into a hydrodynamic model, it accounts for the observed hydrodynamic behaviour. Table 17 summarises the model's ability to qualitatively represent the experimentally observed hydrodynamic multiplicity trends.

Table 17. Comparison between observed multiplicity trends and model capability

Trend number	Description	Model able to represent this trend?
(A)	New rivulets are created as u_L increases, rivulet vs. film flow patterns	Yes
(B)	Liquid flow rate variation induced hysteresis in each mode	Yes
(C)	Gas flow rate variation induced hysteresis (particularly the opposite effect on Levec and Kan-Liquid/Super modes)	Yes
(D)	Lower extent of multiplicity for larger particles	Yes
(E)	Lower wetting in Levec mode, bi-modal distribution	Yes
(F)	Holdup increases in the order Non-pre-wetted, Levec, Kan-Liquid/Super, Kan-Gas	Yes
(G)	Pressure drop increases in the order Non-pre-wetted/Levec, Kan-Gas, Kan-Liquid/Super	Yes
(H)	Gas-liquid mass transfer coefficient hysteresis	Yes
(I)	Similarity between Kan-Liquid and Super modes	Yes
(J)	Small flow rate changes have no effect after the first cycle	Yes
(K)	Lower surface tension lowers the extent of multiplicity	Yes
(L)	Surface tension variation induced hysteresis	Yes
(M)	Porous	Yes
(N)	Boundary	Yes
(O)	Differences in functional pressure drop vs. u_L behaviour in different modes at high P	Yes
(P)	Pressure drop determines extent of multiplicity	Yes
(Q)	Kan-Liquid takes longer to reach steady state than Levec	Yes
(R)	Pore-scale low frequency instability in Levec mode	Yes
(S)	Holdup distribution by pore different in different modes	Yes
(T)	Fraction of dry pores behaviour vs. u_L and u_G by mode	Yes

Note that although the detailed tomographic analysis of Chapter 6 contributes only two trends, the results of that investigation were used extensively in the identification,

development and validation of the proposed mechanism. The key feature is that the analysis provides high definition 3D images that allow *pore-scale* statistics to be calculated. The importance of modelling trickle flow multiplicity at the pore-scale is evident throughout the latter parts of this work.

In so far as hydrodynamic multiplicity modelling is concerned, it is recommended that future studies address the issue of quantitative prediction (possibly by incorporating the capillary mechanism into pore-network or discrete-cell models). Although this seems relatively straightforward, present attempts showed that the additional complexity in the pore-geometry, pore-connection structure and pore-scale flow patterns will introduce parameters that can only be correlated empirically (and will therefore require new insights or a larger experimental database). It is believed that the qualitative insights offered in this chapter will in future contribute to the development of a fully predictive hydrodynamic multiplicity model.

It is further recommended that the important issue of the impact of hydrodynamic multiplicity on trickle bed reactor performance should also be evaluated, experimentally and theoretically, by future investigators. The next chapter presents data and ideas that highlight the way forward in this regard.

Chapter 8. Impact of Multiplicity on Reactor Performance[5]

Previous chapters have focussed on generating hydrodynamic multiplicity data and on explaining the observed trends by means of a fundamental interpretation based on the pore-scale structure of the bed. This chapter now considers the implications that hydrodynamic multiplicity has on the performance of a trickle bed reactor. This chapter does not form part of the main strategic outline of this work, but is presented as interesting additional evidence of the importance of the multiplicity phenomenon.

8.1 Multiplicity in an Industrial Reactor

This section provides the first (published) evidence that hydrodynamic multiplicity is encountered in industry. Returning to Figure 4, note that the state can be changed from the Levec mode (point A) to a mode in-between Kan-Liquid and Levec (point E) by performing a liquid flow rate variation induced hysteresis loop. Also, getting back from E to A is achieved by shutting off the liquid flow rate, allowing the bed to drain and then re-introducing the liquid flow rate. In an industrial setting, pressure drop and gas and liquid flow rates are usually recorded. Examining this data for a period of 2 years (2004-2005) for a hydroprocessing trickle bed reactor at a large petrochemical plant in South Africa, it was found that it is common for the liquid flow rate to be increased and decreased incrementally over periods of days (all at approximately constant gas flow rate). It is equally common for the liquid flow rate to be shut-off (during a trip for example) and re-established. More specifically, we are looking for the following

[5] The work reported in this section was completed at the Chemical Reaction Engineering Laboratory (CREL) at Washington University in St Louis, USA. It has been accepted for publication in AIChE Journal (2007) and the second section is written in paper format.

sequence of events: the flow rate was increased up to $u_{L,max}$, then decreased down to $u_{L,1}$, then interrupted (u_L = 0) and then re-established at $u_{L,1}$. This is shown schematically in Figure 73a. The corresponding hysteresis loop is shown in Figure 73b. Note that hysteresis is present when $\Delta P_A < \Delta P_B$, and that ΔP_A is the pressure drop in the Levec mode but ΔP_B is not necessarily the pressure drop in the Kan-Liquid mode (since $u_{L,max} < u_{L,pulse}$). Figure 74 is the actual industrial data for cases that correspond to Figure 73a (experimental conditions are listed in Table 18). Note that the bed was not re-packed during this period and that there was no appreciable fouling that could account for the observed trends.

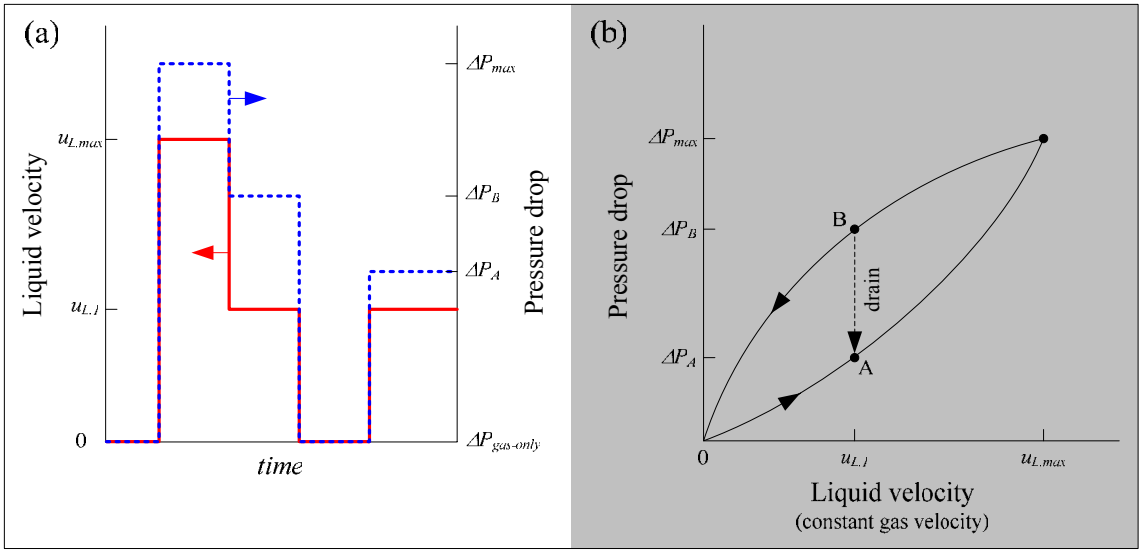

Figure 73. Schematics of the method of investigating hysteresis in an industrial reactor. (a) Liquid velocity (red) and pressure drop (blue) against time for the cases of interest, (b) The equivalent pressure drop hysteresis loop.

This figure establishes that pressure drop hydrodynamic multiplicity occurs in an industrial hydroprocessing reactor. Unfortunately, other information (for example conversion/selectivity) that can be used to establish the effect that multiplicity has on the reactor performance is not available. In fact, Figure 74 provides a motivation for investigating both the nature of hydrodynamic multiplicity and its potential impact on reactor performance.

Table 18. Experimental conditions in industrial reactor

Liquid	Petrochemical
Gas	Hydrogen
Liquid density	620 kg/m^3
Surface tension	0.015 kg/s^2
Particle size	3 mm extrudate
Column diameter	1.8 m
Bed length	7.8 m
Pressure	4 MPa (gauge)
Temperature	571 K

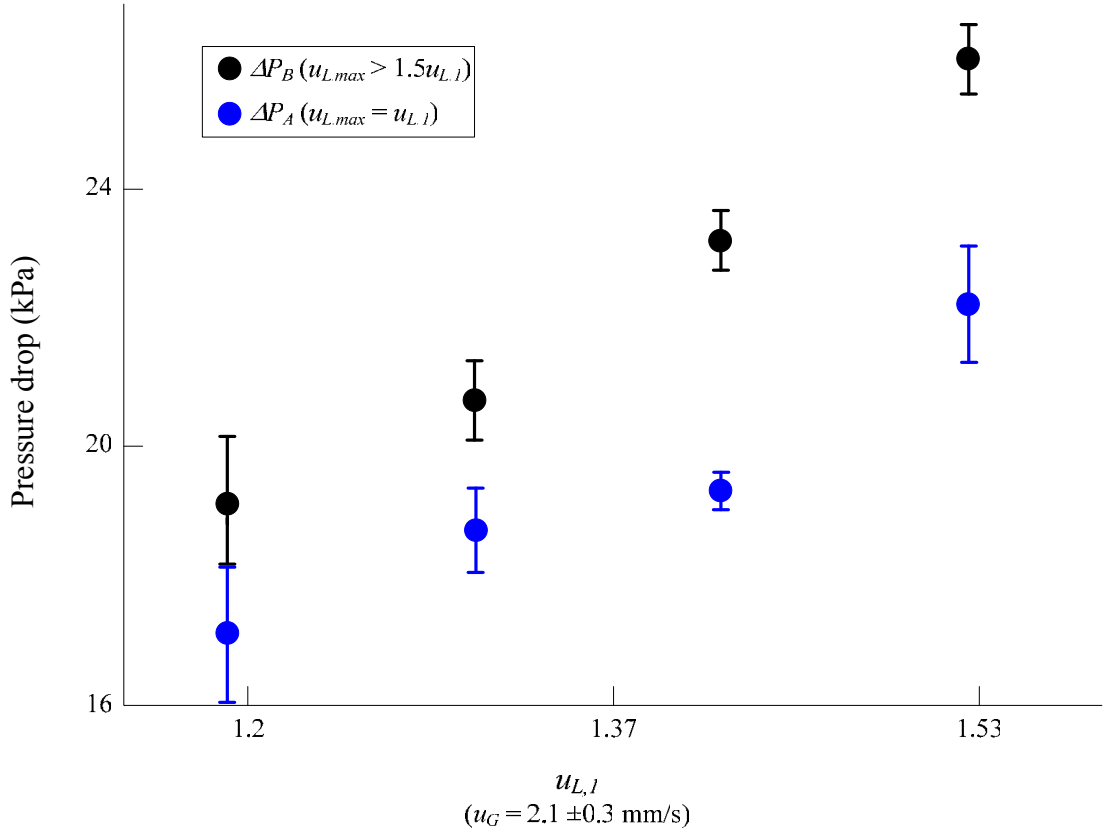

Figure 74. Pressure drop hysteresis in an industrial reactor. Error bars indicate relative standard deviations of the pressure drop signal over a period of approximately 2 days. The difference between the upper and lower legs is 8-20%.

8.2 Expectations of Impact on Reactor Performance

On the basis of the observed behaviour (Chapters 2 and 4 to 6), the expected impact on the reactor performance can be formulated. There are (in general) three reagent phases (solid, gas and liquid) of which the solid is fixed and in the form of porous catalyst particles. Consider therefore, the rate processes of the gas and liquid phase reagents and the impact that hydrodynamic multiplicity has on each. If mass transfer is treated by applying the boundary layer concept, the concentration profiles of the reagents can be sketched qualitatively as shown in Figure 75 (adapted from Mills & Dudukovic, 1980), where the liquid phase reagent has been assumed to be non-volatile (as will be the case in the next section). Note that for illustrative purposes these figures are drawn assuming that both gas and liquid phase reagents are limiting the overall reaction rate. Gas phase reagents undergo the following rate processes (as numbered in Figure 75):

1) Gas-side gas-liquid mass transfer
2) Liquid-side gas-liquid mass transfer
3) Liquid-solid mass transfer
4) Internal diffusion
5) Reaction
6) Gas-solid mass transfer (directly to the dry surface)

Non-volatile liquids are subject to the following steps:

1) Liquid-solid mass transfer
2) Internal diffusion
3) Reaction

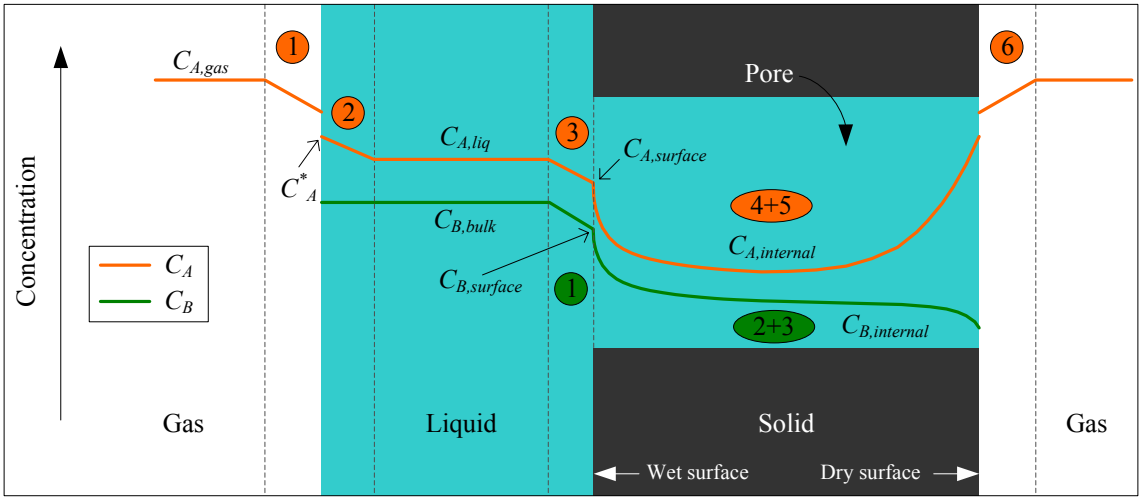

Figure 75. Concentration profiles and rate processes for gas phase reagents and non-volatile liquid phase reagents (based on Mills & Dudukovic, 1980).

If the overall rate is limited by the *chemical reaction kinetics (steps 5 and 3 for gas and liquid respectively)*, the sole effect of hydrodynamic multiplicity is that the liquid is maldistributed in some modes (Levec) but not in others (Kan-Liquid/Super). This means that a fraction of the bed may not be contacted (renewed) at all by the liquid phase reagent and that there will be no reaction in these particles. We have recently shown how such a fraction will influence the overall effectiveness factor (Van Houwelingen et al., 2007), and will not delve into the detail here. If the overall rate is inhibited by *internal mass transfer (steps 4 and 2 for gas and liquid respectively)*, the hydrodynamic multiplicity impacts the overall performance by changing the wetting efficiency (since wetting efficiency directly impacts the boundary condition at the particle surface). If it is also liquid limited, higher wetting efficiency leads to higher particle effectiveness factors according to the model proposed by Dudukovic (1977), and it is therefore concluded that the Kan-Liquid mode would outperform the Levec mode for such a case. If instead, it is gas limited, the additional dry areas in the Levec mode would facilitate the gas supply to the interior of the catalyst (step 6 in the figure) and result in a comparatively higher particle effectiveness factor in the Levec mode. If the *external liquid-solid mass transfer step (steps 3 and 1)* is limiting (for either the gas or liquid limited conditions), the multiplicity impacts both the mass transfer area (wetting efficiency) and the value of the

mass transfer coefficient itself (though the average interstitial liquid velocity which is related to the holdup). The next section examines these effects in detail. If it is a gas limited reaction and the *external gas-liquid mass transfer (gas step 1)* is limiting the rate, one would expect the Kan-Liquid mode to outperform the Levec mode, since the former has a much higher volumetric gas-liquid mass transfer coefficient (see Chapter 4). Of course, this effect would be offset by increased gas supply through the dry surface *(step 6)* in the Levec mode (where the wetting is lower). Liquid limited reactions where volatile liquid phase reagents are present would likely also benefit from the lower wetting in the Levec mode, although there is of course less area for direct liquid-solid mass transfer. In the general case, it is necessary to consider all these steps for any reaction and it is informative to write the species balance for the liquid and gas phase reagents in the bulk liquid and solid at the phase interfaces:

$$-u_L \frac{dC_B}{dz} = k_{LS} a_{LS} \left(C_B - C_{B,surface} \right) \tag{33}$$

$$-u_L \frac{dC_A}{dz} = -k_{GL} a_{GL} \left(C_A^* - C_A \right) + k_{LS} a_{LS} \left(C_A - C_{A,surface} \right) \tag{34}$$

$$D_{A,eff} \left(\frac{\partial C_{A,internal}}{\partial r} \right)_{r=R} = \begin{cases} k_{LS} a_{LS} \left(C_A - C_{A,wet\ surface} \right) & \text{on wetted surface} \\ k_{GS} a_{GS} \left(C_A^* - C_{A,\ dry\ surface} \right) & \text{on dry surface} \end{cases} \tag{35}$$

$$D_{B,eff} \left(\frac{\partial C_{B,internal}}{\partial r} \right)_{r=R} = \begin{cases} k_{LS} a_{LS} \left(C_B - C_{B,wet\ surface} \right) & \text{on wetted surface} \\ 0 & \text{on dry surface} \end{cases} \tag{36}$$

The third and fourth equations are the boundary conditions for the solution of the internal concentration profile of each reagent and can in the symmetric case (e.g. fully wetted) be solved for a particle effectiveness factor. Different assumptions can be applied to simplify the calculation of such effectiveness factors. For liquid limited reactions, the

Dudukovic (1977) model alluded to previously was applied and it was shown that the maldistribution effect is the major impact of multiplicity (Van Houwelingen et al., 2007). For gas limited reactions, the catalyst is treated as separate zones (wet and dry, see for example Rajashekharam et al., 1998). However, it is in the mass transfer steps shown in the equations above that the effect of multiplicity is particularly obvious since the mass transfer coefficients (and areas) are directly impacted (although there are no mass transfer correlations that accommodate hydrodynamic multiplicity and we are therefore restricted to qualitative evaluations). The next section explores these effects experimentally and is intended as a proof-of-concept study. The concept explored here is how multiplicity impacts reactor performance and whether or not this effect can be used to make an appreciable impact on that performance.

8.3 Experimental Case Study: Alpha-Methyl Styrene Hydrogenation

8.3.1 Introduction

In this section, the impact of hydrodynamic multiplicity on trickle bed reactor performance is investigated experimentally and then rationalized in terms of the body of knowledge regarding multiplicity that has been built up in the previous chapters. The Kan-Liquid and Levec modes are compared as two extremes of hydrodynamic multiplicity in pre-wetted beds (since by now the importance of the pre-wetting step is well established). Also, indications are that the Super mode is comparable to the Kan-Liquid mode, while the effect of gas velocity changes is small compared to liquid velocity variation induced hysteresis (as shown in Chapters 4 and 6). The extent of variation in the hydrodynamic parameters between these two modes is large and is again summarized in Table 19 for the reader's convenience. These large differences are likely to greatly influence a trickle bed reactor's performance.

Table 19. Comparison between Levec and Kan-Liquid modes (approximate)

Parameter	Extent*		Reference	Conditions
Pressure drop	2 – 8		Loudon et al. (2006)	3 mm glass spheres, water, N_2 (ambient), u_L = 1-9 mm/s, u_G = 2-9 cm/s
Liquid holdup	1.4 – 1.7		Loudon et al. (2006)	As above
	1.6		Van Houwelingen et al. (2006)	2.5 mm alumina spheres, water, air (ambient), u_L = 1.6, 5.4 mm/s, u_G = 2, 15 cm/s
Wetting efficiency	1.16 – 1.28		Van Houwelingen et al. (2006)	As above
Gas-liquid mass transfer (volumetric)	1.1 – 2.4		Loudon et al. (2006)	As above
Liquid-solid mass transfer	No data		-	-
	Levec	**Kan-Liquid**		
Maldistribution (percentage completely dry particles)	5 – 13%	0%	Van Houwelingen et al. (2007)	2.5 mm alumina spheres, water, air (ambient), u_L = 1.6, 5.4 mm/s, u_G = 2, 15 cm/s

* Extent according to equation 1: Kan-Liquid value divided by Levec value

However, reaction studies generally do not take this effect into account (see for example Wu et al., 1996, and Rajashekharam et al., 1998) and there is no study that directly quantifies the impact of hydrodynamic multiplicity on reactor performance in pre-wetted beds. Several authors (Nemec & Levec, 2005, Bartelmus & Janecki, 2003, Nigam et al., 2002, Lakota et al., 2002) confined their hydrodynamic investigations to the Kan-Liquid mode of operation because this mode exhibits the highest pressure drop and therefore the highest degree of gas-liquid interaction. On this basis, it is assumed that a trickle bed reactor will always perform better in this mode. Hydrodynamic multiplicity has also been neglected in reaction studies due to other arguments, particularly that the impact of hysteresis will not be large because reactions are usually run at higher pressures

(increased gas-liquid interaction) with low surface tension liquids and porous particles (i.e. particles with high wettability). These issues were addressed in Chapter 4.

Recently, Van Houwelingen et al. (2007) showed that based on particle wetting efficiency distributions, the Kan-Liquid mode (higher wetting) is expected to outperform the Levec mode (lower wetting) for liquid limited reactions, especially in the case of little internal diffusional resistance (small adjusted Thiele moduli). This is due to liquid maldistribution that leads to the existence, in the Levec mode, of particles that are not contacted by the flowing liquid and therefore do not contribute to the reaction. Khadilkar et al. (1996) showed that an upflow (fully wetted) reactor outperforms a downflow (partially wetted) reactor for liquid limited conditions. This also leads one to expect the Kan-Liquid mode to outperform the Levec mode for liquid limited reactions. Khadilkar et al. (1996) also showed the downflow mode to be superior to the upflow mode for gas limited conditions and attributed this to the state of partial wetting that exists in the downflow mode. This leads one to expect the Levec mode to outperform the Kan-Liquid mode in this case. For severely gas limited reactions, Van Houwelingen et al. (2006) also expected the Levec mode to outperform the Kan-Liquid mode. This is because the lower wetting efficiency (more gas-solid area) in the Levec mode allows greater access for the gas phase to the particle interior through the gas-solid surface area (although it is also likely to be more prone to liquid diffusional limitations due to the presence of particles with very low wetting efficiencies, Beaudry et al., 1987).

Although a number of authors have speculated on the impact of multiple hydrodynamic states (MHS) on reactor performance, reaction studies that address this issue are rare in literature. A recent review of MHS investigations (Maiti et al., 2006) indicate that authors have generally concerned themselves only with qualifying the effect of hysteresis on pressure drop, holdup and wetting efficiency (mostly at low pressure using air and water as fluids). It is apparent that reaction data is necessary to:

- determine the extent of the impact that hydrodynamic multiplicity has on reactor performance, and

- provide quantitative knowledge on which a conceptual foundation for the understanding of the impact of multiplicity can be built (i.e. to verify or refute the expectations of reactor performance based on hydrodynamic concerns).

This section addresses these issues by comparing reaction data for the Levec and Kan-Liquid modes for the hydrogenation of α-methylstyrene (AMS) over porous Pd/alumina extrudate. This reaction is commonly used as a model reaction for pyrolysis gasoline hydrogenation (Nijhuis et al., 2003). Additionally, as discussed in section 8.1, hydrodynamic multiplicity is not expected to impact the performance when it is limited by the chemical reaction kinetics and AMS hydrogenation in a TBR is a mass-transfer limited reaction. Moreover, the reaction can be run as liquid- or gas-limited by changing the operating conditions (Khadilkar et al., 1996). At low AMS concentration and high pressure the reaction is limited by the rate of transfer of the liquid reagent (AMS) to the catalyst. Conversely, at high AMS concentration and low pressure, the reaction is limited by the rate of transfer of hydrogen. This is expressed as a ratio of effective diffusivities and feed concentrations:

$$\gamma = \frac{D_B C_{B,feed}}{b D_A C_A^*} \tag{37}$$

where

D_B = Liquid phase diffusivity of the liquid reagent (AMS)

$C_{B,feed}$ = Liquid reagent concentration in the feed

b = Stoichiometric coefficient (equal to 1)

D_A = Liquid phase diffusivity of the gaseous reagent

C_A^* = saturated hydrogen concentration in the liquid

Using this criterion, the reaction is liquid limited when $\gamma << 1$ and gas limited when $\gamma >> 1$. If γ is bigger than 1 but close to 1, it is possible that some liquid internal diffusion limitations exits for parts of the catalyst particle that is poorly wetted (Beaudry et al.,

1987). Note that for gas-limited conditions ($\gamma>1$) where the gas phase is continuously supplied (as in a trickle bed reactor), the depletion of the liquid phase reagent actually reduces γ down the length of the bed and it is possible to enter into the liquid limited regime.

Some instances of MHS in a TBR with chemical reaction are discussed in literature. Rajashekharam et al. (1998) showed how the conversion in a denitrogenation reaction is higher in a decreasing liquid flow rate mode (possibly Kan-Liquid) than in an increasing liquid flow rate mode (Levec). They attributed the difference to the temperature history in the bed. Similar temperature effects were observed by Hanika et al. (1981), Germain et al. (1974) and more recently Kirillov & Koptyug (2005). In these cases, it was shown how vaporization of the reaction mixture leads to complex thermal behaviour, including hot spot formation and temperature induced hysteresis. These studies do not explicitly consider the hydrodynamic effects that accompany changes in flow rates.

Ravindra et al. (1997b) studied the liquid phase oxidation of sulphur dioxide to sulphuric acid over activated carbon. In this case, the gas phase reagents are oxygen and SO_2 and the liquid phase reagent is water (which is also the solvent). The reaction is conducted at atmospheric pressure and room temperature. For these conditions, the reaction is severely gas-limited ($\gamma \approx 10^7$). The authors report that a pre-wetted bed outperforms a non-pre-wetted bed for a range of liquid velocities from 1 to 7 mm/s. The authors attribute the difference in performance between these modes to the different flow morphologies and mixing characteristics in the two modes of operation. It is likely that the severe maldistribution associated with the Non-pre-wetted mode also played a role in their results.

Table 19 suggests that hydrodynamic multiplicity may greatly influence the performance of a TBR. Therefore, this study focuses exclusively on the impact of hydrodynamic multiplicity (of all the hydrodynamic parameters) although due consideration is given to temperature effects.

Experimental details including the setup, analytics, operating procedures and experimental precautions are reported in Appendix A.

8.3.2 Results and Discussion

Figure 76a to Figure 76c and Figure 77a and Figure 77b show the conversion as a function of liquid velocity for $\gamma > 1$ and $\gamma < 1$ respectively (i.e. gas limited and liquid limited respectively). For the gas limited data ($\gamma > 1$), a complicating factor is the fact that γ decreases down the length of the catalyst bed as the liquid reagent is depleted. This effect is more severe for values of γ near 1 for low velocities where the conversion is high. In these cases the γ value at the exit of the bed can be below 1 and there are two regimes in the bed: the first being gas-limited and the second liquid-limited. However, for the case of large entrance γ and high velocities, the exit γ is still above 1. It is specifically these conditions that are used to evaluate the functional behaviour of a gas limited system. In order to keep conversions low enough to be properly measurable, the catalyst bed height was halved for the experiments depicted in Figure 76c and Figure 77. The hydrogenation reaction is considered mildly exothermic ($-\Delta H$ = 110 kJ/mol), and corresponding temperature rises in the reactor are shown in Figure 76d to Figure 76f and Figure 77c and Figure 77d. Also shown on these figures are the adiabatic temperature rises calculated from the measured conversions assuming constant specific heat capacities (liquid specific heat capacity of 190 kJ/kmol.K and gas specific heat capacity of 29 kJ/kmol.K) and thermal equilibration between the gas and the liquid. As indicated, there were significant heat losses to the environment for the conditions where high AMS feed concentrations were used (gas limited conditions).

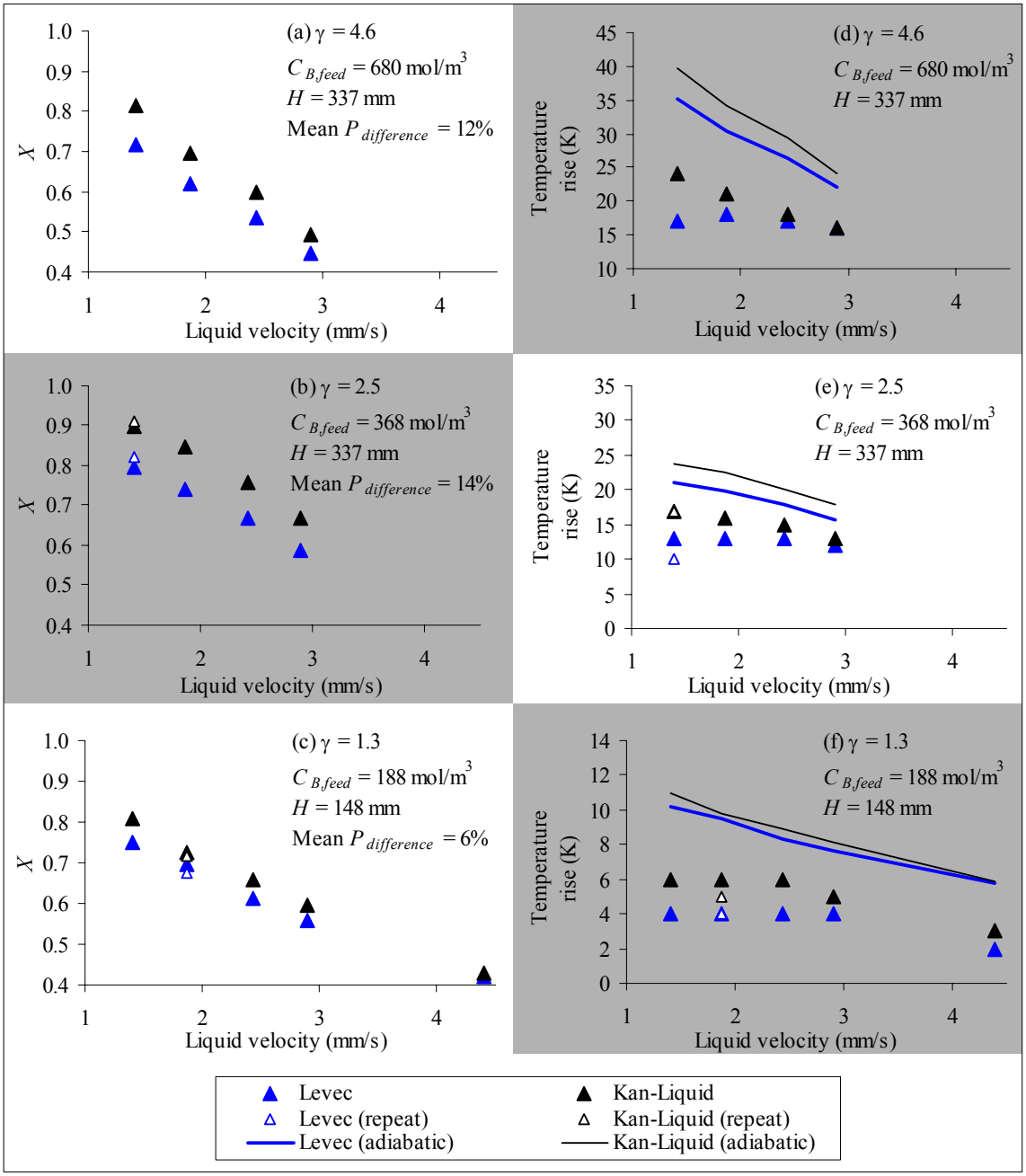

Figure 76. Conversion and temperature rise for gas limited conditions

A representative plot of the measured pressure drop (Figure 78) in both modes show trends similar to those observed in literature, although the difference between the modes is only about 5-25% (probably due to the low gas velocity used here, as well as the end effects and the presence of the glass bead beds inside the reactor).

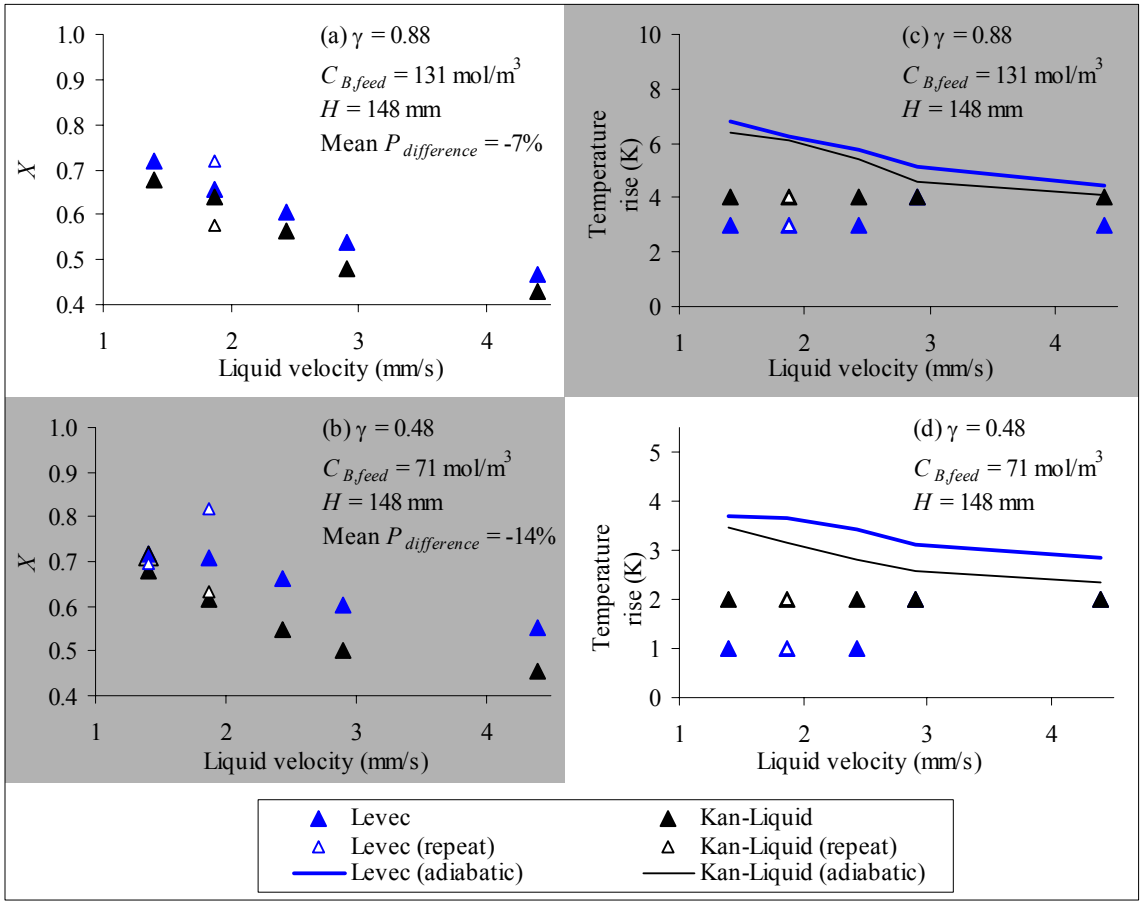

Figure 77. Conversion and temperature rise for liquid limited conditions

The results indicate clearly that a significant change in reactor performance occurs as a result of flow multiplicity. Moreover, higher conversions are not always achieved in one particular mode. For gas limited reactions (large γ, Figure 76), the Kan-Liquid mode outperforms the Levec mode. As the liquid feed concentration (and γ) is reduced the difference between the modes becomes smaller (as both gas and liquid limitations become important). When $\gamma < 1$ (liquid limitations, Figure 77), the Levec mode outperforms the Kan-Liquid mode (and apparently increasingly so as γ is reduced further). The difference in performance is considerable. A measure of this difference can be gained from defining the productivity and the productivity difference between modes respectively as (Levenspiel, 1998):

$$P = \frac{XC_{B,feed}Q_L}{W_{Pd}} \tag{38a}$$

$$P_{difference} = \frac{P_{Kan-L} - P_{Levec}}{P_{Levec}} \times 100\% \tag{38b}$$

For gas limited conditions (γ = 4.6 and 2.5), the productivity is roughly 10-15% higher in the Kan-Liquid mode. For liquid limited conditions (γ = 0.48), the productivity is 2-20% higher in the Levec mode (14% on average). It seems as though the modes are equally productive when γ = 1. The productivity difference between modes is shown in Figure 79 as a function of γ or 1/γ (a γ value of 2 for the gas-limited condition corresponds to a 1/γ value of 2 for the liquid-limited condition). The coupling between reactor performance and hydrodynamics is intricate. It is desirable to reconcile the conversion data with the hydrodynamics of the different pre-wetting modes. Because of the unavailability of quantitative kinetic and hydrodynamic data for this system and conditions, the discussion is restricted to a qualitative rationalization of the observed behaviour.

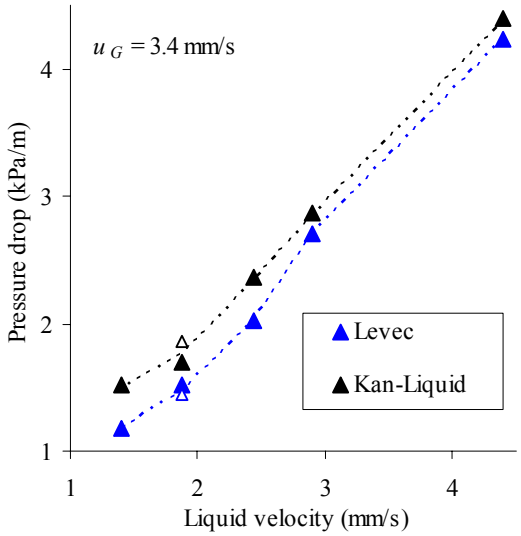

Figure 78. Representative pressure drop plot

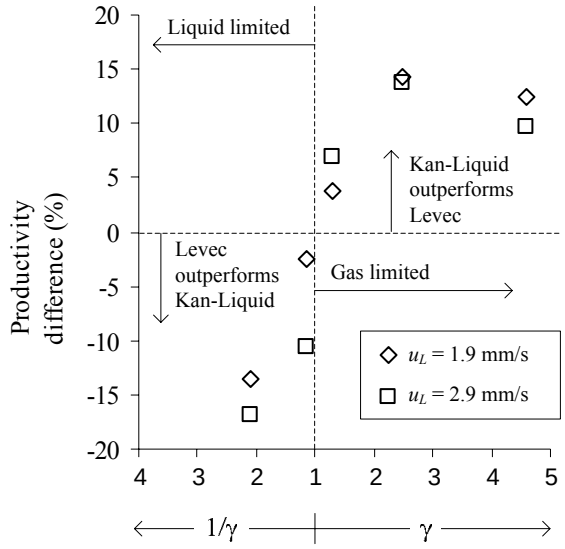

Figure 79. Productivity difference as a function of the degree of gas or liquid limitation

To start, a comparison between the gas-limited exothermic reaction data of Rajashekharam et al. (1998) and the gas limited condition (Figure 76) reveals a fundamental dissimilarity in the thermal behaviour. In their work, an initial *increase* in the liquid velocity (presumably in the Levec mode) resulted in an *increase* in the temperature. This happens despite a decrease in the overall conversion, and therefore is likely to be attributed to non-adiabatic effects (e.g. the heating of the reactor by the heaters mounted on the reactor wall). A subsequent decrease in the liquid velocity (the return leg, Kan-Liquid) then yielded a higher conversion of the feed reagent at a higher temperature (compared to the increasing liquid velocity leg, Levec). The hysteresis was therefore attributed to the fact that the bed was warmer on the decreasing liquid velocity leg (Kan-Liquid mode) which led to a higher conversion. In this study, the steady state temperature slightly *decreased* as the liquid flow rate was *increased* on the Levec mode (see Figure 76e for example). This corresponds to a lower AMS conversion. The lowest temperature in the bed was reached during pulsing flow. Upon returning to lower velocities (Kan-Liquid mode), the temperature was higher than it was before. The temperature history in the bed cannot therefore account for the hysteretic behaviour. Instead, the higher conversion due to hydrodynamic effects in turn resulted in a higher

bed temperature. This interpretation is further supported by the liquid limited data (Figure 77), where almost no temperature variation occurred as a result of flow rate changes but a considerable difference in conversion is observed. From these observations it is evident that the multiplicity in conversion is caused by a hydrodynamic effect and not a temperature history effect. It is therefore imperative to determine the nature of these hydrodynamic multiplicity effects on the reactor performance.

Considering that the reaction is mass transfer limited and that the active metal is deposited on the support in an egg-shell configuration (i.e. on the outer shell of each particle), external mass transfer is expected to play the most important role. Insofar as the gas limited case is concerned, note that the gas phase reactant (A) can be supplied to the catalyst particle either through the liquid or directly to the dry surface. However, for the conditions in this study (small, porous particles, a low surface tension liquid and the presence of a particle pre-wetting procedure), it is likely that the wetting efficiency is close to 1 (Al-Dahhan & Dudukovic, 1995). The focus should therefore be on the gas-liquid and liquid-solid mass transfer steps for hydrogen, and $(k_{LS}a_{LS})_A$ is typically an order of magnitude larger than $k_{GL}a_{GL}$ (compare for example the data of Tan & Smith (1982) to that of Goto & Smith, 1975). This means that the total gas-liquid-solid mass transfer coefficient is approximately equal to the gas-liquid mass transfer coefficient (i.e. all of the resistance is in the gas-liquid mass transfer step). Changes in $k_{LS}a_{LS}$ due to hydrodynamic multiplicity are therefore insignificant compared to changes in $k_{GL}a_{GL}$. Based on this analysis, it is anticipated that, for the present system (gas limited conditions), gas-liquid mass transfer is the controlling rate. This conclusion accords with the observed behaviour of the reactor in that it is known that the volumetric gas-liquid mass transfer rate is appreciably larger in the Kan-Liquid mode (Table 19). The present results are in agreement with the work of Ravindra et al. (1997b) who found a higher reaction rate in the hydrodynamic mode with a higher wetting efficiency (but also a higher volumetric gas-liquid mass transfer coefficient).

The liquid limited case presents an interesting phenomenon in that the Levec mode has a higher conversion than the Kan-Liquid mode (Figure 77) despite the expectation of a lower average wetting efficiency (Table 19). Having established that this is not a temperature effect, the interplay between wetting efficiency and holdup and how they affect the volumetric liquid-solid mass transfer coefficient need to be clarified. Unfortunately, mass transfer coefficient correlations are generally inaccurate and also does not account for hydrodynamic multiplicity. For these reasons, the present discussion is limited to a qualitative rationalization of the observed trends. Note that a smaller holdup corresponds to a larger interstitial velocity, which corresponds to an increased k_{LS} (Lakota & Levec, 1990). Also, the mass transfer area (a_{LS}) is obviously proportional to the wetting efficiency (f). For the two modes, all other parameters in typical mass transfer correlations (like superficial velocities and the bed properties) are equal, so that is possible to estimate the ratio of volumetric mass transfer coefficients in the two modes:

$$\frac{\left[k_{LS}a_{LS}\right]_{Levec}}{\left[k_{LS}a_{LS}\right]_{Kan-L}} = \left(\frac{\left[\varepsilon_L\right]_{Kan-L}}{\left[\varepsilon_L\right]_{Levec}}\right)^{\frac{1}{2}}\left(\frac{\left[f\right]_{Levec}}{\left[f\right]_{Kan-L}}\right) \tag{39}$$

In equation 39 the power of 0.5 is predicted by film theory and was confirmed over a wide range of operating conditions (Lakota et al., 2002). Evaluation of equation 39 requires estimates of the ratios of holdup and wetting efficiency in the two modes. For the present conditions, the use of small particles and a low surface tension liquid is expected to yield high wetting efficiency (Al-Dahhan & Dudukovic, 1995) (especially at high liquid velocity), meaning that the wetting efficiency ratio can be expected to be close to 1 (because wetting nears 1 for both cases). The ratio of liquid-solid mass transfer coefficients in the two modes is therefore roughly proportional to the square root of the inverse ratio of holdup. Wang et al. (1995) showed that smaller particles have more severe holdup hysteresis and one can therefore expect the holdup ratio to be larger than that reported for the 3 mm spheres (Table 19). Since the holdup in the Levec mode is lower than that in the Kan-Liquid mode, the Levec coefficient exceeds the Kan-Liquid

coefficient. This then serves as a possible explanation for the higher conversion that was achieved for the Levec mode in the liquid limited reaction experiments (Figure 77). A proper evaluation of the effect of pre-wetting on mass transfer limited reactions therefore has to take into account both the difference in interstitial velocity (holdup) and the difference in mass transfer area (wetting efficiency). Note that in this case, the depletion of the liquid reagent serves to make the conditions more liquid limited as conversion increases down the length of the reactor.

8.3.3 Reaction Case Study Conclusions

The effect of hydrodynamic multiplicity on a mass transfer limited reaction was shown to be significant when either gas or liquid limitations are dominant. The observed trends are counter-intuitive when evaluated from a partial wetting perspective: the Kan-Liquid mode outperforms the Levec mode for gas limited conditions, while the Levec mode outperforms the Kan-Liquid mode for liquid limited conditions. However, the reaction data can be rationalized qualitatively when it is considered that the wetting for the conditions in this study is likely to be nearly complete. In such a case, hydrodynamic multiplicity impacts the applicable mass transfer coefficients directly in a manner consistent with the available literature and the observed behaviour of the reactor. It is likely that the effects described in this study (mass transfer rates) are applicable to a range of conditions similar to those employed, while the full range of effects probably warrant consideration in the general case. These should include stagnancy, the effect of gas flow, maldistribution, localized hot spot formation, particle scale phenomena (in particular the use of uniformly impregnated particles) and the use of different particle sizes, particle geometries and operating conditions. However, there is limited data available on these issues as researchers have generally not considered hydrodynamic multiplicity apart from specifying operating in the Kan-Liquid mode. This study introduces the idea of optimising the hydrodynamic conditions in the reactor by exploiting the multiplicity behaviour in order to suit specific reaction conditions.

8.4 Conclusions

This chapter discussed the industrial implications of hydrodynamic multiplicity. First, experimental evidence of the existence of pressure drop multiplicity was presented, but unfortunately the implications for the reactor performance were not clear. To illustrate that hydrodynamic multiplicity directly impacts the performance of a trickle bed reactor, an experimental case study was completed in a pilot scale hydrogenation reactor. The results indicate that for the conditions examined, hydrodynamic multiplicity greatly affects the conversion. Moreover, different modes yield optimal performance depending on the system conditions. These results again emphasize the importance of properly understanding hydrodynamic multiplicity.

Chapter 9. Conclusions

As a whole, this work advanced the understanding of trickle flow to the extent of comprehending the role that capillary phenomena play in establishing diverse hydrodynamic states under different operating conditions. This is accomplished as illustrated in Figure 1. First, a conceptual framework was introduced by which hydrodynamic multiplicity can be studied successfully. This framework was then applied to the existing multiplicity data and some deficiencies were identified. Additional experimental insights were generated both at the traditional bed scale and at the more informative pore scale. These experimental investigations included extending the scope of the data (to include bed characteristics, operating conditions and procedures that have not been investigated before), as well as advancing existing visualization techniques through novel applications and improved processing strategies.

The major conclusions of this study are as follows:

- *Hydrodynamic multiplicity significantly impacts all the hydrodynamic parameters* investigated.
- The *limiting cases framework* proves to be both applicable to and useful for the study of hydrodynamic multiplicity.
- A proposed *capillary gate mechanism* is capable of providing qualitative rationalizations of all of the experimentally observed *characteristic trends* (that embodies the behaviour of the flow in the various hydrodynamic states).
- It is further established experimentally that *hydrodynamic multiplicity directly impacts trickle bed reactor performance*, and that different hydrodynamic modes are preferable depending on the reaction specifics.

It is recommended that:

- The development of a *fully predictive hydrodynamic multiplicity model* be pursued. The model should be based (at least in part) on the experimental and theoretical insights provided in this work.
- The impact of hydrodynamic multiplicity on trickle flow performance be studied in depth, in particular for industrially important conditions (for example, systems with multiple reactions or systems limited by chemical kinetics, internal mass transfer, external mass transfer or combinations thereof).

In conclusion, this work has emphasized the importance of hydrodynamic multiplicity, has shown experimentally that its effects are far reaching and potentially advantageous, and that it can be understood in relatively simple terms if capillary effects are appropriately included in a pore-level description of trickle flow.

APPENDIX A. Experimental Detail for Reaction Study

The trickle bed reactor facility is shown schematically in Figure 80. The inner diameter of the reactor was 0.05 m. Pre-purified hydrogen from a rack of two cylinders was fed into the reactor at a controlled flow rate. Liquid was charged into the feed tank which was subsequently pressurized with nitrogen. The liquid feed was made up of α-methyl styrene, AMS, (99%, Aldrich) in hexane (95%, Aldrich) as solvent with AMS concentrations from 1 to 9 % v/v (70 to 680 mol/m^3). The AMS concentration was determined by a Gas Chromatograph (Varian) that was pre-calibrated for a range of AMS concentrations between 7.7 and 680 mol/m^3. Analytical reproducibility was within approximately 2% on AMS concentration. The pressure difference between the feed tank and the reactor was kept at 340 kPa and was used to supply liquid into the reactor. The pump was used only to circulate the feed prior to operation in order to ensure a uniform feed concentration. Experiments were conducted for liquid velocities ranging from 1.4 to 4.4 mm/s (maximum liquid velocity used for pulsing pre-wetting was 9.4 mm/s) and the gas velocity was set at 3.4 mm/s at 790 kPa for all the runs (hydrogen is therefore in stoichiometric excess for all experiments except the most severely gas limited condition – excess between 4 and 1100 % depending on the liquid velocity and concentration). A differential pressure transducer (Validyne DP15-30) was used to measure the pressure drop over the entire reactor (i.e. catalyst bed, glass bead beds, the entrance and the exit). A thermocouple capable of registering intervals of 0.5 degrees Centigrade is located at the exit of the bed. The liquid is funnelled at the bed exit by a metallic sieve and the thermocouple is placed in the liquid stream. The feed was always introduced at 19 degrees Centigrade. The column itself is insulated with ceramic material to reduce heat losses to the environment.

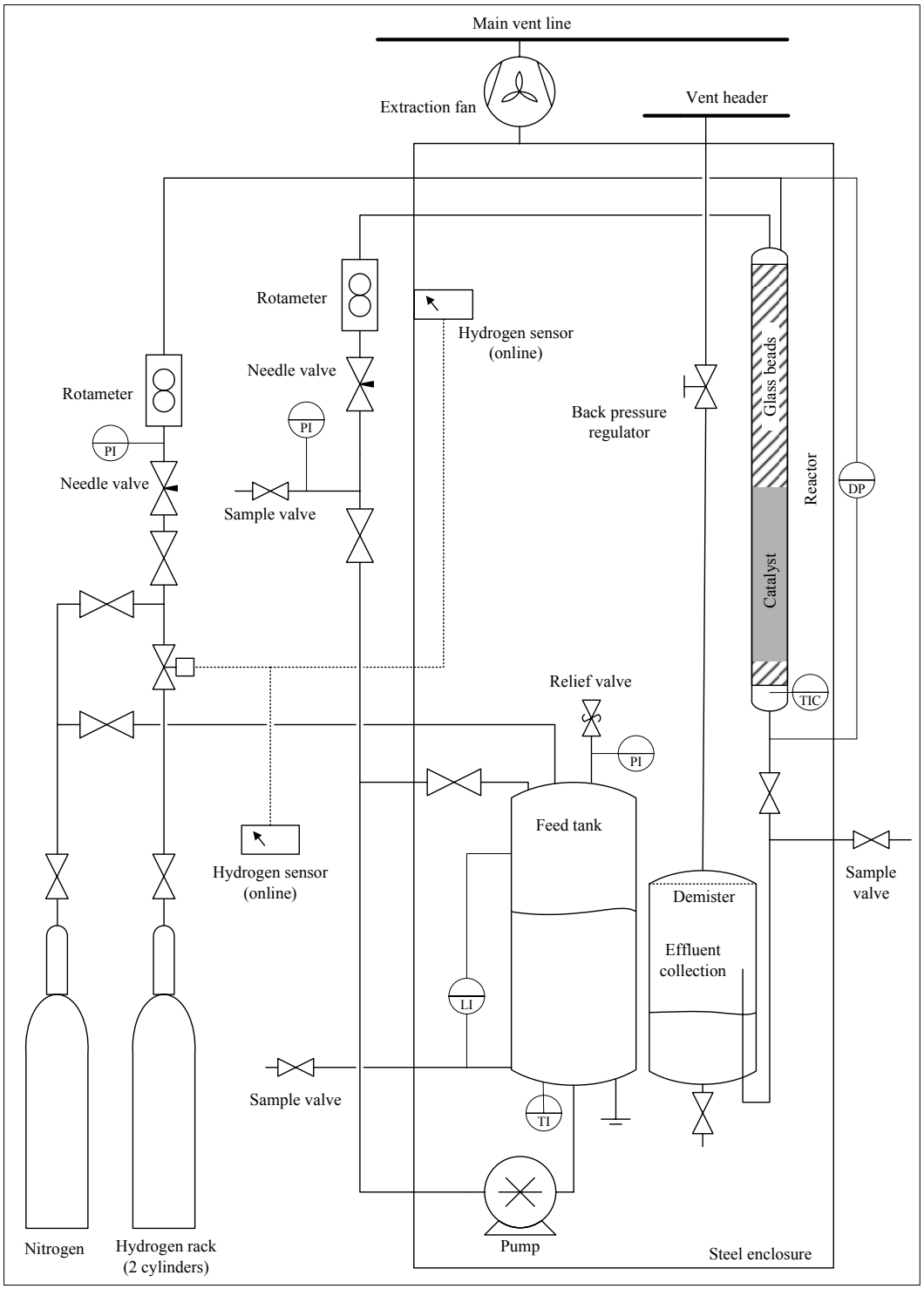

Figure 80. Experimental setup for reaction study

A heater was used to heat the catalyst for activation purposes, but was turned off during the reaction run. A bed of glass beads at the reactor entrance ensures that the liquid is saturated with hydrogen prior to it entering the catalyst bed. This was confirmed by estimating the hydrogen concentration in the liquid at the catalyst bed entrance by assuming plug flow of the liquid and a gas-liquid mass transfer rate characterized by a volumetric coefficient. Using either the Goto & Smith (1975) or the Larachi et al. (1999) correlation to estimate the coefficient, the concentration at the catalyst bed entrance was determined to be within 1% of the saturated concentration. The glass beads also serve as a distributor for the gas and liquid phases prior to it entering the catalyst bed. All experiments reported here were conducted at 790 kPa absolute pressure. Although it is possible to increase γ by operating at a lower pressure, there is indication that the intrinsic kinetics is dependent on the pressure (Khadilkar, 1998) which makes comparison between the gas- and liquid limited runs difficult. At 800 kPa the kinetics are usually taken to be dependent on both reactant concentrations (Khadilkar, 1998). Operating at a single pressure for all the runs eliminates any hydrodynamic differences that might have occurred due to changes in the pressure. At this pressure, γ ranged between 0.48 and 4.6 for the different AMS concentrations. For each condition, liquid samples were taken at intervals of 5 minutes. Steady state was assumed once the pressure drop, temperature rise and conversion had all stabilized. Steady state was usually achieved in about 10-15 minutes but sampling continued to 25 minutes in each case.

The catalyst bed height was either 337 mm or 148 mm depending on the degree of liquid limitation. That is, it was necessary to reduce the bed height of the cases where $\gamma < 2$ in order to keep the conversion in the measurable range (10 - 90%). For the shortest bed, the bed height was approximately 70 times the equivalent particle diameter (1.9 mm).

The catalyst was 1% Pd egg-shell on porous cylindrical alumina extrudate (Engelhard) with diameter 1.5 mm and length 4.3 ± 1.8 mm (equivalent diameter 1.9 mm, particle to column diameter ratio approximately 26). It was activated in situ at 120 ^{o}C for 5 hours

with hydrogen flowing at the operating velocity. After activation the catalyst activity decreases before it stabilizes (compare Wu et al., 1996). Consequently, it was necessary to operate the reactor for a prolonged period (approximately 9 hours) at a liquid velocity of 3.4 mm/s in the Kan-Liquid mode in order to reach stable operation. During this time the activity was monitored by sampling the reactor effluent intermittently and calculating the conversion. After an initial decrease the conversion stabilized at approximately 6 hours. As a final check, the conversion of a Kan-Liquid mode experiment at the end of the experimental program yielded approximately the same conversion as the initial stabilization run, thereby confirming that the catalyst was stable throughout the experimental program.

Additional experimental precautions were taken as follows:

- The absence of homogeneous side reactions was confirmed by operating the setup with only glass beads (no catalyst) loaded into the reactor. No reaction was detected. A polimerization inhibitor (p-tert-butylcatechol) present in the feed is likely to be responsible for the absence of oligomeric or polymeric activity (Meille et al., 2002).
- At the reaction conditions, the vapour pressures of AMS, cumene and hexane are well below 30 kPa (Watson & Harold, 1993). Therefore there is little expectation of liquid vaporization.
- The presence of hydrodynamic effects on the reaction rate was confirmed by performing two liquid limited reaction experiments. In the first, 158 grams of catalyst were loaded and the liquid superficial velocity was set to 2.7 mm/s (yielding a weight hourly space velocity of 0.12). The conversion was 44%. Another bed was then packed with 500 grams of catalyst and the liquid velocity was set to 8.4 mm/s (again the weight hourly space velocity was 0.12). The conversion for this run was 81%. For a chemically controlled reaction rate, the conversion is a function of the space velocity and not the superficial velocity (as shown in Wu et al., 1996). These two experiments therefore show that

hydrodynamic effects are present – the high superficial velocity in the second run facilitates transport to the catalyst and therefore yields a higher conversion.

Since hysteresis is involved, the exact operating procedure needs to be reported. The catalyst was saturated internally with feed by leaving the reactor flooded with feed overnight. Due to capillary action the catalyst interior is expected to remain filled throughout the experiments. The bed was then drained with the gas flowing at the operating velocity for 15 minutes. The liquid was introduced at the lowest velocity and steady state was achieved. After the last steady state sample had been taken, the liquid flow rate was increased to the next higher setting. This was repeated until the highest setting had been completed (i.e. the Levec mode). The liquid flow rate was then increased to 9.4 mm/s (pulsing flow) for 20 seconds and reduced to the 4.4 mm/s. After that operating condition had been completed, the liquid flow rate was reduced to the next lowest setting and so on until the Kan-Liquid mode had been completed. Several of the runs (five in each mode) were repeated in order to determine the reproducibility of results. These runs were conducted by establishing a Levec point (i.e. increasing the flow rate from zero to the operating velocity, e.g. 1.9 mm/s), then increasing the flow rate to 9.4 mm/s (pulsing) and then decreasing it directly back to 1.9 mm/s (i.e. the Kan-Liquid point). The repeat runs are shown on the figures in the results section. In most instances the reproducibility was within a few percent. Although there were differences in a limited number of cases, the trends of which pre-wetting mode yielded higher conversions were never reversed.

References

Al-Dahhan, M.H., Dudukovic, M.P. (1995a) Catalyst wetting efficiency in trickle-bed reactors at high pressure. *Chem. Eng. Sci.*, *50,* 2377-2389.

Al-Dahhan, M.H., Wu, Y., Dudukovic, M.P. (1995b) Reproducible technique for packing laboratory-scale trickle-bed reactors with a mixture of catalyst and fines. *Ind. Eng. Chem. Res., 34,* 741-747.

Al-Dahhan, M.H., Larachi, F., Dudukovic, M.P., Laurent, A. (1997). High pressure trickle-bed reactors: A review. *Ind. Eng. Chem. Res., 36,* 3292-3314.

Al-Dahhan, M.H., Khadilkar, M.R., Wu, Y., Dudukovic, M.P. (1998) Prediction of pressure drop and liquid holdup in high-pressure trickle-bed reactors. *Ind. Eng. Chem. Res., 37,* 793-798.

Al-Dahhan M.H., Highfill, W., Tee Ong, B. (2000) Drawbacks of the Dissolution Method for Measurement of the Liquid-Solid Mass-Transfer Coefficients in Two-Phase Flow Packed-Bed Reactors Operated at Low and High Pressures. *Ind. Eng. Chem. Res., 39,* 3102-3107.

Anadon, L.D., Lim, M.H.M., Sederman, A.J., Gladden, L.F. (2005) Hydrodynamics in Two-Phase Flow Within Porous Media. *Magnetic Resonance Imaging*, *23,* 291–294.

Attou, A., Boyer, C., Ferschneider, G. (1999) Modeling of the hydrodynamics of the cocurrent gas-liquid trickle flow through a trickle-bed reactor. *Chem. Eng. Sci., 54,* 785-802.

Bacri, J.C., Chaouche, M., Salin, D. (1992) Modele simple de permeabiltes relatives croisees. *Comptes. Rendus de l'Academie des Sciences,* Paris, t.311,serie II,591.

Baldwin, C.A., Sederman, A.J., Mantle, M.D., Alexander, P., Gladden, L.F. (1996) Determination and characterization of the structure of a pore space from 3D volume images. *J. Colloid. Int. Sci., 181,* 79-92.

Bartelmus, G, Janecki, D. (2003) Hydrodynamics of a cocurrent downflow of gas and foaming liquid through the packed bed. Part II. Liquid holdup and gas pressure drop. *Chem. Eng. Process., 42,* 993-1005.

Basavaraj, M.G., Gupta, G.S. (2004) New Calibration Technique for X-ray Absorption Studies in Single and Multiphase Flows in Packed Bed. *I.S.I.J. Int., 44,* 50-58.

Basavaraj, M.G., Gupta, G.S., Naveen, K., Rudolph, V., Bali, R. (2005) Local Liquid Holdups and Hysteresis in a 2-D Packed Bed Using X-ray Radiography. *AIChE Journal, 51,* 2178-2189.

Bear, J. (1972) *Dynamics of fluids in porous media.* Dover Publications, New York.

Beaudry, E.G., Dudukovic, M.P., Mills, P.L. (1987) Trickle-Bed Reactors: Liquid Diffusional Effects in a Gas-Limited Reaction. *AIChE Journal, 33,* 1435-1447.

Biswas, J., Bhaskar, G.V., Greenfield, P.F. (1988) Stratified flow model for two-phase pressure drop prediction in trickle beds. *AIChE Journal, 34,* 510-517.

Boyer, C. and Fanget, B. (2002) Measurement of Liquid Flow Distribution in Trickle Bed Reactor of Large Diameter with a New Gamma-Ray Tomographic System. *Chem. Eng. Sci., 57,* 1079-1089.

Burghardt, A., Bartelmus, G., Jaroszynski, M., Kolodziej, A. (1995) Hydrodynamics and Mass Transfer in a Three-Phase Fixed-Bed Reactor with Cocurrent Gas-Liquid Downflow. *Chem. Eng. J., 58,* 83-99.

Canny, J. (1986) A Computational Approach to Edge Detection. *IEEE Transactions in Pattern Analysis and Machine Intelligence, 8,* 679-698.

Carbonell, R.G. (2000) Multiphase flow in packed beds. *Oil & Gas Sci. Tech., 55,* 417-425.

Cassanello, M.C., Martinez, O.M., Cukierman, A.C. (1992) Effect of liquid axial dispersion on the behaviour of fixed bed three phase reactors. *Chem. Eng. Sci., 47,* 3331-3338.

Chan, S.K., Ng, K.M. (1986) Geometrical characteristics of a computer-generated three-dimensional packed column of equal and unequal sizes spheres – with special reference to wall effects. *Chem. Eng. Comm., 48,* 215-222.

Charpentier J.C., Prost C., Le Groff P. (1969) Chute de pression pour des écoulements à co-courant dans les colonnes à garnissage arrosé: comparaison avec le garnissage noyé. *Chem. Eng. Sci., 24,* 1777-1794.

Charpentier J.C., Favier, M. (1975) Some liquid holdup experimental data in trickle-bed reactors for foaming and non-foaming hydrocarbons. *AIChE Journal., 21,* 1213-1218.

Chaouki, J., Larachi, F., Dudukovic, M.P. (1997) Noninvasive Tomographic and Velocimetric Monitoring of Multiphase Flow. *Ind. Eng. Chem. Res., 36,* 4476-4503.

Chen, S., Doolen, G.D., Eggert, K.G. (1994) Lattice-Boltzman fluid dynamics. *Los Alamos Science, 22,* 99-111.

Christensen, G., McGovern, S.J., Sundaresan, S. (1986) Cocurrent Downflow of Air and Water in a Two-Dimensional Packed Column. *AIChE Journal, 32,* 1677-1689.

Chu, C.F., Ng., K.M. (1988) Model for pressure drop hysteresis in trickle beds. *AIChE Journal, 35,* 1365-1369.

Colombo, A.J., Baldi, G., Sicardi, S. (1976) Solid-liquid contacting effectiveness in trickle bed reactors. *Chem. Eng. Sci., 31,* 1101-1108.

Crine, M.D., Marchot, P., L'Homme, G.A. (1979) Mathemical modelling of liquid trickling flow through a packed bed using the percolation theory. *Comput. Chem. Engng., 3,* 515-523.

De Beer, F.C. (2005) "Characteristics of the neutron/X-ray tomography system at the SANRAD facility in South Africa" *Nuclear Instruments and Methods in Physics Research A 542,* 1–8.

De Klerk, A. (2003a) Liquid Holdup in Packed Beds at Low Mass Flux. *AIChE Journal., 49,* 1597-1600.

De Klerk, A. (2003b) Voidage Variation in Packed Beds at Small Column to Particle Diameter Ratio. *AIChE Journal, 49,* 2023-2029.

Dierick, M., Masschaele, B., Van Hoorebeke, L. (2004) Octopus, a fast and user-friendly tomographic reconstruction package developed in LabView®. *Measurement Science and Technology, 15,* 1366-1370.

Dudukovic, M.P. (1977) Catalyst Effectiveness Factor and Contacting Efficiency in Trickle-Bed Reactors. *AIChE Journal, 23,* 940-944.

Dudukovic, M.P., Larachi, F., Mills, P.L. (2002). Multiphase catalytic reactors: A perspective on current knowledge and future trends. *Catalysis Reviews, 44,* 123-246.

Dullien, F.A.L. (1991) Characterization of porous media – pore level. *Transp. Porous Media, 6,* 581-606.

Dwivedi, P.N, Upadhyay, S.N. (1977) Particle-Fluid Mass Transfer in Fixed and Fluidized Beds. *Ind. Eng. Chem. Process Des. Dev., 16,* 157-165.

Ebach, E.A., White, R.R. (1958) Mixing of fluids flowing through beds of packed solids. *AIChE Journal, 4,* 161-169.

Ellman, M.J., Midoux, N., Laurent, A., Charpentier, J.C. (1988) A new, improved pressure drop correlation for trickle-bed reactors. *Chem. Eng. Sci., 43,* 2201-2206.

Ellman, M.J., Midoux, N., Wild, G., Laurent, A., Charpentier, J.C. (1990) A new, improved liquid holdup correlation for trickle-bed reactors. *Chem. Eng. Sci., 45,* 1677-1684.

Ergun, S. (1952). Fluid flow through packed columns. *Chemical Engineering Progress, 48,* 89-94.

Feldkamp, L.A., Davis, L.C., Kress, J.W. (1984) Practical cone-beam algorithm. *Journal of the Optical Society of America, 1,* 612-619.

Fourar, M., Lenormand, R., Larachi, F. (2001) Extending the F-function concept to two-phase flow in trickle beds. *Chem. Eng. Sci., 56,* 5987-5994.

Fukutake, T., Rajakumar, V. (1982) Liquid holdup and abnormal flow phenomena in packed beds under conditions simulating the flow in the dropping zone of a blast furnace. *Transactions ISIJ, 22,* 355-364.

Germain, A.H., Lefebvre, A.G., L'Homme, G.A. (1974) Experimental study of a catalytic trickle bed reactor. *Advances in Chemistry Series 133, Chemical Reaction Engineering-II.,* 164.

Gianetto, A., Baldi, G., Specchia, V., Sicardi., S. (1978). Hydrodynamics and solid-liquid contacting effectiveness in trickle-bed reactors. *AIChE Journal, 24,* 1087-1104.

Gianetto, A., Spechhia, V. (1992) Trickle-bed reactors: State of art and perspectives. *Chem. Eng. Sci., 47,* 3197-3213.

Gierman, H. (1988) Design of laboratory hydrotreating reactors - scaling down of trickle flow reactors. *Applied Catalysis, 43,* 277-286.

Gladden, L.F., Alexander, P., Britton, M.M., Mantle, M.D., Sederman, A.J., Yuen, E.H.L. (2003a) In situ magnetic resonance measurement of conversion, hydrodynamics and mass transfer during single- and two-phase flow in fixed-bed reactors. *Magnetic Resonance Imaging, 21,* 213-219.

Gladden, L.F., Lim, M.H.M., Mantle, M.D., Sederman, A.J., Stitt, E.H. (2003b) MRI Visualisation of Two-Phase Flow in Structured Supports and Trickle-Bed Reactors. *Catalysis Today, 79–80,* 203–210.

Goto, S., Smith, J.M. (1975) Trickle-Bed Reactor Performance – Part 1. Holdup and Mass Transfer. *AIChE Journal, 21,* 706–713.

Gunjal, P.R., Kashid, M.N., Ranade, V.V., Chaudhari, R.V. (2005) Hydrodynamics of trickle-bed reactors: experiments and CFD modelling. *Ind. Eng. Chem. Res., 44,* 6278-6294.

Hanika, J., Vosecky, V., Ruzicka, V. (1981) Dynamic Behaviour of the Laboratory Trickle Bed Reactor. *Chem. Eng. J., 21,* 108-114.

Herskowitz, M., Smith, J.M. (1983) Trickle-bed reactors: a review. *AIChE Journal, 29,* 1-18.

Hoek, P.J., Wesselingh, J.A., Zuiderweg, F.J. (1986) Small Scale and Large Scale Liquid Maldistribution in Packed Columns. *Chem. Eng. Res. Des. 64,* 411-418.

Holub, R.A., Dudukovic, M.P. and Ramachandran, P.A. (1992) A Phenomenological Model for Pressure Drop, Liquid Hold-up and Flow Regime Transition in Gas-Liquid Trickle Flow. *Chem. Eng. Sci., 47,* 2343-2348.

Iliuta, I., Larachi, F., Grandjean, B.P.A. (1999a). Residence time, mass transfer and back-mixing of the liquid in trickle flow reactors containing porous particles. *Chem. Eng. Sci., 54,* 4099-4109.

Iliuta, I., Larachi, F., Grandjean, B.P.A., Wild, G. (1999b) Gas-liquid interfacial mass transfer in trickle-bed reactors: state-of-art correlations. *Chem. Eng. Sci., 54,* 5633-5645.

Iliuta, I., Larachi, F. (1999c) The generalized slit model: pressure gradient, liquid holdup and wetting efficiency in gas-liquid trickle flow. *Chem. Eng. Sci., 54,* 5039-5045.

Iliuta, I., Larachi, F., Al-Dahhan, M.H. (2000) Double-slit model for partially wetted trickle flow hydrodynamics. *AIChE Journal, 46,* 597-609.

Iliuta, I., Grandjean, B.P.A., Larachi, F. (2002) New mechanistic film model for pressure drop and liquid holdup in trickle flow reactors. *Chem. Eng. Sci., 57,* 3359-3371.

Iliuta, I., Larachi, F. (2005) Modelling the hydrodynamics of gas-liquid packed beds via slit models: a review. *Int. J. Chem. Reactor. Eng., 3,* 1-25.

Jiang, Y., Khadilka,r M.R., Al-Dahhan, M.H., Dudukovic, M.P. (1999) Two-phase flow distribution in 2D trickle-bed reactors. *Chem. Eng. Sci., 54,* 2409-2419.

Jiang, Y., Khadilkar, M.R., Al-Dahhan, M.H., Dudukovic, M.P. (2000) Single phase flow modelling in packed beds: discrete cell approach revisited. *Chem. Eng. Sci., 55,* 1829-1844.

Jiang, Y., Khadilkar, M.R., Al-Dahhan, M.H., Dudukovic, M.P. (2002) CFD of multiphase flow in packed-bed reactors: I. k-fluid modelling issues. *AIChE Journal, 48,* 701-710.

Kan, K.M., Greenfield, P.F. (1978) Multiple Hydrodynamic States in Cocurrent Two-Phase Down-Flow through Packed Beds. *Ind. Eng. Chem. Process Des. Dev., 17,* 482-485.

Kan, K.M., Greenfield, P.F. (1979) Pressure Drop and Holdup in Two-Phase Cocurrent Trickle Flows through Packed Beds. *Ind. Eng. Chem. Process Des. Dev., 18,* 740-745.

Kantzas, A. (1994) Computation of Holdups in Fluidized and Trickle Beds by Computer-Assisted Tomography. *AIChE Journal, 40,* 1254-1261.

Khadilkar, M.R. (1998) *Performance Studies of Trickle Bed Reactors.* D. Sc. Thesis, Washington University in St Louis, USA.

Khadilkar, M.R., Wu, Y.X., Al-Dahhan, M.H., Dudukovic, M.P., Colakyan, M. (1996) Comparison of Trickle-bed and Upflow Reactor Performance at High Pressure: Model Predictions and Experimental Observations. *Chem. Eng. Sci., 51,* 2139-2148.

Khanna, R., Nigam, K.D.P. (2002) Partial wetting in porous catalysts: wetability and wetting efficiency. *Chem. Eng. Sci., 57,* 3401-3405.

Kirillov, V.A., Koptyug, I.V. (2005) Critical Phenomena in Trickle-Bed Reactors. *Ind. Eng. Chem. Res., 44,* 9727-9738.

Kobayashi, S., Kushiyama, S., Iida, Y., Wakao, N. (1979) Flow characteristics and axial liquid dispersion of two phase downflow in packed columns. *Kagaku Kogaku, 5,* 256-262.

Ku, T.C., Ramsey, J.H., Clinton, W.C. (1968) Calculation of Liquid Droplet Profiles from Closed-Form Solution of Young-Laplace Equation. *IBM J. Res.Develop., November,* 441-447.

Kuipers, J.A.M., Van Swaaij, W.P.M. (1997) Computational fluid dynamics applied to chemical reaction engineering. *Rev. Chem. Eng., 3,* 1.

Kundu, A., Saroha, A.K., Nigam, K.D.P. (2001) Liquid distribution studies in trickle-bed reactors. *Chem. Eng. Sci., 56,* 5963-5967.

Kundu, A., Nigam, K.D.P., Duquenne, A.M., Delmas, H. (2003) Recent developments on hydroprocessing reactors. *Rev. in Chem. Eng., 19,* 531-605.

Lakota, A., Levec, J., Carbonell, R.G. (2002) Hydrodynamics of Trickling Flow in Packed Beds: Relative Permeability Concept. *AIChE Journal, 48,* 731-738.

Lakota, A., Levec, J. (1990) Solid-Liquid Mass Transfer in Packed Beds with Cocurrent Downward Two-Phase Flow. *AIChE Journal, 36,* 1444-1448.

Lanfrey, P. (2006) *Flow Distribution and Hydrodynamics in a High-Pressure Trickle Bed Reactor.* A report to the Chemical Reaction Engineering Laboratory, Washington University in St Louis, St Louis, USA.

Larachi, F., Laurent, A., Midoux, N., Wild, G. (1991) Experimental study of trickle-bed reactor operating at high pressure: two-phase pressure drop and liquid holdup. *Chem. Eng. Sci., 46,* 1233-1246.

Larachi, F., Grandjean, B., Iliuta, I., Bensetiti, Z., Andre, A., Wild, G., Chen, M. (1999) Excel Worksheet Simulators for Packed Bed Reactors. http://www.gch.ulaval.ca/bgrandjean/pbrsimul/pbrsimul.html, [2005, November 8].

Larachi, F., Iliuta, I., Al-Dahhan, M.H., Dudukovic, M.P. (2000) Discriminating Trickle-Flow Hydrodynamic Models: Some Recommendations. *Ind. Eng. Chem. Res., 59,* 554-556.

Lazzaroni, C.L., Keselman, H.R., Figoli, N.S. (1988) Colorimetric Evaluation of the Efficiency of Liquid-Solid Contacting in Trickle Flow. *Ind. Eng. Chem. Res., 27,* 1132-1135.

Lazzaroni, C.L., Keselman, H.R., Figoli, N.S. (1989) Trickle Bed Reactors. Multiplicity of Hydrodynamic States. Relation between the Pressure Drop and the Liquid Holdup. *Ind. Eng. Chem. Res., 28,* 119-121.

Levec, J., Grosser, K., Carbonell, R.G. (1988) The Hysteretic Behaviour of Pressure Drop and Liquid Holdup in Trickle Beds. *AIChE Journal, 34,* 1027-1030.

Levec, J., Saez, A.E., Carbonell, R.G., (1986). The hydrodynamics of trickling flow in packed beds. Part II: Experimental observations. *AIChE Journal, 32,* 369-380.

Levenspiel, O. (1998) *Chemical Reaction Engineering*. John Wiley & Sons, New York.

Loudon, D.S., Van der Merwe, W., Nicol, W. (2006) Multiple Hydrodynamic States in Trickle Flow: The Effect of Prewetting Procedure on Liquid Holdup, Pressure Drop and Gas-Liquid Mass Transfer. *Chem. Eng. Sci. 61,* 7551-7562.

Lutran, P.G., Ng, K.M., Delikat, E.P. (1991) Liquid Distribution in Trickle Beds. An Experimental Study using Computer-Assisted Tomography. *Ind. Eng. Chem. Res., 30,* 1270 - 1280.

Macdonald, I.F., El-Sayed, M.S., Mow, K., Dullien, F.A.L. (1979) Flow through porous media — the Ergun equation revisited. *Ind. Eng. Chem. Fundamentals, 18,* 199–208.

Maiti, R., Khanna, R., Nigma, K.D.P. (2005) Trickle-bed reactors: porosity-induced hysteresis. *Ind. Eng. Chem. Res., 44,* 6406-6413.

Maiti, R., Khanna, R., Nigam, K.D.P. (2006) Hysteresis in Trickle-Bed Reactors: A Review. *Ind. Eng. Chem. Res., 45,* 5185-5198.

Mantle, M.D., Sederman, A.J. and Gladden, L.F. (2001) Single- and Two-Phase Flow in Fixed-Bed Reactors: MRI Flow Visualisation and Lattice-Boltzmann Simulations. *Chem. Eng. Sci., 56,* 523-529.

Manz, B., Gladden, L.F., Warren, P.B. (1999) Flow and dispersion in porous media: lattice-Boltzmann and NMR studies. *AIChE Journal, 45,* 1845-1854.

Marcandelli, C., Lamine, A.S., Bernard, J.R. and Wild, G. (2000) Liquid Distribution in Trickle-Bed Reactor. *Oil & Gas Sci. Tech., 55,* 407-415.

Marchot, P., Toye, D., Pelsser, A-M., Crine, M., L'Homme, G. and Olujic, Z. (2001) Liquid Distribution Images on Structured Packing by X-Ray Computed Tomography. *AIChE Journal, 47,* 1471-1476.

Meille, V., de Bellefon, C., Schweich, D. (2002) Kinetics of α-Methylstyrene Hydrogenation on Pd/Al_2O_3. *Ind. Eng. Chem. Res., 41,* 1711-1715.

Meister, E.C., Latychevskaia, T.Y. (2006) Axisymmetric Liquid Hanging Drops. *J. Chem. Edu., 83,* 117-126.

Melli, T.R., Scriven, L.E. (1991) Theory of two-phase cocurrent downflow in networks of passages. *Ind. Eng. Chem. Res., 30,* 951-969.

Michell, R.W., Furzer, I.A., (1972) Mixing in trickle flow through packed beds. *Chem. Eng. Journal, 4,* 53-63.

Middleman, S. (1998) *An Introduction to Fluid Dynamics*. John Wiley & Sons, New York.

Mills, P.L., Dudukovic, M.P. (1980) Analysis of catalyst effectiveness in trickle-bed reactors processing volatile or non-volatile reactants. *Chem. Eng. Sci., 35,* 2267-2279.

Mills, P.L. and Dudukovic, M.P. (1981). Evaluation of liquid-solid contacting in trickle-bed reactors by tracer methods. *AIChE Journal, 27,* 893-903.

Narasimhan, C.S.L., Verma, R.P., Kundu, A., Nigam, K.D.P. (2002) Modeling Hydrodynamics of trickle-bed reactors at high pressure. *AIChE Journal, 48,* 2459-2474.

Nemec, D., Bercic, G., Levec, J. (2001) Gravimetric method for the determination of liquid holdup in pressurized trickle-bed reactors. *Ind. Eng. Chem. Res., 40,* 3418-3422.

Nemec, D., Levec, J. (2005a) Flow through packed bed reactors: 1. Single-phase flow. *Chem. Eng. Sci. 60,* 6947-6957.

Nemec, D., Levec, J. (2005b) Flow through packed bed reactors: 2. Two-phase concurrent downflow. *Chem. Eng. Sci., 60,* 6958-6970.

Nigam, K.D.P., Iliuta, I., Larachi, F. (2002) Liquid back-mixing and mass transfer effects in trickle-bed reactors filled with porous catalyst particles. *Chemical Engineering and Processing, 41,* 365-371.

Nijhuis, T.A., Dautzenberg, F.M., Moulijn, J.A. (2003) Modeling of monolithic and trickle-bed reactors for the hydrogenation of styrene. *Chem. Eng. Sci., 58,* 1113-1124.

Palmisano, E., Ramachandran, P.A., Balakrishnan, K., Al-Dahhan, M.H. (2003) Computation of effectiveness factors for partially wetted catalyst pellets using the method of fundamental solution. *Computers and Chemical Engineering, 27,* 1431-1444.

Piche, S., Larachi, F., Iliuta, I., Grandjean, B.P.A. (2002) Improving the prediction of liquid back-mixing in trickle-bed reactors using a neural network approach. *J. Chem. Technol. Biotechnol., 77,* 989-998.

Pironti, F., Mizrahi, D., Acosta, A., Gonzalez-Mendizabal, D. (1999) Liquid-solid wetting factor in trickle-bed reactors: its determination by a physical method. *Chem. Eng. Sci., 54,* 3793-3800.

Prchlik, J., Soukup, J., Zapletal, V. Ruzicka, V. (1975) Liquid distribution in reactors with randomly packed porous beds. *Coll. Czech. Chem. Commun., 40,* 845-853.

Propp, R.M., Colella, P., Crutchfield, W.Y., Day, M.S. (2000) A numerical model for trickle bed reactors. *J. of Computational Physics, 165,* 311-333.

Puranik, S.S., Vogelpohl, A. (1974) Effective interfacial area in irrigated packed columns. *Chem. Eng. Sci., 29,* 501-507.

Rajashekharam, M.V., Jaganathan, R., Chaudhari, R.V. (1998) A trickle-bed reactor model for hydrogenation of 2,4 dinitrotoluene: experimental verification. *Chem. Eng. Sci., 53,* 787-805.

Ravindra, P.V, Rao, D.P, Rao, M.S. (1997a) A Model for the Oxidation of Sulphur Dioxide in a Trickle-Bed Reactor. *Ind. Eng. Chem. Res., 36,* 5125-5132.

Ravindra, P.V., Rao, D.P. and Rao, M.S. (1997b) Liquid Flow Texture in Trickle-Bed Reactors: An Experimental Study" *Ind. Eng. Chem. Res., 36,* 5133 - 5145.

Reinecke, N. and Mewes, D. (1996) Tomographic Imaging of Trickle-Bed Reactors. *Chem. Eng. Sci., 51,* 2131-2138.

Saez, A.E., Carbonell, R.G., (1985) Hydrodynamic parameters for gas-liquid cocurrent flow in packed beds. *AIChE Journal, 31,* 52-62.

Saez, A.E., Carbonell, R.G., Levec, J. (1986) The Hydrodynamics of Trickle Flow in Packed Beds. Part 1. Conduit Models. *AIChE Journal, 82,* 353-365.

Saroha, A.K., Nigam, K.D.P., Saxena, A.K., Kapoor, V.K. (1998) Liquid distribution in trickle-bed reactors. *AIChE Journal, 44,* 2044-2052.

Satterfield, C.N., (1975) Trickle-Bed Reactors. *AIChE Journal, 21,* 209-228.

Schmit, C.E., Cartmel, D., Eldridge, R.B. (2000) Process Tomography: An Option for the enhancement of packed vapour-liquid contactor model development. *Ind. Eng. Chem. Res., 39,* 1546-1553.

Sederman, A.J. and Gladden, L.F. (2001) Magnetic Resonance Imaging as a Quantitative Probe of Gas-Liquid Distribution and Wetting Efficiency in Trickle-Bed Reactors. *Chem. Eng. Sci., 56,* 2615 - 2628.

Sie, S.T., Krishna, R., (1998) Process Development and Scale-Up: III. Scale-Up and Scale-Down of Trickle Bed Processes. *Reviews in Chemical Engineering, 14,* 203-252.

Sims, W.B., Schulz, F.G., Luss, D. (1993) Solid-liquid mass transfer to hollow pellets in a trickle bed. *Ind. Eng. Chem. Res., 32,* 1895-1903.

Souadnia, A., Latifi, M.A. (2001) Analysis of two-phase flow distribution in trickle-bed reactors. *Chem. Eng. Sci., 56,* 5977-5985.

Sullivan, S.P., Sani, F.M., Johns, M.L., Gladden, L.F. (2005) Simulation of packed bed reactors using lattice Boltzmann methods. *Chem. Eng. Sci., 60,* 3405-3418.

Tan, C.S., Smith, J.M. (1982) A Dynamic Method for Liquid-Particle Mass Transfer in Trickle Beds. *AIChE Journal, 28,* 190-195.

Toye, D., Marchot, P., Crine, M. and L'Homme, G. (1995) Analysis of Liquid Flow Distribution in Trickling Flow Reactor using Computer Assisted X-ray Tomography. *Chem. Eng. Res. Des. 77,* 511-518.

Toye, D., Marchot, P., Crine, M., Pelsser, A-M., and L'Homme, G. (1998) Local Measurements of Void Fraction and Liquid Holdup in Packed Columns using X-ray Computed Tomography. *Chem. Eng. Proc., 37,* 511-520.

Tsochatzidis, N.A., Karabelas, A.J., Giakoumakis, D., Huff, G.A. (2002) An investigation of liquid maldistribution in trickle beds. *Chem. Eng. Sci., 57,* 3543-3555.

Tung, V.X., Dhir, V.K. (1988) A hydrodynamic model for two-phase flow through porous media. *Int. J. Multiphase Flow, 14,* 47-65.

Turpin, J.L., Hunington, R.L. (1967) Prediction of pressure drop for two-phase, two-component concurrent flow in packed beds. *AIChE Journal, 13,* 1191-1202.

Van der Merwe, W., Maree, C., Nicol, W. (2004) Nature of residual liquid holdup in packed beds of spherical particles. *Ind. Eng. Chem. Res., 43,* 8363-8368.

Van der Merwe, W. and Nicol, W. (2005) Characterization of Multiple Flow Morphologies within the Trickle Flow Regime. *Ind. Eng. Chem. Res., 44,* 9446 – 9450.

Van der Merwe, W., Nicol, W., De Beer, F.C. (2006) Internal Wetting Dynamics of Alpha- and Gamma-Alumina Catalyst Spheres using X-Ray Computed Tomography. *South African Journal of Science, 102,* 585-588.

Van der Merwe, W., Nicol, W., De Beer, F.C., (2007). Trickle flow distribution and stability by X-ray radiography. *Chemical Engineering Journal, 132,* 47-59.

Van der Westhuizen, I. (2006) *Trickle flow multiple hydrodynamic states: the effect of flow history, surface tension and transient upsets.* M.Eng. dissertation, University of Pretoria, Pretoria, South Africa.

Van Houwelingen, A.J., Sandrock, C., Nicol, W. (2006) Particle Wetting Distribution in Trickle-Bed Reactors. *AIChE Journal, 52,* 3532-3542.

Van Houwelingen, A.J., Van der Merwe, W., Nicol, W. (2007) Extension of liquid-limited trickle-bed reactor modelling to incorporate channelling effects. *Chem. Eng. Sci., 62,* 5543-5548.

Van Swaaij, W.P.M., Charpentier, J.C., Villermaux, J. (1969) Residence time distribution in the liquid phase of trickle flow in packed columns. *Chem. Eng. Sci., 24,* 1083-1095.

Wammes, W.J.A., Middelkamp, J., Huisman, W.J., deBaas, C.M., Westerterp, K.R. (1991) Hydrodynamics in a cocurrent gas-liquid trickle bed at elevated pressures. *AIChE Journal, 37,* 1842-1862.

Wang, R., Mao, Z., Chen, J. (1994) Hysteresis of gas-liquid mass transfer in a trickle bed reactor. *Chinese J. Chem. Eng., 24,* 236-240.

Wang, R., Mao, Z., Chen, J. (1995) Experimental and Theoretical Studies of Pressure Drop Hysteresis in Trickle Bed Reactors. *Chem. Eng. Sci., 50,* 2321 - 2328.

Wang, R., Luan, M., Mao, Z., Chen, J. (1997) Correlation between hysteresis of gas-liquid mass transfer and liquid distribution in a trickle bed. *Chinese J. of Chem. Eng., 5,* 135-139.

Wang, R., Mao, Z., Chen, L., Chen, J. (1998a) Experimental evidence of hysteresis of pressure drop for countercurrent gas-liquid flow in a fixed bed. *Chem. Eng. Sci., 53,* 367-369.

Wang, R., Mao, Z., Chen, J. (1998b) A new instrumentation for measuring the small scale maldistribtuion of liquid flow in trickle beds. *Chem. Eng. Comm., 163,* 233-244.

Wang, Y., Zaisha, M., Jiayong, C. (1999) The relationship between hysteresis and liquid flow distribution in trickle beds. *Chinese J. of Chem. Eng., 7,* 221-229.

Watson, P.C., Harold, M.P. (1993) Dynamic Effects of Vaporization with Exothermic Reaction in a Porous Catalytic Pellet. *AIChE Journal, 39,* 989-1006.

Welty, J., Wicks, C.E., Wilson, R.E. (1984) *Fundamentals of momentum, heat and mass transfer – 3rd ed.* John Wiley, New York.

Wu, Y., Al-Dahhan, M.H., Khadilkar, M.R., Dudukovic, M.P. (1996) Evaluation of Trickle Bed Reactor Models for a Liquid Limited Reaction. *Chem. Eng. Sci., 51,* 2721-2725.

Yang, X.L., Euzen, J.P., Wild, G. (1990) Residence time distribution of the liquid in gas-liquid cocurrent upflow fixed bed reactors with porous particles. *Chem. Eng. Sci., 45,* 3311.

Yin, F., Afacan, A., Nandakumar, K., Chuang, K.T. (2002) Liquid Holdup Distribution in Packed Columns: Gamma Ray Tomography and CFD Simulation. *Chem. Eng. Proc., 41,* 473-483.

Zimmerman, S.P., Ng, K.M. (1986) Liquid distribution in trickling flow trickle-bed reactors. *Chem. Eng. Sci., 41,* 861-866.